THE CRYOGENIC DARK MATTER SEARCH LOW IONIZATION-THRESHOLD EXPERIMENT

BY

RITOBAN BASU THAKUR

DISSERTATION

Submitted in partial fulfillment of the requirements
for the degree of Doctor of Philosophy in Physics
in the Graduate College of the
University of Illinois at Urbana-Champaign, 2015

Urbana, Illinois

Doctoral Committee:

Professor Douglas Beck, Chair
Daniel Bauer, Director of Research (Center for Particle Astrophysics, Fermilab)
Professor Brian Fields
Professor Jon Thaler

Abstract

Over 80 years ago we discovered the presence of Dark Matter in our universe. Endeavors in astronomy and cosmology are in consensus with ever improving precision that Dark Matter constitutes an essential 27% of our universe. The Standard Model of Particle Physics does not provide any answers to the Dark Matter problem. It is imperative that we understand Dark Matter and discover its fundamental nature. This is because, alongside other important factors, Dark Matter is responsible for formation of structure in our universe. The very construct in which we sit is defined by its abundance. The Milky Way galaxy, hence life, wouldn't have formed if small over densities of Dark Matter had not caused sufficient accretion of stellar material.

Marvelous experiments have been designed based on basic notions to directly and in-directly study Dark Matter, and the Cryogenic Dark Matter Search (CDMS) experiment has been a pioneer and forerunner in the direct detection field. Generations of the CDMS experiment were designed with advanced scientific upgrades to detect Dark Matter particles of mass $\mathcal{O}(100)$ GeV/c^2. This mass-scale was set primarily by predictions from Super Symmetry. Around 2013 the canonical SUSY predictions were losing some ground and several observations (rather hints of signals) from various experiments indicated to the possibility of lighter Dark Matter of mass $\mathcal{O}(10)$ GeV/c^2. While the SuperCDMS experiment was probing the regular parameter space, the CDMSlite experiment was conceived to dedicatedly search for light Dark Matter using a novel technology.

"CDMSlite" stands for CDMS - **l**ow **i**onization **t**hreshold **e**xperiment. Here we utilize a unique electron phonon coupling mechanism to measure ionization generated by scattering of light particles. Typically signals from such low energy recoils would be washed under instrumental noise. In CDMSlite via generation of Luke-Neganov phonons we can detect the small ionization energies, amplified in phonon modes during charge transport. This technology allows us to reach very low thresholds and reliably measure and investigate low energy recoils from light Dark Matter particles. This thesis describes the physics behind CDMSlite, the experimental design and the first science results from CDMSlite operated at the Soudan Underground Laboratory.

To my parents, wherever I stand today, it is because of their selfless love and endless support.
To my uncle, for teaching me semiconductor physics whilst my peers worried about cricket balls.

To Fermilab, for inspiring and enabling me to pursue great physics; never a dull day at WH !
And to the wonderful city and people of Chicago, for letting me maintain a very interesting life.

Acknowledgments

My participation in the field of Dark Matter physics was serendipitous. I will use this opportunity to thank those who knowingly or unknowingly helped me in this most wonderful journey.

At UIUC after a year of thorough coursework I joined the Nuclear Physics group under an amazing advisor, and amongst a brilliant group of friends. While I was learning great physics, I had not found that one question I would answer for my PhD. The inspiration came from Joel Primack's colloquium, "The History and Future of Dark Matter". With gusto he examined the Dark Matter *problem*. The message sank in and I spent days reading papers and doing calculations; my bafflement only increased. It is difficult to accept nonchalantly the fact that all our progress explained just 5% of the universe. A solid 27% is something observed repeatedly, always indirectly, and with barely any documented properties. Thus from this colloquium I had found my purpose.

With trepidation I told my advisor, Doug Beck, where my mind was and that I wanted to switch projects. This was non-trivial since UIUC did not have any Dark Matter experiments (although Brian Fields had a great theory course). Doug was fantastically welcoming and announced his full support. From personal studies and a TV program I found the "CDMS experiment" to be absolutely fascinating. That summer I went to Boston and had extremely educative discussions with Chris Stubbs (at Harvard) and Tali Figueroa (at MIT and a CDMS PI) on the prospects of pursuing a PhD in Dark Matter physics, particularly with the CDMS collaboration. The final step toward this goal was achieved with great support from Erik Ramberg (Fermilab) and Tali. They helped me meet Dan Bauer, CDMS PI and deputy director of the Center for Particle Astrophysics at Fermilab. He would become my research advisor at Fermilab, where all my exciting years of graduate school have been spent. Dan was more than generous in accepting me into his group, and not enough words can be strung together to express my gratitude. With Doug letting me go and Dan taking me in, I was able to work on the very science and experiment I yearned for.

My years at Fermilab have been splendid. Working with the best minds in particle astrophysics has been a very special experience. Having Dan as my advisor has been tremendous, his sage words and continued support have immensely improved my scientific purview. Alongside Dan I worked very closely with Jeter Hall (now at PNNL), Lauren Hsu, Sten Hansen and Ben Loer on CDMS. Particularly, Jeter introduced me to CDMSlite and patiently answered a multitude of silly questions everyday. Jeter and Lauren were instrumental not only in my "orientation" of the CDMS experiment, but vital in teaching me experimental high-energy physics techniques. Working with Sten was extremely beneficial for my hardware efforts, and Ben has graciously humored and supported me on various cool projects. While my undeclared incessant walk-ins probably interrupt their work flow, I come out of their offices with new ideas every time. This truly applies to all members of FCPA, PPD and SiDet who have immensely enlightened me. I am greatly indebted to Fermilab for the intellectual exposure and liberty of research I experienced.

Beyond Fermilab I was also heartily welcomed by the CDMS collaboration, and what a fantastic collaboration it is! I thank Matt Pyle and Bruno Serfass for providing me with a plethora of essential information, supporting discussions and some solid good times. Chats with Nader Mirabolfathi, Kyle Sundqvist and Arran Phipps helped me understand our detectors. On the software end, without Lauren, Bruno and Ben, nothing of value would get done. Between the hardware and software there's the DAQ, and on that I have received immense support from Joel Sanders, Ben Loer and Don Holmgren. Then of course David Moore, Scott Hertel and Ray Bunker, CDMS alumni who helped me learn various nuances of the analyses. Dave and Scott mentored me on the first of several Soudan shifts, bestowed upon me numerous MATLAB tricks, and in one instance helped me save the experiment from an underground fire (of course with Dan on the phone). This document is heavily influenced by their splendid theses. I have been fortunate in cherishing several scientific discussions and beverages with Adam Anderson, Julien Billard, Brett Cornell, Alex Leder, Mark Pepin, Yohan Ricci, Kristi Schenck, Silvia Scorza and Brad Welliver to name a few.

This extraordinary list naturally extends to include friends at Fermilab, Souvik Das, Joe Grange, Walter Hopkins, Gene Kafka, Teppei Katori, Tim Linden, Vito Lombardo, Joel Mosseau, Adam Patch, Federico Sforza and all the GSA/URA cohorts! Being at Chicago, I befriended several U Chicago folks particularly Chris Kelso, Gabe Lee and Josh Schiffrin who have patiently humored me. An essential tip of the hat to the Urbana gang for all those nights with outrageous integrals, philosophical disseminations and delectable libations: Vineet Abhishek, Nachiketa Chakraborty, Onyeama Osuagwu, Sandeep Pawar, Maksim Sipos and Alex Weiss, thanks for being there for me.

I must sincerely acknowledge the indispensable suggestions generously provided by several CDMS PI's, particularly Blas Cabrera, Priscilla Cushman, Richard Partridge, Bernard Sadoulet, Philippe Stefano, Wolfgang Rau. Even the shortest communications with Blas greatly influenced my knowledge of detector physics and I am quite indebted for his mentorship. I am particularly grateful to Bernard's Berkeley team for hosting me several times to run experiments at their test facility. Finally, the staff at Soudan (Jim, Dano, Dave, Denise and others) should be graciously thanked, without whom none of this would ever happen. I have been a troublemaker and these kind people graciously helped me in doing things right. And last but not least, Mike Suchor (UIUC) and Seton Handsville (FCPA), for helping me with every bit of non-physics task that I came across. Without them I simply would not have been able to live, travel and do good science.

This research was partly supported by URA Visiting Scholar Award # 13-S-04.

Table of Contents

Chapter 1

Existence of Dark Matter

The formation of the structure we see in the cosmos today has been driven by the interaction of mass and energy in an expanding universe. Decades of research, including precision measurements and groundbreaking work in theoretical and computational cosmology, have concluded that dark matter constitutes ∼27% of the mass / energy content of the universe. Dark Matter is pivotal in determining the structures seen in "normal matter" which is abundant at a ∼5% level. Dark energy, effectively a fluid with negative pressure, dominates at ∼68% level and little is known about it.

The central role of dark matter in the dynamics of the universe was discovered by Fritz Zwicky in his study of the Coma cluster in 1933[1]. A historical quote describing the dark matter problem in Coma, from Ref. [1], states

"If this [overdensity] is confirmed we would arrive at the astonishing conclusion that dark matter is present [in Coma] with a much greater density than luminous matter."
He continues: "From these considerations it follows that the large velocity dispersion in Coma (and in other clusters of galaxies) represents an unsolved problem."

The history of dark matter is covered in several popular publications, Refs. [1, 2, 3, 4]. This chapter will overview the important measurements which have given us the current picture of the constitution of the universe shown in Fig. 1.1, particularly focusing on why the various observations require a new type of matter. This data driven model of cosmology is called the ΛCDM model where Λ is symbolic for dark energy and CDM stands for Cold (non-relativistic) dark matter.

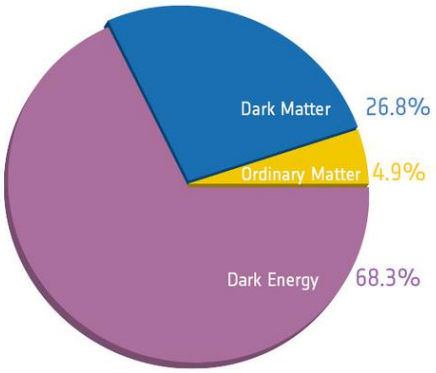

Figure 1.1: Current distribution of mass-energy in the universe as interpreted from the latest measurements by the Planck experiment [5, 6, 7].

[1]Zwicky's noted mass-to-light excess was a factor of 400, which was later corrected to be a factor of 50, [1].

1.1 A short summary of the early universe

The history of the universe is understood in the paradigm of big-bang cosmology. The mass-energy content of the universe drives its expansion and local gravitational effects produce various structures, which have been well measured. As many good references on cosmology are available [8, 9, 10, 11], I will briefly summarize the essential structures relevant to understanding dark matter using the graphical guide shown in Fig. 1.2.

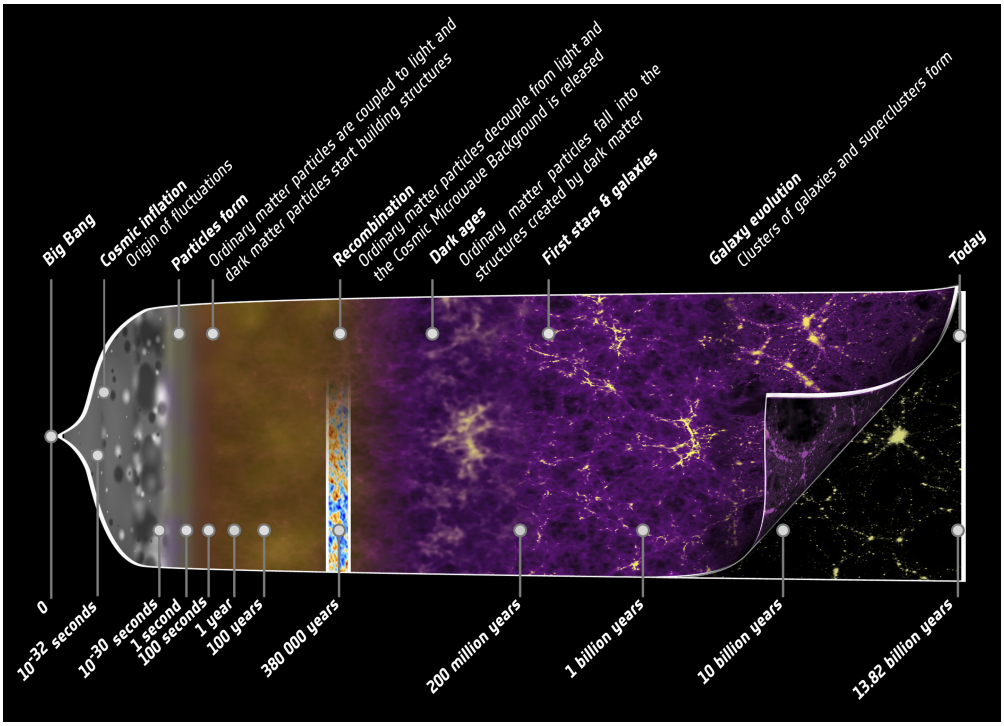

Figure 1.2: A schematic, showing the evolution of the universe, taken from [12].

- **0 to 100 seconds:** Following a period of rapid inflation, normal matter particles such as leptons and baryons as well as dark matter formed from fluctuations of primordial quantum fields in processes known as leptogenesis and baryogenesis and "darkogenesis"; the exact physical mechanisms active in this period are still topics of active research. The extremely high temperatures (T= $10^{30} - 10^{15}$ K in roughly $10^{-35} - 10^{-10}$ seconds) resulted in a universe primarily constituted of out-of equilibrium quark-gluon and lepton-photon plasma.

  With rapid expansion and cooling, equilibration mechanisms altered the density of various particle species. Particle populations were unstable when the average temperature was higher than those particles' rest masses. However as the temperature decreased, mechanisms of creation / annihilation of such particles were exponentially suppressed and their number densities underwent a "freeze-out". Weakly interacting particles, such as dark matter, are estimated to have frozen out at T$\sim 10^{14} - 10^{13}$ K, and neutrinos at T$\sim 10^{10}$ K; further discussion is presented in Sec. 2.1.2.

- **100 seconds to 380,000 years:**

  The temperature at the beginning of this epoch was T$\sim 10^9$ K and the universe was cold enough for light nuclei to be formed in equilibrium, and this is the the period of Big-Bang-Nucleosynthesis (BBN). BBN describes how light nuclei formed in the early universe after neutrons and protons were stable. Apart from massive stars and rocky objects, most of the universe is still comprised of light nuclei like H and He. BBN predictions have been generally matched by observation and these provide an important independent measurement of the current baryon density $\Omega_b \lesssim 0.05$ [13, 14].

  As the temperature reduces from 10^9 K to 3000 K, "recombination" sets in. Recombination is a short period where radiation and matter decouple, i.e., the universe has expanded enough that photons can stream freely with mean free paths in the order of the universe's scale as electrons and protons form neutral hydrogen. These decoupled photons are redshifted as the universe expands and form the Cosmic Microwave Background (CMB) seen today. The CMB is a black body spectrum with small spatial undulations which are very helpful in characterizing the distribution of dark matter from this period; the CMB dark matter connection will be explored in Sec. 1.2.5.

- **380,000 years to 200 million years:** Colloquially called the "Dark ages", in this epoch the gravitational over densities formed by clustering dark matter over the last epoch causes diffuse baryonic matter to fall into the gravitational wells seeding the birth of Large Scale Structures (LSS). Measurement of LSS give us a clear indication of the dark matter content of the universe, and will be discussed in Sec. 1.2.4.

- **200 million years to 13.8 billion years (today):** This is the epoch where structure formation of "normal matter" happens. First, the in-falling baryons produce stars, which slowly cluster into galaxies. Then these galaxies ,via gravitational attraction, produce galaxy clusters and super clusters leading to large scale structures. Such formation processes are ongoing, albeit at a smaller rate. At the present time (10-13.8 billion years), structures are generally affected by local gravitational effects and all large scale dynamics starts being dominated by dark-energy. This is also the epoch where gas clouds in galaxies cool and coalesce to form rocky systems like asteroids and planets. Galaxies and galaxy clusters show the presence of dark matter in stark detail, and their role in understanding dark matter will be discussed in Sec. 1.2.3 and 1.2.2

1.2 The Structural case for Dark Matter

Dark matter provides the scaffolding on which structures of normal matter form. These structures span seven orders of magnitude in length-scales (in units of kiloparsecs[2]) as shown in 1.1.

Item	Length-scale (in kiloparsecs)
Dwarf galaxies (Spheroidal)	$\mathcal{O}\left(10^{-1 \text{ to } 0}\right)$
Dwarf galaxies (Elliptical)	$\mathcal{O}\left(10^{0 \text{ to } 1}\right)$
Spiral galaxies	$\mathcal{O}\left(10^{1 \text{ to } 2}\right)$
Galaxy clusters	$\mathcal{O}\left(10^{2 \text{ to } 3}\right)$
Super-clusters	$\mathcal{O}\left(10^{3 \text{ to } 4}\right)$
Large Scale Structures	$\mathcal{O}\left(10^{4 \text{ to } 5}\right)$
CMB	$\mathcal{O}\left(10^{6}\right)$

Table 1.1: Various astrophysical and cosmological structures as observed in our universe, spanning 7 orders of magnitude in length-scales, indicate consistently to the existence of dark matter.

For any species s that contributes to the mass-energy of the universe, the cosmological density is defined as $\Omega_s = \rho_s / \left(3H^2/8\pi G\right)$, where ρ_s is the mass-density of the species and the combination $\left(3H^2/8\pi G\right)$ is the critical density of the universe, governed by the Hubble expansion constant H and gravitational constant G [8, 9, 10, 11]. In the following discussion the fraction Ω_{DM}/Ω_M will be used to indicate the over density of dark matter over normal matter (since baryons are typically heavier than leptons, normal-matter is referred to as baryonic matter).

1.2.1 Dwarf Galaxies

Dwarf galaxies span a range of 0.1 to a few kpc in diameter and typically contain a few billion stars. Hence compared to galaxies like the Milky Way with $\mathcal{O}\left(100\right)$ billion stars, these are small and faint galaxies often difficult to detect. However advances in telescope technology, particularly the Sloan Digital Sky Survey (SDSS) [15], led to detection of several dwarf galaxies and numerous studies show excesses in the mass-luminosity relation, indicating a large abundance of dark matter relative to normal matter [16, 17, 18, 19].

From spectroscopic techniques one can measure the velocity-dispersion of stars in dwarf galaxies [20, 17]. The velocity dispersions would be expected to decrease with increasing distance from the galactic center following the virial theorem[3]. Some measurements of such velocity-dispersions in spheroidal dwarfs are shown in Fig. 1.3.

[2] 1 kpc=3261.63344 light years. For reference the Milky-Way galaxy is about 31-37 kpc in diameter, and the sun is at 8.3 kpc from its center.

[3] For a stable system of bound particles, the virial theorem relates the average kinetic to potential energy as, $\langle \text{KE} \rangle = -0.5 \langle \text{PE} \rangle$. In the case of quasi-identical particles in a gravitational field, the RMS velocity, hence dispersion of velocities, is a good measure of the mass content of the system, $\sqrt{\langle v^2 \rangle} \sim \sigma_v \sim \bar{M}(r)/r$.

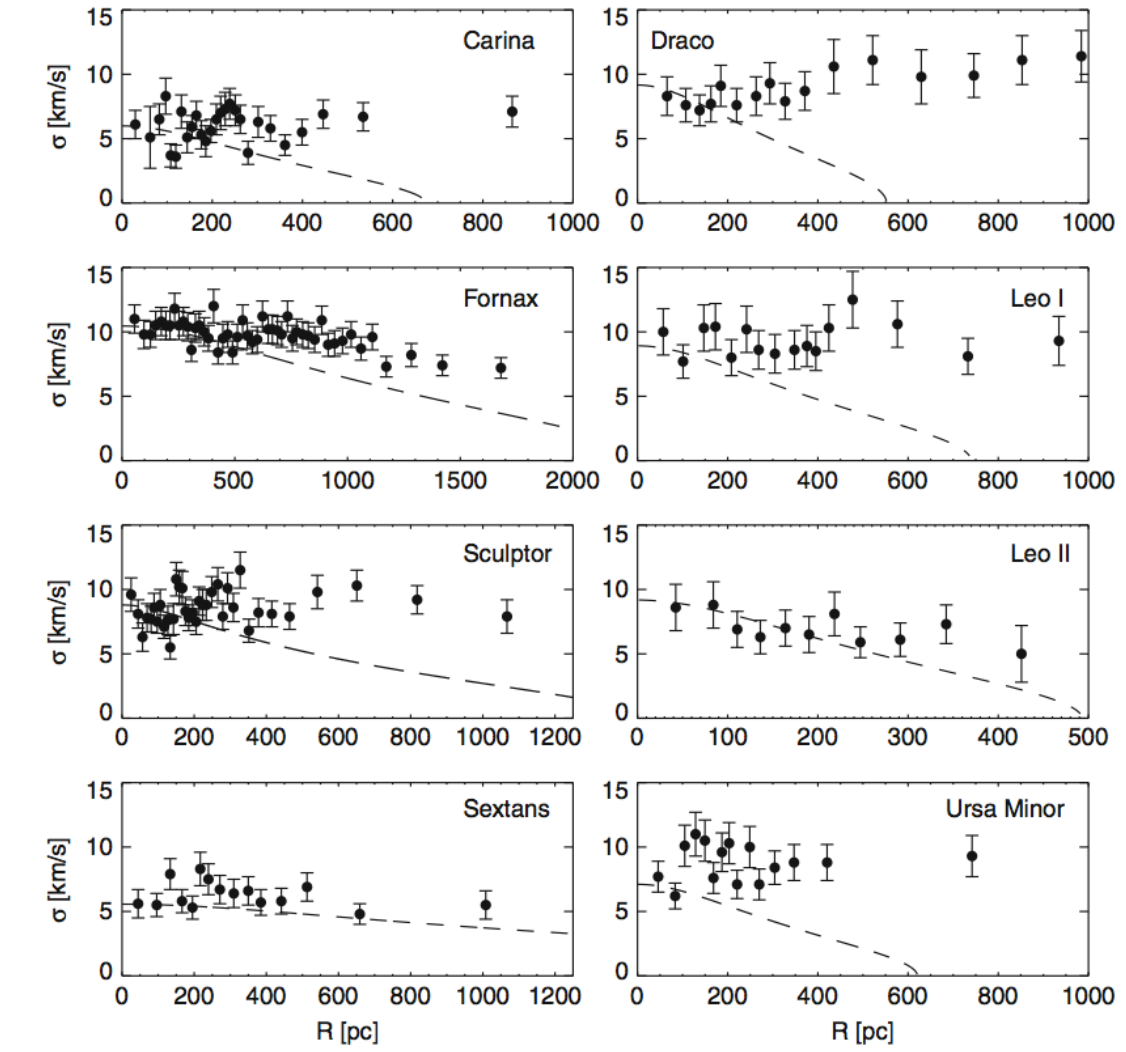

Figure 1.3: Velocity dispersion measured as a function of distance in various dwarf galaxies (spheroidal) [18]. Dwarf spheroidal radii are < 500 pc (e.g., Segue I has 30 pc half-light radius), and beyond that length-scale the velocities are expected to fall with distance. The expectations based on normal matter are drawn in dashed lines. Clear excesses are noted and are attributed to the presence of substantial dark matter.

As shown in Fig. 1.3, the velocity-dispersion does not reduce with distance as expected, particularly far from the half-light-radii which are $\lesssim 100$ pc. This indicates that gravitational mass content extends well beyond such optical length-scales, i.e., these galaxies reside in large dark matter halos. These velocities can be used to infer the extent of gravitational mass in such galaxies. A survey done by Strigari et al [16] compares the inferred mass from velocity dispersion to the luminosity as measured for a variety of dwarf galaxies (including those from Fig. 1.3). Stellar formation theory predicts the mass-luminosity ratio to scale as a power law viz. $(M_\star/M_\odot)^{3-4} \approx L_\star/L_\odot$. In Fig. 1.4 from the survey, this relation is not only absent, but the masses given the measured luminosities are noticeably higher than what the standard power-law predicts [16, 18].

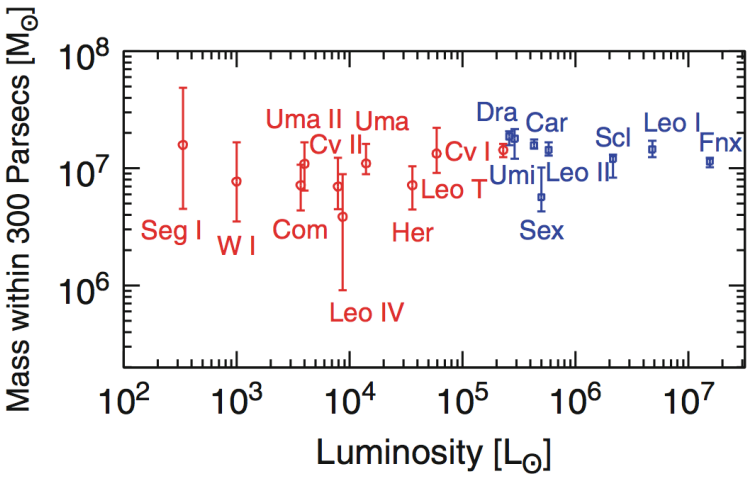

Figure 1.4: Plot showing mass inferred from velocity dispersion versus luminosity for various dwarf galaxies [16]. Ultra-faint galaxies discovered recently (2004-2008) are shown in red and standard galaxies are in blue.

From these observations, dwarf galaxies are found to be the most dark matter rich astrophysical objects. An estimate for the dark matter fraction in dwarf galaxies may be obtained from Ref. [19]. For Draco as a particular example, the dynamical mass to stellar mass ratio, Ω_{DM}/Ω_M, is about 38.

1.2.2 Spiral Galaxies

Spiral galaxies like the Milky Way also show clear evidence for dark matter, with pioneering measurements made by Vera Rubin of Andromeda Galaxy's rotation curve [21]. Such velocities are inferred from the Doppler shifts of various spectral lines (e.g., rotational CO lines or the 21 cm spin-flip transition of neutral hydrogen). While most of the luminous matter resides within 50 arc-minutes from the galactic center for Andromeda (M31), the velocities of stars out to over 100 arc-minutes appear spatially constant, Fig. 1.5. While one expects the velocities of stars to fall with distance as $v(r) \approx \sqrt{G\bar{M}/r}$ ($\bar{M}$ is the mass of the galaxy), the data shows consistent high velocities well over 50 arc-minutes.

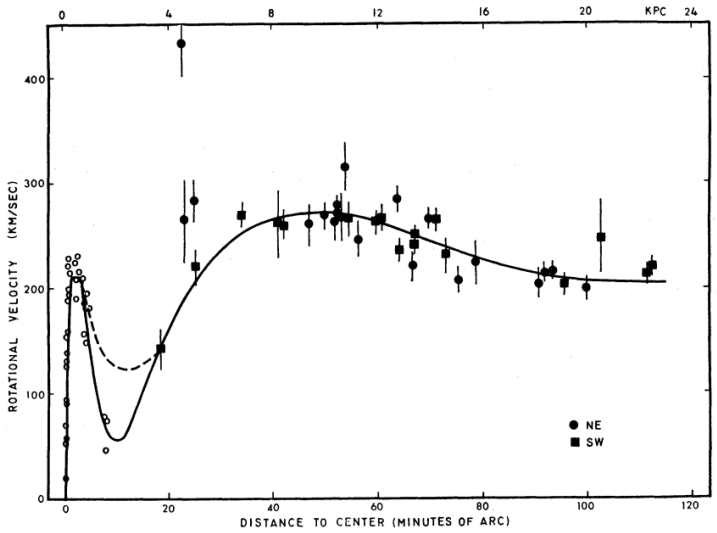

Figure 1.5: Rotational velocities for stars in Andromeda (M31) [21]

Rotation curves for many other spiral galaxies, shown in Fig 1.6 confirm the notion that these objects reside within extended halos of dark matter [22, 23].

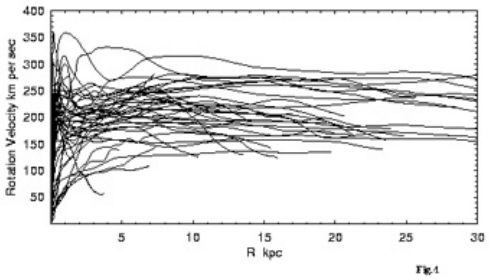

(a) Rotation curves from many spiral galaxies [22]

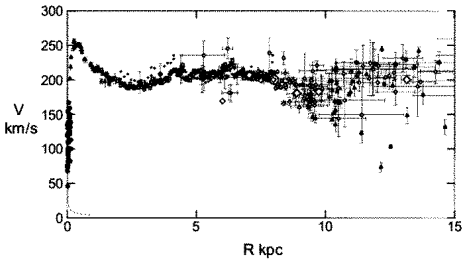

(b) Rotation curves from many Milky-Way [23]

Figure 1.6: Several rotation curve measurements showing that dark matter is abundant in various galaxies, in particular the Milky-Way.

For the Milky Way as an example, the dark matter to normal matter ratio can be inferred by approximating the luminous mass via the number of stars ($\approx 3 \times 10^{11}$), and from the dark matter halo mass inferred from rotation curves. The Milky Way's total mass is $\approx 1.25 \times 10^{12} M_{\odot}$, thus $\Omega_{DM}/\Omega_M \gtrsim 3$. Not all stars are sun-like, hence this is merely a working approximation.

1.2.3 Galaxy Clusters

In these conglomerates of gravitationally bound galaxies the evidence for dark matter has been thoroughly accounted for. The Coma cluster, mentioned in the introduction, was studied by Zwicky and provided the first solid evidence for dark matter via discrepancies in velocities and luminosities, in a manner similar to the dwarf galaxy studies outlined earlier.

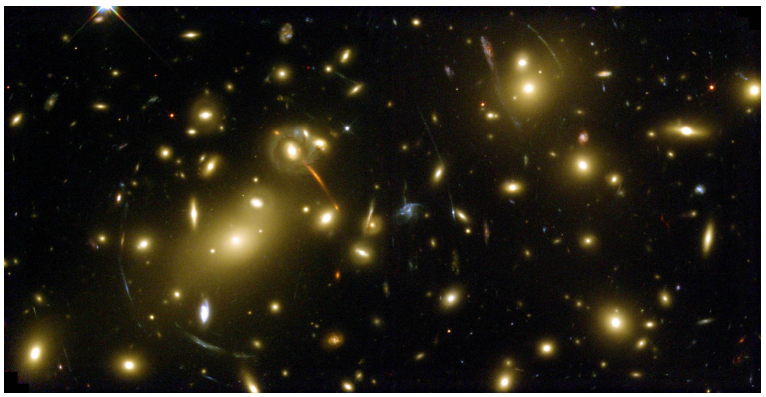

Figure 1.7: Gravitational lensing observed in Abell 2218 cluster is indicative of a large dark matter-halo [24]. Credit: NASA.

Since Zwicky's discovery of dark matter in the Coma cluster, galaxy clusters have provided additional evidence for dark matter via gravitational lensing. General relativity tells us that an object between a light source and us will warp space time by virtue of its mass-energy, and distort the straight-line path that the photons would normally take. This causes point-like background sources to be shaped into arcs or rings. Precise measurements of such geometrical distortions are predictive

of the line-of-sight mass-abundance. The Abell 2218 cluster, Fig. 1.7, produces prominent arc like images of background sources. The mass content required for such space-time curvature is not accounted for by the foreground luminous objects, and thus points to the presence of dark matter. In the primary publication on Abell 2218 [24], studies of optical and x-ray emissions along with lensing conclude a baryonic fraction of $f_b \approx (0.04 \pm 0.02)h^{-3/2}$, which assuming a reduced Hubble constant of $h \approx 0.72$, gives us $\Omega_{DM}/\Omega_M > 10$.

Interacting galaxy clusters have proven particularly helpful in not only "seeing" dark matter but also understanding some fundamental properties. These interacting clusters are imaged in three ways, optical photons, x-ray emissions and gravitational-lensing. In the cluster IE 065756 also known as the "Bullet-cluster", shown in Fig. 1.8, the dark matter passed through with minimal interaction, while the normal matter is seen to have experienced "friction". Interestingly, from these bullet clusters one can constrain the dark matter self interaction cross sections to be $\sigma_{DM-DM}/m_{DM} < 1$ cm^2/g.

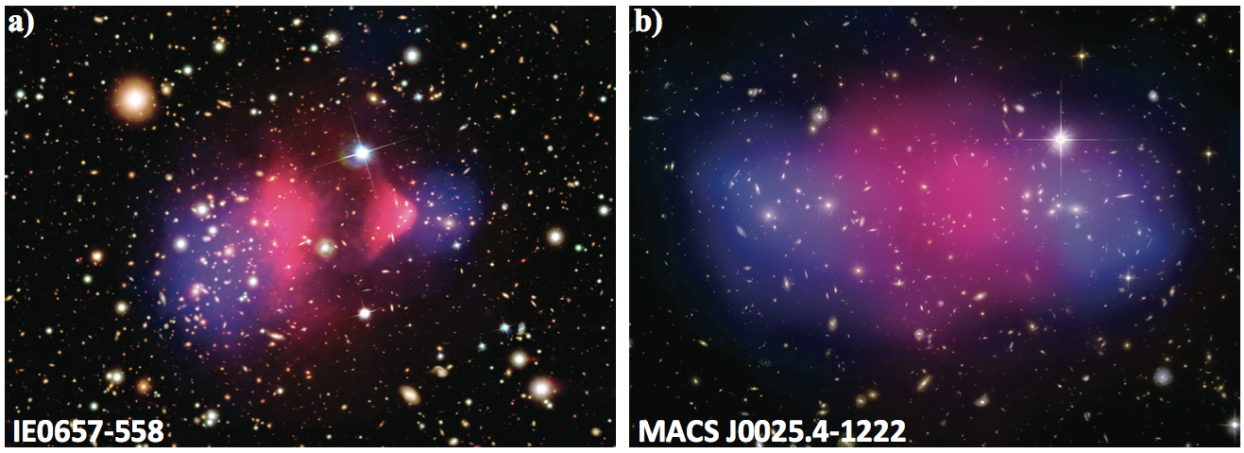

Figure 1.8: Two examples of galaxy mergers imaged in in three ways, optical photons (true yellow-scale color), x-ray emissions (false red-scale color) and gravitational-lensing (false blue-scale color). The distribution of x-rays and lensing indicates strongly the presence of dark matter halos in these galaxies. Figure adapted from Ref. [25]

1.2.4 Large Scale Structures (LSS)

Surveys of the universe in large redshift slices have revealed informative structures. The Sloan Digital Sky Survey (SDSS), Two-degree-Field Galaxy Redshift Survey (2dFGRS) and others have generated vast and detailed catalogues up to distances of 338 Mpc (or 0.078 redshift). Filamentary structures are seen in these data, and the characteristic length-scale of such structures are indicative of the amount of dark matter present in the universe. Light and fast dark matter particles should have washed out structural details whereas slow and heavy dark matter would cause matter to aggregate in clumps. Sophisticated simulations of clustering done with varying dark matter properties show qualitative matches between cold (non relativistic) dark matter with $\Omega_{DM}/\Omega_M \sim 5$, and various LSS observations, see Fig. 1.9 from Ref. [26, 27].

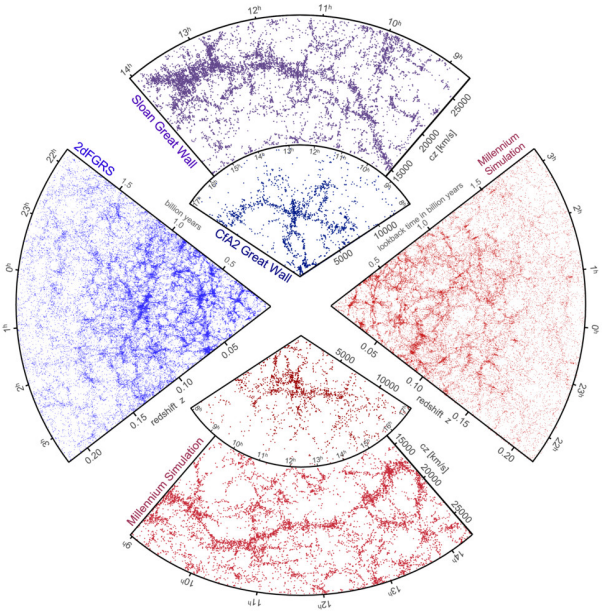

Figure 1.9: The top left figures are data from Large Scale Structures from SDSS, 2dFGRS and CfA. At the bottom and on the right, mock galaxy surveys constructed using semi-analytic Millennium simulation are shown. Striking similarities are seen between data and simulation for cold dark matter present at relative abundance of $\Omega_{DM}/\Omega_M \sim 5$ [26]

In the early universe, prior to recombination, photons and baryons were coupled tightly into a plasma via electron scattering. For any compact hot-spot of matter and radiation at this time, the high radiation pressure drove this spot to expand against gravitational forces. At recombination the formation of neutral hydrogen reduced the radiation pressure, thus the outward shock could not compete with gravity and the matter eventually collapsed back. The maximum radius of this shock front and the final distribution from gravitational collapse was controlled by the amount of dark matter to normal-matter present at that time. This phenomenon of Baryon Acoustic Oscillation (BAO), has been measured by the Baryon Oscillation Spectroscopic Survey (BOSS[4]), by studying the two-point correlation[5] of structures, such as those from Fig. 1.9. The impressive result from a recent publication [28], is shown in Fig. 1.10. The BAO radius peaks at $\mathcal{O}(100)$ Mpc as is expected from the ΛCDM model where $\Omega_M \approx 5\%$, $\Omega_{DM} \approx 27\%$, $\Omega_\Lambda \approx 68\%$ [28, 6, 7].

[4]BOSS is the largest component of the third Sloan Digital Sky Survey (SDSS-III).

[5]The two point correlation function encodes structural similarities, such as number of stars in a box at two different points (1,2) as $C(x) = \langle n(r_1)n(r_2 = r_1 + x)\rangle$.

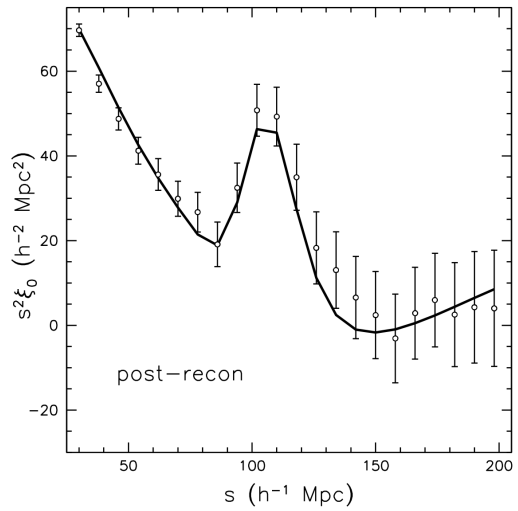

Figure 1.10: Two point correlation function of matter distribution as measured and computed by the BOSS experiment [28]

1.2.5 Cosmic Microwave Background

Around 380,000 years after the Big-bang the universe had expanded and cooled enough for neutral hydrogen production to dominate, and thus radiation streamed freely. To first order the photons from this recombination era have a black body intensity distribution. However when these photons started streaming the universe wasn't absolutely isotropic and various structures present at that time affected how the photons propagated. Today, we measure these photons as red-shifted in the microwave band ($\mathcal{O}(100)$ GHz) with a blackbody temperature of 2.7 K and anisotropies at the level of ± 0.57 mK. This radiation is called the Cosmic Microwave Background (CMB). Several experiments starting with the discovery of the CMB by Penzias and Wilson in 1965 to the recent Planck experiment in 2013 have measured the CMB intensity and polarization fields with unprecedented precision. The power spectra, computed in spherical coordinates, from various experiments are shown in Fig. 1.11.

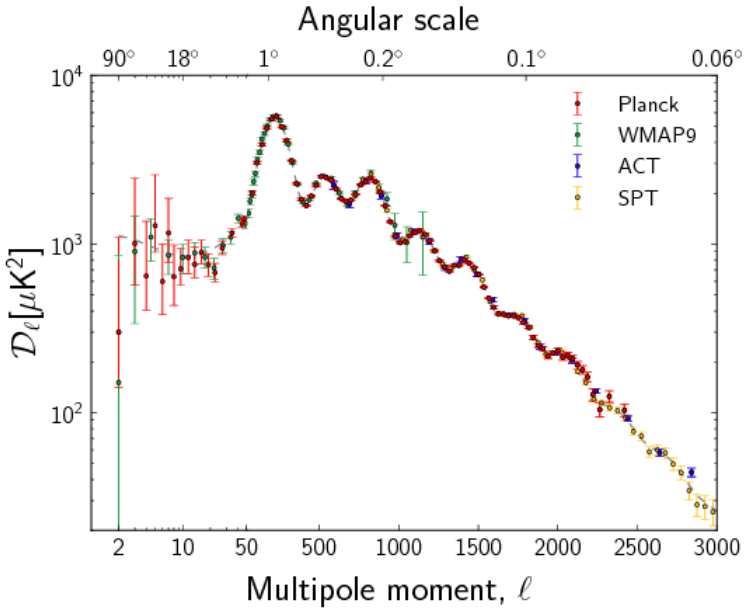

Figure 1.11: Compilation of various CMB temperature anisotropy power spectrum measurements from Ref. [7]. The horizontal axis is logarithmic up to multipole l=50, and linear beyond that. The vertical axis is the power measured per multipole value. Underlying the various data points a best-fit curve is present, and is derived from theoretical predictions of a ΛCDM universe. The best fit values indicate $\Omega_{DM} = 26.8\%$.

The location of the various spectral peaks and their relative amplitudes inform us of the nature of the universe at time of decoupling. In the pre-recombination plasma, regions of mass over-density cause gravitational infall, only matched by the radiation pressure, and this plasma oscillates driven by instabilities. Dynamically, the baryons and dark matter behave differently since baryons are affected by both the "gravitational-pull" and "radiative-push", whereas dark matter experiences primarily gravity. During recombination when the photons start free streaming, the compactions and rarefactions from the BAO imprint their profile onto the photons.

The location of the first peak in the spectrum in Fig. 1.11, is sensitive to the mass-density and curvature of the universe. The ratio of the first and second peaks depend on baryon density, and the third peak compared to the first two provides information on the dark matter density [29, 30]. In the complete decomposition of spectral information to obtain these densities parametric degeneracies exist, which are broken by making parallel measurements of baryonic density from Big Bang Nucleosynthesis (BBN), dark energy from Supernova surveys etc. During the recombination epoch, dark energy had a minimal role and thus BBN measurements [13, 14] provide the most important constraints on Ω_M. The CMB and BBN measurements combined can hence provide absolute constraints on Ω_{DM}. The current densities of matter, dark matter and dark energy, as shown in Fig. 1.1, are 4.9%, 26.8% and 68.3% respectively. Thus $\Omega_{DM}/\Omega_M \sim 5.5$, i.e., $\sim 84\%$ of the universe's mass is in the form of dark matter.

Chapter 2

Identification of Dark Matter

2.1 Properties of Dark Matter

2.1.1 General qualities

From the various astrophysical and cosmological observations described thus far, dark matter is likely to consist of particles that are:

- **Massive, cold and weak:** All evidence for dark matter till date have been on inferred from gravitational effects, thus unless it is attributed to a novel modification of standard gravity, it is likely constituted of some massive particle(s). The mass estimate of a dark matter particle is strongly dependent on the theory, some examples will be discussed later in Sec. 2.2. While Modified Newtonian Dynamics[1] had been proposed to explain rotation curves, the bullet clusters discussed in Sec. 1.2.3 make it challenging to describe the patterns noted in x-ray and gravitational lensing maps [31]. Furthermore, the absolute success of the ΛCDM model to explain all the spectral modes seen in the CMB cannot be matched by such theories.

  Structure formation physics, outlined in the previous chapter, strongly indicate that dark matter can't be relativistic as this would wash out several of the smaller length scales seen in LSSs. Particularly the BAO peak measured at 100 Mpc by BOSS shows the necessity of dark matter to be non relativistic or cold. Similarly, the location and ratio of the spectral peaks in the CMB vary greatly if dark matter is non-relativistic [29], thus to match with the measurements dark matter must be cold. Finally since no evidence of dark matter particle interactions have been detected so far, and we infer that dark matter is probably weakly interacting. The strength of interaction, much like the particle mass scale is subject to choice of model, and hence these comments are not absolute.

- **Stable and Abundant:** Properly comparing the dark matter abundance as measured in the early universe (CMB, BAO etc.) to current times (rotation curves, dwarf galaxies etc.), we note that the amount of dark matter has not decreased drastically with time, thus implying dark matter particles are stable over several billion years, and today there is about 5 times more dark matter than baryons.

- **Collisonless and dissipationless:** In the description of the bullet clusters in Sec. 1.2.3, we saw that matter in merging galaxies, via collisions, form a shock front while the dark

[1] In MOND, Newtonianian gravitational acceleration gets a multiplicative correction as $\vec{a} = \vec{g}/\mu(\vec{a}/a_0)$. The function μ depends on acceleration itself as $\mu(x) \to 1,\ x \gg 1$ and $\mu(x) \to x,\ x \ll 1$. This ensures that near galactic centers, standard gravity explains standard stellar orbital speeds, however far away the speeds correct themselves so as to not fall off as $1/\sqrt{r}$. Note that MOND is an empirical and simple theory, and perhaps more elaborate modifications of gravity may be constructed to explain dark matter as a gravitational effect.

matter clusters showed no deformation. Thus self interaction of dark matter is very weak. In terms of galaxy formation we understand the flatness of spiral galaxies, for example, as sourced from small initial momentum dispersion and driven by dissipations from interactions (friction). The dark matter halos appear to be more symmetric with no great evidence of over-densities, suggesting that dark matter rarely dissipates energy.

2.1.2 The "freeze-out" argument

Using the the properties discussed above, one can construct a simple model to shed some light on dark matter physics. Consider a particle χ which can pairwise annihilate into Standard Model particles, ψs. By crossing symmetry the reverse also happens. In some fixed region, we thus expect the number densities to come to equilibrium. Folding in metric dilution from universal expansion via a scale-factor $a(t) \equiv r(t)/r(0)$ (corresponds to Hubble expansion, $\dot{a} = Ha$), the time evolution of the number density is given by Eq.(2.1).

$$\frac{d(n_\chi a^3)}{dt} = -\langle \sigma v \rangle \left(n_\chi^2 - n_{eq,\chi}^2 \right) \tag{2.1}$$

In Eq.(2.1) simplifying assumptions have been made such that the particle antiparticle densities are equal, and the cross-sections are the same for annihilation and production channels. In equilibrium the number densities are $n_\psi = n_\chi \equiv n_{eq,\chi}$. Accounting for $a(t)$, this equation can be solved to various levels of accuracy. To gauge the physical outcome a simple algebraic manipulation of Eq.(2.1) is helpful. We carry out the time derivative, keeping in mind the Hubble expansion rate, $H = \dot{a}/a > 0$ and "reaction rate", $\Gamma = n\langle \sigma v \rangle$ and obtain Eq.(2.2) .

$$a^3 \frac{dn_\chi}{dt} = a^3 n_\chi \left[-3H + \Gamma \left(\left(\frac{n_{eq,\chi}}{n_\chi} \right)^2 - 1 \right) \right] \tag{2.2}$$

In Eq.(2.2) the number density is controlled by a competition between the Hubble expansion and the annihilation rates. When $n_\chi > n_{eq,\chi}$ in Eq.(2.2) the right hand side is negative and the rate will decrease until the number density reaches an equilibrium. After this it will "freeze-out" to a constant value[2]. The relic density can be calculated from this freeze out [32], is shown in Fig. 2.1.

$$\Omega_\chi h^2 \approx \frac{3 \times 10^{-27} cm^3 \ /s}{\langle \sigma v \rangle} \tag{2.3}$$

Using reasonable values of $v \approx c \times 10^{-3}$ and $\Omega_\chi h^2 \approx 0.1$, we get $\sigma \approx 10^{-33}$ cm$^2 \sim \sigma_W$. For comparison charge-current neutrino-nucleon cross-sections are $\sigma/E_\nu \sim \mathcal{O}\left(10^{-38}\right)$ cm^2/GeV [33]. Thus dark matter under this thermal freeze-out mechanism has a cross-section comparable to the weak scale. Hence the most common dark matter candidates are called Weakly Interacting Massive Particles or WIMPs, and this mechanism is colloquially known as the "WIMP miracle"[3]

2.2 Dark matter candidates

There is strong evidence that dark matter requires new physics beyond the Standard Model. It does not interact via electromagnetic or strong channels. For if it did, we should be able to see it on

[2]Note: $n_\chi \approx n_{eq,\chi} \rightarrow dn_\chi/dt + 3H = 0 \rightarrow d(n_\chi a^3)/dt = 0$

[3]It is possibly a coincidence and not a "miracle".

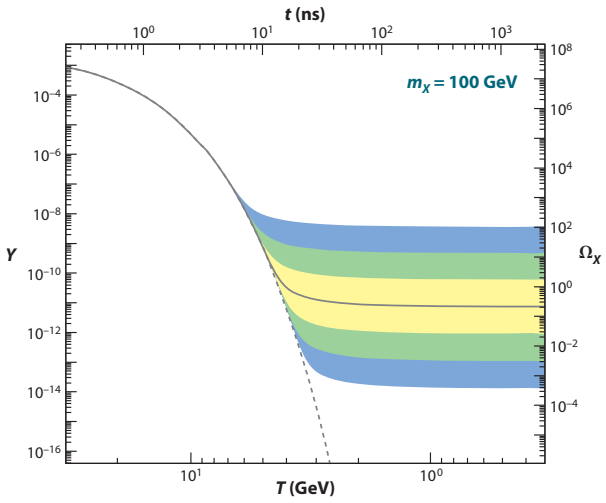

Figure 2.1: Equilibration of dark matter number density in the freeze-out process. The dashed curves shows the equilibrium density if there is no freeze-out. Due to Hubble expansion, after $\mathcal{O}(10)$ ns the number density becomes constant. These rates are computed for a 100 GeV/c^2 dark matter; the colored bands represent varying uncertainties on the cross-sections.

earth or produce it in colliders, and furthermore Big Bang Nucleosynthesis would have drastically different results [13, 34, 14]. The only known neutral WIMPs are neutrinos. It can be shown that the relative abundance of neutrinos scales with the sum of the neutrino masses. Laboratory limits constrain $m_\nu \lesssim 2$ eV, implying a relic density of $\Omega_\nu h^2 \lesssim 0.007$ or $\Omega_\nu h^2 = 0.058 \times \Omega_\chi h^2$ [35]. Additionally, the relativistic nature of neutrinos disallow them from being dark matter from the structure formation point of view.

The need for new physics beyond the Standard Model (SM) was initially theoretical, stemming from attempts at unification of fundamental forces in the early universe. Today it is a practical necessity evident from the abundance of dark matter and dark energy. Theories of unification thus "naturally predict" some dark matter particles. Super Symmetry (SUSY) has been the most prominent of these theories; here every SM particle has a super-partner linked by boson-fermion conversion[4]. SUSY is based on the idea that at high energy scales (early universe) there are fundamental particles which via breaking of supersymmetry form the two separate sectors constituting the observed SM particles and the predicted super partners. Accounting for various mass-scales and coupling-constants, full SUSY can be intractable and one often works with constrained versions of the theory to compute practical predictions [36].

Most SUSY models have a dark matter candidate called the neutralino (χ). Neutralinos are neutral under standard charge quantum numbers, weakly interacting and often one of the lightest massive particles [32]. Due to lack of compelling evidence for SUSY at colliders, and the lack of dark matter signals in direct detection experiments, numerous modifications of SUSY dark matter have been pursued. I will briefly outline some of these candidates, particularly focusing on light dark matter, i.e., dark matter particles with mass $\lesssim \mathcal{O}(10)$ GeV/c^2. The relevance of this mass-scale is empirically driven by the fact that direct detection experiments are rapidly ruling out parameter space for most high mass dark matter models, and because the few experiments which see evidence for dark matter like signals, indicate masses of $\lesssim \mathcal{O}(10)$ GeV/c^2. Details on this will be presented later in Sec. 2.6. General surveys of dark matter candidates may be found in Ref. [35, 37].

[4]For every SM fermion there is a super partner boson and vice-versa, such as electron (fermion) $\leftrightarrow$ selectron (boson), gluon (boson) $\leftrightarrow$ gluino (fermion) etc.

2.2.1 Neutralinos

In this context there are three major classes of SUSY theories listed in order of reducing constraints, (i) minimal supersymmetric extension to the Standard Model (MSSM) [36] (ii) next-to-minimal supersymmetric extension to the Standard Model (NMSSM) [38] and (iii) phenomenological Minimal Supersymmetric Model (pMSSM). In NMSSM, a singlet chiral super field is added to MSSM. In pMSSM the parameters that control the breaking of super symmetry are allowed to float to match experimental constraints [39].

In MSSM neutralino masses had been initially constrained to be $\gtrsim$ 40 GeV/c^{2}from LEP searches [30]. It has been shown that minimizing the mass difference between neutralinos and sbottoms can allow for $\mathcal{O}(10)$ GeV/c^2 WIMPs which satisfy various collider constraints whilst supporting the canonical dark matter properties. Similarly, another option of lowering the stau mass has also been studied [40, 41].

Hints of light WIMPs in direct and indirect detection searches resulted in NMSSM theories with light neutralinos, where instead of fine-tuning MSSM, constraints are reduced to provoke light dark matter more "naturally" by including a singlet super field which provides an additional neutralino degree of freedom allowing for the models to have light dark matter [42, 43, 44]. Finally in the pMSSM framework, one allows for several ($\lesssim$20) SUSY parameters to float, and the viability of theories are tested by imposing various experimental constraints. Recent studies of pMSSM phase space suggests that SUSY theories with light dark matter respecting experimental bounds are possible [45, 46].

2.2.2 Asymmetric Dark Matter (ADM)

While ADM theories work in the SUSY framework, they are considered more natural as they do not rely on the WIMP coincidence discussed in Sec. 2.1.2, provide light dark matter without any tuning, and by construction addresses the matter-antimatter asymmetry problem.

The large matter-antimatter asymmetry observed today is best quoted in the number density fraction of (anti)baryons to photons as $\eta = (n_b - n_{\bar{b}})/n_\gamma$. Following BBN measurements from [13, 14] the asymmetry is constrained to $5 \times 10^{10} < \eta < 6.5 \times 10^{10}$. In the standard neutralino dark matter models the measurement of this asymmetry and the fraction $\Omega_{DM}/\Omega_b \approx 5$ are treated as coincidences. ADM theories connect these, by having a higher dimensional operator that couples some seed asymmetry physics to both dark and visible sector. The theories then dictate that such operators (or the effective mediator) freeze out prior to dark matter becoming non relativistic as the universe cools. This results in frozen-in asymmetry and in each sector particle-antiparticle annihilations proceed to equilibration where only the asymmetric populations remain, and these are the baryons and dark matter we see today. This means that dark matter and normal matter have similar number densities, and thus one obtains a mass prediction for ADM.

$$n_{DM} \approx n_b \;\Leftrightarrow\; m_{DM} \approx m_b \frac{\Omega_b}{\Omega_{DM}} \tag{2.4}$$

This naturally implies $m_{DM} \sim 5$ GeV/c^2 for $m_b \approx m_p = 1$ GeV/c^2. For this general theory small tuning can easily allow for m_{DM} = 5-15 GeV/c^2. The strength of such ADM-nucleon interaction however depends strongly on the choice of the ADM model, such as specifics of asymmetry transfer

and annihilation modes [47, 48, 49]. While originally motivated by the light dark matter situation in direct detection experiments (see Sec. 2.6), constraints from indirect detection from astrophysical and solar processes are being explored [50, 51].

2.2.3 WIMPless dark matter

Like ADM, these theories aim to work around the WIMP coincidence mentioned in Sec. 2.6. The central argument lies in the relic density relation for some decaying species (X).

$$\Omega_X \sim \frac{1}{\langle \sigma v \rangle} \sim \frac{m_X^2}{g_X^4} \tag{2.5}$$

In the WIMP coincidence scenario having $\sigma_X \sim \sigma_W$ gives the observed $\Omega_{X=DM} \sim 0.1$. In these models the right relic density is obtained not by dark matter annihilation, but by the correct choice of (m_X, g_X). The typical theory relies on gauge mediated SUSY breaking where one ends up with a MSSM sector and a hidden sector which contains the dark matter with appropriate (m_X, g_X). This relieves MSSM from having to provide the dark matter particle and satisfy various stringent experimental constraints, and it is no longer necessary that $m_{DM} \approx m_W$, hence such theories are WIMP-less. Other connector sectors are often introduced to allow interaction between the hidden, MSSM and visible sectors [52, 53, 54].

2.2.4 Dark forces

These are simple theories predicting a dark sector comprising of a dark force (new boson) and some dark matter. Specifically these are QED like U(1) theories, and have a dark-photon and a dark-fermion. The dark-photons can interact with normal photons via kinetic mixing and effectively mediate both dark matter annihilation and dark matter-nucleon scattering. While SUSY is not required these theories can be built within a SUSY framework. Such theories with $\mathcal{O}(10)$ GeV/c^2 dark matter have been used to match possible astrophysical annihilation signals via the kinetic mixing of photons. These models are exciting from an experimentalists' view point as well, since non-standard searches can be pursued with dark-box setups where one looks for photon transmission across opaque barriers via conversion to dark-photons [55, 56, 57].

2.2.5 Miscellaneous models

The list of all possible light dark matter models is long and constantly evolving based on experimental constraints. In the sections above I overviewed those that are contemporarily popular. Some other models include mirror matter, scalar singlets, sterile neutrinos and Klauza-Klein states, see Ref. [35, 37]. Operator based dark matter modeling has also been proposed, where the dark matter nucleon coupling is made to depend on dipole/ anapole moments, isospin violation and momentum dependence, see Ref. [58, 59] for recent reviews.

2.2.6 Axions

Axions are the most popular dark matter candidate apart from WIMPs. The theoretical motivation for axions is very strong and does not require complex SUSY like new theories. In QCD the lack of CP violation is known as the strong CP problem. While the QCD Lagrangian has terms that allow for CP violation no such CP violation has been observed, primarily evidenced by the small dipole moment of the neutron. The Peccei-Quinn mechanism addresses this mismatch by introducing a new U(1) symmetry the breaking of which which effectively balances the CP violating terms. In this mechanism the symmetry must be spontaneously broken, which results in a pseudo Nambu-Goldstone boson, called the axion. The axion mass (m_a) and decay-constant (or energy scale f_a) are related as $m_a \approx 6$ meV $\times$ (10^9 GeV/f_a). Much like experimental searches for WIMP dark matter, there are numerous active experimental efforts in detecting axions. A summary of coupling constants and masses probed thus far is presented in Fig. 2.2. Detailed discussion on axions as dark matter and experimental pursuits may be found in Ref. [60, 61, 62, 63, 64].

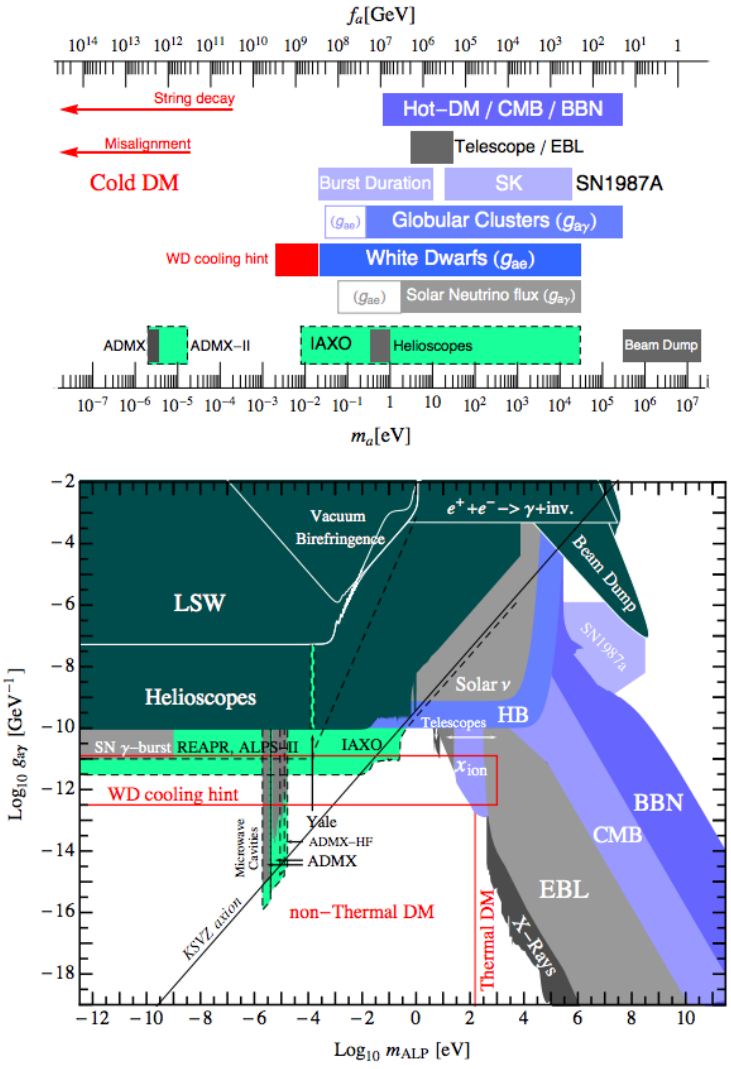

Figure 2.2: Summary of experimental constraints for axions in coupling constant and axion mass adapted from a recent survey in Ref. [64]. The top plot shows constraints for classical axions, while the bottom plots shows constraints for generalized axion like particles. In the bottom plot the photon-axion coupling constant is related to the axion decay constant as $f_a \cdot g_{a\gamma} \sim 10^{10}\text{GeV} \cdot 10^{-13}\text{GeV}$.

2.3 Methodology for identifying Dark Matter

Till date all evidence for dark matter has been obtained via astrophysical / cosmological observations primarily relying on gravitational effects. To probe the particle physics properties of dark matter there are three broad paths physicists are pursuing, schematically shown in Fig. 2.3.

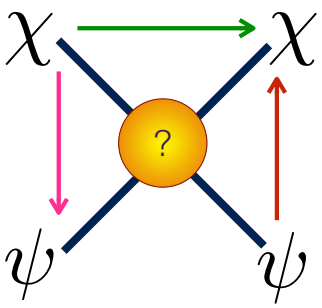

Annihilation $\chi\bar{\chi} \rightarrow \psi\bar{\psi}$

Production $\psi\bar{\psi} \rightarrow \chi\bar{\chi}$

Scattering $\chi\psi \rightarrow \chi\psi$

Figure 2.3: Three ways to hunt for Dark matter. The arrows correspond to the direction of time. Dark matter particles and standard model particles are designated as χ and ψ respectively. The parameters of interest are the dark matter particle's mass (m_χ) and the interaction strength between dark matter and nucleons (effectively the cross-section $\sigma_{\chi,\psi=N}$).

Dark matter search results, in the simplest representation, may be quantified in the plane of dark matter nucleon cross-section[5] and dark matter mass. Closed contours for levels of discovery significance would be drawn in the case of positive signals. However in the absence of significant and verifiable discoveries, limit curves are drawn in this plane where parameter space above the curve are ruled out. As an example consider Fig. 2.4 from the first CDMS II WIMP search analysis [65]. For WIMP masses $\gtrsim 20$ GeV/c^2 portions of theoretically allowed parameter spaces (gray regions) predicting cross-sections of $\gtrsim 10^{-42}$cm^2 were ruled out by the experiment (slid / dashed curves).

Figure 2.4: An old result from the CDMS II experiment showing limits in cross-section mass plane for WIMP dark matter scattering off nucleon. The curves are different 90% CL limits and exclude parameter space above them. The gray regions represent parameter space for dark matter modeled via Minimal Supersymmetric Standard Model.

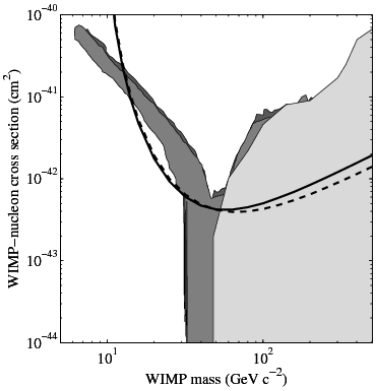

[5]The cross-section is generally normalized to a single nucleon. For indirect detection, the results are reliant on the astrophysical distribution of dark matter and instead of just the cross-section (σ), experiments constrain the thermally averaged $\langle\sigma v\rangle$ to account for velocity dispersions.

2.4 Indirect detection

The relic density discussion in Sec. 2.1.2 relied on the argument of dark matter annihilation in the early universe to form other particles. Today, in regions of dark matter over-densities such as dwarf spheroidals, similar annihilation processes can be expected and dark matter can be identified by searching for such spectral excesses. The Fermi-LAT gamma ray telescope has published limits on dark matter annihilation in dwarf galaxies [66]. These studies compute limits on $\langle \sigma v \rangle$ by assuming general process like $\chi\chi \to \psi\bar{\psi} \to 2\gamma$ and then comparing the measured photon spectrum to those expected from various dark matter models. Such studies have begun constraining the thermal relic picture described in Eq. 2.3, see Fig. 2.5.

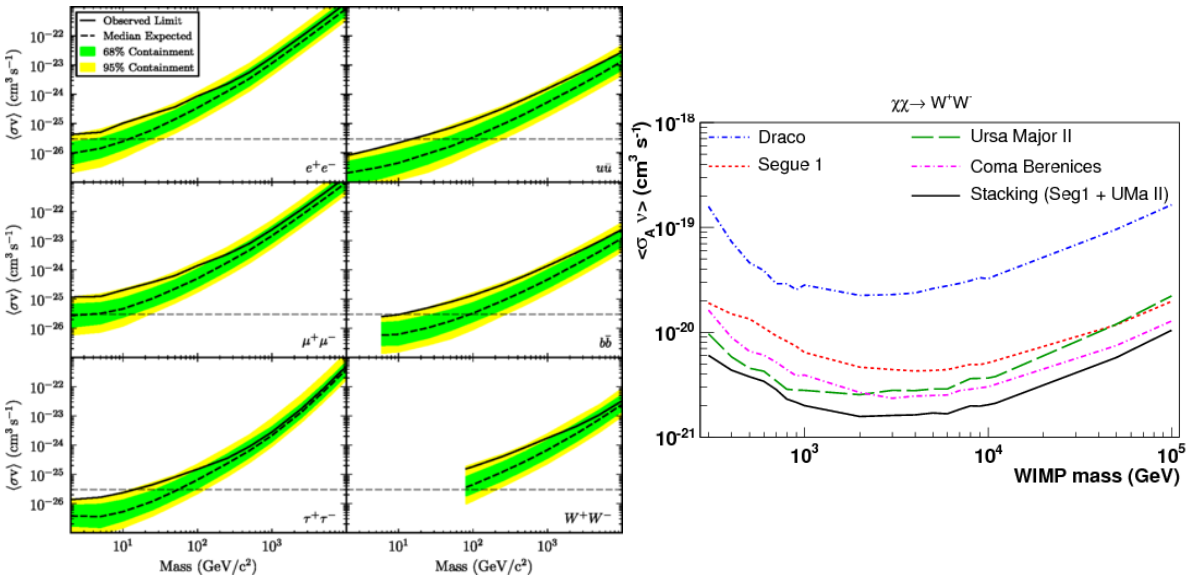

Figure 2.5: *Left plots:* Limits on dark matter annihilation in dwarf galaxies by the Fermi collaboration [66]. Each subplot shows limits computed by assuming varying intermediate decay channels.
Right plot: Similar limits from in dwarf galaxies surveys by the Ice-Cube experiment, derived by searching for excess neutrinos produced as $\chi\chi \to W^+W^- \to \nu\bar{\nu}$, [67].

Other searches focus on deviations in particle-to-antiparticle ratios sourced by annihilating dark matter. The positron excess as measured by the Alpha Magnetic Spectrometer and other experiments have been investigated in the paradigm of dark matter annihilation [68, 69]. Similarly excess neutrino production from annihilating dark matter has been looked into by the Ice-Cube experiment [67], see Fig. 2.5. These experiments have constrained the annihilation cross-sections for dark matter, but no clear evidence of discovery exists in these particular searches.

Recent independent analyses of gamma ray excess around the galactic center by Hooper et al [70] indicate the possibility of canonical cold dark matter annihilating to gamma rays in the dark matter halo of our galaxy. Description of this galactic halo will be provided in the direct detection section. Another variety of gamma-ray searches look for spectral peaks whose central values are directly related to m_χ; an interesting excess at 130 GeV has been explored in the context of annihilating dark matter in Ref. [71].

2.5 Production

Dark matter may be produced in colliders by creating new particles from the high energy collisions. These particles may directly be stable dark matter or they may be unstable "mediators" which would decay to the stable dark matter particles. Typical collider searches look at missing energy (E_T^{miss}) in final states since dark matter once produced will stream freely through the detector volume, see Refs. [72, 73]. Signal-to-background for E_T^{miss} searches can suffer from mis-reconstructed events etc. and thus one of the choice methods is tagging on mono-jets, Fig. 2.6. Requiring such initial/final state radiation events, improves data quality and is also necessary to balance the two WIMPs momentum, so that they are not produced back-to-back resulting in negligible E_T^{miss}.

To interpret the spectrum of such events, effective field theories with heavy mediators are employed. The energy-scale for such theories is $\sim M_{\text{mediator}}/\sqrt{g_\psi g_\chi}$, where $g_{\psi/\chi}$ are the coupling constants for mediator-standard model particle and mediator-dark matter particle. One then writes all possible operators that can contribute to dark matter production at the relevant energy scale. For each effective operator, the expected spectrum is compared to the measurements, and this constrains the coupling constants and thus one obtains model dependent limits in the plane of dark matter-nucleon cross-section and dark matter mass, see Fig. 2.6.

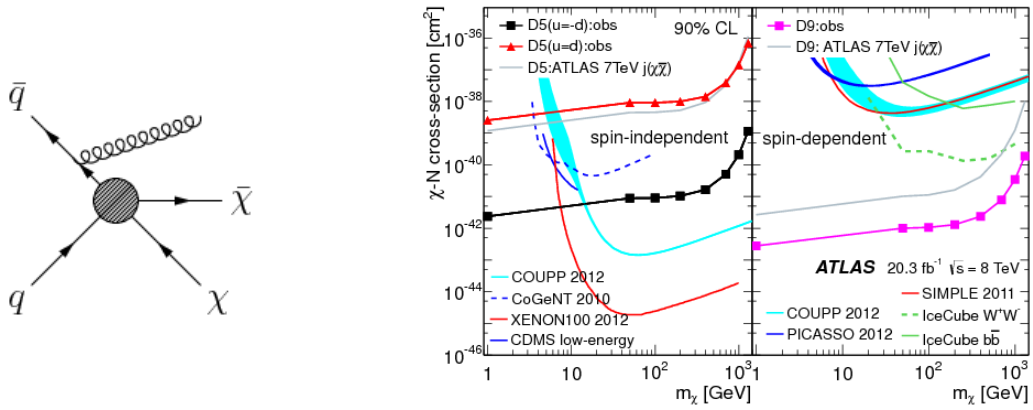

Figure 2.6: *Left plot:*An example of mono-jet tagged search fro dark matter production in colliders [72]. The mono-jet can be radiated gluons, weak bosons or photons.
Right plot: Limits from the ATLAS experiment on W/Z-boson mono-jet searches from Ref. [73].

Other possible searches have been proposed based on heavy quark productions with b-tagging and "sibling" production. The first idea deals with dark matter produced in association with bottom or top quarks where final states with E_T^{miss} and one or more b-jets are predicted. Based on high b-tagging efficiencies, limits are derived on an effective scalar operator coupling dark matter to quarks [74]. The latter idea works in the context of a dark sector where the WIMP is the lightest stable particle. The colliders are supposed to generate higher mass "siblings" which then decay into the WIMPs.

2.6 Direct detection

WIMP dark matter is considered neutral, i.e., it generally lacks standard quantum numbers beyond some mass m_χ. WIMPs can thus scatter elastically off a nucleus[6] of mass m_N, causing it to recoil with energy E_r given by Eq. 2.6

$$E_{\mathrm{r}}(\theta) = \frac{\mu^2 v^2}{m_N}\left(1-\cos\theta\right) \tag{2.6}$$
$$E_{\mathrm{r}} = \frac{1}{2} m_\chi v^2 \cdot \frac{2m_N/m_\chi}{\left(1+m_N/m_\chi\right)^2}$$

In the first equation of Eq. 2.6 the factor $\mu = \left(m_\chi m_N\right)/\left(m_\chi + m_N\right)$ is the reduced mass of the two-body system and θ is the scattering angle in the center of mass frame. In the second equation we average over recoil angle to a get a simple estimate for the nuclear recoil energy in terms of the WIMP's kinetic energy and the ratio of WIMP-nucleon masses. Fig. 2.7. shows this energy for Ge and Xe targets for varying WIMP mass.

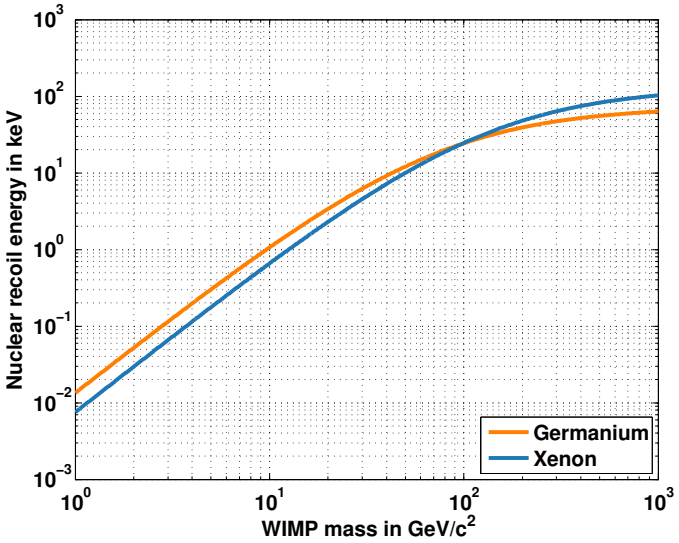

Figure 2.7: Nuclear recoil energies calculated from simple kinematics for Ge and Xe targets, assuming WIMP velocities of $10^{-3}c$, following Eq. 2.6.

From Fig. 2.7 it is clear that Ge is a better target for lighter ($\ll 100$ GeV/c^2) WIMPs and that a 10 GeV/c^2 WIMP will produce small, ~ 1 keV, recoil energies. We also note that, to deposit a minimum recoil energy E_r, a WIMP must travel faster than a minimum velocity given by Eq. 2.7.

$$v_{min} = \sqrt{\frac{m_N E_r}{2\mu^2}} \tag{2.7}$$

These calculations can now be refined by introducing particle and astrophysics of dark matter.

[6]WIMPs can scatter off electrons as well, but the energy transfer scales as the ratio of target mass to WIMP mass, and thus for WIMPs with masses over 1 GeV/c^2 electrons will not receive enough recoil energy to ionize.

2.6.1 Local astrophysical distribution of dark matter

In the calculations performed earlier we assumed a WIMP speed of $10^{-3}c$. In reality there is a distribution of velocities best understood in the context of local dark matter distribution. Our Milky-Way galaxy resides in a halo of dark matter which extends well beyond 100 kpc in radius. The mean density near $r_\odot$ is roughly constant at $\rho \approx 3$ GeV/c^2/cm^3 [75]. The velocity distribution based on the argument that dark matter has thermalized is approximated by a Maxwell-Boltzmann distribution with a kinematic cut off as,

$$f(v) = N\left(v_0, v_{esc}\right) \cdot e^{-(v/v_0)^2} \cdot \Theta\left(v_{esc} - v\right) \tag{2.8}$$

Here v is the velocity of a dark matter particle in galactic rest frame, and $v_0 \approx 220$ km/s is the characteristic halo velocity at $r_\odot$. We assume the halo is a bound system and $v_{esc} \approx 544$ km/s is the velocity above which a dark matter particle is not gravitationally bound. Finally N is a normalization constant for the probability density $f(v)$; these numbers are from Ref. [25]. While this Standard Halo Model (SHM) is used for most direct detection studies, N-body simulations indicate that it is likely to have non-gaussian tails and statistical dispersions from streams and clusters of dark matter [76]. These uncertainties can impact dark matter signal in direct detection experiments, particularly for light WIMPs and will be discussed in Sec. 4. The lower and upper bounds on these velocities are (195, 255) km/s for v_0 and (498, 608) km/s for v_{esc} following Ref. [77, 78, 79, 80].

2.6.2 Scattering cross-sections

The mathematical form of WIMP-nucleon cross-sections are typically calculated from a simple four-point Fermi-interaction, following Fig. 2.3, with a Lagrangian as shown in Eq. 2.9.

$$\mathcal{L} \supset 4\left(\chi^\dagger\chi\right)\left[f_p\psi_p^\dagger\psi_p + f_n\psi_n^\dagger\psi_n\right] + 16\sqrt{2}G_F\left(\chi^\dagger\frac{\boldsymbol{\sigma}}{2}\chi\right)\left[a_p\psi_p^\dagger\frac{\boldsymbol{\sigma}}{2}\psi_p + a_n\psi_n^\dagger\frac{\boldsymbol{\sigma}}{2}\psi_n\right] \tag{2.9}$$

As shown in Ref. [81] a generalized Lagrangian with all operators ((pseudo) scalars, vectors, axials and (pseudo) tensors), in the low energy limit, reduces to Eq. 2.9 where χ and ψ are the nucleon and WIMP fields. The first term represents spin-independent scattering where $f_{p/n}$ are the effective coupling constants. The second term represents spin-dependent scattering where G_F is the standard weak-scale Fermi-constant, $a_{p/n}$ are effective coupling constants and the terms $\left(\chi^\dagger\frac{\boldsymbol{\sigma}}{2}\chi\right)$ are the spin-densities. Finally, from this Lagrangian, we obtain spin independent (SI) and spin dependent (SD) differential cross-sections in terms of recoil momentum q,

$$\frac{d\sigma_{SI}}{dq^2} = \frac{1}{\pi v^2}\left[Zf_p + (A-Z)f_n\right]^2 F^2(q) \qquad \frac{d\sigma_{SD}}{dq^2} = \frac{8G_F^2}{\pi v^2}J(J+1)\Lambda^2 F_S(q)^2 \tag{2.10}$$

If $f_p \approx f_n$, then for the spin independent case, we have A^2 enhancement in the cross section. Thus direct detection experiments use nuclei with atomic masses around 10-100 GeV/c^2. The next consideration in predicting event rates from these cross-sections are the form factors (F, and F_S) which parametrize how an impinging WIMP resolves nuclear structure. Typically the phenomenological Helm form factor is used for $F(q)$ which convolutes a hard sphere with symmetric Gaussian smearing and follows from the A^2 coherent scattering discussion. For spin dependent scattering, $\Lambda F_S(q)$ is the effective spin-form-factor and is computed for every nucleus using internal spin structure information. Details on these calculations and further references are present in [82, 83, 81, 32] and some original publications on form factors are [84, 85, 86].

2.6.3 Event Rates

Signal

Combining information from astrophysics and particle physics, the expected differential rate of nuclear recoils is,

$$\frac{dR}{dE_r}(E_r) = \frac{\rho}{m_\chi m_N} \int_{v_{min}}^{v_{esc}} d^3v \; v f(v) \; \frac{d\sigma_{\chi,N}}{dE_r}(v, E_r) \tag{2.11}$$

This event rate is roughly exponential with energy which can be seen by noting that $d\sigma_{\chi,N}/dE_r \propto F(q)/v^2$ where roughly, $F(q) \sim e^{-(q/q_0)^2}$. Following Ref. [32], if we approximate the dark matter halo to be Maxwellian with infinite cut-off, then we get $dR/dE_r \propto e^{-(q/q_0)^2} \times e^{-(v_{min}/v_0)^2}$. Following Eq. 2.7, $v_{min} \propto \sqrt{E_r} \propto q$, which implies $dR/dE_r \propto e^{-E_r/E_{r,0}}$, where $E_{r,0}$ is a kinematic constant. Thus the expected WIMP spectrum is a featureless exponential.

In any experimental measurement there is noise and hence some *smallest* discernible signal amplitude. Limited by such signal-to-noise depreciation every experiment thus has a lowest energy above which the measurements are useful; this is called the energy threshold, E_{th}. Thus for a fixed exposure the integrated counts as a function of recoil energy is, $\int_{E_{th}}^{\infty} dE_r \frac{dR}{dE_r}$. This integrated rate as a function of energy threshold is shown in Fig. 2.8.

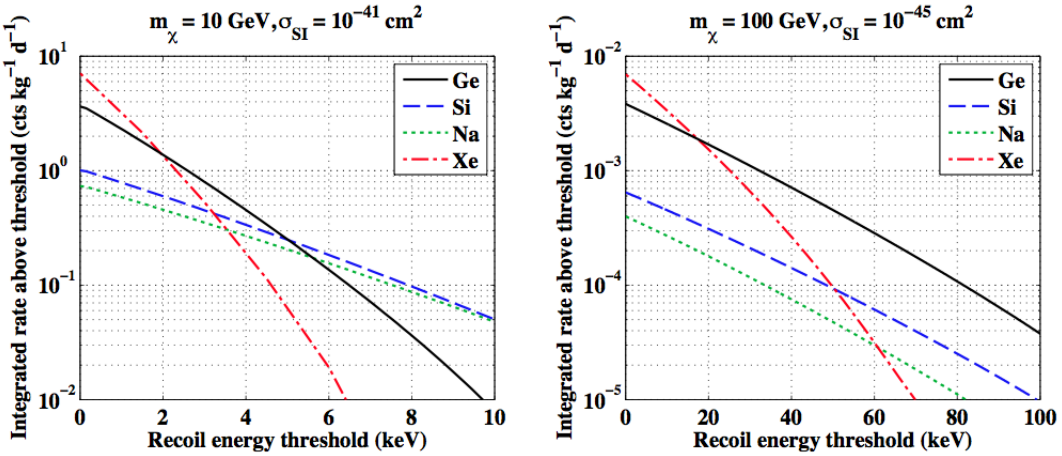

Figure 2.8: Expected WIMP dark matter nuclear recoil integrated rates for various nuclei, as a function of threshold energy. The left plot is for a 10 GeV/c^2 (light) WIMP with a cross-section of 10^{-41} cm^2, and the right plot is for a heavier 100 GeV/c^2 WIMP with a cross-section of 10^{-45} cm^2. This shows the necessity for lower thresholds in detecting lighter WIMPs.

The signal rate for galactic dark matter as measured on earth is not constant with time since in the galactic rotation frame, the earth has several orbits [83]. The revolution around the sun introduces annual modulation of this rate at a 10% level, highest around June and lowest around December. The daily rotation of earth adds a diurnal modulation at a 1% level. As WIMP rates are exceedingly small and several environmental backgrounds have annual and diurnal variations, detecting few percent effects are very challenging. The experiment described in this thesis was designed as a low-threshold light-WIMP discovery experiment and was not optimized to find statistical modulations. The CDMS experiment has separately pursued the search for annual modulation and details on this may be found in Ref. [87, 88].

Backgrounds

The integrated signal rate for a 10 GeV/c^2 WIMP, as shown in Fig. 2.8, is very small. A 1 kg detector with 2 keV$_{\rm nr}$ threshold, running for 1 year will count $\lesssim 2$ events. Thus it is imperative to understand all possible backgrounds in such experiments. Experiments are housed in some mechanical structure and these can be background sources. Consider a recent radioactivity measurement of copper detector housings by the EDELWEISS collaboration [89], a level of 1.4 mBq/kg. With 100 g of this Cu supporting a 1 kg detector for 1 year, there will be over 4400 background events. Folding in geometric and spectral suppression[7] of 1/100 for these events to penetrate the detector, the signal-to-background ratio is around 2:44, i.e., much less than unity.

Practically many more environmental sources of backgrounds are present such as terrestrial radioactivity, cosmic ray muons, radon in air and cosmogenic activation of the detector material themselves. Thus all direct detection experiments invest heavily in various forms of shielding and background discrimination tactics. These procedures involve moving underground to use rock overburden in reducing cosmic ray flux, building layers of lead and polyethylene to moderate or stop αs, βs, γs and neutrons, and using carefully screened radio pure detector housing materials. Even if all the external shields are 100% efficient, we must still veto particles from radioactive decays in materials near the detectors. Most of these decays produce electron recoils although neutrons can produce nuclear recoils similar to those produced by dark matter.

For the same kinetic energy, nuclear recoils produce denser ionization tracks and also lesser ionization than electron recoils. Experiments use a variety of detector physics techniques to reject backgrounds, based on this feature. CDMS and CRESST, for example, measure the lattice vibrations and the ionization produced, and the ratio of these allow such background rejection. Liquid noble-gas experiments sense the difference in the amount of scintillation light produced from primary recoils and from ionization to reject electron recoils. Most experiments have demonstrated successful discrimination against electron recoils at powers $\gtrsim 1:10^4$, above 20 keV$_{\rm nr}$. However rejection powers drop rapidly with energy and for low energy recoils this is a very challenging endeavor. Other major complications include neutron backgrounds since neutrons produce nuclear recoils identical to WIMPs, and surface events where ionization is not measured perfectly near detector surface leading to poor background rejection. Great attempts are made with neutron moderation and detector fiducialization to address these issues [90, 91].

Sensitivity

Since the WIMP spectrum is quasi-exponential, the lower the detection threshold, the greater the general sensitivity to WIMP recoils. The general profile of the sensitivity, often computed as the 90% confidence upper limit to the WIMP-nucleon cross-section (σ_{SI}) for a certain WIMP mass (m_χ), as a function of WIMP mass can be estimated following the differential rates discussed in Eq. 2.11 and Fig. 2.8. Simplifying the velocity distribution as a general Maxwellian without any cut-offs, the approximated rate[8] is,

$$\frac{dR}{dE_r}(E_r) \propto \frac{\rho\sigma_{SI}}{m_\chi \mu^2 v_0} \exp\left(-\frac{E_r m_N}{2\mu^2 v_0^2}\right) \tag{2.12}$$

[7]Suppression factors must be estimated via simulation. For CDMS detectors, the geometrical factor is <1/2 and the spectral density below 20 keV$_{\rm nr}$ is ∼1/25, thus 1/100 is a conservative estimate.

[8]The cross-section $\sigma_{SI} \approx 4\mu^2/\pi\,[Zf_p + (A-Z)f_n]^2$ is obtained from Eq. 2.10 by integrated over energy transfer.

For heavy WIMPs, i.e., $m_\chi \gg m_N$ the reduced mass is approximately $\mu \approx m_N$. In this limit the relation between the differential rate, cross-section and mass, holding everything else constant is given by Eq. 2.13.

$$\frac{dR}{dE_r} \sim \frac{\sigma_{SI}}{m_\chi} \exp\left(-\frac{E_r}{2m_N v_0^2}\right) \tag{2.13}$$

We measure the differential rate (LHS of Eq. 2.13) and try to constrain σ_{SI} and m_χ (RHS of Eq. 2.13). Thus Eq. 2.13 shows that at high masses, for a given mass m_χ, the limit on cross-section scales as $\sigma_{SI} \propto m_\chi$.

For $m_\chi \ll m_N$ the reduced mass is $\mu \approx m_\chi$ and the approximate rate is given by Eq. 2.14.

$$\frac{dR}{dE_r} \sim \frac{\sigma_{SI}}{m_\chi^3} \exp\left(-\frac{E_{th} m_N}{2m_\chi^2 v_0^2}\right) \tag{2.14}$$

In this limit, we cannot consider arbitrarily small recoil energies and we evaluate the rate at threshold, i.e., $E_r = E_{th}$. In Eq. 2.14, the RHS is again measured and we see that the upper limit on σ_{SI} rapidly increases with decreasing WIMP masses as $\sigma_{SI} \sim \exp\left(m_\chi^{-2}\right)$.

In summary the sensitivity to WIMPs degrades at both low and high WIMP masses, albeit quite differently. At high masses the loss in sensitivity increases linearly with mass, while at low masses the loss is much more drastic and increases quasi-exponentially near threshold. We also see in the low WIMP mass range, from Eq. 2.14, the sensitivity improves exponentially with reduced thresholds. This scaling is apparent in all direct detection limits such as Fig. 2.4.

Finally the overall scale of an experiment's sensitivity depends on exposure (product of an experiment's effective detector mass and live-time), contingent on the level of background present. Above 10-20 $\mathrm{keV_{nr}}$ most direct detection experiments have excellent background rejection. In the limit that neutrons are well moderated, for an exposure of MT, the expected background rate is $\ll$1. Following Poisson statistics the 90% upper confidence limit for zero measured events is 2.303, hence if no events are observed an experiment can readily set 90% (upper) exclusion limits [92]. In such cases more the exposure, smaller the cross-section that may be excluded, i.e., $1/\sigma_{SI} \propto MT$.

Now let's consider measurements in 5-15 $\mathrm{keV_{nr}}$ where the background levels are non trivial but can be estimated by material assay and simulations. In this case upon background subtraction, the variance on the subtraction will be proportional to the square root of the background counts. Since the background counts scale with exposure, the sensitivity scales as $1/\sigma_{SI} \propto \sqrt{MT}$.

Finally, consider measurements under 2 $\mathrm{keV_{nr}}$ where background levels are not known very well. In this case in the limit of $MT \to \infty$ the systematic errors will dominate any statistical errors in background estimates. Thus the experiment is background limited, i.e., $1/\sigma_{SI} \not\propto MT$.

2.6.4 Experimental landscape

Several direct detection experiments have been competing to discover dark matter over the last two decades. Various detection schemes, such as production of ionization, scintillation and heat, have been investigated. Most experiments aim at using multiple excitation methods to not only detect nuclear recoils but also discriminate against backgrounds such at electron recoils. A schematic of these different detection mechanisms and experiments is shown in Fig. 2.9. Comprehensive summaries of various experiments and their scientific reach are present in Ref. [93, 90].

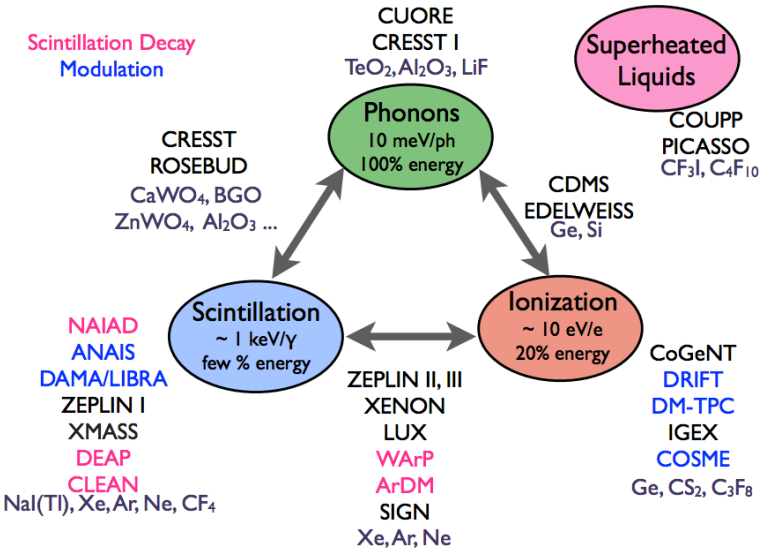

Figure 2.9: Summary of various detection techniques employed by direct detection experiments from Ref. [93]. Experiments often attempt exploiting multiple excitation channels for better signal-to-background selection.

The landscape of results from these direct detection experiments have been primarily dominated by null results. However the few experiments which observed excesses unaccountable by basic background modeling hinted at the possibility of light WIMPs. The general landscape of signal hints and exclusion limits in 2013 is shown in Fig. 2.10. The various colored patches represent experimental results where WIMP like signals were measured over the expected backgrounds. The curves (typically 90% confidence levels) are exclusion limits from other experiments which do not observe WIMP like signals.

While at high WIMP masses, all experiments agree on null results, in the low mass region ($m_\chi \lesssim 10$ GeV/c^2) tension in the interpretation of results between various experiments is clearly seen. I will briefly review the experiments shown in Fig. 2.10, particularly highlighting the experiments that found positive results for light WIMPs.

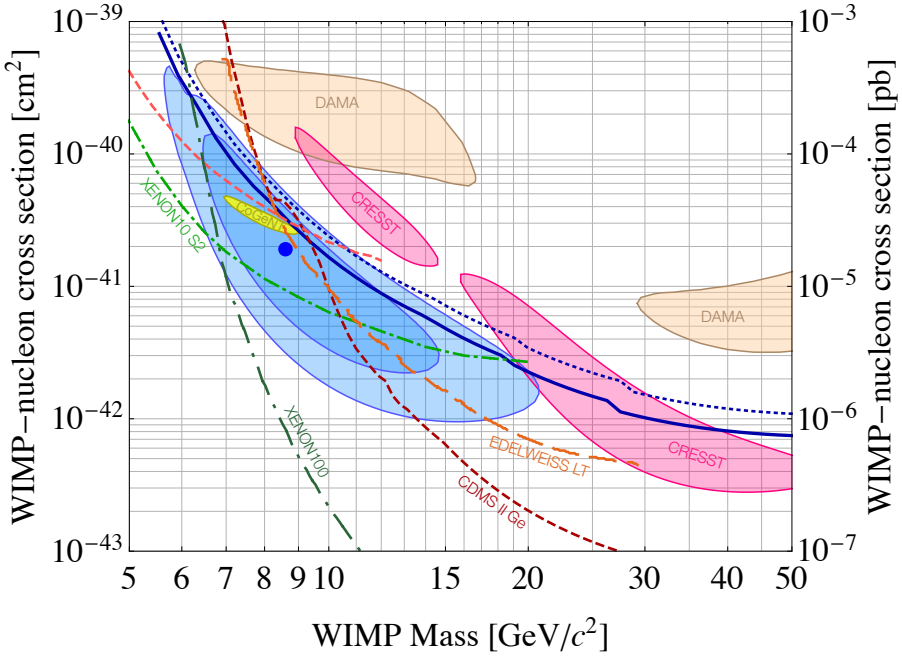

Figure 2.10: The direct detection low mass WIMP search landscape in 2013. The colored patches are excesses in signal over background from various experiments, interpreted as dark matter. The curves are exclusion limits from experiments which rule out parameter space in this plane of WIMP-nucleon cross-section and WIMP mass [94, 90].

CDMS-Si

The blue patches in Fig. 2.10 are results from the CDMS II experiment [95], where specific analysis of 8 Si detectors with an exposure of 140 kg-days and effective threshold of ~7 keV$_{nr}$, found three WIMP like events [94]. Since the atomic mass of Si is lower than Ge, it has better kinematic matching to lighter WIMPs and is hence a better target than Ge or Xe. This experiment used ultra-cold Si ZIP detectors with athermal phonon and ionization sensors. The ratio of phonons to ionization, called ionization yield discriminates between good nuclear recoils (primarily WIMPs and neutrons) with low yield and electrons recoils (primarily background radiation) with high yield. For electron recoils occurring near the detector surface, anisotropic electric fields and charge-traps can reduce the ionization signal and such can get reconstructed to lower yield. In CDMS II the rise-time of pulses were used to discriminate against surface events. Thus the experiment defined WIMP acceptance for events with relatively low ionization yield and a high timing parameter [96].

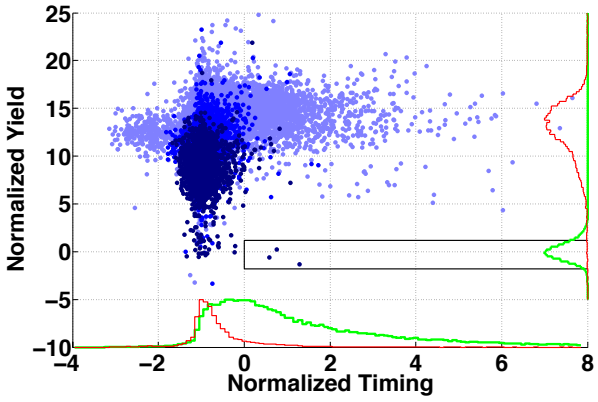

Figure 2.11: All good WIMP search events in the plane of normalized yield and normalized pulse timing for the CDMS II Si analysis. Also shown are the expected distributions from bulk nuclear recoils in green and surface events in red. WIMP signals are expected in the black box, and three events were found here with energies in 8-12 keV$_{nr}$, [94].

All good WIMP search events in the plane of normalized yield and normalized pulse timing are

shown in Fig. 2.11 and three events are seen to pass all cuts. These events deposited recoil energies in 8-12 $\mathrm{keV_{nr}}$, and may be interpreted as WIMPs at a 3 σ level with best fit mass of 8.6 $\mathrm{GeV/c^2}$ and WIMP-nucleon cross-section of 1.9×10^{-41} $\mathrm{cm^2}$.

CoGeNT

The CoGeNT experiment operates a 440 g P-type point-contact Ge detector for WIMP search at the Soudan Underground Laboratory. The very low capacitance of this cylindrical point-contact detector ensured that the noise pedestal was an impressively low 500 $\mathrm{eV_{ee}}$ (or $\sim$2.3$\mathrm{keV_{nr}}$). This low threshold allowed CoGeNT to effectively search for ionization produced by light WIMP recoils. An exposure of 266 kg-days yielded a spectrum of nuclear recoil energies where a quasi-exponential signal over background was observed, see Fig. 2.12 from Ref. [97].

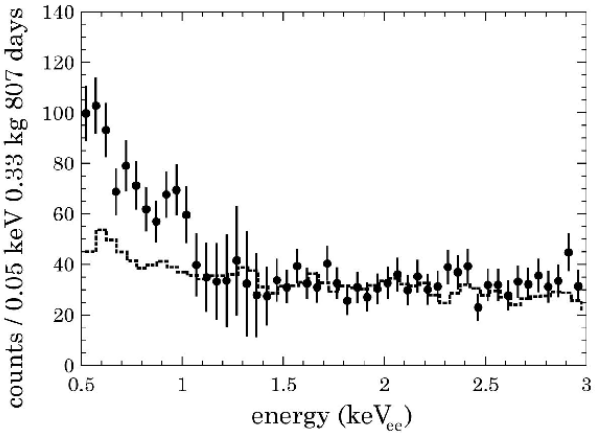

Figure 2.12: The final irreducible spectrum of bulk events from CoGeNT's 266 kg-days of exposure [97]. These events are left over after subtracting various standard backgrounds such as activation lines and Compton recoils. The expected backgrounds obtained from simulations are shown in dashed lines, while the data appears with black error bars.

After modeling expected background rates from surface events, activation of Ge isotopes and Compton γ recoils and subtracting these, they were left with an excess of events shown in Fig. 2.12. With large statistical significance, these data can be interpreted as WIMPs with best fit mass of 8.2 $\mathrm{GeV/c^2}$ and WIMP-nucleon cross-section of 3.2×10^{-41} $\mathrm{cm^2}$.

While the cylindrical point-contact detector allows for identification of surface / bulk events via slow / fast pulses, the discrimination power is low under 0.9 $\mathrm{keV_{ee}}$ and the uncertainty in this may be used to partially explain the excess. Furthermore these events showed signs of annual modulation, as expected from dark matter, however the amplitude of the modulation was noted to be excessive as discussed in the CDMS annual modulation analysis [87, 88].

CRESST II

The CRESST II experiment, unlike CDMS or CoGeNT, uses multiple target nuclei to fight systematics in detection of WIMP like events. CRESST II employed an array of $\mathrm{CaWO_4}$ detectors equipped with scintillation and phonon sensors. The low atomic mass of oxygen and a $\sim$10 $\mathrm{keV_{nr}}$ threshold ensured sensitivity to light WIMP recoils. In 2011, a run with 730 kg-days of exposure found an excess of events in the 10-40 $\mathrm{keV_{nr}}$ range, which could be interpreted as light WIMPs. Likelihood analyses indicted two best fit parameters: mass of (11.6, 25.3) $\mathrm{GeV/c^2}$ and WIMP-nucleon cross-section of $(3.7,\ 0.16) \times 10^{-41}$ $\mathrm{cm^2}$ with significances of (4.2, 4.7) σ respectively, see Fig. 2.13 from [98].

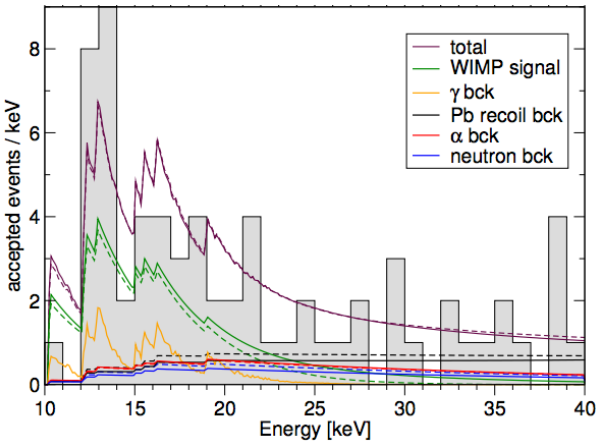

Figure 2.13: Spectrum of low energy events as observed by the CRESST II experiment. The gray histogram is the measured spectrum and the curves are the best fit WIMP signals (green lines) and backgrounds (various colors). A likelihood analysis provided two best fit WIMP models shown by dashed and solid lines, see Ref. [98].

DAMA/LIBRA

The DAMA/LIBRA experiment has the highest significance of "discovery" of all dark matter experiments till date. This experiment has been running for over a decade with 250 kg of extremely radiopure thallium-doped NaI scintillator crystals. With a large exposure of 1.2 ton years of data collected over 13 annual cycles, the DAMA/LIBRA experiment has seen low energy excess with annually modulating rates, matching the expected dark matter behavior at 8.9 σ level of significance. Like CoGeNT this is an ionization only experiment and nuclear and electron recoils are not distinguished. The low energy (2-6 $\mathrm{keV_{nr}}$) spectrum and the corresponding frequency spectrum for modulation is shown in Fig. 2.14, Ref. [99]. These data may be interpreted as WIMPs with best fit mass of $\sim$10 GeV/c^2 and WIMP-nucleon cross-section of $\sim 2 \times 10^{-40}$ cm^2. However uncertainty in conversion of recoil to ionization energy can alter the best fit measures to higher masses and lower cross-sections [90, 100]. These signals may be from muon flux and other seasonal backgrounds, such discussions are still ongoing and a complete conclusion is yet to be reached.

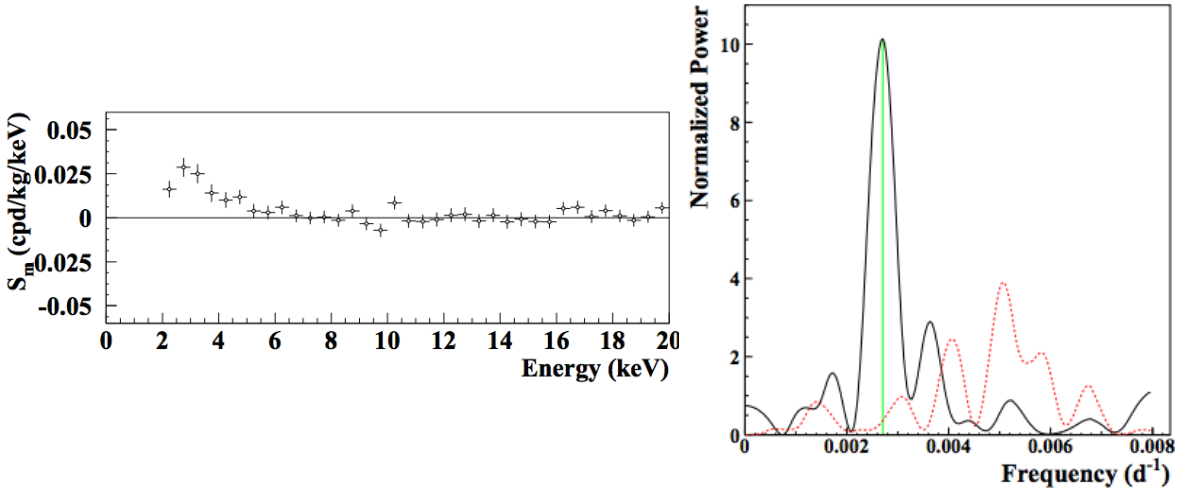

Figure 2.14: *Left plot:* Spectrum of low energy (2-6 $\mathrm{keV_{nr}}$) events as measured by DAMA/LIBRA. *Right plot:* Periodicity analysis of these data show a clear peak at the 144 $\pm$ 8 days, very close to the expected annual modulation signature from galactic dark matter [99].

Null results

The CDMS and EDELWEISS low threshold Ge experiments are in disagreement with DAMA and CRESST, however they do not exclude the CoGeNT and CDMS-Si signals [101, 102]. The XENON 10 S2 and XENON 100 experiments are most constraining, see Fig. 2.10 and Ref. [103, 104]. Various phenomenological propositions alleviate these mismatches by exploiting experimental uncertainties and by building isospin violating models sensitive to the neutron/proton ratio, see Ref.[100, 105].

2.7 Pros and Cons for various search methods

Indirect detection

The annihilation rate scales with the square of dark matter density (as two dark matter particles must annihilate to photons for example). Thus studies of dark matter rich dwarf galaxies have high signal-to-background quality. Deep gravitational potentials which host dense dark matter halos will have correlated high baryon densities, and careful analysis of baryonic contributions to annihilation products must be done. Numerous astrophysical uncertainties over the large line-of-sight distances may further conspire to provide fake signals. For example, excess gamma rays can be explained by unresolved millisecond pulsars and excess positrons can be assigned to high energy cosmic rays.

Production

Colliders use controlled beams and thus uncorrelated backgrounds and astrophysical uncertainties do not affect such searches. However, it is difficult to predict if dark matter can be produced in our TeV scale colliders, and furthermore address how such dark matter decays or escapes the various detectors. Thus collider searches are necessarily model dependent and any dark matter like discovery may not be entirely representative of all the astrophysical dark matter.

Direct Detection

These methods study local dark matter scattering off fixed nuclei, and in principle interpretation of the results require minimal assumptions. The dark matter halo of the milky way has been well studied and no theories have to be invoked for simple kinematic scattering. As dark matter interactions are extremely weak ($\sigma_{\text{DM, nucleon}} \lesssim 10^{-4}\sigma_{\text{Weak}}$) these experiments count very rare events. Thus astrophysical (e.g., muon showers) and terrestrial (e.g., radioactive materials) backgrounds have to be exceptionally minimized for decent signal-to-background quality. Furthermore uncertainties in understanding low energy scatters from lack of characterization of detectors at an atomic level can affect the interpretation of the results.

We need all three search methods to fully characterize dark matter once it is discovered. To test the possibility of an annihilation signal being truly sourced by dark matter, we must observe commensurate scattering rates in terrestrial detectors. Given the diversity in the standard-model (only 5% constituent of the universe) it is a natural expectation that the dark sector has multiple quantum numbers vis-à-vis a variety of dark matter particles. The dark matter detected on earth may be different from the dark matter discovered in Draco, and only controlled production at a collider will enable us to understand the differences. More technically, each method search suffers from unique systematics and combined interpretations must be pursued to break degeneracies and to characterize the discovery of particle dark matter.

Chapter 3

The SuperCDMS experiment

The Super Cryogenic Dark Matter Search experiment is one of the leading direct detection experiments searching for galactic dark matter, by measurement of nuclear recoils produced by dark matter scattering off target nuclei. The number of expected signal events is < 1 for a typical one kg detector with $\gtrsim 2$ keV$_{\rm nr}$ threshold running for one year, see Fig. 2.8. Comparatively, background rates are orders of magnitude higher. Various strategies implemented to reduce backgrounds and detect WIMP nuclear recoils will be discussed in this chapter.

3.1 SuperCDMS detectors

SuperCDMS uses interleaved Z-sensitive ionization and phonon detectors (iZIPs) to detect dark matter scattering off target nuclei. The target detectors are ultra pure[1], cylindrical germanium crystals with diameter, thickness and mass of $\sim$ 75 mm, 25 mm, 600 g. Particle interactions are expected to excite electrons and holes along with lattice vibrations. To measure these excitations both faces of every iZIP have charge and phonon sensors lithographed on them Fig.3.1.

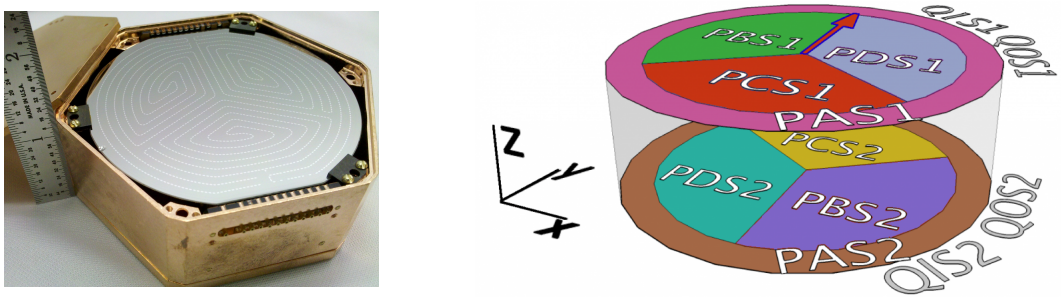

Figure 3.1: *Left plot:* An iZIP detector in its housing. The spiral patterns are the lithographed sensors. *Right plot:* Arrangement of phonon and charge sensors on each face of an iZIP. The labels indicate the channel and side, PAS1 for example stands for **P**honor sensor **A** on **S**ide **1**. In this manner each side has four phonon sensors (A...D), an **O**uter charge sensor ring (QO) and an **I**nner charge sensing disc (QI) [87].

A summary of the essential detector physics will be presented here. Detailed documentation of detector physics and design may be found the PhD theses of Scott Hertel and Matt Pyle [87, 106]. Fundamental condensed-matter treatment of charge propagation and phonon physics has been worked on by Kyle Sundqvist and Steve Leman [107, 108].

[1]Etch pit densities of $\mathcal{O}\left(10^3\right)$ /cm^2 and impurity densities of $\mathcal{O}\left(10^{10}\right)$ /cm^3.

3.1.1 Ionization production and measurement

Production

Germanium is a semiconductor, where the band-gap at ∼50 mK between valence and conduction bands is $E_g = 0.74$ eV. The energy required to liberate a single electron-hole pair is dependent on energy transport in the crystal. On average the single-pair excitation energy, for a photons source, is parametrized as $\varepsilon_\gamma \approx E_g + \langle E_K \rangle_{e/h} + r\hbar\omega_R$ and is 3 eV for Ge [109]. Here the first term is the band-gap, the second term is the kinetic energy in the electrons and holes and the last term is the energy emitted as Raman phonons. This is the energy the lattice requires from momentum conservation to have a charge "leap" from valence to the conduction band[2].

Thus for electron recoils, such as excitation by photons, the number of electrons and holes produced is $N_{\mathrm{e/h}} = E_\gamma/\varepsilon_\gamma$ for deposited energy E_γ. For nuclear recoils this number is lower due to inertia of the moving nucleus, and there is an effective inefficiency in exciting charges. Both electron recoils and nuclear recoils produce phonons and charge carriers, however for nuclear recoils the ratio of energy in ionization to phonons is lower compared to the that for electron recoils. This is the ionizing efficiency or "yield" (Y) and is a quantity of great relevance to direct detection experiments. Thorough discussion on yield in the context of stopping-power is present in Ref. [87]. The number of electrons and holes produced for deposited energy E is thus described by Eq. (3.1).

$$N_{\mathrm{e/h}}(E) = Y(E)\frac{E}{\varepsilon_\gamma} \;\Rightarrow\; Y(E_r) = \frac{E_i}{E_r} \tag{3.1}$$

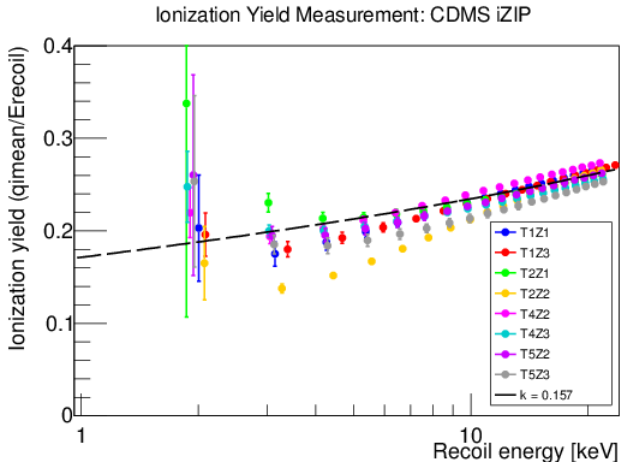

Figure 3.2: Ionization yield as a function of recoil energy for nuclear recoils. Measurements from all SuperCDMS iZIP are shown with colored markers. The black curve represents the theoretical Lindhard model [110].

If the impinging particle produces electron recoils then Y is constant and calibrated to unity. For nuclear recoils, $Y(E) < 1$ is an energy dependent function, typically decreasing with energy. Fig. 3.2 shows both measurements and theoretical expectation of ionization yield for Ge iZIPs. A more detailed discussion on yield will be presented later in Sec. 8.2.2. In Eq. (3.1), yield is defined

[2]While the microphysics of this process is not entirely understand, laboratory measurements are fairly robust. The variance in ε_γ can be of concern in understanding low energy recoils. Since iZIPs are operated at 50 mK, a Boltzmann suppression of $e^{-(\text{few meV}/(k_B \times 50mK))} \sim e^{-10^3}$ ensures that in quasi-equilibrium the uncertainty in charge production is small. However the initial charge cloud is very dense before cascades and the instantaneous local temperatures are $\gg$ meV, and in such cases the Boltzmann suppression can be just a couple of e-folds.

in terms of number of electrons and holes excited and also equivalently, as the ratio of ionization energy (E_i, measured in electron equivalent $\mathrm{keV_{ee}}$ units) to recoil energy (E_r, measured in nuclear recoil $\mathrm{keV_{nr}}$ units).

Measurement

When a particle scatters in an iZIP, primary recoil phonons and a cloud of ionization are produced. The detector is biased through a source and impedance (V_b, R_b), and this drifts out the electrons and holes from the primary cloud. As these charges approach the surface, they induce image charges generating a time varying current across the bias resistor. This signal is read out by a coupling capacitor (C_C) and finally amplified via a JFET (field emission transistor) with a low pass filter (in practice $R_{fb}C_{fb} \approx 40\mu s$). A schematic of the electronics is shown in Fig. 3.3, and a thorough layout is presented in Fig. A.1 in the Appendix.

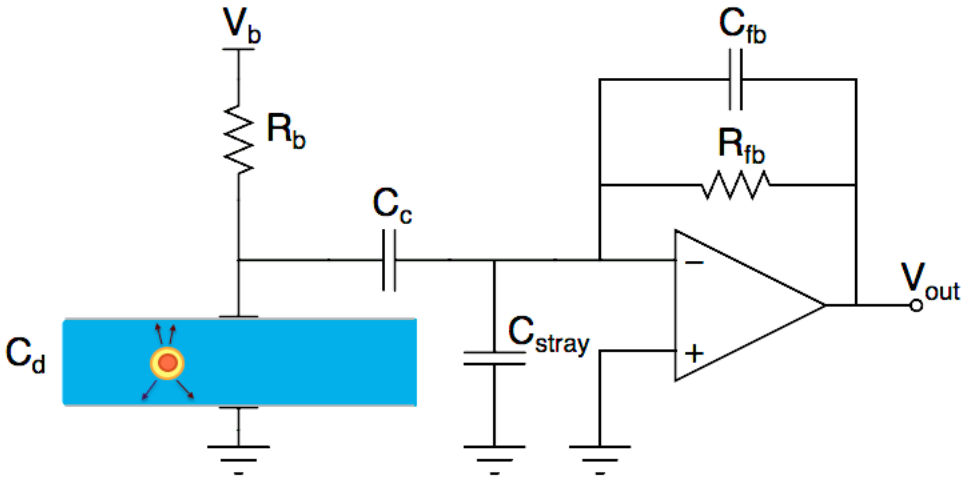

Figure 3.3: Ionization readout electronics for an iZIP. Drifting charges induce image charges on the sensors which are read out via a coupling capacitor and amplifier setup [25]. A charge cloud is shown with a "hotspot" in the detector volume, with drift tracks from electrons and holes upon biasing the detector.

The charge sensing is unfortunately noise limited. The average scale of the the total noise, dominated by the JFET voltage noise and Johnson noise from the resistors, is $\sim 100\ \mathrm{nV}/\sqrt{\mathrm{Hz}}$. Under 10 kHz environmental 1/f noise is predominant. Such a noise spectrum implies that a standard charge pulse with exponential fall-time of 40 μs cannot be distinguished from noise if its amplitude is < 5 keV. This noise limitation of charge energy measurement is manifested in the large error-bars in the yield plot shown in Fig. 3.2. Hence this standard method for reading ionization is ineffective in searching for low energy recoils produced by light WIMPs where characteristic ionization energies are $\lesssim 1$ keV. The crux of this thesis will be measuring ionization of sub-keV energies using phonons.

3.1.2 Phonon production and measurement

Production

For every interaction in a crystal there is an initial "hot-spot" with high density of out of equilibrium phonons called athermal phonons. As the system equilibrates energy is carried by thermal phonons.

The true power of CDMS detectors come from the ability to measure low energy athermal phonons. Phonons are produced at several stages:

1. Primary recoil phonons: In case of electron recoils, these are the phonons emitted when the charge pairs transition from valence to conduction bands. For nuclear recoils these phonons have two sources, one from the charge excitation and the other from the nucleus physically moving. Thus the energy in primary recoils is proportional to the energy deposited by an impinging particle.

2. Luke-Neganov phonons: These originate from drift heating, first observed by Luke, Neganov and Torfimov [111, 112]. As the electrons and holes are accelerated by the applied bias, they scatter on lattice sites facing an effective drag, where the work done in drifting them is emitted as phonons. For a detector bias V_b and thickness D, the mean energy in these phonons is given by Eq. (3.2).

$$\langle E_{\mathrm{L}} \rangle = \langle N_{\mathrm{e}} \cdot eV_b \cdot d_j/D \rangle_j + \langle N_{\mathrm{h}} \cdot eV_b \cdot (D - d_j)/D \rangle_j \tag{3.2}$$

   Here d_j is the distance the electron travels, hence $D - d_j$ is the hole transport length for some interaction j. On average, using Eq. (3.1) this reduces to $E_{\mathrm{L}} = N_{\mathrm{e/h}} \times eV_b = E_i/\varepsilon_\gamma \times eV_b$. Further details on Luke-Neganov phonons will be presented in Sec. 4.2.

3. Relaxation phonons: A small portion of the deposited energy does not generate charge pairs, in general, $N_{e/h} = (E - \delta_K)/\varepsilon_\gamma$, where δ_K is the kinetic energy of the charge carriers since they may not be produced at rest. Typically $E \sim \mathcal{O}\,(1 - 100)$ keV while $\delta_K < 1$ keV, and it is a small effect. Since we measure image charge and do not physically extract the ionization produced, momentum conservation demands that this energy is contained in the crystal. It is retrieved as the excited charge carriers relax to the Fermi-sea via down-scattering near the detector edges, releasing relaxation phonons. There are subtleties in the relaxation mechanism arising from various electron-phonon and phonon-phonon scattering which depend on surface deformities, nature of surface deposits etc. and are discussed in Ref. [106].

The total phonon energy is given by Eq. (3.3), not accounting for surface losses / bulk trapping.

$$\begin{aligned} E_{\mathrm{t}} &= E_{\mathrm{r}} + E_{\mathrm{L}} \\ &= E_{\mathrm{r}} + N_{\mathrm{e/h}} \times eV_b \\ &= E_{\mathrm{r}}\,(1 + \mathrm{Y}(E_{\mathrm{r}})/\varepsilon_\gamma \times eV_b) \end{aligned} \tag{3.3}$$

Propagation & Dynamics

Phonons are propagating quasiparticles and typically are of two types, optical and acoustic. Acoustic phonons are lattice vibrations where the lattice sites move in phase resulting in branches where $\omega \sim k$. In contrast for optical phonons, the lattice sites oscillate out of phase and $\omega \nsim k$. Acoustic phonons are lower in energy compared to optical phonons. For Ge, the acoustic branch ranges continuously from $\sim$ (0, 20) meV and the optical branch sits at $\sim$ 30 meV. Apart from the energetics, phonons have varying polarizations: fast/slow transverse and longitudinal. The propagation of any phonon mode can be classified as diffusive or ballistic, depending on the level of scattering experienced. Ballistic modes travel with the least amount of scattering, while the scattering for diffusive

phonons depend on its momentum and nature of the crystal. For iZIPs the rough diffusive-ballistic boundary is $\mathcal{O}(1)$ meV or ∼250 GHz.

For interactions of interest, the energies deposited are $\gtrsim$ 1 keV, thus all the primary recoil phonons are "highly" energetic. The Luke phonons, as described later in Sec. 4.2, are emitted from drifting charges whose kinetic energies $\gtrsim$ 30 meV. Thus the two primary sources of phonons start off diffusively however they do not propagate indefinitely via diffusion. Two main scattering mechanisms impact their propagation. Firstly mass anisotropies across lattice sites results in isotopic scattering with a rate $\Gamma_{\text{Iso,Ge}} \approx 3.67 \times 10^{-41}(\nu/\text{Hz})^4[\text{Hz}]$. Secondly, higher order elastic coefficients allow the decay of longitudinal (L) modes into transverse (T) modes as $\text{L} \rightarrow \text{T} + \text{L/T}$ in a process called anharmonic decay where a high energy phonon decays into two phonons at a rate of $\Gamma_{\text{AD, Ge}} \approx 1.62 \times 10^{-54}(\nu/\text{Hz})^5[\text{Hz}]$.

The initial phonons originating from the "hot-spot" are $\gg$1 THz with mean free paths <1 mm, thus anharmonic decay rapidly starts down-converting these phonons. Under 1 THz isotopic scattering takes over until such quasi-diffusive propagation gives way to full ballistic propagation where the mean free paths are ∼ 1 cm (characteristic length scale of an iZIP) at phonon frequencies of ∼0.3 THz, see Ref. [106, 82].

Measurement I: QETs

Traditional thermometers measure thermal phonons and are largely insensitive to the nature of the initial interaction. The initial athermal phonons contain rich spectral information which allow for studying position dependence and optimize energy resolution. The prowess of iZIPs is in the ability to measure these athermal phonons with Transition Edge Sensors (TESs). In implementation, iZIPs have surface lithographed Quasiparticle-trap-assisted Electrothermal- feedback Transition-edge-sensors (QETs) at superconducting temperatures. Ref. [106, 87] describe the design and physics of QETs in great detail, thus only the necessary physics of these devices will be covered here.

QETs are designed with large aluminum "collector-fins" with smaller tungsten "trap" structures overlapping on the edges forming a "bi-layer", see Fig. 3.4. As discussed, phonons in iZIPs have $\nu \gtrsim \mathcal{O}(100)$ GHz. For Al and W the superconducting transition temperature (T_C) and Cooper-pair bonding energies (2Δ) are (1.18, 0.08) K and (340, 20) μeV respectively. When phonons scattering in the crystal contact the Al fins, some energy is lost into breaking Cooper-pairs, generating Bogoliubov quasi-particles. These particles diffuse into the W, which is "cooler", and break Cooper-pairs in W. Since the pair-breaking energy for W is much lower than Al, the final quasiparticles are trapped and cannot diffuse back into the Al. As a result, the phonon energy is concentrated in quasiparticles which effectively heat up the TES from superconducting to normal state. The sharp change in resistance provides accurate measurement of the phonon energy.

Measurement II: TES operation

The TESs are operated in negative electro-thermal feedback (ETF) mode, with the TES held at constant voltage. The resistance, and hence the current, is dependent on temperature. A schematic of the thermal circuit is shown in Fig. 3.5.

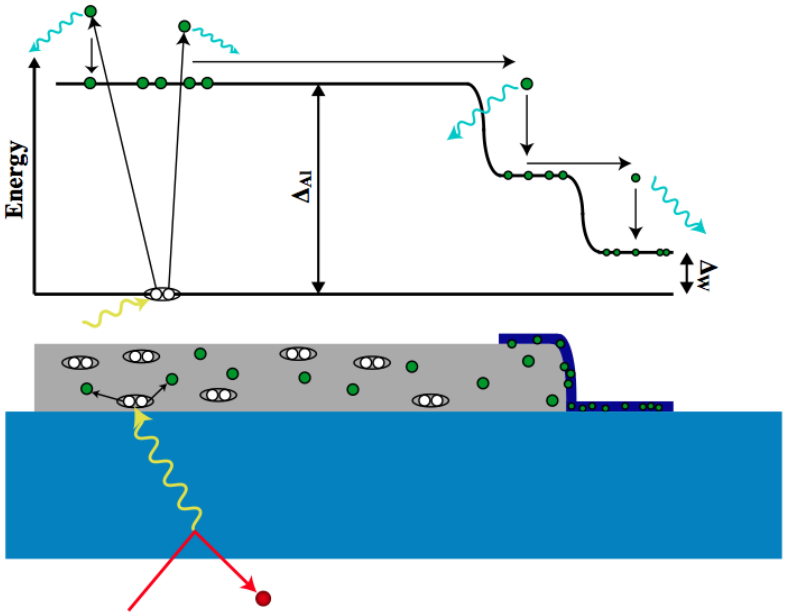

Figure 3.4: Schematic of phonon measurement by QET system [25]. In blue, the iZIP volume is shown with an interacting producing phonons (yellow waves). On contact with the superconducting Al (gray) they break Cooper-pairs (drawn as pairs of white circles) to produce quasiparticles (green circles). These quasiparticles diffuse into the W bi-layer (dark blue) and are trapped since $\Delta_{Al}/\Delta_W \approx 17$. This results in a superconducting to normal transition with high sensitivity.

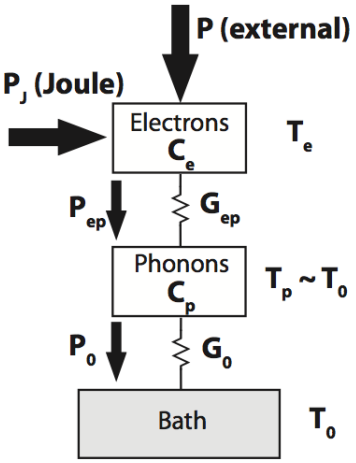

Figure 3.5: Simplified thermal circuit of TESs operation from Ref [82]. Here G_{ep} is the electron-phonon coupling constant, and G_0 is the coupling for phonons to the thermal bath, and generally $G_{ep} \ll G_0$. Power enters the system via bolometer phonons and Joule heating, and post equilibration, is dissipated in the bath.

Having the TESs voltage-biased results in Joule heating with $P_J = V^2/R$. Additionally the phonons generated in the crystal volume provide an external power source, P. Since the electron-phonon coupling in the TES depends on temperature as $G_{ep} \propto T^4$, at $\mathcal{O}(10)$ mK temperatures it is very small. Thus all of $P_J + P$ goes into self-heating of the electrons-system to a temperature much greater than the bath temperature, i.e., $T_e \gg T_0$. The change in temperature affects the Joule component (setting aside external power) and thereby the TES response.

$$\frac{dP_J}{dT} = \partial_R P_J \cdot \partial_T R = \frac{-V_b^2}{R_0}\partial_T R = -\alpha\frac{P_{J,0}}{T_0} : \quad \alpha = \frac{T_0}{R_0}\partial_T R|_{I_0} \tag{3.4}$$

In Eq.(3.4), the sensitivity of the TES (how rapidly the resistance increases given a small change in temperature at some temperature T_0, for current and resistance of I_0, R_0) is parametrized as α and can be $\gtrsim 10^3$. Thus heating causes drop in resistance which leads to drop in Joule power and the TES cools down to a quiescent state after energy input; this is the ETF effect. As a

result the signal we expect to measure will be a pulse with a rise-time given by the injection rate and a fall-time which depends on this feedback along with the time-scales associated with phonon scattering and absorption in the iZIP.

The finite impulse response can be easily derived from the power transaction equation. For a self-heated TES with heat capacity C and thermal coupling G to a bath, the change is temperature scales as $\delta T(t) \sim \exp(-t/\tau_{ETF})$ where the time-constant $\tau_{ETF} = (G/C) \times (1 + \mathcal{L})$. The ETF loop-gain is parametrized as $\mathcal{L} \equiv \alpha P_{J,0}/(GT_0)$. For iZIPs τ_{ETF} is $\mathcal{O}(100)$ μs. In practice, because phonons may scatter multiple times in an iZIP (Al coverage is 6% of face-area), the actual time scale of a phonon pulses are closer to 800μs. Finally, it can be shown that the fundamental energy resolution of these TES devices scale as, $\sigma_E \propto \sqrt{k_B G T_c^2} \propto T_c^3$. This implies that TESs with lower transition temperatures have better energy resolution. In reality one is limited from realizing this ideal power law due to additional noise from the TES readout electronics.

Measurement III: Read out electronics

A schematic of the superconducting, phonon measurement electronics is shown in Fig. 3.6. The QET is voltage biased with a shunt resistor R_{sh} and draws current I_b (when the TES is superconducting $R_{TES}(T < T_c)$ hence the shunt is essential). Heating from phonon absorption changes R_{TES} in the ETF mechanism described earlier. This causes a change in current through the SQUID coupling inductor L_i, leading to an effective change of flux in the SQUID (technically a SQUID array is used). Given this changing flux and SQUID impedance Z_{sq}, the SQUID draws a current I_{sq} which is sensed by an amplifier. The amplifier is operated in an inverting mode with the positive input held at a "lock-point" voltage V_{LP}, the negative input is referenced to the SQUID and the output is feedback coupled to the SQUID via inductor L_{fb}. Once the SQUID responds, the voltage difference across the amplifier is altered from V_{LP} referenced to ground. Thus the amplifier's output reaches voltage V_{out} such that the current driven through L_{fb} neutralizes the flux differential in the SQUID. This results in trans-resistance, i.e., the voltage variation at the output given a current at the input, of $R_{fb} \times L_i/L_{fb} = 1.2\text{k}\Omega \times 10$ due to a 10:1 coil ratio.

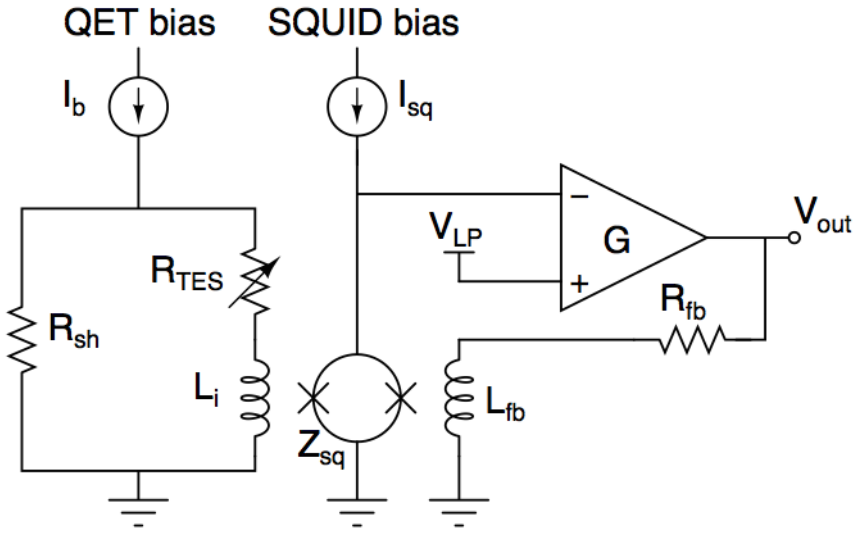

Figure 3.6: TES readout electronics utilize SQUID-amplifiers in closed-loop mode. Amplification is achieved by varying the coil ratio of the inductive coupling to the SQUID. The typical component values are,
$R_{TES} \approx 100 - 200\text{m}\Omega$,
$R_{sh} \approx 25\text{m}\Omega$,
$R_{fb} \approx 1.2\text{k}\Omega$,
$L_i \approx 250\text{nH}$,
$L_{fb} = 0.1 L_i$

The noise spectrum is expected to be roughly white with a L_i/R_{TES} roll-off at ~80 kHz.

There are three features to this spectrum: (1) the average scale set by Johnson noise in the shunt resistor (heat-sunk to a 600 mK stage in the fridge for the purpose of power management), is $\sqrt{k_B T_{sh} R_{sh}}/R_{TES} \approx 15\text{pA}/\sqrt{\text{Hz}}$. (2) At frequencies under 1 kHz, environmental pick-up and micro-phonics introduce 1/f noise which can be as large as 0.1 nA at 100 Hz. (3) The high-frequency roll-off is pushed upwards from 80 kHz to a few 100 kHz by SQUID resonances. Exact measurement of the noise and how it affects energy resolution will be discussed later in Sec. 5.3.1.

3.1.3 Yield and Surface-event discrimination

Yield selection

For every interaction, iZIPs measure charge and phonons and thus discriminate electron recoils and nuclear recoils. In Sec. 3.1.1, particularly in Eq. (3.1), it was mentioned that nuclear recoils by virtue of the inertia of moving nucleus, produces less ionization than electron recoils, i.e., they have lower ionization yield. It was also discussed that dark matter is expected to produce nuclear recoils, however at a rate substantially smaller than electron recoil(backgrounds). This is the primary reason for direct detection experiments to have electron recoil rejection, which is done by proper yield selection.

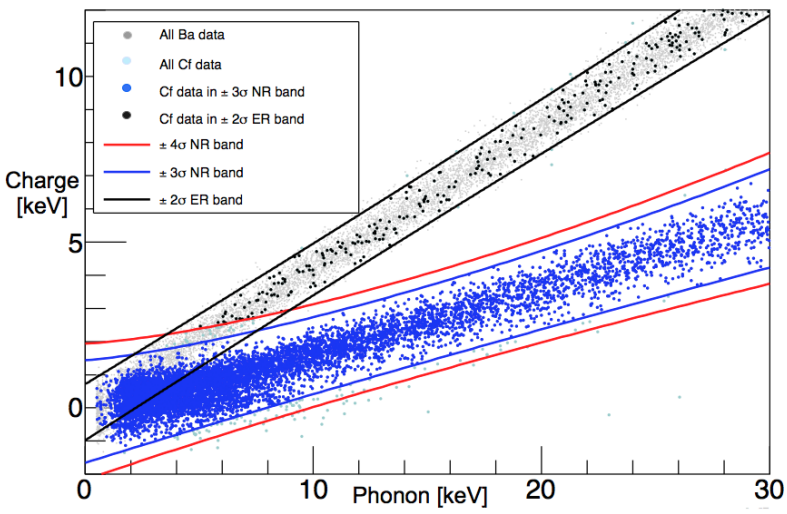

Figure 3.7: Charge energy vs Phonon energy for ^{133} Ba (γ) and ^{252}Cf (neutron + γ) sources. Here electron recoils and nuclear recoils separate into two bands, the former populates the upper band where more charge per keV of phonon energy is produced. In contrast nuclear recoils are seen in the lower band implying lower ionization yield. The electron recoil and nuclear recoil boundaries shown with the solid lines allow selection of nuclear recoils based on yield. In this plot two nuclear recoil bands are shown for varying neutron acceptance.

Fig. 3.7 shows charge and phonon measurements using ^{133} Ba (γ) and ^{252}Cf (neutron + γ) calibration sources. The electron recoils and nuclear recoils are easily distinguished based on the lower ionization yield for nuclear recoils. In analysis, energy dependent bands are constructed from these calibration data to categorize electron recoils and nuclear recoils. Leakage of electron recoils into the nuclear recoil band is $1 : 10^6$ or lower, for recoil energies over ∼10 keV. Charge readout noise at low ionization energies leads to larger yield uncertainties. Thus special analyses are performed to further discriminate on yield at lower energies, [91, 113].

Surface-event discrimination

In iZIPs the interleaving electrodes enable unprecedented rejection of surface events. Electron recoils near the edge can "lose" ionization due to electric field anisotropies at the boundary, defects from surface etches etc. and in effect have lower yield. Fig. 3.8 shows a cross-section of an iZIP

with the interleaved electrodes placed alternating biases. With this field geometry, electrons and holes from events near a surface get sensed explicitly on that side, while good bulk events share ionization with both sides. This method tags surface events, which due to the lower yields may appear to be nuclear recoils hence are a major background.

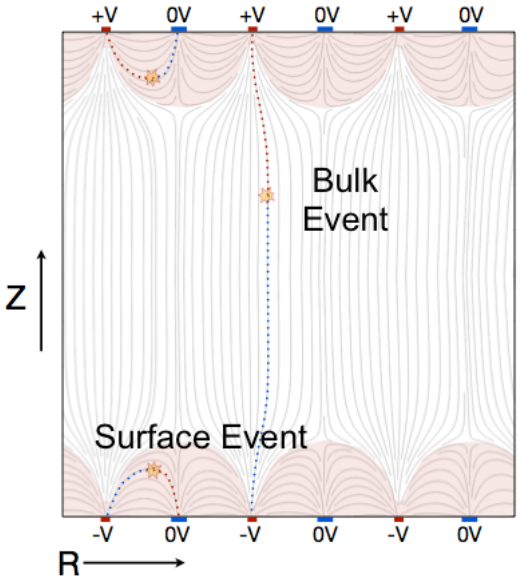

Figure 3.8: Schematic of interleaved electrodes at alternating biases. This potential arrangement leads to parallel electric field lines int he bulk, and looped lines near the surface. The resulting geometry allows tagging surface events from asymmetric charge collection.

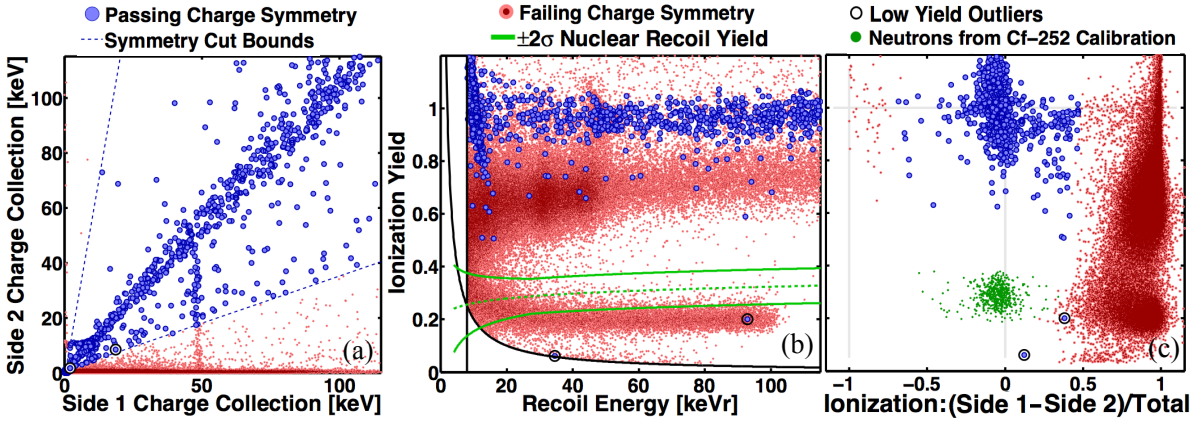

Figure 3.9: Data from ∼900 live hours of an iZIP with the ^{210}Pb source facing side 1. Good bulk events have symmetric charge collection, blue dots. Surface events from βs, γs and nuclear recoil s from ^{206}Pb near side 1 have asymmetric charge collection, red dots. The circled markers are symmetric outliers with very low charge yield. (a) Sharing of charge energy across two sides of the iZIP. Surface events appear strictly near side 1 while internal events appear in a diagonal space. (b) Ionization yield versus phonon recoil energy with nuclear recoil band in green. The hyperbolic black line is the 2 keV$_{ee}$ ionization threshold and the vertical black line is the 8 keV$_{nr}$ recoil energy threshold. Electrons from ^{210}Pb and ^{210}Bi are distinctly separated from low yield ^{206}Pb recoils. (c) Yield vs difference in energy collected on two sides. Additionally bulk nuclear recoils from neutrons are shown for comparison in green.

At Soudan an iZIP with ^{210}Pb source on one side was studied to quantify surface-event rejection efficiencies in conjunction with yield selections. In plot (a) of Fig. 3.9, data from ∼900 live hours

show good bulk events occupying a symmetric / diagonal area (blue dots) while surface events from the Pb source appear biased on side 1 (red dots). In plot (b) the yield vs. recoil energy for these data are shown. Internal bulk events (primarily electron recoils from cosmogenic and neutron activation) occupy the canonical unity yield band, and the expected nuclear recoil band (derived from Fig. 3.7) is shown with green lines. In plot (c) the yield is presented as a function of difference in charge energy from the two sides. For comparison bulk nuclear recoils from neutron calibration data are shown in green. The surface events appear as two bands, neither coincident with the expected electron recoil or nuclear recoil bands.^{210}Pb decay produces several βs, γs and nuclear recoils from ^{206}Pb. Since these occur on the surface, ionization is lost on average and the yields are systematically lower. This study concluded that in the nuclear recoil band between 8-115 keV$_{\rm nr}$the 90%CL upper limit to surface event leakage was 1.7×10^{-5}, see Ref. [91].

3.2 Location and Shielding

The SuperCDMS experiment is currently operating at the Soudan Underground Laboratory in northern Minnesota. This location is essential to reduce muon flux and surface radioactivity. The muon flux is particularly abated by having 714 m of rock overburden. Fig. 3.10 shows various underground laboratories and the effective muon fluxes as a function of their depth.

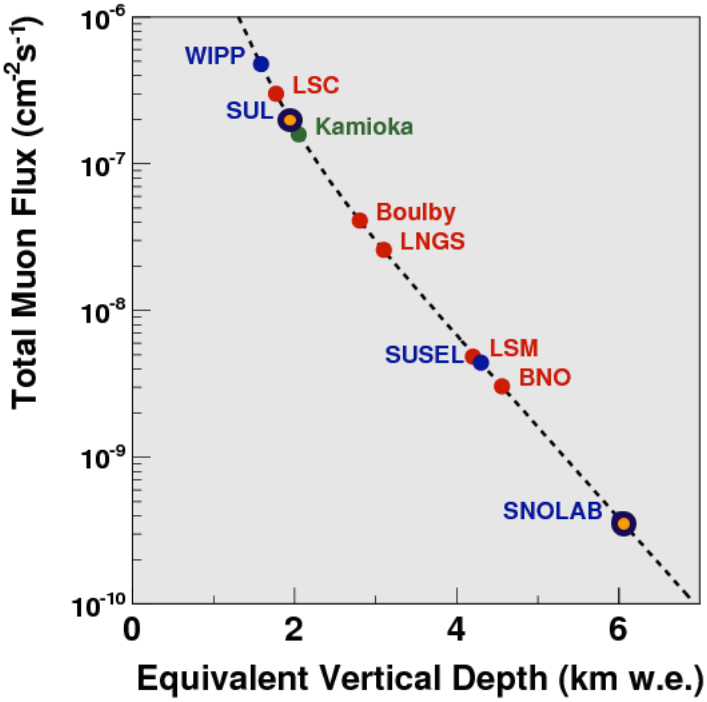

Figure 3.10: Muon flux in various underground laboratories, plot adapted from Ref. [114]. The current and future locations of the SuperCDMS experiment, Soudan Underground Lab (SUL) and SNOLAB at Sudbury respectively, are shown with orange markers. Depth is in kilometers of water equivalent. Further details on these facilities may be found in Ref. [114].

Energetic muons from cosmic rays can be indirect sources of background due to the spallation products (neutrons, αs, βs etc.) they produce. Thus following the rock overburden, the experiment is also surrounded with active scintillating veto panels to provide further rejection power. Internal to the cavern terrestrial radiation becomes the next dominant source of background, primarily from U and Th in the rocks and Rn daughters in the air. These are mitigated by layers of passive shielding where lead is used to stop γs and polyethylene moderates neutrons. Finally the whole experiment is

covered by scintillator panels which make up the muon-veto, and is essential in rejecting energetic background events, particularly originating from cosmic ray showers. The various layers for the SuperCDMS Soudan experiment are shown in Fig. 3.11.

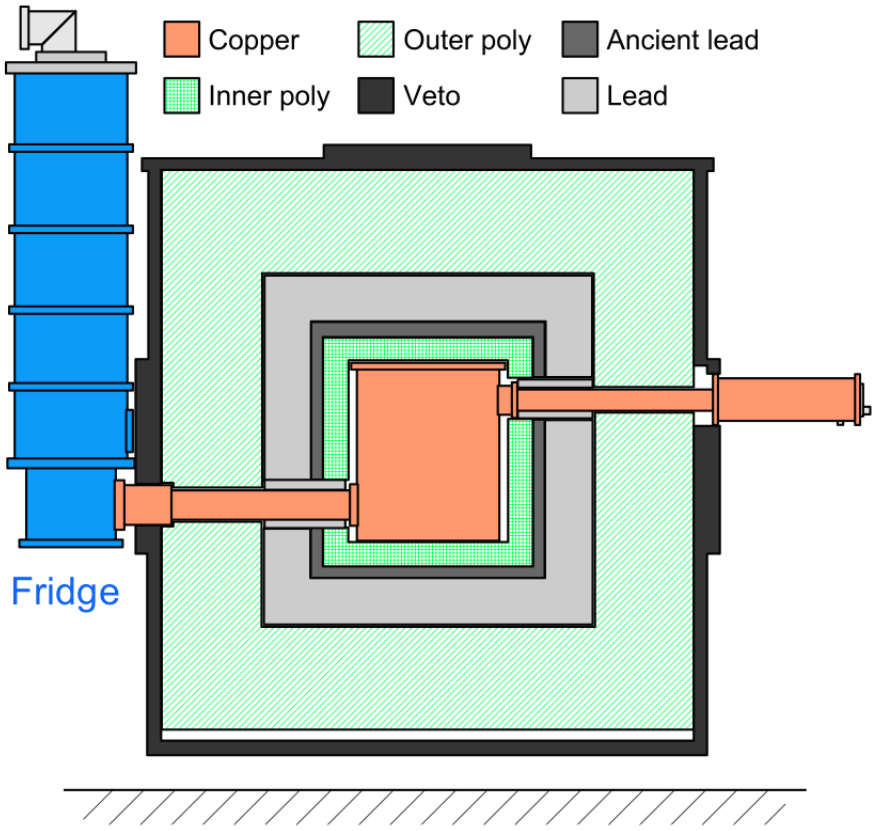

Figure 3.11: Schematic of the shielding for the SuperCDMS Soudan setup. As seen the outermost layer is the active (muon) veto shield. Following that there is ∼40 cm of poly and two layers of lead shielding, ∼18 cm outer and ∼4.5 cm inner, where ancient lead is used because it is low in 210Pb specifically. The final layer is ∼8 cm of poly. The main structure is built from low radioactivity copper. The central Cu structure is the ice-box which can concentric Cu cans and holds the detectors at ∼50 mK. This setup is covered by scintillating panels which make up the veto. The dilution fridge on the left is connected via the cold stem. All electronics are read out from the icebox via the e-stem and the e-box, shown as the copper structures on the top-right. Figure adapted from Ref. [25].

3.3 Cryogenics

The main copper volume in Fig. 3.11 is called the ice-box and the detectors are housed in here. SuperCDMS detectors are cryogenic solid state detectors and are designed to be operated at 50 mK. Running several kilograms of detector mass at extremely low temperatures is a non trivial effort, and the requisite cooling is obtained in several stages.

An Oxford dilution fridge provides the main cooling power, rated at 400 μW at 100 mK. Since this commercial unit is not constructed from high radio-purity materials, the shielding structure is used to separate the fridge from the detector volume, and connected by the "cold stem". In Fig. 3.11 the fridge is shown as the blue structure to the left with the ice-box in the center, protected by layers of shielding.

The icebox contains concentric copper vessels or cans, which are heat sunk to the different temperature stages of the fridge, and twice insulated from the environment by inner and outer vacuum chambers. From outside to inside these cooling stages are: room temperature (300 K), nitrogen shield (77 K), helium bath (4 K), still (1 K), cold plate (130 mK), mixing chamber (40 mK). These few cm thick radio-pure copper cans also stop αs and βs. A surrounding mu-metal sheet protects the cold electronics from external magnetic fields. Power and read-out lines from the cold electronics are finally passed through an "e-stem", much like the cold-stem, to reach the reach a panel of connectors at the electronics readout box, called the "e-box". The e-stem and e-box are seen to the right of the ice-box in Fig. 3.11. A Gifford-McMahon cryocooler acts as a secondary refrigeration system. It is a closed-circuit helium refrigerator that provides 1.5 W of cooling power at 4K and 40 W at 77K. The cryocooler removes heat coming in from the outside via the stripline traces.

3.4 Detector payload and internal backgrounds

3.4.1 Detector arrangement

SuperCDMS Soudan started operations in 2011 with 15 interleaved Z-sensitive ionization and phonon detectors, discussed in Sec. 3.1. The iZIPs, each in it's own Cu detector housing, are arranged in 5 towers in sets of 3. Each tower is built from ultra-pure Cu. The FET-amplifier system for charge readout and the SQUID-amplifier system for phonon readout are compactly arranged in a SQUET (SQUID + FET) card, Figs. 3.3, 3.6. Each tower has a SQUET card that reads and controls the iZIPs' phonon and charge sensors, and connect to two detector interface boards (DIBs) on each iZIP. Further discussion on DIB connections will be presented in Sec. 5.2.1. Connections from these SQUET cards are then made to the e-box via the e-stem, right side of Fig. 3.11. The general tower assembly is shown in Fig. 3.12, and further details may be found in Ref. [95, 82].

3.4.2 Internal backgrounds

Various shielding structures for background suppression was discussed earlier. However there is residual radioactivity from the fridge stages, tower components and detector housings that affect the dark matter search sensitivity. Following the CDMS II experiment, studies were performed to measure the internal backgrounds and understand what the level of various isotopic sources that may produce them. For the various lead and copper structures, the background rates obtained

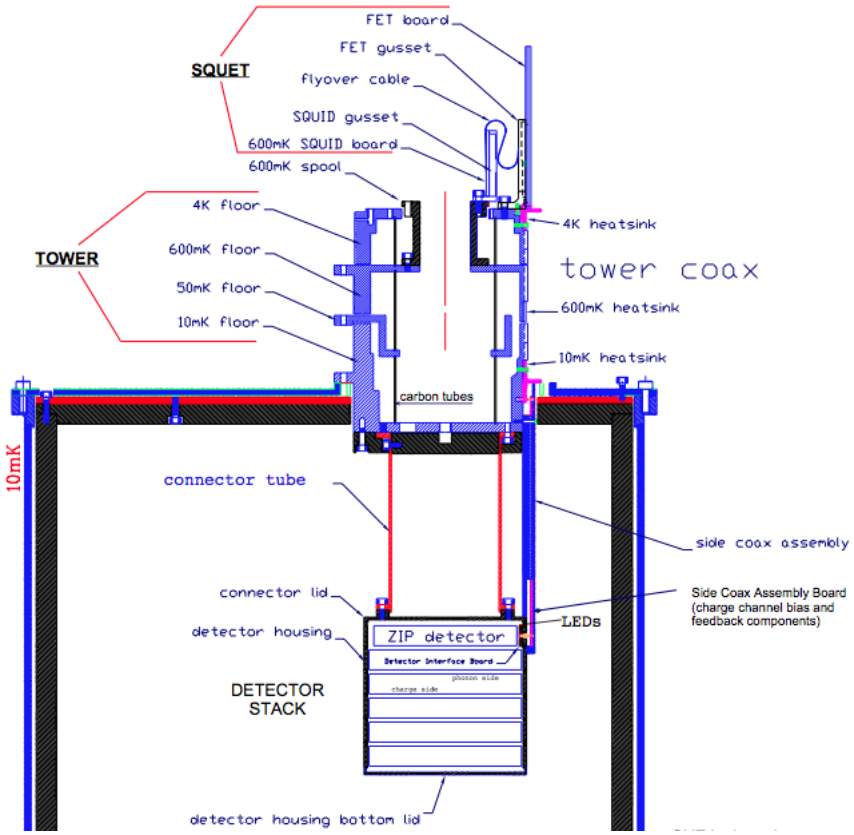

Figure 3.12: Schematic of tower setup and cold electronics in the ice-box.

from matching simulation with measurements are listed in Table 3.1. The cans and inner surfaces rates were too small to be estimated properly. The errors in these measurements are difficult to quantify, however the χ^2 per degree-of-freedom was around 3 implying good fits.

Item	Outer Pb	Inner Pb	Inner poly	Outer surface
^{60}Co	42.92	-	-	-
^{40}K	1.574	4.588	9.672×10^{-4}	-
^{232}Th	6.911×10^{-3}	2.035	4.153	-
^{238}U	1.77×10^{-4}	5.867	4.050	-
^{222}Rn	-	-	-	73.85

Table 3.1: Background events rates as estimated from matching source simulations with measurements from CDMS II. The numbers from this study are for event rates in the bulk of the detectors. Corresponding numbers for surface or outer radii events are comparable. The units are mBq /cm^2 for Inner/Outer surface sources and mBq /kg for everything else. A "-" means that source was not simulated

For the iZIPs used in the SuperCDMS experiment background rates from cosmogenic activation and lead decay-chain were also studied. Compton scatters have a roughly constant rate of ~2 Counts/ keV$_{ee}$/ kg / day . Neutron capture during nuclear recoil calibration with ^{252}Cf and cosmogenic

activation of isotopes produce several spectral peaks from electron capture processes. Around 1.3 keV_{ee} the L-shell photons are from $^{68/71}$Ge, ^{68}Ga and ^{65}Zn. The corresponding K-shell photons are seen at 10.36, 9.66 and 8.98 keV_{ee} respectively. The dominant K-shell line is at 10.36 $\text{keV}_{\text{ee}}$and the rate around this energy is $\sim$40 Counts/ keV_{ee}/ kg / day . The net L-shell rate at 1.3 keV_{ee} is $\sim$10 Counts/ keV_{ee}/ kg / day . Details on these spectral peaks are presented later in Sec. 6.4.2. Surface nuclear recoils from Pb decay chains discussed in Fig. 3.9, add low energy backgrounds at the level of $\lesssim$1 Counts/ keV_{nr}/ kg / day .

3.5 Warm Electronics and Data processing

3.5.1 Warm Electronics

Signals from the detectors are read out at the E-box as mentioned. The essential steps for filtering, triggering and data acquisition are summarized below, and further technical details may be found in Refs. [95, 82].

1. **FEB:** Signals and control lines from each DIB of an iZIP are fed into Front End Boards (FEBs) via 50-wire cables. FEBs are custom electronics containing amplifiers and other components for the charge and phonon readout circuits, as well as control circuits for the detector LEDs, charge biasing, SQUID biasing, etc.

2. **RTF:** The FEB output must be polished before data acquisition to prevent collection of spurious signals. The Receiver Trigger Filter (RTF) boards are designed to correct for baseline fluctuations, amplify and filter the signals to best select physics-like signals over noise-like fluctuations. Given the phonon timescales, band-pass filters are implemented with poles at 900 Hz and 18 kHz. The filtering and amplification may be tuned based on the noise environment. Finally thresholds are implemented in a comparator to issue triggers based on signal amplitudes compared to the thresholds. In general, triggering is performed on the summed phonon pulse whose threshold is referred to as P_{lo}.

3. **TLB:** The Trigger Logic Board (TLB) accepts the physics triggers from the RTF and veto triggers. Veto triggers are separately processed by veto control electronics which interface with the muon veto scintillators. Based on the inputs, the TLB can issue three types of triggers: (a) A proper phonon signal leads to a "global" trigger where data is acquired for $\sim$1 ms around this trigger time. The exact span of the window may be tuned depending on whether calibration or WIMP search data is being collected. (b) A random trigger may be issued to collect unbiased data for monitoring noise performance (c) A veto multiplicity trigger can be initiated by simultaneous hits on multiple veto panels.

Once a trigger is issued an "event" is recorded and processed for further analysis. An example of a good event from one iZIP is shown in Fig. 3.13.

3.5.2 Data processing

For every recorded events alongside trigger information, the raw data consists of several time-domain pulses: 4 charge pulses (inner / outer $\times$ Side 1/ 2) and 8 phonon pulses (channels A...D $\times$ Side 1/ 2), see Fig. 3.1 and Fig. 3.13. From these raw traces, timing and energy information are first calculated. These variables are called reduced quantities (RQs), and later get combined to provide more complex information regarding physical location of events, nature of recoil etc.

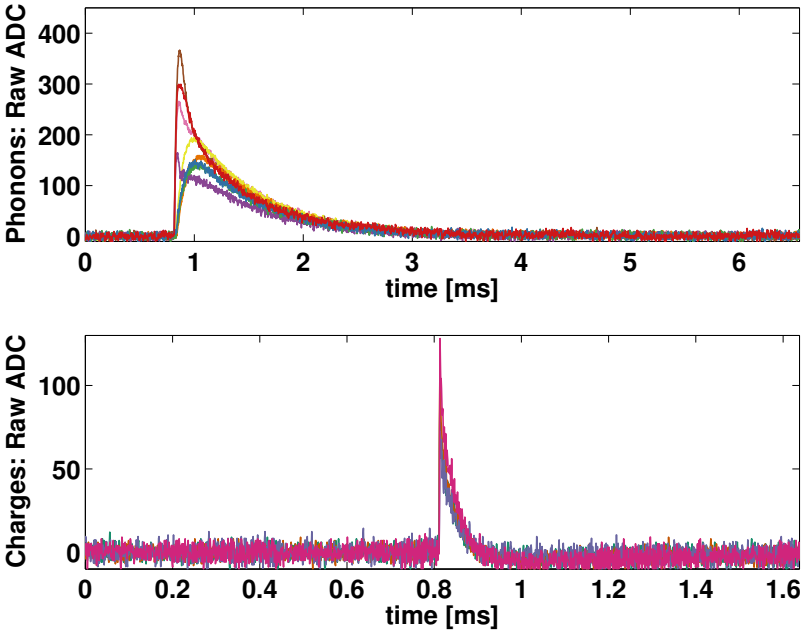

Figure 3.13: Raw pulses or traces from a good event. The top panel shows 8 phonon pulses (4 from each side of an iZIP), and the bottom panel shows 4 charge pulses (2 from each side of an iZIP). Phonon pulses are 6.55 ms in length and sampled at 625 kHz. Charge pulses are 1.64 ms in length and sampled at 1.25 MHz.

The analysis discussed in this thesis relies on the first level energy and timing RQs, and thus I will outline the computation of these quantities only.

Walked times

For every pulse the rise and fall time is calculated by a walking routine. First the pulse is filtered by a 50 kHz Butterworth filter. Then relative to the maximum (called the 100% point), the routine "walks down" left to some fraction, say the 50% percent point, see Fig. 3.14. This gives the 50%-to-100% pulse rise-time as $t_{100} - t_{r,50}$. Similarly, walking to the left of the maximum gives the fall times. This routine is run for various combinations of such percentages of the maxima to characterize pulse shapes.

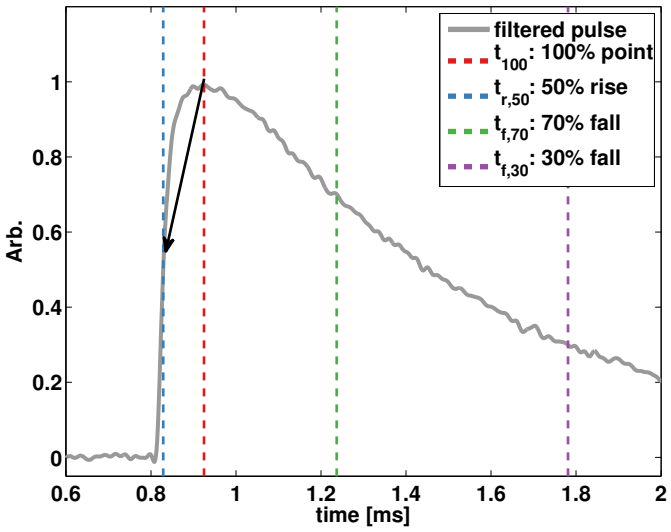

Figure 3.14: Example of walked time calculations. The maximum 100% pulse height occurs at t_{100}, the 50% point on the rising edge is at $t_{r,50}$, similarly the 70% and 30% points on the falling edge are at $t_{f,30/70}$. The black arrow is the direction of "walking-down" to the left to find the 50% rising point.

Optimum Filter

In Optimal Filter (OF) theory, the amplitude of a signal with known profile is estimated by maximizing signal-to-noise. To do this one requires expected noise and signal models, called templates. A phonon template is generated from aligned ensemble average of good phonon pulses obtained from calibration data. This template is the characteristic phonon pulse shape, after averaging over variations from position dependence and random fluctuations. The noise templates are similarly an ensemble average of base-line measurements collected randomly. At the heart of the OF routine, a frequency domain χ^2 is minimized for maximum signal amplitude. If the phonon template, noise template and data are represented by $\tilde{A}(\nu)$, $\tilde{J}(\nu)$, $\tilde{S}(\nu)$ respectively, then the best amplitude (a) and delay (t_0, time shift between signal and template) are those which minimize the χ^2 in Eq.(3.5).

$$\chi^2(a, t_0) = \sum_{\nu} \frac{|\tilde{S}(\nu) - ae^{-i2\pi\nu t_0}\tilde{A}(\nu)|^2}{\tilde{J}(\nu)} \tag{3.5}$$

In Eq.(3.5) optimization is done in frequency domain since noise in frequency domain is primarily uncorrelated[3]. From minimizing this χ^2 we obtain the OF energy estimate and the variance of this estimate, generally called the OF resolution and shown in Eq.(3.6).

$$\hat{a} = \frac{\sum_\nu \tilde{S}(\nu)\tilde{A}^*(\nu)/\tilde{J}(\nu)}{\sum_\nu \tilde{A}(\nu)\tilde{A}^*(\nu)/\tilde{J}(\nu)} = \frac{\hat{\Phi}\odot\tilde{S}}{\hat{\Phi}\odot\tilde{A}}, \quad \sigma_{\hat{a}}^{-2} = \sum_{\nu} |\tilde{A}(\nu)|^2/\tilde{J}(\nu) = \hat{\Phi}\odot\tilde{A} \tag{3.6}$$

In Eq.(3.6), $\hat{\Phi}(\nu) \equiv \tilde{A}^*(\nu)/\tilde{J}(\nu)$ is the Optimal Filter, constructed from the expected signal and noise spectra.

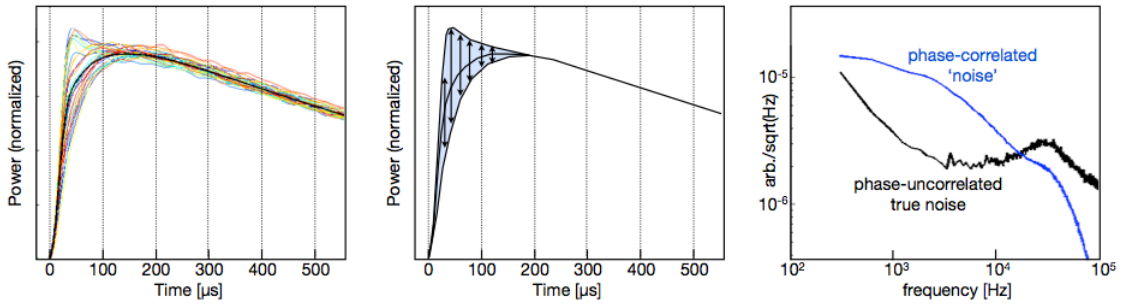

Figure 3.15: Principle behind the Non-Stationary OF is shown by zooming on the rising edge of various phonon pulses. This variations are captured as non-stationary noise and used along with the regular noise spectrum to optimize signal-to-noise computation, so as to get the best energy resolution [87].

For phonon signals variations in rise-time due to variations in event location relative to TESs, resulted in a suboptimal template and lead to higher than expected OF resolutions. To improve on this, the OF algorithm was generalized for non-stationary processes. Here we not only fit a signal to the template, but also utilize the difference in the signal and template. This residual is a time / frequency correlated structure which is used to de-weight all (mainly high) frequency components which reflect pulse shape variations the most, see Fig. 3.15. Thus the initial variations are suppressed by treating the residuals as non-stationary "noise". The theory of optimum filters, including construction of the non-stationary weights is discussed at large in Appendix E.

[3]In case of correlated noise one has to factor in a complex covariance matrix, however the general idea holds true.

Calibration

The raw phonon pulses, as shown in Fig. 3.13 have variations in rise-time and fall-times. While the different rise-times are true physics variations, the fall-times are set by the scattering and absorption of ballistic phonons, and should be similar. Variations in fall-time are generally attributed to anisotropies in TES lithography, for example there are inadvertent temperature gradients across the faces. Thus the phonon pulses are calibrated firstly to have their tails matched. Following this relative calibration, amplitude or global calibration is done using calibration sources such as 356 keV spectral line from ^{133}Ba γ sources. Global calibration is described later, and results from calibrating the event in Fig. 3.13 is shown in Fig. 3.16. Note the different peaky profiles of the energy read by each channel. This is the position dependence that the Non-Stationary OF corrects for.

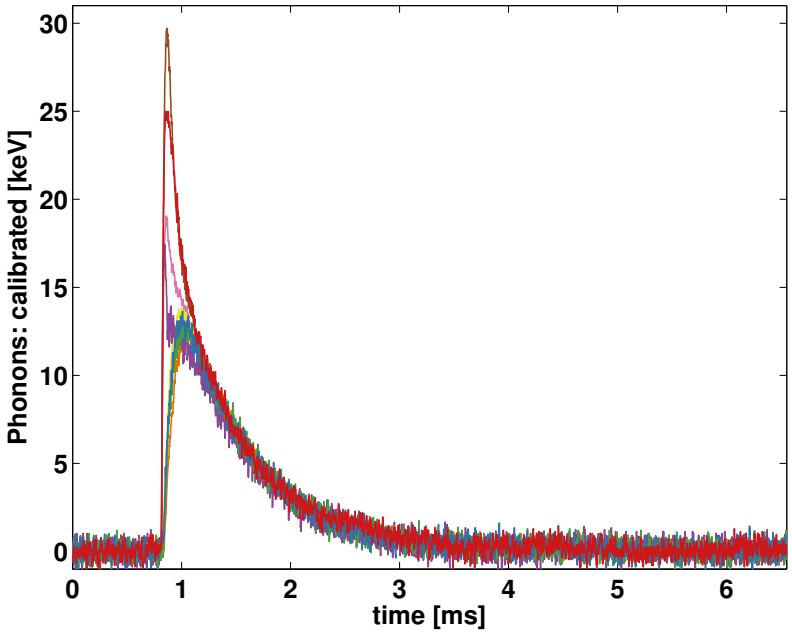

Figure 3.16: Phonon pulses from Fig. 3.13 after tail-matching and global calibration. The various colors stand for the 8 different phonon channels.

For charge pulses, relative calibration is not essential as the fall-times are set by the RC time from the readout circuit shown in Fig. 3.3

Chapter 4

Introduction to the CDMS low ionization threshold experiment

Thus far, all hints of signals from direct detection experiments can be interpreted as coming from light WIMPS, $m_\chi \sim \mathcal{O}(10)$ GeV/c^2, Sec. 2.6.4. In this section I will discuss the challenges associated with detecting such light WIMPs. Finally I will explain how CDMSlite detectors circumvent these issues by employing a novel method of operation.

4.1 Motivation: Challenges in detecting light WIMPs

Consider a simple kinematic example of a 10 GeV/c^2 WIMP, traveling at $\sim 10^{-3}$c and scattering off a Ge nucleus. The nucleus will recoil with energy, $E_r \sim 1$ keV$_{nr}$ and this energy will be distributed into nuclear motion ($\sim$85 %) and electronic excitation ($\sim$15%). Since traditional Ge detectors have nuclear-recoil detection thresholds $\gtrsim 2$ keV$_{nr}$, such a recoil would be sub threshold, unless the WIMP was moving faster. Regular detectors are therefore sensitive to the high velocity end of the WIMP distribution where uncertainties can dominate.

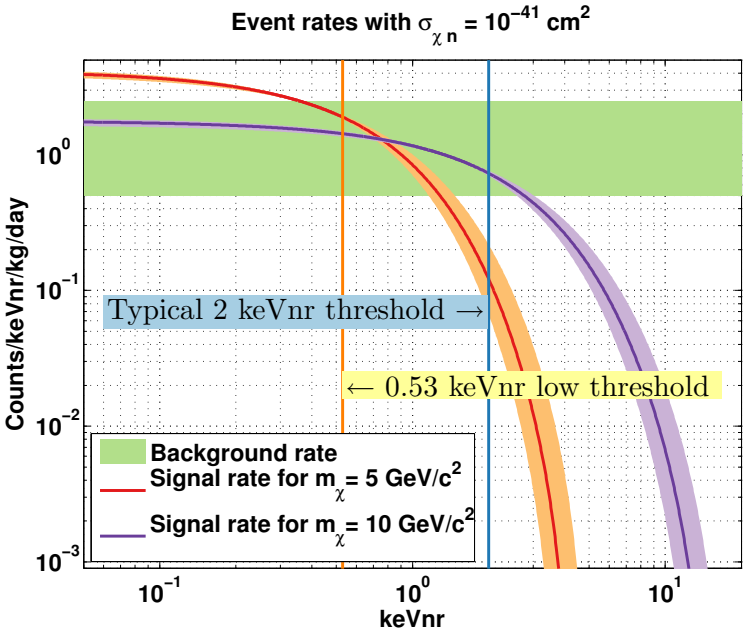

Figure 4.1: Expected direct-detection rates (in counts per nuclear-recoil energy, per detector-mass, per day) for WIMPs with WIMP-nucleon cross-section of 10^{-41}cm^2, as a function of nuclear-recoil energy. WIMPs of masses of 5 and 10 GeV/c^2 (violet and red curves) are considered here, with surrounding bands representing the effect on rates, of varying mean and escape velocities of the Standard Halo Model. The horizontal green band is the expected background rate, including uncertainties at Soudan. Sensitivity to 5 GeV/c^{2}WIMPs increases by an order of magnitude on lowering the traditional threshold from 2 keV$_{nr}$(blue vertical line) to 0.53 keV$_{nr}$(orange vertical line).

Studies of astrophysical distributions indicate that the Standard Halo Model (SHM) is an idealization, and the values of the escape and mean velocities (v_{esc} and v_0) can vary significantly [77]. Fig. 4.1 shows the expected event rates for light WIMPs scattering off Ge atoms with a

WIMP nucleon cross-section ($\sigma_{\chi n}$) of 10^{-41} cm^2. I use the SHM with a range of v_0 and v_{esc} velocities: the lower and upper bounds on each velocity are v_0 = 195, 255 km/s and v_{esc} = 498, 608 km/s respectively. The central lines use the standard values of v_0 = 220 km/s and v_{esc} = 544 km/s [77, 78, 79, 80]. The expected background rate at Soudan, as measured at energies over 10 keV$_{\rm nr}$ is ∼1 Counts/ keV$_{\rm nr}$/ kg / day . This is shown with a larger band covering 0.5-2.5 Counts/ keV$_{\rm nr}$/ kg / day , indicating uncertainties at low energies. From this figure, one can draw two main conclusions: For thresholds > 2 keV$_{\rm nr}$ (1) the significance of the observation may rest on the tail profile of the dark matter distribution, (2) and without significant background rejection, signal detection can be very challenging.

Clarification on the 2 keV$_{\rm nr}$ number

Thus far, the lowest nuclear-recoil energy threshold in Ge detectors of ∼2 keV$_{\rm nr}$ come from the CoGeNT experiment (0.5 keV$_{\rm ee}$ threshold = 2.27 keV$_{\rm nr}$) [97], and from the CDMS II experiment (2 keV$_{\rm nr}$ threshold) [102]. For both these experiments a major limiting factor was the trigger threshold energy. This is an essential limitation and I will describe it in some detail.

A detector's electronic read-out has base-line noise on top of which a signal may occur. Such noise is a combination of intrinsic fluctuations in the detector as well as extrinsic environmental pick-up. Experiments should not trigger on noise fluctuations, and hence a threshold for triggering is implemented in data acquisition. The detector's output must be over this threshold value, to ensure that the experiment triggers on proper physics signals. If this is not the case, noise starts to dominate trigger rates and puts unnecessary load on the data acquisition system. Even if noise triggers contain signals, extracting them from random fluctuations can be inefficient as it is difficult to design robust noise rejection algorithms when the signal amplitudes are low enough to be hidden in the noise variations (typically $\mathcal{O}(1)$ keV$_{\rm nr}$). As a result, proper signal detection is practically impossible under ∼2 keV$_{\rm nr}$ and this is the typical trigger-threshold in common Ge detectors.

This section outlined the necessity for light WIMP detectors to have very low thresholds, and discussed why traditional detector technologies loose sensitivity under 2 keV$_{\rm nr}$. In CDMSlite we have demonstrated a new method of in-situ signal amplification which allows us to study sub-keV$_{\rm nr}$ signals, thereby circumventing such detection limitations. The next section will discuss in detail the physics behind this amplification process.

4.2 Towards lower thresholds: The physics of Luke amplification

CDMS detectors measure the ionization and lattice vibrations (phonons) produced by every interaction. As described earlier in Sec. 3.1.1, the ionization is drifted out by applying an electric field across the crystal. In this process there is drift heating, i.e., the moving charges collide with the lattice and lose energy by emitting Luke phonons (see Fig. 4.2). I will now describe this process in greater detail, as it is central to CDMSlite operation.

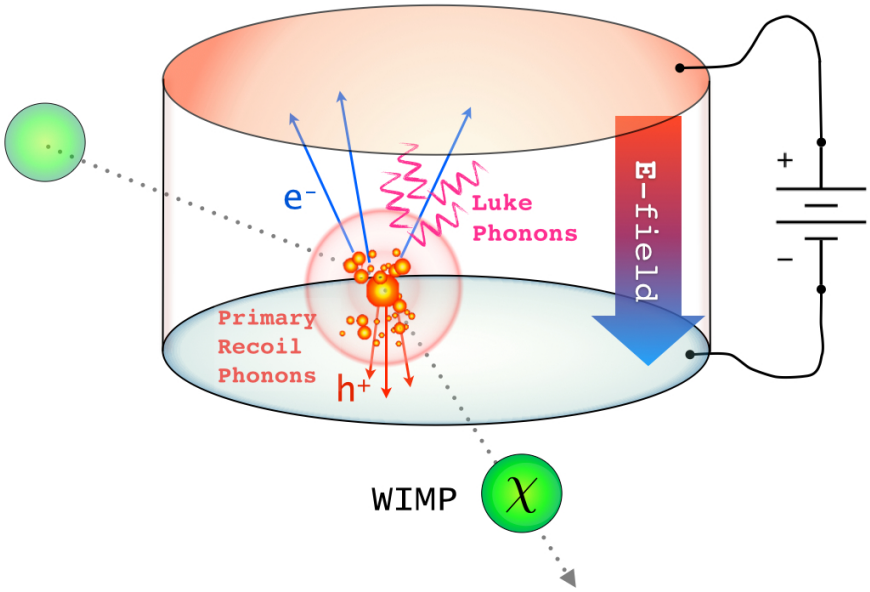

Figure 4.2: Sketch shows emission of Luke phonons from drifting the ionization created by a WIMP recoil. The charge clouds formed upon impact are shown as "fire-balls". Electrons (blue) and holes (red) are drifted out from the clouds by a bulk electric field generated by an external power supply. Note that Luke phonons are emitted by *all* charges moving in the presence of an electric field. Also shown in light-red spherical wave-fronts are the primary recoil phonons. Phonons, both Luke and primary, are read out by transition edge sensors (TESs) lithographed on the detector faces.

Generation of Luke Phonons

To understand Luke phonons we must study the motion of charged particles in a crystal. As an electron (or hole) hops between lattice sites, due to momentum conservation, there is a "kick-back" effect resulting in deformation of the lattice, i.e., charge propagation necessitates phonon production. The one vertex scattering is shown in Fig. 4.3.

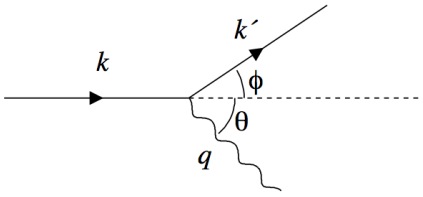

Figure 4.3: Schematic of an electron scattering in a lattice. The initial state is the lattice at rest and an incoming electron with momentum k. The final state involves the lattice with recoil momentum q and an electron with momentum k'. Here ϕ and θ are the angles between the final momenta and the initial electron's momentum.

In Fig.4.3 an electron with four-momentum $(E/c, \hbar\vec{k})$, impinges on a lattice at rest. This interaction produces a phonon with four-momentum $(\hbar\omega/c, \vec{q})$ and the electron is in final state with four-momentum $(E'/c, \hbar\vec{k'})$. Conservation of four-momentum gives the relation $2\left(k\cos\theta - \frac{m}{\hbar}\frac{\omega}{q}\right) = q$. I define $c_s \equiv \omega/q$ as the phonon (sound) speed and $v \equiv \hbar k/m$ as the speed of the charge. Note

that since $q > 0$, it follows that $k \cos\theta > \frac{mc_s}{\hbar}$. This implies that the electron must be supersonic ($v > c_s$), and that the phonon is emitted in a forward cone ($\pi/2 > \theta > 0$). Luke phonons are thus crystal analogs of Cerenkov radiation [108, 115]. Next, we need to understand the distribution of energy between the charge and the phonons, i.e., for a fixed input energy E, what is the energy sharing between the scattered electron (E') and the emitted phonons ($\hbar\omega$) ?

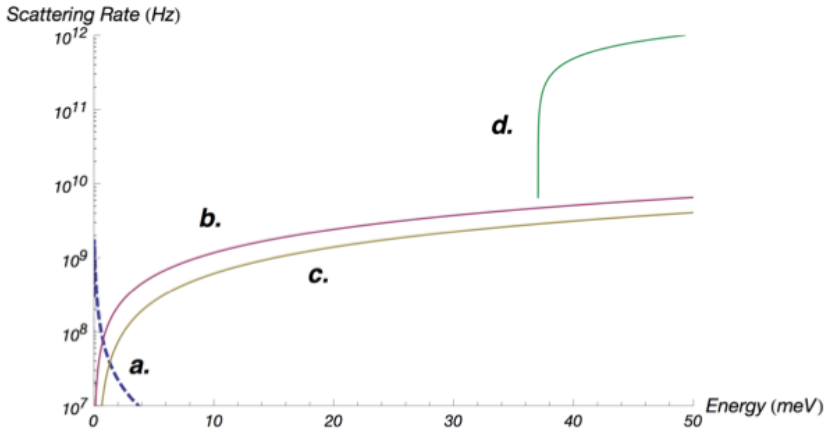

Figure 4.4: Scattering rate of drifting holes: **a.** Impurity scattering for impurity densities of $10^{10}/\text{cm}^3$, **b and c.** acoustic phonon emission from heavy-heavy and heavy-light band transitions **d.** Optical phonon emission. The rates for electrons are similar though the optical branch starts at $\lesssim$30 meV, see Ref. [107]

In semiconductors, propagating charges cannot be accelerated indefinitely, irrespective of field strength, due to electron (hole)-phonon interactions. At low energies ($E <$ 20 / 30 meV for electrons / holes) only acoustic (constant c_s) phonons may be emitted. However over $\mathcal{O}(10)$ meV, other phonon modes (optical, inter-valley etc.) may be excited and the rate of phonon emission increases drastically with energy, see Fig. 4.4, [107]. The competition between power injected by the accelerating field and power lost to phonon emission limits the maximum speed, hence the final energy (E') of a drifting charge. In Ge detectors at 40 mK, electric fields ranging from 1-100 V/cm produce maximum drift velocities of 10^6-10^7 cm/s [116]. A typical $\sim \mathcal{O}(10)$ V/cm field limits the maximum energy[1] of the charges to be $<$ 30 meV. Thus the work done by the electric field in drifting the charge over a typical path length of 1 cm in iZIPs, is $\mathcal{O}(10)$ eV $\gg$ 30 meV. Hence practically all the work done is emitted as Luke phonons. The minute amount that remains as kinetic energy is released when the charges reach the detector boundary. Since crystal momentum is conserved, this energy is lost by emission of relaxation phonons as the electrons (holes) equilibrate down to the Fermi-sea. Finally we obtain a classic result for the energy in Luke phonons,

$$\langle \hbar\omega \rangle \equiv E_{\text{L}} = N_{\text{e/h}} \times eV_b \tag{4.1}$$

Thus, theoretically, our ionization signal (now detected in phonons) can be amplified in-situ by simply increasing the bias voltage. This was first observed by Luke, Neganov and Torfimov [111, 112]. Luke demonstrated that until a break-down voltage was reached, the noise fluctuations remained independent of the bias (Fig. 5 of Ref. [111]). *This* is the promise of Luke amplification: our ability to boost signal-to-noise by simply raising the detector bias.

[1]These numbers are order of magnitude bounds. Effective-mass and energy-momentum relations make these differ slightly for electrons and holes, e.x. electron "mass" is a tensor in Ge. For details refer to [116, 107, 108, 115].

4.3 Necessary units: Energy scales for CDMSlite

The physical quantities measured by CDMS experiments are:

- Charge electrodes measure the image charge for the physical electrons and holes that are drifting inside the detector, see Sec. 3.1.1. Following straight forward calibration procedures we obtain the energy in ions produced by an interaction. The charge thresholds are typically $\gtrsim 5$ $\mathrm{keV_{nr}}$, making them ineffective in detecting ionization produced by a 10 $\mathrm{GeV/c^2}$ WIMP recoil, which would deposit energy around 1 $\mathrm{keV_{nr}}$.
- Transition edge sensors (TESs) measure the energy in phonons, see Sec. 3.1.2. The phonon population comprises both primary recoil and Luke phonons. Hence we measure the total phonon energy, or E_{t} which is,

$$\begin{aligned} E_{\mathrm{t}} &= E_{\mathrm{r}} + E_{\mathrm{L}} \\ &= E_{\mathrm{r}} + N_{\mathrm{e/h}} \times eV_b \\ &= E_{\mathrm{r}}\,(1 + \mathrm{Y}(E_{\mathrm{r}})/\varepsilon_\gamma \times eV_b) \end{aligned} \tag{4.2}$$

The units for E_{t} are $\mathrm{keV_t}$. This is the observable that benefits directly from Luke amplification. Here $\mathrm{Y}(E_{\mathrm{r}})$ is the ionization yield defined earlier in Sec. 3.1.1. For electron recoils (γs, βs . . .) the yield is normalized to unity. For nuclear recoils (neutrons, WIMPs) one has to include the energy dependent ionization yield function. The average electron recoil energy required to generate an electron-hole pair in Ge is $\varepsilon_\gamma = 3$ $\mathrm{eV_{ee}}$. For nuclear recoils this is "quenched" by $\mathrm{Y}(E_{\mathrm{r}})$.

If the nature of the interaction is known, then we can convert the measured E_{t} [$\mathrm{keV_t}$] to the recoil (source) energy E_{r} [$\mathrm{keV_{nr}}$ or $\mathrm{keV_{ee}}$]. For electron recoils (since $Y(E_{\mathrm{r}}) \equiv 1$) we obtain,

$$E_{\mathrm{r,ee}} = \frac{E_{\mathrm{t}}}{1 + g_L(V_b)} \tag{4.3}$$

For convenience I defined $g_L(V_b) \equiv eV_b/\varepsilon_\gamma$ as the Luke-gain. The recoil energy obtained [2] in this manner by knowing (or assuming) that the interactions are from electron recoils, is called *electron-equivalent* recoil energy, or $E_{\mathrm{r,ee}}$, with units of $\mathrm{keV_{ee}}$. Similarly, if we know (or assume) that the incoming particles produce nuclear recoils, we obtain E_{r} by solving Eq. (4.2). The resulting recoil energy is the *nuclear-recoil* energy, or $E_{\mathrm{r,nr}}$ with units of $\mathrm{keV_{nr}}$.

Utilizing the concepts developed here, the next chapter will review tests of Luke amplification performed with various germanium detectors by the CDMS and SuperCDMS collaboration.

[2] Here we assumed that the ionization yield viz. the number of electron-hole pairs generated is constant for electron recoils and energy dependent for nuclear recoils. It is possible that that in both cases the number of charge particles extracted depend on the local electric field. At this introductory level we also ignore notions of charge trapping and field effects on propagating charges; this is addressed later.

Chapter 5

Preliminary tests of CDMSlite

The first experimental tests of the CDMSlite mode of operation were done with silicon detectors by D. Akerib et al. [117] and J. Hall [118], and I performed the preliminary analyses. Since the first science result (topic of this thesis) has been achieved with a germanium detector, and the current payload at Soudan is entirely germanium iZIPs, the scope here is restricted to germanium bolometers used in CDMSlite mode[1].

5.1 Tests with a CDMS II style ZIP detector

During the CDMS II experiment at Soudan [96, 95, 102], CDMSlite tests were carried out on a 1 cm thick Ge detector designated T3Z2 (G25). The CDMS II experiment used ZIP detectors where one side had only charge electrodes and the other only TESs. Thus, setting these up in CDMSlite configuration involved biasing the charge electrodes while grounding and reading out the TESs. The experiment had 4 live-days of exposure with 40 V across G25.

5.1.1 Luke amplification

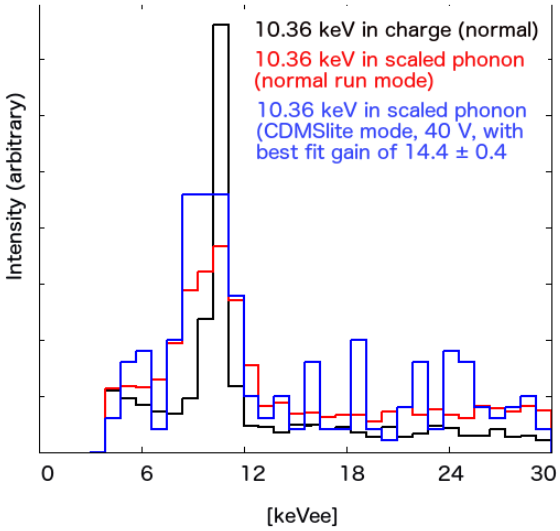

Figure 5.1: Low background data ($E_{r,ee}$ spectra) from the first Ge-CDMSlite run during CDMS II. 10.36 keV_{ee} activation photons (K-shell X-rays) were measured in pure charge energy (shown in black) in a normal 3 V bias run. The corresponding measurements with phonons is shown for both normal mode (3 V, in red) and CDMSlite mode (40 V, in blue).

Luke amplification was tested by studying 10.36 keV_{ee} photons generated by cosmogenic activation and thermal neutron capture; further details on activation lines are provided in Sec. 6.4.2.

[1]Silicon detectors will be discussed later as future prospects for SuperCDMS SNOLAB.

Following Eq. (4.2), recoils from 10.36 keV_{ee} photons, will produce phonons of energy $10.36 \times (1 + g_L(V_b))$, on average. Sufficient calibration data existed for normal CDMS II operation (3 V bias) where the 10.36 keV_{ee} line was seen in both charge and phonon energies (at $\sim 10.36 \times 2$ keV_{t} for 3 V bias). Thus for the data with 40 V of bias, spectral matching provided the Luke amplification. Figure 5.1 shows the spectra scaled with the best fit gain. This is compared to the line as seen in normal operation, in both charge and phonon energies [119]. The best-fit Luke amplification inferred from measurement was 14.44 ± 0.27, very close to the expected value of $g_L(40V) = 14.33$.

5.1.2 Noise

In this run the data were collected in two modes. In the first mode, LED flashing (photo-electric effects) to equilibrate the detector's charge population was performed, following which immediately, the high voltage was applied and data was taken. In the second mode after the LED flashing, a significant wait period (∼500 minutes) was added. These modes were testing the optimal operation procedure. If the time-constant for charge traps to fill and the electron-hole system to equilibrate is significant, then immediate biasing can lead to instabilities. Figure 5.2 shows the histogram of the reconstructed energies of noise events. Roughly, one expects random noise to have a Gaussian probability distribution function[2]. We see that the histograms are indeed Gaussian-like, and for mode 2 where we wait after LED flashing, the noise is lower and no different from standard low voltage CDMS II operation. However in mode 1 the average noise fluctuations and the base-line noise resolution is higher [120]. For these studies, we ignored the first 5 hours of every run (totaling ∼10 hours). This is because, at the onset, the base-line noise is high ∼10 keV_{t} r.m.s, due to initial leakage current. It decreases exponentially with a time-constant τ ∼2 hours (see Appendix B).

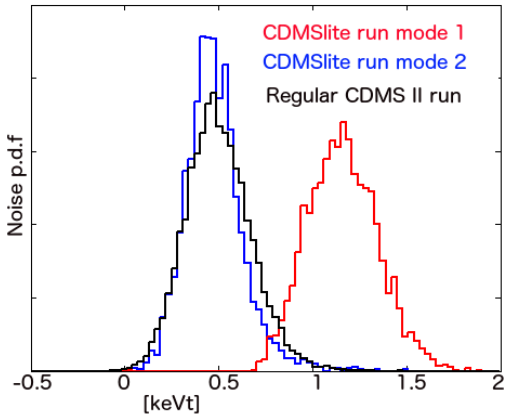

Figure 5.2: Probability distribution functions of noise events from the first CDMSlite (Ge) run during CDMS II. After LED flashing adding a wait period makes the noise similar to normal running (black vs. blue). However biasing and taking data immediately after a LED flash leads to higher noise (red) due to out of equilibrium charge populations.

Thus the first CDMSlite Ge test produced expected results: at 40 V of bias we had a Luke-gain of ∼14. The noise in the best operation mode is not affected by the bias, though this mode gives a low live-time to run-time ratio. Following Fig. 5.2, in the worst case we had a base-line resolution, σ, of 186 eV_{t}. This was 7% more than the normal run's resolution of 175 eV_{t}. In the best case, the resolution was 10% lower than in normal operation. These distributions are centered above zero; this is a pulse-fitting systematic due to the optimal filtering and we can correct for it, see Sec. 3.5.2. From these distributions, the detection threshold inferred at a $\mu + 5\sigma$ level was 85 eV_{ee}. If we didn't accept the live-time to run-time loss, then the projected threshold would be 144 eV_{ee}.

[2]This is contingent on the exact noise power spectrum and hardware sampling and filtering.

It is possible that the actual trigger efficiency was higher because causal hardware filtering used in triggering is different from the acausal optimal filtering used to obtain energy estimators. We had thus demonstrated a new detector setup with the lowest thresholds at that time, and of sizable mass.

While this was extremely promising, the amount of data collected was too small for science analysis. We proceeded to implement CDMSlite with newer iZIP detectors which were being installed at Soudan for the SuperCDMS experiment.

5.2 The first iZIP test

The **i**nterleaved **Z**-sensitive **I**onization and **P**honon sensors are the cutting edge in bolometers being used for direct detection of Dark Matter [106, 121, 91, 122]. The SuperCDMS collaboration has deployed 15 iZIP detectors at Soudan Underground Laboratory and this style of detectors will be used for the larger SuperCDMS experiment at SNOLAB. Thus before pursuing a science run, we had to establish operational procedures for running iZIPs in CDMSlite mode.

5.2.1 Hardware: Operating an iZIP for CDMSlite

An introduction to iZIPs was provided earlier in Sec. 3.1. iZIPs are instrumented identically on both faces to read charge and phonons. This dual sided readout makes floating one side at a high potential while measuring phonons from the opposite side non-trivial. This sub-section will review the new electronics introduced to operate iZIPs in CDMSlite mode; additional details presented in Appendix A.

Each iZIP has 6 channels on each face of the detector. These channels are wire bonded to two ports, called detector interface boards (DIBs), on the outer edge of each crystal. The wire bonding was done minimizing on wire length, so as to reduce the possibility of shorts and cross-talk between wires. Due to such wiring, each DIB connects to the *nearest channels*. This is as opposed to having one DIB connect entirely to one face or side, and the other to the opposite one. This is shown schematically in Fig. 5.3 and with an actual photograph in Fig. 5.4.

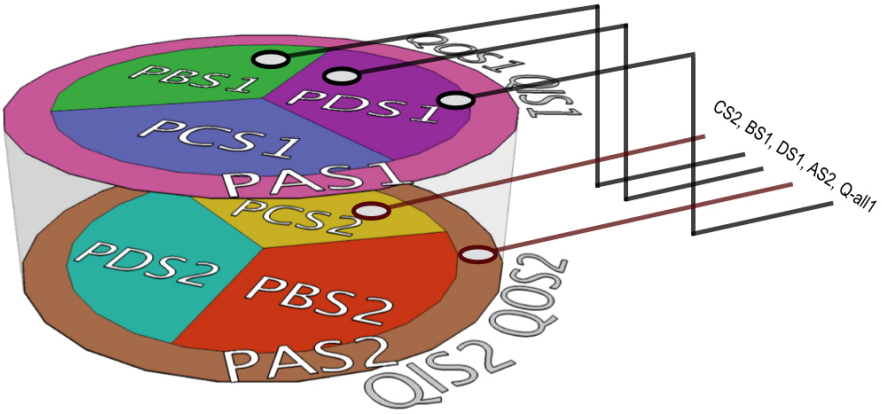

Figure 5.3: Schematic of one DIB wiring of an iZIP. Note that each DIB connects partially to both sides of the detector. Here S1 and S2 refer to the detector's top side and bottom side. The labels A...D are the 4 phonon channels present on each side. The labels Q... refer to charge channels, 2 per side (inner disc and outer ring electrodes). The second DIB is connected to the complementary set of channels

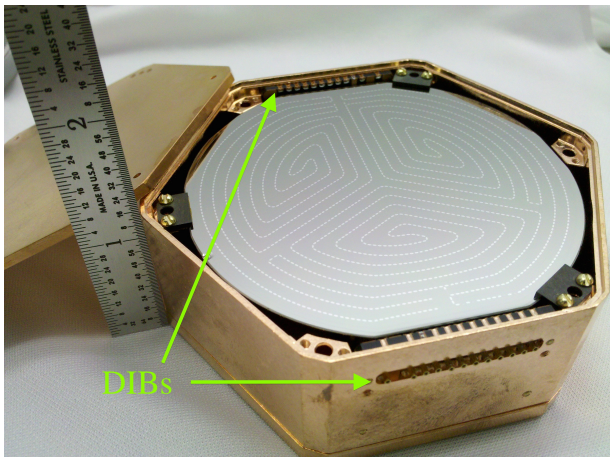

Figure 5.4: An iZIP in its copper housing. Note the location of DIBs as outlined in the schematic.

Each DIB is connected to the DAQ with individual electronics chains for filtering, triggering and digitizing signals. Farther down the pipeline, and only in software, is the mapping done to reconstruct various side dependent quantities. This is an obstacle for directly running iZIPs in CDMSlite mode with the standard hardware chain. We can't simply interface one DIB to a high voltage power supply and the other to the DAQ as this would not lead to correct application of a bias across the crystal. This problem was addressed by designing an "iZIP adapter board". In this circuit all the traces (wires) from both DIBs are split and bundled to map to physical detector sides. On the input it connects to the wiring from the two DIBs via D-50 connectors[3], labelled as ports (P1 ... P3) in Fig. 5.5. On the output end one D-50 connector carries traces from one side, eventually reaching the DAQ. The traces from the other side are connected to a high voltage power supply via a biasing resistance network (See Appendix A). A layout for biasing side 2 of an iZIP and reading out side 1 is shown in Fig. 5.5.

[3]Cables with 50 individual wires wrapped in a grounding sheath and a metal bulk-head which looks like a "D".

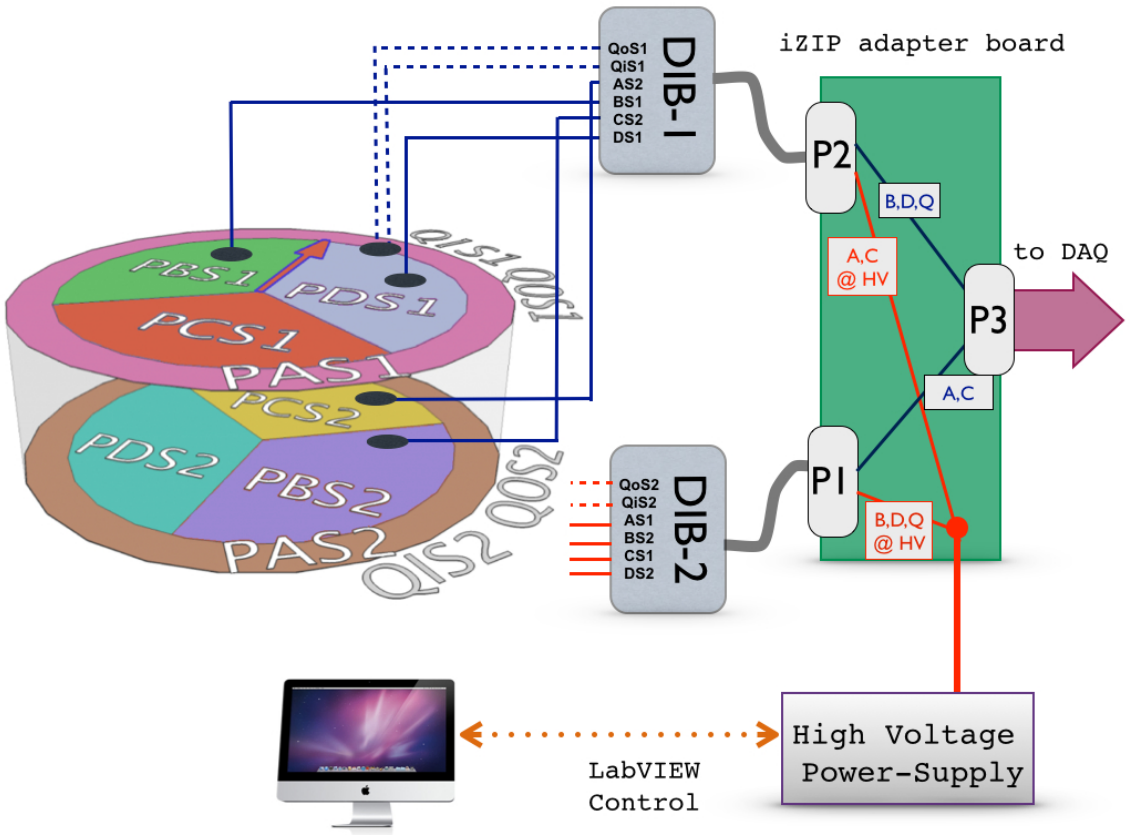

Figure 5.5: Schematic showing the biasing and readout of an iZIP in CDMSlite mode. On the adapter board a resistor network is used to ensure safe biasing, see Appendix A for details.

5.2.2 Calibration runs

I performed the first CDMSlite iZIP run at the Berkeley test facility, with assistance from M. Pyle and B. Serfass. A collimated ^{241}Am source was placed on one side of an iZIP detector (designated G8F). Various biases were applied using the adapter board and we studied the spectral lines expected from this source.

Type	Energy in keV	Intensity
γ	59.5	35.9%
γ	26.3	2.4%
γ	13.9	42%

Table 5.1: Photon energies associated with the α decay by which ^{241}Am transmutes to ^{237}Np . There are other high energy αs and βs in the decay chain, hence the sum of intensities of the table 5.1 is <100%.

Fig. 5.6 shows the scaled $E_{\mathrm{r,ee}}$ spectra that were measured at various voltages. Varying biased allows for testing the linearity of Luke amplification.

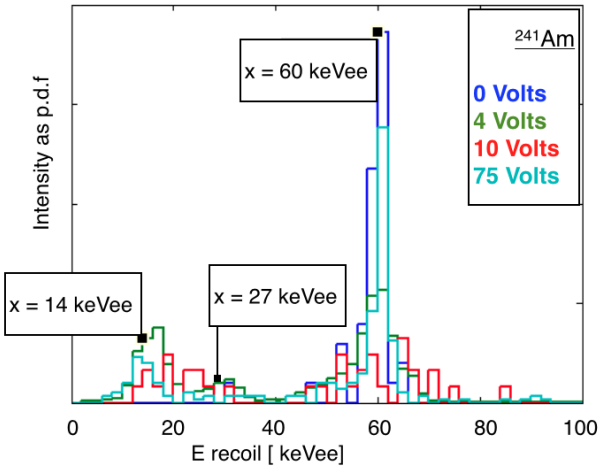

Figure 5.6: Luke gain corrected $E_{\mathrm{r,ee}}$ spectra of ^{241}Am source, as measured with a Ge iZIP at different detector biases. Spectral lines at 13.9, 26.3 and 59.5 keV$_{\mathrm{ee}}$ are visible. This analysis was restricted to $<$ 100 keV$_{\mathrm{ee}}$.

While spectral resolution improves with bias, the effect is slightly masked by energy estimators being of lower signal-to-noise [123]. For estimating the energy we relied on pulse integrals, as opposed to superior optimal filtered quantities, see Sec. 3.5.2. Hence variance from integrating baseline fluctuations is convoluted in the energy resolution. The goal was to see if the iZIPs could be biased in a stable manner, and if so, how well could we reconstruct known spectral features. As figure 5.6 demonstrates we were successful in achieving our main objective.

Finally, we wanted to check if the Luke-gain follows the theoretical curve for electron recoils. Calibrating to the 4 V bias data (standard iZIP operation), the amplification was measured, and is shown on Fig. 5.7.

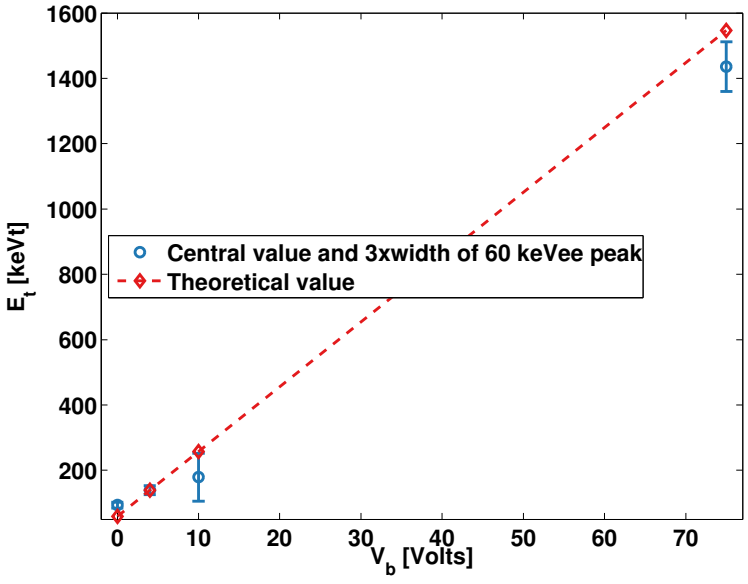

Figure 5.7: Luke gain as a function of applied bias using the 59.5 keV_{ee}peak from a ^{241}Am source. Note that the calibration is done with the standard 4 V bias, and hence the perfect alignment at that point.

The gain is close to the theoretical expectation. The discrepancies in Fig. 5.7 may well be the results of a simple analysis and crude hardware setup. In retrospect some variability in signal quality may have been introduced by the adapter board, as discussed later in section 6.1.2. This was a test facility run which proved that iZIPs can be operated in CDMSlite mode and we thus moved on to the full WIMP search program at Soudan.

5.3 First iZIP test at Soudan

5.3.1 Choice of detector

SuperCDMS at Soudan has detector payload of 15 iZIPs. For a first CDMSlite science run at Soudan, we wanted to choose a detector with the lowest intrinsic threshold and backgrounds to get the best science reach.

Threshold survey

A survey of phonon base-line (noise) resolution for every iZIP was performed [124]. Fig. 5.8 shows the base-line resolution calculated via the standard optimal filter estimators, see Sec. 3.5.2.

Figure 5.8: Distribution of phonon base-line energy resolution (σ) of various iZIPs calculated in the optimum filter framework. The three iZIPs with best resolution are T1Z3, T2Z1 and T5Z2 with σ = 138, 144 and 153 $\mathrm{keV_t}$ respectively.

In Fig. 5.8 "original" resolution is calculated using a phonon pulse template (purple markers in Fig. 5.9) and the noise power spectral density (PSD) from randomly sampled noise events (red markers in Fig. 5.9). The noise at Soudan has an environmental low frequency ($\sim$1/f) component which is not intrinsic to the detector. Thus the calculations were repeated to estimate the *best* possible resolution, by artificially removing the excess 1/f components under 3 kHz (yellow markers in Fig. 5.9), and these resolutions are called "modified" .

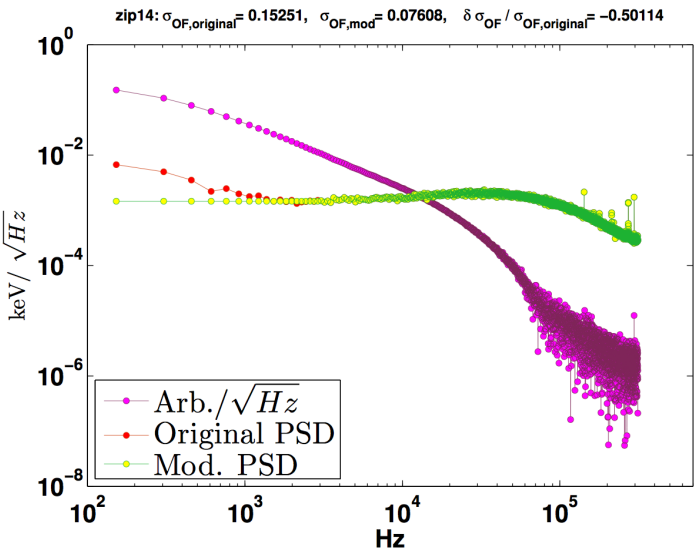

Figure 5.9: Power spectral density of randomly sampled noise events for detector T5Z2. The actual ("original") measured spectrum is shown in red. This contains a low frequency excess which is environmental pick-up. A spectrum without such excess is manually constructed ("modified PSD") and shown in green yellow markers. Here the spectral measure is fixed under 3 kHz. The purple markers represent the PSD for good phonon pulses.

Backgrounds survey

The dominant backgrounds for CDMSlite are expected from electron recoils (γs). A background survey was performed for all detectors [125]. For the three iZIPs with lowest thresholds, we compare the resolution and backgrounds in table 5.2.

iZIP	σ	Mean γ rate in 5-25 keV$_{ee}$	Mean γ rate in 10-50 keV$_{ee}$
T1Z3	138 eV$_t$	73 counts/kg/day	110 counts/kg/day
T2Z1	144 eV$_t$	52 counts/kg/day	60 counts/kg/day
T5Z2	153 eV$_t$	58 counts/kg/day	62 counts/kg/day

Table 5.2: Table of resolution and backgrounds for iZIPs deemed best for CDMSlite Run 1.

Final selection

From table 5.2, we see that while T1Z3 has the lowest resolution, the background rate is significantly higher than T2Z1 and T5Z2. T2Z1 was one of the best iZIPs overall and was reserved for the extended low-threshold "normal" SuperCDMS experiment, and thus the options were T5Z2 and T1Z3. Due to low-frequency noise, fine tuning the trigger thresholds to exploit the 15 eV$_t$ of resolution difference between T1Z3 and T5Z2 was challenging. From background considerations, T5Z2 was ultimately chosen to run in CDMSlite mode. T5Z2 had two other necessary benefits over other iZIPs: (1) There were no electronics issues such as shorts, i.e., bad undesired connections to ground preventing it from being operated in CDMSlite mode. (2) The crystal was seen to withstand up to 90 volts of bias before break-down. Break-down is the process where a large electric field causes trapped charges to drift sporadically and the TESs inoperably heat up (details on measurements are in Sec. 6.3 and theoretical arguments are in Appendix B).

5.3.2 Electronics setup and noise control

Before connecting detectors to room-temperature electronics, diagnostic tests are conducted to ensure that the cold electronics resistances are all correct. Upon performing these tests with the CDMSlite adapter board connected to T5Z2, several disconnected lines were seen to have resistances of few MΩs. The problem was traced to poor quality of humi-seal covering the board which was conducting surface leakage currents. The humi-seal originally intended for preventing humidity and dust from providing such leakage currents, was counter effective and was manually removed; refer to Appendix A for details.

The introduction of the adapter board resulted in increased sensitivity to environmental noise. This is because the extra trace lengths and grounding points on this board may form electrical loops and act as antennae. From Fig. 5.5, the major grounding points are seen to be the D-50 port casings (P1 ... P3) and the ground contact for the power supply. The noise pick-up, corresponding to the setup in Fig. 5.5 was a few volts peak to peak, larger than the acceptable $\mathcal{O}(100)$ mV peak to peak level. Our empirical solution involved: (1) placing the board between two aluminum plates (2) connecting all the D-50 casings to the plates and (3) connecting the shield of the high-voltage cable to the board's ground. With this grounding scheme the peak to peak noise was reduced to $\lesssim$200 mV, which was a good operational level and we were ready for data taking.

5.3.3 Ba calibration run

For the first operational test of T5Z2 in CDMSlite mode, we attempted a ^{133}Ba calibration run. In a good detector we expect a spectral peak at 356 keV$_{ee}$. The list of electron-capture spectral lines expected from ^{133}Ba, is shown in table 5.3.

Type	Energy in keV	Intensity
γ	383	9%
γ	356	62%
γ	303	18%
γ	276	7%

Table 5.3: Dominant photon lines associated with ^{133}Ba $\rightarrow$ ^{133}Cs.

For this first calibration run, we partially inserted the ^{133}Ba source into the source tube, which reduces the rate and prevents smearing from multiple scatters and pile-ups[4].

[4]If a second scatter happens while the phonons from the first scatter are still being absorbed in the TES fins, the reconstructed event will appear deformed, visibly with one pulse riding on another; hence called "pile-ups".

Reconstruction of high energy photon events with high detector bias

The bias for this run was 80 volts, just short of detector break-down which happens around 85-90 V. Following Eq. (4.3), a 356 keV_{ee} photon produces over 9.8 MeV of total (heat) energy, well over the detector operation point. At such high energies, the temperature increase causes multiple TESs to go normal and stop responding to further variation in energy. This produces abnormal pulses, whose level of distortion can vary from altered sharpness of the cusp to almost saturated pulses, see Fig. 5.10.

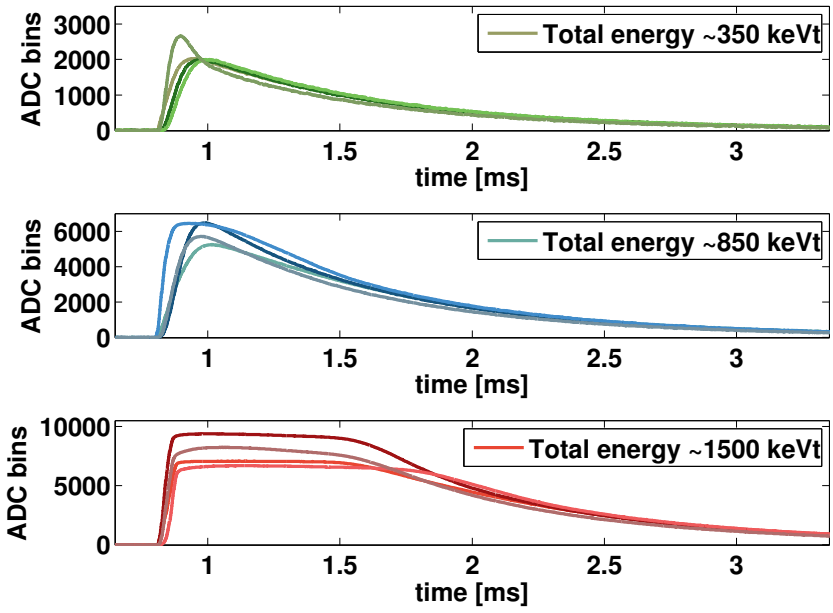

Figure 5.10: Raw pulses from three different energy ranges, showing deformation of pulse shape due to local TES saturation, with increasing energies (note the the increasing y-axis range). Each plot has four pulses corresponding to the four phonon channels present on one side of an iZIP. Each channel has 458 TESs, whose mean energy is shown in each of the four curves. The exact characteristics of pulse shape deformation depend on the nature (particularly T_C) of the TESs that constitute that channel. Above ∼1 MeV the pulses are extremely deformed and energy reconstruction becomes difficult.

Spectra

In analyzing these data, pulse integrals were used to estimate the energy deposited. While a clear line corresponding to the 356 keV_{ee} γs was visible, the distorted pulse shapes necessitated a special calibration procedure [126]. These measurements and calibrations are outlined in Fig. 5.11.

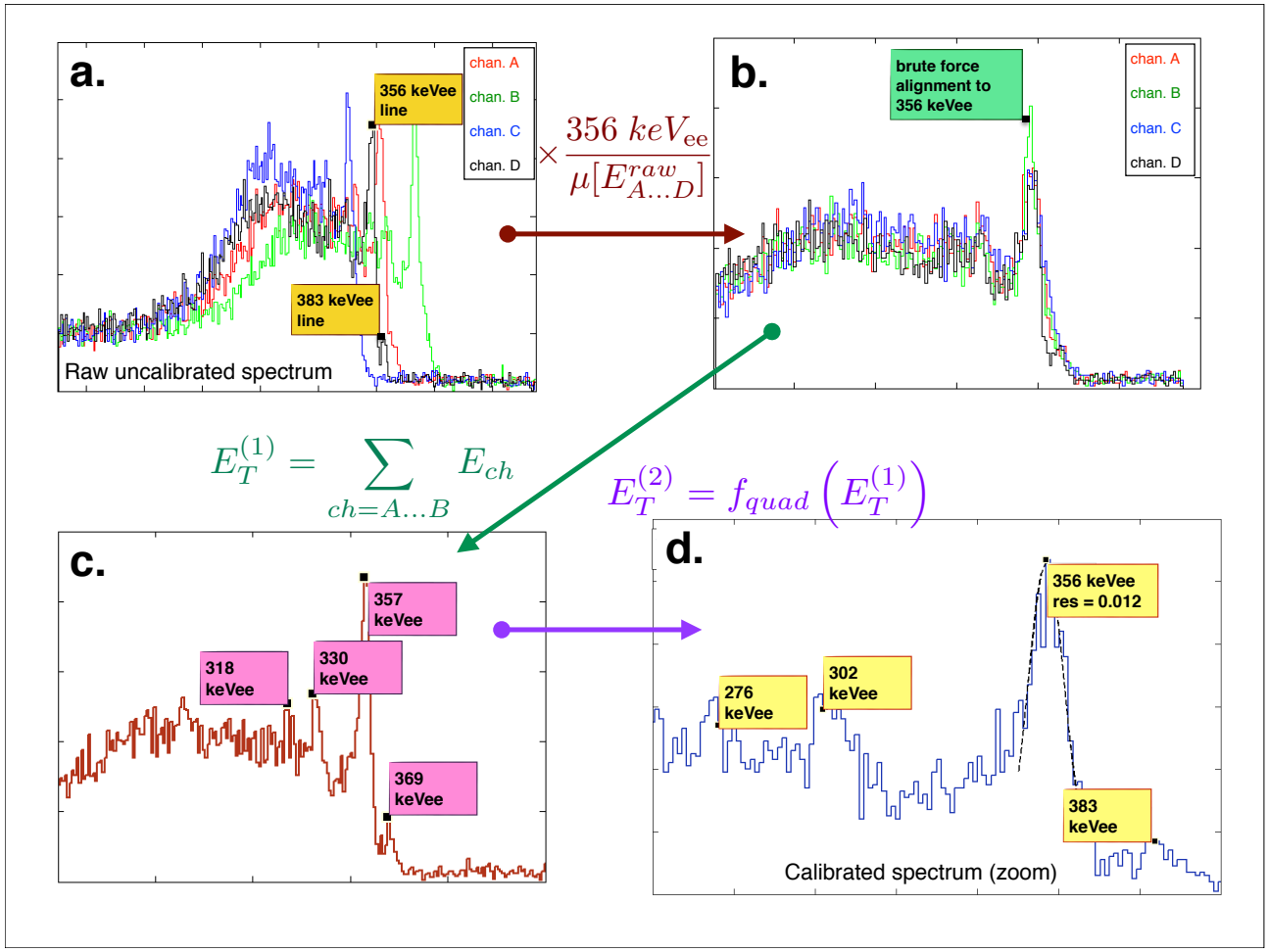

Figure 5.11: Schematic for the calibration done on ^{133}Ba data on T5Z2 with 80 V.
Subfigure (a): Note that in the raw spectrum various lines are already visible.
Subfigure (b): The 356 keV_{ee} lines from all 4 phonon channels are aligned by brute force.
Subfigure (c): Spectrum of summed energies from all channels, $E_T^{(1)}$. The relative positions of the peaks are not at the source energies. The deformed pulses give rise to a non-linear reconstructed energy scale.
Subfigure (d): A monotonic quadratic deconvolution is done to obtain the correct energy scale, $E_T^{(2)}$. The spectrum of this second order energy is shown in blue. The 356 keV_{ee} line has a resolution (σ/μ) of 0.012.

This first run gave us superb results. Even though T5Z2 was operated beyond it's optimal range, we were able to resolve various spectral lines, particularly the 356 keV_{ee} line with a resolution of 0.012. Previously measured resolution was ∼0.008, where T5Z2 was operated normally, pulse shapes weren't compromised and tuned optimal filtering was used to measure the energies.

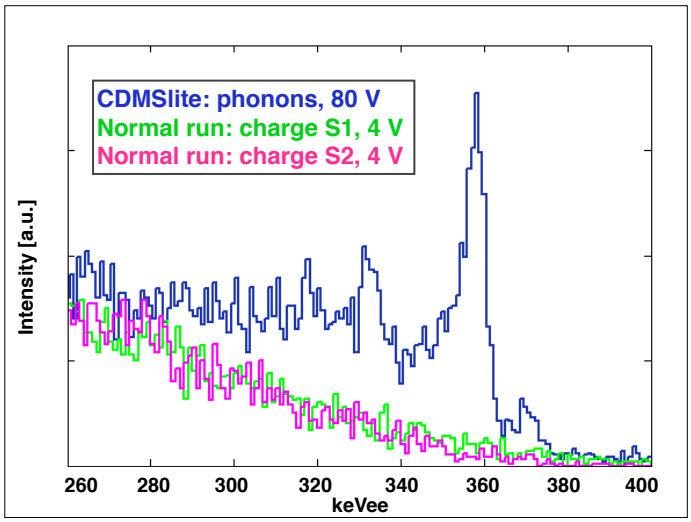

Figure 5.12: Comparing the ionization spectrum of ^{133}Ba between 80 V CDMSlite run versus measurements with regular charge electrodes in normal (4V) running mode.

Fig. 5.12 shows the ionization as measured by the charge electrodes (on each side) with T5Z2 in normal mode and in CDMSlite mode. Due to the optimized source location, and high Luke-amplification we can extract multiple spectral features even with compromised pulses.

5.3.4 Signal-to-noise Optimization

For detector biases > 90 volts, leakage current starts dominating the thermal load and overheats the system making the TESs go normal (see Appendix B for details). Thus the linear Luke amplification is compromised by rapid non-linear increase in noise. The leakage current is less significant at lower biases, and there is some optimal bias that maximizes signal-to-noise. We obtain this optimal bias value by performing a bias-scan on T5Z2. From an ensemble of ($\gtrsim$100) randomly collected noise traces at various biases, we calculated PSDs and with a template from good pulses, we found the energy resolution following optimal filter theory, see Sec. 3.5.2. The results from such a bias-scan on T5Z2 are shown in Fig. 5.13.

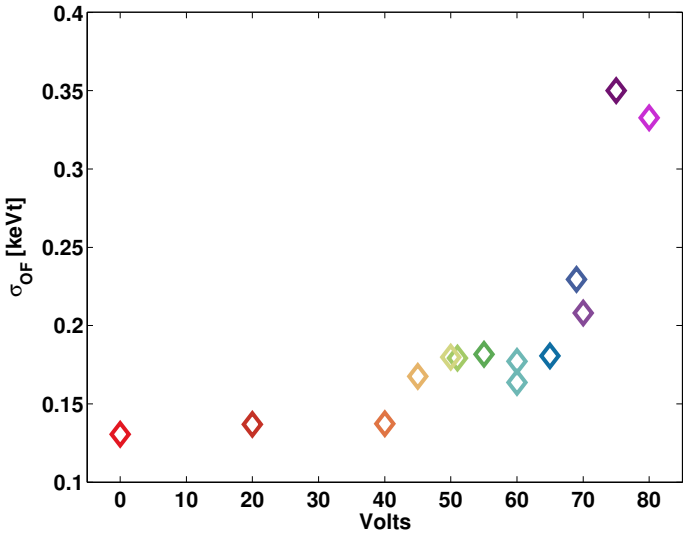

Figure 5.13: Base-line energy resolution calculated with optimal filter method on random noise events at various biases. A clear trend is observable. Under ∼40 V, the noise seems relatively independent of bias. The colors indicates different biases.

Following this noise measurement, we calculated the signal-to-noise-ratio (SNR). Here signal is the Luke-gain defined earlier as $g_L(V_b) = eV_b/\varepsilon_\gamma$. The noise, also dimensionless, is defined as $\sigma_{OF}(V_b)/\sigma_{OF}(0\text{ V})$. Thus SNR $\equiv \{eV_b/\varepsilon_\gamma\}/\{\sigma_{OF}(V_b)/\sigma_{OF}(0\text{ V})\}$. SNR as a function of bias voltage is shown in Fig. 5.14.

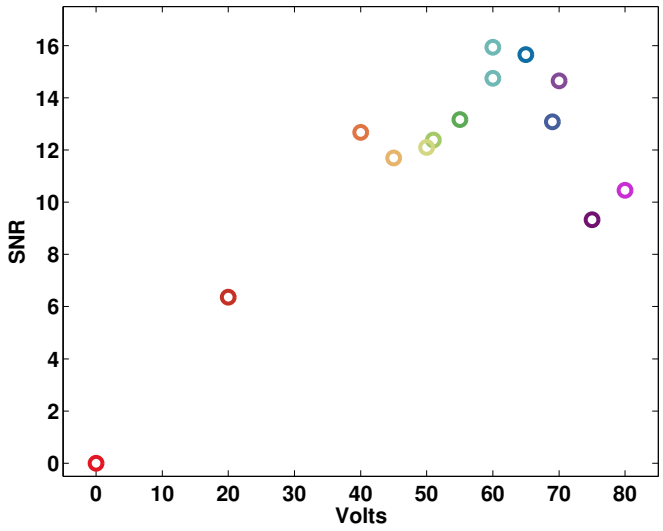

Figure 5.14: Signal-to-Noise Ratio constructed assuming linear Luke-gain and noise from base-line energy survey shown in Fig. 5.13. The optimal voltage is in the 60-70 V range.

Based on this study we concluded that the applied bias should be 60 V $< V_b <$ 70 V for SNR maximization. We chose 69 V to get the best amplification. It should be mentioned that these bias-scan runs were all less than 15 minutes in duration. We later discovered that the noise reduces after about 10 minutes of biasing, see Sec. 6.3 for examples and details. Thus these short runs were helpful to gauge the optimal-point. The overall σ-scale would have reduced had we taken random noise events after a longer wait period, however the optimal bias should remain unaffected; this was verified with tests after Run 1 concluded [127].

Chapter 6

CDMSlite Run 1: Operations and Calibrations

This chapter will describe the operation of CDMSlite Run 1 at Soudan and the subsequent data selection and energy calibration.

6.1 Operation

6.1.1 Run periods

T5Z2 was run in CDMSlite mode from August to September of 2012, following a few months of detector testing. During this period neutron calibration with ^{252}Cf was performed twice. Gamma calibration with ^{133}Ba was done 10-15 hours every week. Such calibrations were done for the entire SuperCDMS experiment and were not solely optimized for CDMSlite. The data with 69 V of bias on T5Z2 can be divided into three major time blocks, see table 6.1.

Set index	Start date	End date	Live hours	Comments
1.	August 18$^{\text{th}}$	August 29$^{\text{th}}$	161.1	First neutron calibration happens in between, just under 6 hours on Aug 22$^{\text{nd}}$.
2.	September 7$^{\text{th}}$	September 14$^{\text{th}}$	111.2	Second neutron calibration happens right before this, just under 3 hours on Aug 30$^{\text{th}}$.
3.	September 18$^{\text{th}}$	September 25$^{\text{th}}$	105.9	N/C
			378.2	**Total live-hours**

Table 6.1: Table describing CDMSlite WIMP search dataset when T5Z2 was operated with 69 V bias. The color coding in table 6.1 will be used from here on.

6.1.2 Run stability

Given the cosmogenic activation and the activation from intentional neutron calibrations, we expect to see a γ line at 10.36 keV$_{\text{ee}}$ in these Ge iZIPs; further details on activation lines are presented in Sec. 6.4.2. In these CDMSlite data the 10.36 keV$_{\text{ee}}$ line was expected[1] to be observed at $\sim$124 keV$_{\text{t}}$.

[1]The actual Luke-gain following Eq. (4.2) is $\times$24. However, in this setup we can't read the side at high-voltage, while Al fins on both sides absorb phonons, see Fig. 5.5, resulting in a factor of $\times 1/2$. Thus 10.36$\times$12= 124.32 keV$_{\text{t}}$.

Fig. 6.1 shows the total phonon energy as a function of time. The activation line is visible, but varies slightly with time.

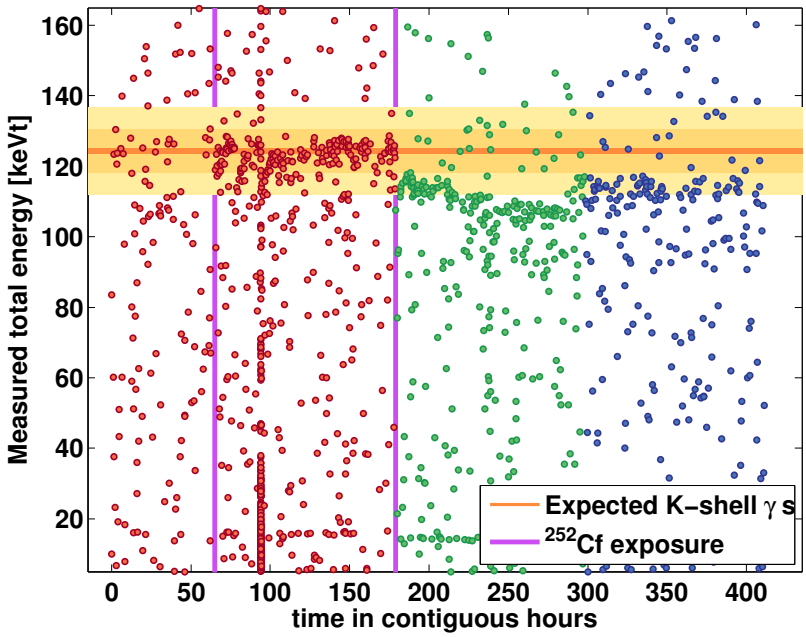

Figure 6.1: Total phonon energy (keV_t) as a function of time (contiguous hours, i.e., any gaps of inactive running have been removed). Here the location of the K shell photons is shown with the orange horizontal line. The larger yellow bands marks the expected spread from a 5% and 10% variation in the energy scale. The periods of the neutron activation via exposure to ^{252}Cf are shown with vertical lines.

It was mentioned earlier in Sec. 5.3.2 that the humi-seal cover on the CDMSlite adapter board was compromised. This resulted in exposed electronics, where over time humidity and dust settled, apparently generating parasitic resistances. The current from the power supply could therefore find other paths to ground, effectively varying the bias on the crystal and hence the Luke-gain. This hypothesis was later confirmed with several tests done at Berkeley and Fermilab.

In order to properly correct for this gain variation, via calibration of the 10.36 keV_{ee} line, data periods where this line was not visible, had to be removed.

6.2 General removal of bad time periods

During the course of the experiment there were instances where the quality of the data collected was questionable. We categorically remove any such periods from our data set.

6.2.1 Bad time period categories

- **Periods unsuitable for calibration:** The 10.36 keV_{ee} line can be broadened if the bias-voltage, and hence the Luke-gain were to vary over short time-scales; this makes calibration difficult. Also, electronic glitches or excess environmental vibrations can cause rapid influx of noise producing trigger bursts, which make some data periods unsuitable for further analysis.

Fig. 6.1, shows several features, including a trigger burst at hour 99, and a widely dispersed activation line in the period between hours 60 and 110, indicating bias voltage flucuations. Thus we explicitly rejected data from hours 60-110.

- **Runs that are short :** In SuperCDMS, WIMP-search data sets consist of several three hour long *series*. In CDMSlite operation, there is an initial period of high noise which can last up to 20 minutes (see Sec. 6.3). We wanted to consider consistently long, stable and sufficient data per series, and hence rejected all series shorter than 2.75 hours, keeping the upper 90% of the data, see Fig 6.2.

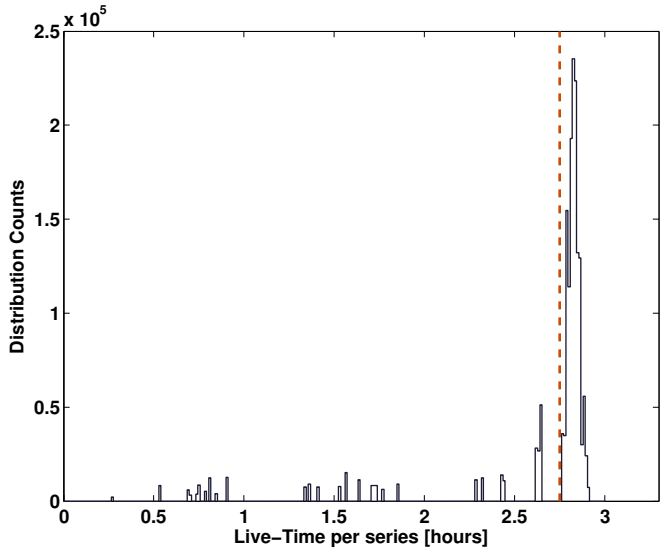

Figure 6.2: Distribution of live-time per series for CDMSlite Run 1. The orange line is at 2.75 hours and 90% of the data are above this mark, and are used for further analysis.

The data following the removal of these time-periods are shown in Fig. 6.3.

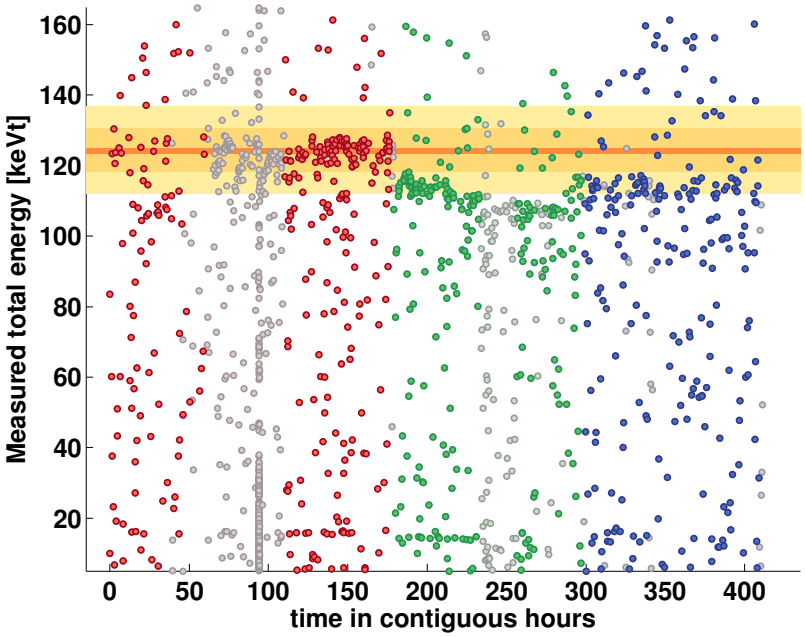

Figure 6.3: Total phonon energy (keV_t) as a function of time (contiguous hours). Gray markers (background) show all data points as seen in Fig. 6.1. In color markers we show events passing the good time period selection. The three colors (red, green. blue) are representative of the three blocks of Run 1 data.

6.3 Specific removal of time periods: The initial leakage current

Upon biasing the crystal with the high voltages required for CDMSlite, the initial noise is very high and decays exponentially with time. A theoretical model is presented in the Appendix B, and here I will describe the measurements and treatment of leakage current in analysis.

6.3.1 Measurement

Fig. 6.4 shows the energy measured as a function of time-since biasing T5Z2. We measure noise with high r.m.s which quasi-exponentially decreases with time since bias. Such flared noise at the sub 10 minute level, along with four sample events drawn from various times with the corresponding raw pulses are shown in Fig. 6.4.

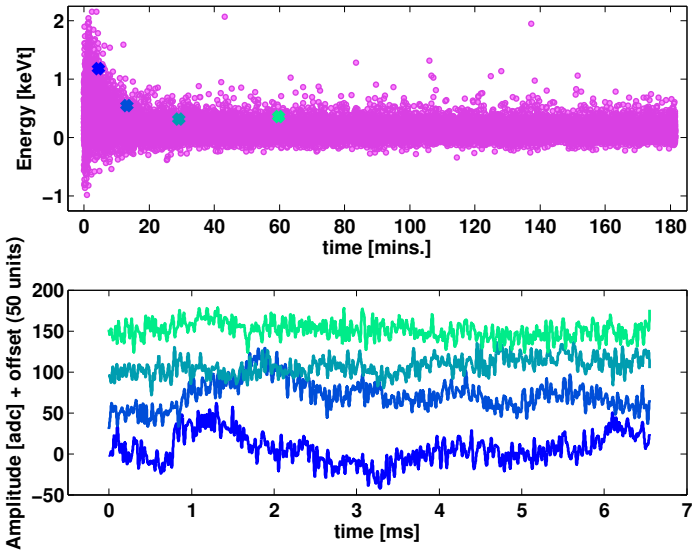

Figure 6.4: *Top plot:* Total phonon energy (keV_t) as a function of time, for one series with 69 V bias. Here we see the exponentially decreasing noise in pink markers. Four events are chosen randomly with blue-green cross markers.
Bottom plot: The raw pulses corresponding to the 4 events are shown here. Notice how the the earlier events i.e. ones drawn from the high noise period have greater low frequency drifts. These correspond to unresolved bursty train of charge carriers extracted by the immediate application of the high bias.

Leakage current, produced by bursts of electrons and holes appear as the crystal tries to equilibrate with the high electric field. Such bursty trains of charge carriers produce signals, which when folded in with our filtering and sampling band-widths appear as low frequency fluctuations (see Appendix B for further description of this process).

6.3.2 Cut definition

To achieve the lowest energy threshold, we needed to remove these high noise periods from the beginning of each data series. A systematic scheme was developed to find a statistically significant acceptance time for every series. To do this we binned the energy in time, and fit an exponential of the form $S(t) = \text{Amp} \times e^{-t/\tau_{2\sigma}} + \text{DC}$ to the upper $\mu + 2\sigma$ edge of the fits. Here "Amp" is the amplitude of the time varying leakage current, "DC" is the constant and final base-line, and $\tau_{2\sigma}$ is the time-constant of decay.

From these data, we found the ratio "Amp/DC" ≈ 2, and thus the noise may be modeled with a Gaussian distribution with standard deviation, $\sigma(t) \approx \sigma_0(1 + 2e^{-t/\tau_{2\sigma}})$, where the equilibrium base-line, from Fig. 5.8, is $\sigma_0 = 153$ eV_t. The probability of having noise fluctuations greater than $2\ \sigma_0$ is $< 2.7\%$ for $t > 4 \times \tau_{2\sigma}$. Since $\tau_{2\sigma} \sim 10$ minutes, and each run is 165-180 minutes (note the

live-time per series selection shown in Fig. 6.2), a four time-constant cut allowed us to keep around 70% of the data[2].

We thus selected events as good, when their time of occurrence was greater than $4 \times \tau_{2\sigma}$, of the initial noise, and this left us with sufficient data with $< 3\%$ chance of having leakage current noise in these data. A table listing all cuts leading to live-time loss is shown in 6.2.

Cut	**Live-Time in hours**
None	378.2
Removal of hours 60-110	334.5
Removal of short series	289.0
Removal of data during initial leakage current	**247.6** (Final)

Table 6.2: Table describing live-time loss in CDMSlite WIMP search dataset with succession of bad time removal cuts. The final live-time was 10.31 days.

Having selected the useful data set we now return to the task of energy calibration.

[2]The four time constant or $< 2.7\%$ choice was somewhat conservative. To jointly minimize the live-time loss and the probability of having excess fluctuations above 2 σ_0, we can find the optimal number of time-constants via $\min_n \left[(n\ \tau_{2\sigma} \text{ minutes}/180 \text{ minutes}) \times \int_{2\sigma_0}^{\infty} \mathcal{N}(0, \sigma(n\ \tau_{2\sigma})) \right]$. For the approximate numbers discussed here, the best n is just over 3. However low-frequency noise is not well characterized and we conservatively used the $4 \times \tau_{2\sigma}$ cut.

6.4 Calibration: Fixing the energy scale

In Run 1 the Luke-gain had time variation of ∼10% as seen by tracking the 10.36 keV_{ee} photons, see Fig. 6.3. Thus energy calibration was performed to convert this (time varying) keV_t unit to a proper and constant ionization unit. We did this by using just the 10.36 keV_{ee} photons and verified the calibration with other activation lines.

6.4.1 10.36 keV_{ee} photon alignment

In CDMSlite we measure ionization via Luke phonons. To convert the measured total phonon energy (keV_t) to ionization energy (keV_{ee}) an algorithm is employed to correct for time variation in the energy scale and give a final ionization equivalent energy where the line is at 10.36 keV_{ee}.

From Fig. 6.3 we see that the 10.36 keV_{ee} line is well contained between 90 and 150keV_t. In this scheme we bin in time and find the mean energy value in this range. Then the mean values, as function of binned-time, are fit with segmented polynomials. These polynomials are used to scale the total energies to a ionization energy where the activation line appears at 10.36 keV_{ee} relatively constant in time. The algorithm is described in detail in Appendix C, and Fig. 6.5 shows the calibrated energies as a function of time.

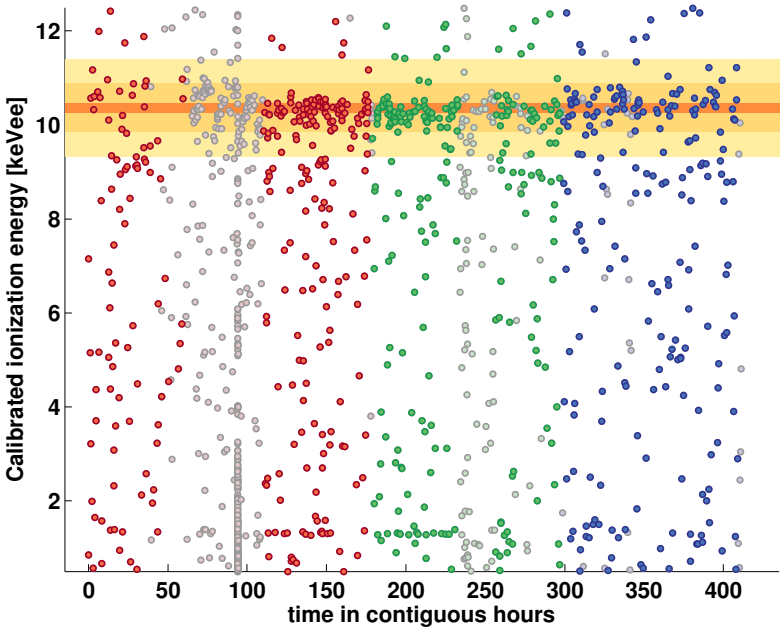

Figure 6.5: Ionization energy as a function of time, following energy calibration. Here the location of the K shell photons is shown with the orange horizontal line. The larger yellow bands marks the expected spread from a 5% and 10% variation in the energy scale.

6.4.2 The first spectrum: verification of calibration

The efficacy of this calibration is tested by looking at other activation lines as shown in Fig. 6.6. The four known lines are [128]:

1. **10.36 keV_{ee} γs:** Primarily thermal neutron capture (from ^{252}Cf) on ^{70}Ge produce these γs. The reaction chain is: $n + {}^{70}Ge \rightarrow {}^{71}Ge^*$, ${}^{71}Ge^* + e^- \rightarrow {}^{71}Ga + \gamma$. For the electron capture corresponding to K-shell electron levels, 10.36 keV_{ee} γs are emitted. This activation has an 11.4 day half-life. Secondarily, cosmogenically generated ^{68}Ge decays to ^{68}Ga with a

270 days half-life, producing x rays around this energy. The iZIPs have been underground for a significant period so the main contribution is from neutron capture.

2. **9.66 keV$_{ee}$ γs:** ^{68}Ga decays into ^{68}Zn with a half-life of 67 minutes (with a 12% branching ratio to produce this X-ray). This activation should be proportional to the amplitude of the 270 day half-life 10.36 keV$_{ee}$ γ peak, and is thus expected to be small.

3. **8.98 keV$_{ee}$ γs:** Cosmogenically generated ^{65}Zn will decay to ^{65}Cu with a 244 day half-life.

4. **1.29 keV$_{ee}$ γs:** The origin is similar to point 1 above, here the γs correspond to a L-shell electron capture.

The spectrum in Fig. 6.6 shows two main activation lines at 1.29 and 10.36 keV$_{ee}$, along with weaker lines corresponding to cosmogenic activations: 8.98 keV$_{ee}$ (^{68}Ga) and 9.66 keV$_{ee}$ (^{68}Zn). No other significant lines were found [129].

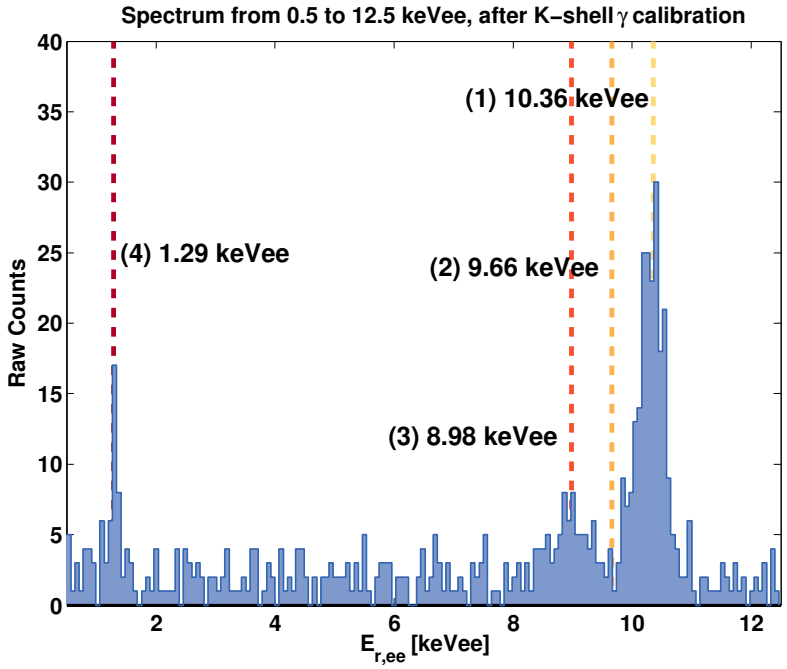

Figure 6.6: Energy spectrum following calibration of K-shell, 10.36 keV$_{ee}$ photons. There are four other activation lines, which are observable at the expected locations, thereby showing the validity of the calibration process. See main text for details on the other activation lines.

This shows that we have correctly calibrated our ionization energy scale. The resolution (σ/μ) on the K and L shell peaks were 1.9% and 3.3% respectively[3]. The resolution of the L-shell line is evidence of great detector performance and absence of overfitting, which could have happened if the energy scaling algorithm was tuned to minimize the 10.36 keV$_{ee}$ peak's width. In that case, the L-shell line (and the ones in between) would get smeared since the photons are uncorrelated.

[3]Previous best measurements in CDMS-II were ∼3% and ∼2% for the 10.36 keV$_{ee}$ line in charge and phonons respectively. For the 1.29 keV$_{ee}$ line, these values were ∼20% and ∼9% in charge and phonons respectively. Note that the 1.29 keV$_{ee}$ line fell under ionization threshold for most ZIPs, and the 20% number is a crude estimate.

6.5 Noise: Estimating the ultimate limitation

When signal amplitudes falls within the r.m.s of base-line noise, the low-threshold reach is fundamentally limited. In this section I will quantify the final resolution achieved in CDMSlite Run 1.

6.5.1 Energy distribution of noise

There is some probability with which noise fluctuations may be fit by a signal-template[4] yielding non trivial inferred energies. Thus the distribution of such reconstructed energies calculated from noise events, see Fig. 6.7, gives us the statistical signal-to-noise limit.

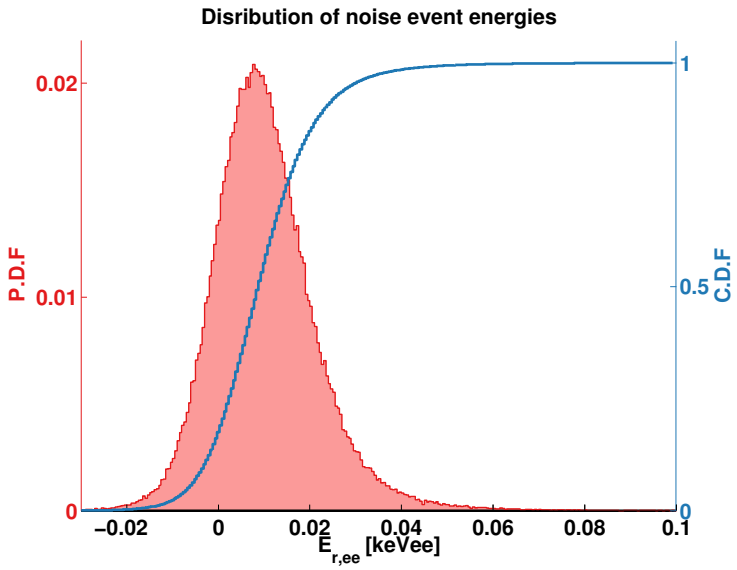

Figure 6.7: Distribution of reconstructed energy from randomly triggered noise events. In pink shade (left axis) the probability distribution function (P.D.F) is shown. This P.D.F is integrated to yield the cumulative distribution function (C.D.F). The C.D.F is shown in blue (right axis). The effective width of this distribution is 14 eV_{ee}.

The P.D.F in Fig. 6.7 is not zero-centered since the optimum filter has a positive amplitude bias as the optimization works by maximizing the amplitude (normal phonon pulses are positive in energy), see Sec. 3.5.2. If the noise fluctuations have large dips it can fit a negative amplitude and hence negative values also exist. There is a positive skew due to low-frequency noise from microphonics. Such noise may be fit with a phonon signal and thus get reconstructed to greater than central values. This can happen since phonon pulses have large power at low frequencies.

There are several possible methods of obtaining an effective width of this non-gaussian P.D.F. Using an iterative Gaussian fitter, which cuts outliers "smartly" discounting the skew until the width stabilizes, we obtain a 1 σ width of 10 eV_{ee}. However from the C.D.F we can quote the plus / minus half-widths at 50% ± 34.13%. These give $\sigma_{+/-}$ = 22.5 / 18.9 eV_{ee}, which may be combined to obtain an effective width of $\tilde{\sigma} = \sqrt{1/(\sigma_+^{-2} + \sigma_-^{-2})} \approx 14$ eV_{ee}. Although this value is biased upwards from the skew, it is the best zero energy resolution measured with any Ge dark matter detector till date. From this distribution at just over a $\mu + 5\sigma$ level, the inferred threshold was 85 eV_{ee}, albeit not the trigger threshold which determines the experiment's performance at low energies. This issue is discussed in Sec. 7.5.

[4]Signal-template is the expected phonon pulse, which is obtained via performing ensemble average of good events.

Chapter 7

Analysis

There are two general types of events which trigger the data-acquisition system and must be addressed in analysis. These are events produced by particle interactions in the detectors (called physics / good events), and events which do not originate from particle interactions, but rather from some electronics glitch or noise (referred to as non-physics / bad events). Events can be further classified based on the number of detectors triggered as singles or multiples. For WIMP searches we are exclusively interested in physics events where a single detector triggered.

These categorizations are not straightforward at low energies, i.e., in the low signal-to-noise regime. With decreasing amplitude or signal-to-noise, the distinction between good and bad events becomes fuzzy. Also at low energies, with variability in detection thresholds between iZIPs, the singles-multiples discrimination becomes difficult. Thus in the analysis, we devise various event selection cuts to find the best physics events to compare with expected WIMP signals. In this chapter I will define these cuts and describe their performance across pertinent energy ranges.

7.1 Electronic Glitches

Glitch events are generated by voltage spikes on the TES bias lines, directly heating them, and their temporal width is much shorter than pulses produced by particle interactions. While the exact source of glitches is not fully known, depending on the level of the voltage spike, several charge and phonon sensors can be triggered. In Run 1 we used two different glitch rejection cuts derived from studies performed by R. Bunker [130].

7.1.1 Glitches identified via multiple triggers

For 15 iZIPs, in total, 30 phonon and 30 charge triggers are possible since each iZIP has two sides capable of producing triggers. In the 30×30 plane of triggers, good events with recoil energies over threshold, should generally lie on the diagonal, i.e., it is very unlikely to have energetic good events with more phonon triggers than charge triggers and vice versa. Glitches are seen to occupy off-diagonal areas on this plane, see Fig. 7.1.

Cut definition

The diagonal bounds for good events are shown in Fig. 7.1. The "trigger-glitches", generally occur outside these lines. They satisfy the condition that the excess in number of phonon triggers over charge triggers is either greater than six hits or the excess in the number of charge triggers over phonon triggers is greater than one hit, additional details available in Sec. 3 of [131] and Sec. 2 of [132]. The power of such trigger correlated selection drops for low energy events near various detector thresholds and we thus quantify the efficiency of this cut in a few ways.

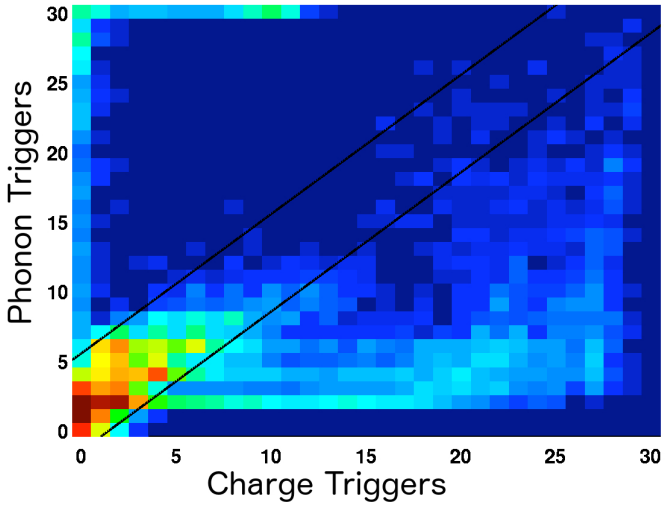

Figure 7.1: Number of phonon triggers versus number of charge triggers in the 30×30 trigger plane. The number of phonon and charge triggers are strongly correlated for good events. Questionable multiple trigger events like glitches live in the various off-diagonal sectors. Here the good-events region is shown within the diagonal lines. Clear tails of excess triggers from glitches are seen.

Cut efficiency

When the signal-to-noise ratio is low, good events may get unintentionally removed by the glitch cut based on correlated triggers. As mentioned earlier, we use Ba sources for general γ calibration. The high rates and broad spectrum ensures that we have a large sample of good physics events to test this cut on. Thus the efficiency of good events to pass this cut is well approximated by calculating the passage fraction for the ^{133}Ba data. Across various energy intervals, we count the number of good events[1], and define fraction of these events which pass the cut as the passage fraction.

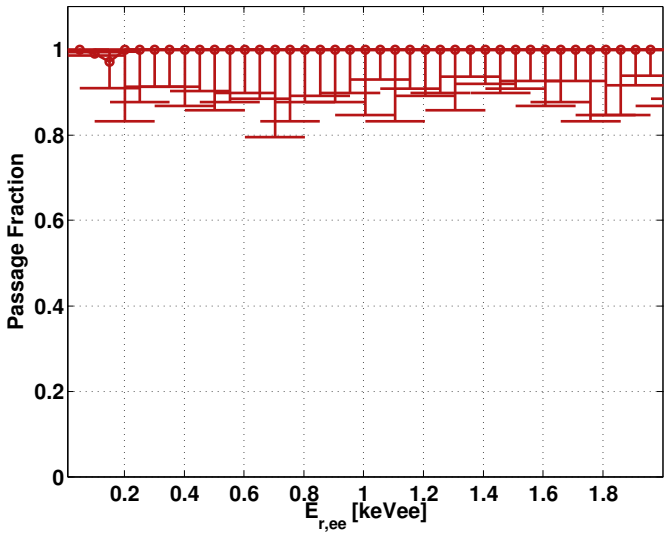

Figure 7.2: Efficiency of the trigger based glitch cut calculated on ^{133}Ba calibration data. Note that the energy axis has the Luke-gain factored out, and hence is a measure of electron recoil energies. The cut is generally energy independent with a $\lesssim$5% dip around 150 $\mathrm{eV_{ee}}$. This marks the energy scale where we transition from triggering on real events to triggering on noise.

The passage fraction, proxy for efficiency is presented[2] in Fig. 7.2. For true efficiency we must

[1] "Good" here refers to events that don't occur in bad operation periods and which look like phonon pulses, i.e., acceptable χ^2 metrics from optimum filtering.

[2] The plots shown here are for Ba data collected in September of 2012 when the Luke gain was relatively constant Fig. 6.1. These were verified against all Ba data as well.

ideally test the cut on a pure sample of triggering good phonon pulses. In reality, the Ba data where there are a lot of good phonon pulses per second, becomes the data-set of choice. Hence the passage fraction calculated on these data is a good proxy for the intended efficiency calculation.

The efficiency of this cut is ∼100 % at high energies. At $\lesssim$ 150 eV_{ee} noise starts to dominate and the efficiency can show small modulations (<5%) as different detectors have different thresholds, and the probability of triggering is driven by the nature of noise fluctuations. Below this energy, noise triggers dominate and these measurements should not be interpreted as robust efficiencies of good low energy events.

7.1.2 Glitches identified via pulse shape

When the amplitude of glitch events are very small, they may fall below the trigger thresholds of some detectors, thereby effectively occupying the good events' band shown in Fig. 7.1. In such cases it is beneficial to exploit differences between the pulse shapes of glitches and phonons. We start this investigation by looking at glitches in time domain, Fig. 7.3.

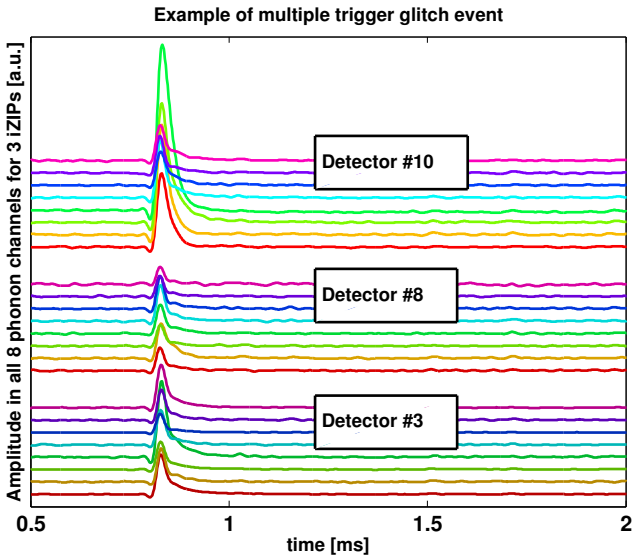

Figure 7.3: Example of raw phonon pulses from an event classified as multiple triggering glitch event. In three randomly chosen iZIPs, across all eight phonon channels (rainbow colors) similar pulses with characteristically sharp rise and fall times (∼ 10 μs and ∼ 25 μs respectively) are seen. For a normal phonon pulse the sharpest rise and fall times are ∼ 50 μs and ∼ 800 μs respectively, thus glitch events morphologically distinct from physics events.

Fig. 7.3 shows the temporal nature of these glitches. From ensemble averages, we construct glitch"templates" to see how, in general, glitch pulses compare with phonons pulses, Fig. 7.4.

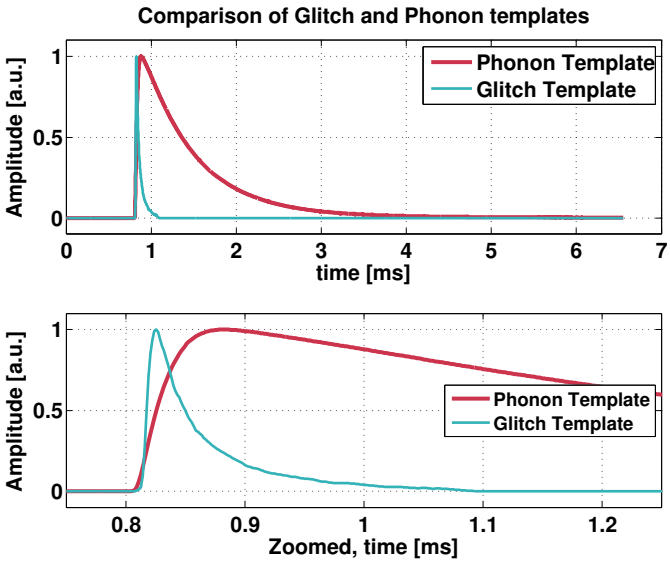

Figure 7.4: Comparison of phonon and glitch templates. We notice the distinctly different pulse shapes, where glitches have more high frequency power (short time-scales) compared to phonons.

Cut definition

Using the templates shown in Fig. 7.4, we study how well an event matches a glitch or phonon pulse shape, by computing goodness of fit or χ^2 measures: a χ^2_{ph} metric quantifies the fit to the phonon template, and a χ^2_{gl} quantifies the fit to the glitch template.

Any χ^2 metric is lower for better fits and higher for worse fits and is typically a quasi-quadratic function of the fit amplitude[3]. We use the differential, $\Delta\chi^2 = \chi^2_{ph} - \chi^2_{gl}$ as a discriminating variable. For a physics event $\chi^2_{ph} \approx 1$ and χ^2_{gl} is some large number, thereby making $\Delta\chi^2 < 0$. Conversely for a glitch event we expect $\Delta\chi^2 > 0$.

Scanning through events of varying energies (or amplitudes) we thus trace out two branches in the plane of $\Delta\chi^2$ vs. energy. This plane is shown for events collected via random triggering, Fig. 7.5 and also for events which triggered the DAQ system, Fig. 7.6. We see that a large population of glitches ($\Delta\chi^2 > 0$) at low energies. This is the signal region for light WIMP recoils, hence using the $\Delta\chi^2$ quantity to reject glitches becomes extremely helpful.

[3]These are the standard optimum filter χ^2 measures as defined in Sec. 3.5.2. In theory, $\chi^2 \in [1, \infty)$. However, practically, high frequency noise makes the minimum slightly larger than 1 and the maximum is some large number limited by sampling bandwidth.

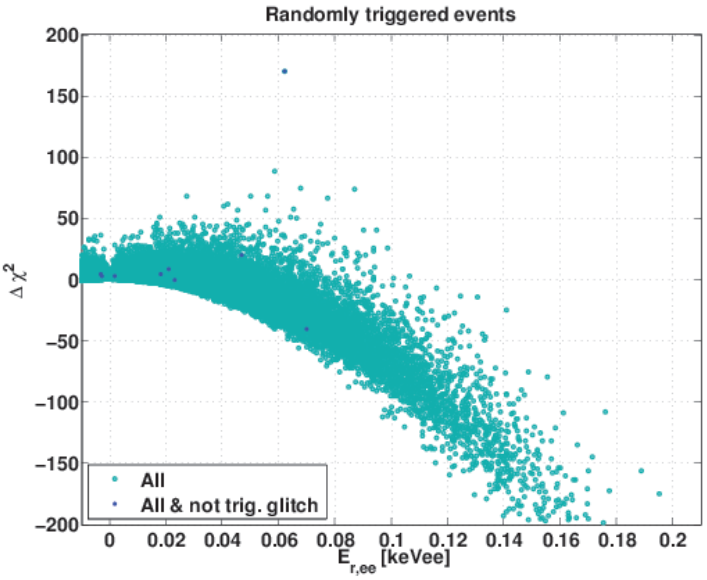

Figure 7.5: $\Delta\chi^2-$Energy plane: The plot shows the distributions for events collected via random sampling. In this plane, $\Delta\chi^2 > 0$ implies glitches and $\Delta\chi^2 < 0$ implies phonons. The population after removing glitches based on triggers is shown with solid dark markers.

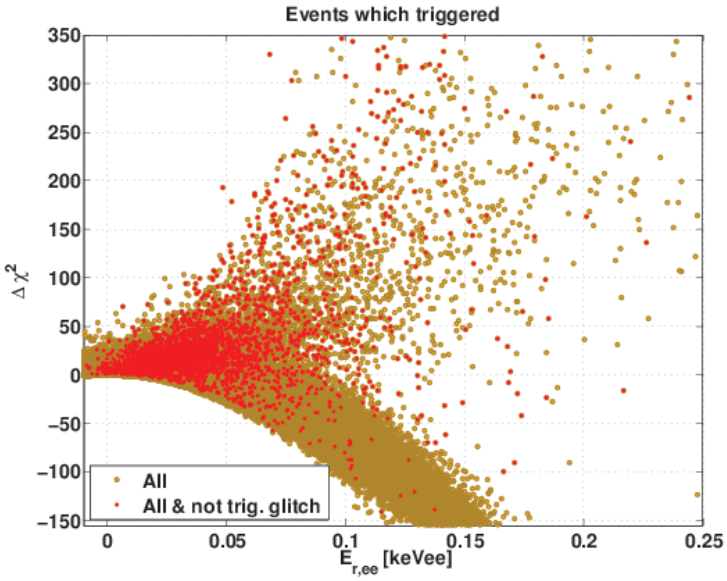

Figure 7.6: $\Delta\chi^2-$Energy plane: The plot shows the distributions for events which triggered the DAQ. In this plane, $\Delta\chi^2 > 0$ implies glitches and $\Delta\chi^2 < 0$ implies phonons. The population after rejecting glitches based on triggers is shown with solid markers. Many glitch events which passed the trigger correlated cut, become prominent here.

At low energies there is a smearing effect merging the two branches. To select glitches, we pass events on the positive branch over some cut-off, $\Delta\chi^2 > \eta$. Conversely, good event selection satisfies $\Delta\chi^2 \leq \eta$. In implementation we used $\eta = 10$, for which the passage fraction calculated on randomly sampled good events was $\gtrsim 99.97\%$ for both CDMSlite and regular data, additional details available in Sec. 4 of [131] and Sec. 3 of [132].

Cut Efficiency

The passage fraction for the template based glitch cut calculated on Ba data is shown in Fig. 7.7; it dips at low energies with a minimum at $\sim$0.1 keV_{ee}. From Fig. 7.6, the dispersion in the $\Delta\chi^2$ discriminant under 0.15 keV_{ee} implies that with lower signal-to-noise, some good events may have $\Delta\chi^2 > 10$, resulting in the drop in passage fraction.

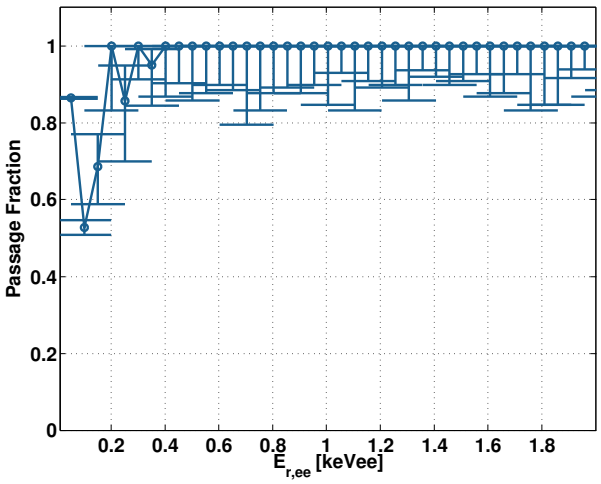

Figure 7.7: Passage fraction of the $\Delta\chi^2 < 10$ cut calculated on Ba calibration data

In calculating this passage fraction trigger correlated glitches were not removed. If the trigger correlated glitches were removed from these Ba data, the expectation is that the efficiency should increase overall. This expectation is indeed matched as seen by comparing Fig. 7.8 with Fig. 7.7.

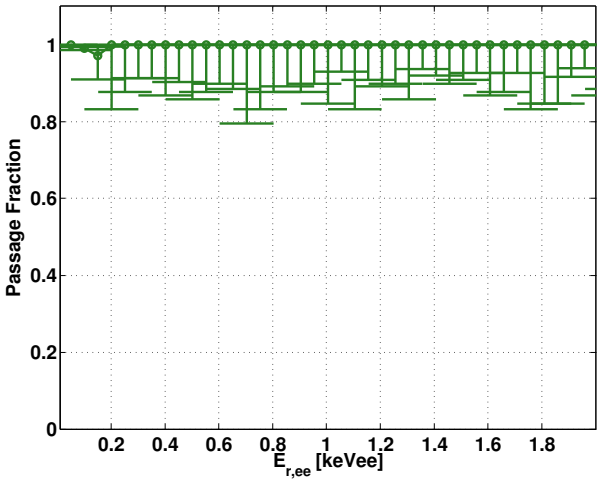

Figure 7.8: Passage fraction of the $\Delta\chi^2 < 10$ cut calculated on Ba calibration data, after removing trigger correlated glitches.

The passage fraction was also evaluated for low background data and agreed well with the observations described above, within large statistical errors. Note that apparent rise in efficiency under 0.14 keV_{ee} is due to the large population of noise triggers where discrimination of any type is poor.

To make a better estimate of the true efficiency, a Monte Carlo technique called "pulse + noise MC" was designed. In this scheme, we add model pulses of varying amplitudes to a data-base of noise events, and thus test the performance of cuts on these simulated events, as a function of pulse amplitude, [133]. Refer to Appendix D, particularly section D.2, for detailed description of this study.

For these simulations, the efficiency was obtained in a "blind" and an "unblind" manner. In the blind method, the passage fraction was calculated for a data set comprising phonon + noise[4], glitch + noise, and just noise events. While not the true efficiency, it characterizes the performance of this cut with regard to real data where good events cannot be precisely selected; the result is shown in Fig. 7.9. In the unblind method, we selected events that were simulated explicitly with a phonon template. The passage fraction calculated on such phonon + noise events is the *true* efficiency, and is shown in Fig. 7.10

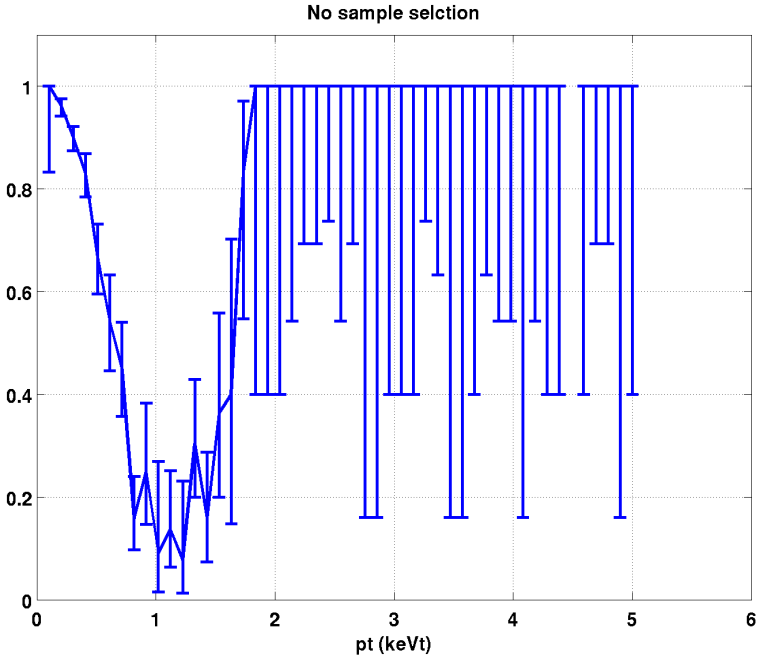

Figure 7.9: Passage fraction of the $\Delta\chi^2 < 10$ cut calculated in a blind manner, i.e., evaluated on all events in the data base without any discrimination.

[4]Here phonon + noise means a time domain model of a phonon pulse is added to some randomly sampled noise

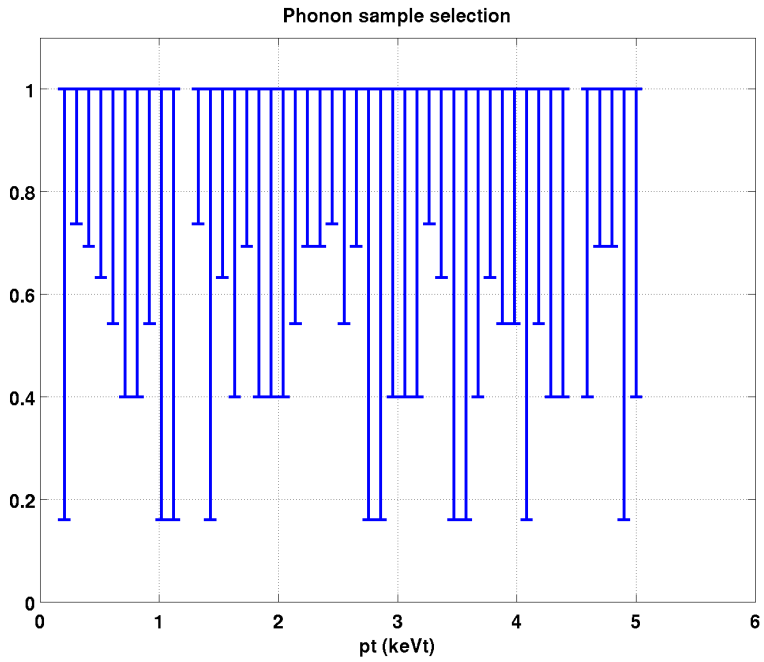

Figure 7.10: Passage fraction of the $\Delta\chi^2 < 10$ cut calculated in an unblind manner, i.e., evaluated on all phonon + noise events only.

This cut shows no energy dependance and is 100% efficient when we use it unblind, on phonon+noise samples, see Fig. 7.9. However if applied blindly to an unknown set of events, a dip is observed around 1.2 keV_t, as seen in Fig. 7.10. These MC calculations were performed with the energy-scale representative of total phonon energy collected on Side 1 of the detector. Following Eq. (4.3) we get a conversion factor of 12, which translates 1.2 keV_t to 0.1 keV_ee. Via this **pulse + noise MC** we can thus explain the dip observed in real data at $\sim$0.1 keV_ee, and realize that this feature is not representative of true efficiency.

7.2 Low-frequency noise

Low-frequency noise at Soudan produces excess triggers and dominates the low energy spectrum. However in randomly triggered data their population is marginal, as seen in the non-Gaussian tail in Fig. 6.7. Quantifiably, the base-line resolution shown in Fig. 6.7 was 14 eV_ee, whereas the noise pedestal appeared around 200 eV_ee. This section will describe methods for rejection of such events so as to reach a lower WIMP search threshold.

7.2.1 Low-frequency noise versus phonon pulses

The difference between low-frequency noise events and events from particle interactions is seen by comparing pulses in time domain. Noise events are shown in Fig. 7.11, and good events from 1.29 keV_ee γs are shown in Fig. 7.12.

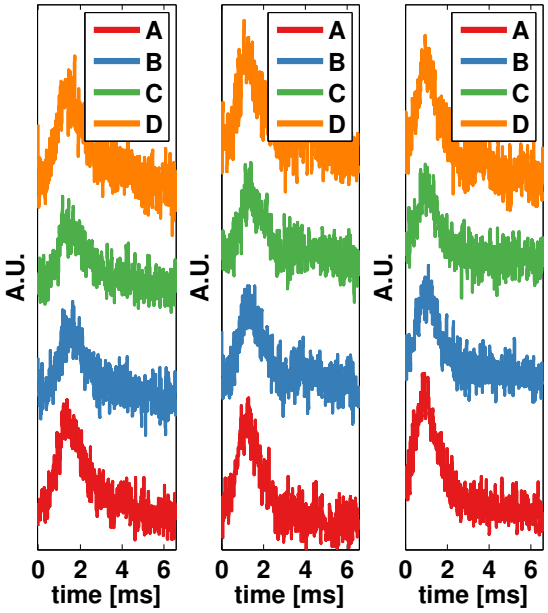

Figure 7.11: Three events with effective energies in 120-200 eV_{ee}, that occur at good periods, and are not glitches. Signals from individual phonon channels have been stacked with offsets for visual clarity. For all such events the characteristic rise-times and fall-times are both around 1 ms, and there is no major channel-to-channel variation.

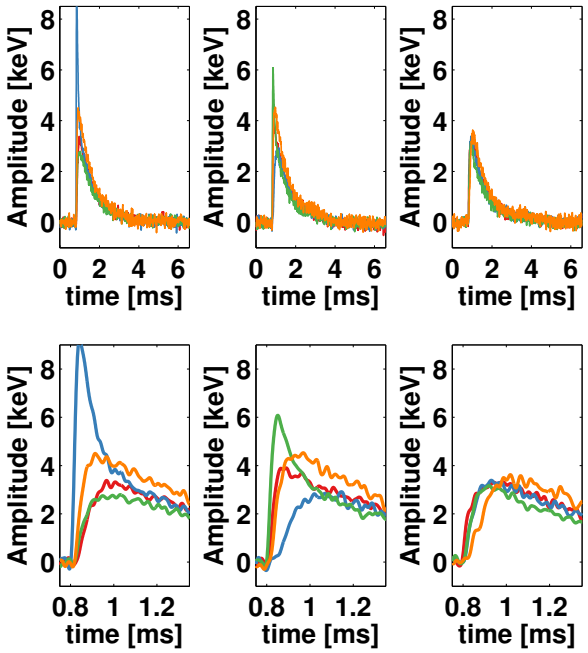

Figure 7.12: Three events with energies in 1.2-1.4 keV_{ee}, that occur at good periods and are not glitches. The bottom row is a zoom-in of the events from the first row. Note that the rise-times and fall-times are $\sim$50 μs and $\sim$800 μs respectively, with noticeable channel-to-channel variance on the rising edge. The color coding for channels A ... D are identical to Fig. 7.11

The key difference between these events is the time-scales of the pulses. For good events the signal in all channels have a characteristic $1/e$ fall-time of $\sim$800 μs. Furthermore the primary channel's (the channel with the most energy deposition) pulse is peaky, with sharp rise-times $\sim$50 μs. When compared in frequency-space,

$$\frac{\tau^{-1}_{\text{rise, noise}}}{\tau^{-1}_{\text{rise, primary-phonon}}} \approx \frac{1.25 \text{ kHz}}{20 \text{ kHz}} \ll 1 \tag{7.1}$$

Thus such spurious low energy triggers are called low frequency noise.

7.2.2 Timing discrimination

For every event we computed two timing metrics to pursue pulse shape discrimination. These are the rise-time of the primary channel's phonon pulse and the fall-time of the total phonon pulse[5], specifically defined as

$$\begin{aligned} \Delta_{\text{rt, prim}} &\equiv \text{Rise-time of primary-phonon pulse, 10\% to 100\% amplitude.} \\ \Delta_{\text{ft, pt}} &\equiv \text{Fall-time of total-phonon pulse 95\% to 20\% amplitude.} \end{aligned} \tag{7.2}$$

These metrics are calculated via a "walking-routine" as discussed in Sec. 3.5.2. The notation `xx % to yy %` implies the time-span over which the pulse's amplitude "walks" from `xx %` to `yy %` of the maximum amplitude, for rising or falling edges, respectively. Depending on the percentages, these are expected to systematically differ from the time constants quoted earlier.

Events passing various quality cuts discussed so far, can be viewed in the plane of $\Delta_{\text{rt, prim}}$ versus $\Delta_{\text{ft, pt}}$, where good events, particularly those from the activation lines, occupy a clear region as shown in Fig. 7.13.

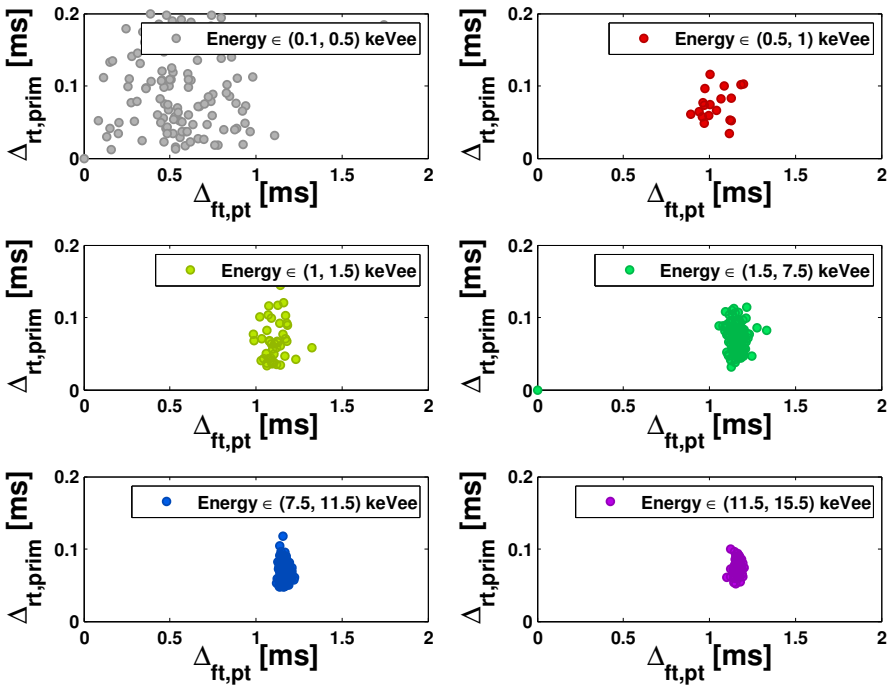

Figure 7.13: Events from various energy ranges plotted in the rise-time vs fall-time, i.e., $\Delta_{\text{rt, prim}}$ versus $\Delta_{\text{ft, pt}}$ plane. Good events, particularly the L and K shell γs (blue and yellow markers) have concentrated distributions around $\Delta_{\text{rt, prim}}$ ~0.07 ms and $\Delta_{\text{ft, pt}} \sim$ 1.1 ms.

Triggering events with energy <500 eV_{ee} have a large scatter, indicating that a majority of these are low-frequency noise. The distributions, when seen in an unbinned manner by plotting rise/fall-time versus energy show a large population of such noise triggers under ~200 eV_{ee}, Figs. 7.14 and 7.15.

[5]Fall-times for all channels are similar. Considering the total pulse's fall-time improves the SNR by 50%.

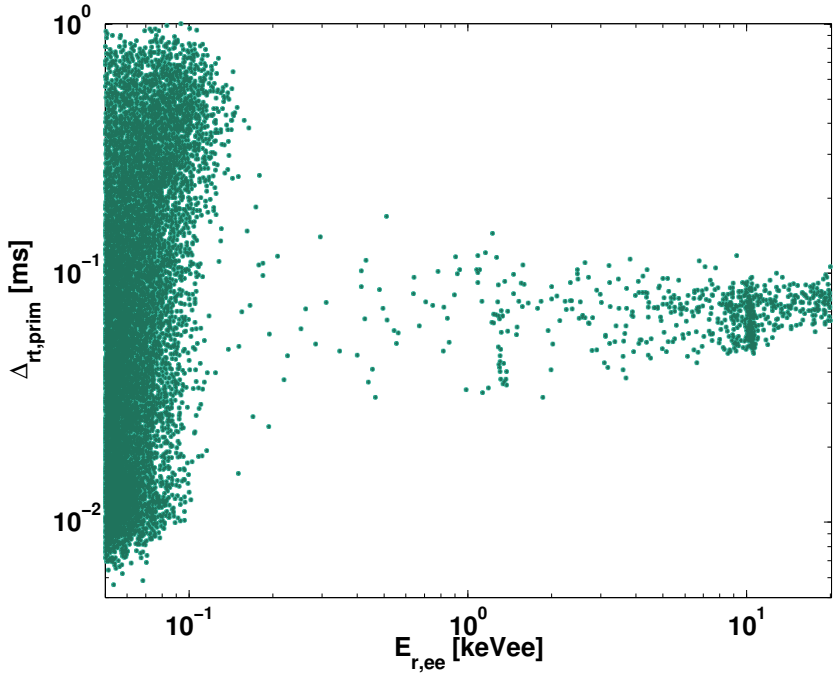

Figure 7.14: Log-log plot of $\Delta_{\mathrm{rt,\ prim}}$ versus ionization energy. The $\Delta_{\mathrm{rt,\ prim}}$ distribution is tight for good events, but flares at energies < 200 $\mathrm{eV_{ee}}$.

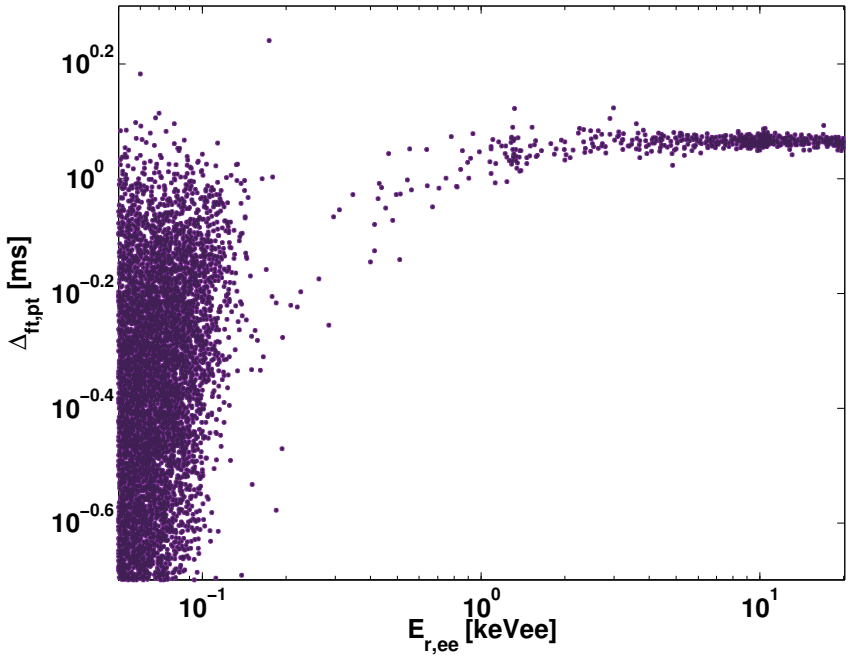

Figure 7.15: Log-log plot of $\Delta_{\mathrm{ft,\ pt}}$ versus ionization energy. The $\Delta_{\mathrm{ft,\ pt}}$ distribution is tight for good events, but flares at energies < 300 $\mathrm{eV_{ee}}$.

Cut definition and efficiency

For the first science analysis of CDMSlite, we used simple rectangular event selection cuts, where events are selected if their $\Delta_{\mathrm{rt,\ prim}}$ and $\Delta_{\mathrm{ft,\ pt}}$ values are within a range, broadly defined by the high energy bands in Figs. 7.14 and 7.15. These cut boundaries were chosen for the tightest constraints giving efficiencies $\geq$95% above 3 $\mathrm{keV_t}$ ($\approx$ 125 $\mathrm{eV_{ee}}$). In most cases the fall-time cut was seen to introduce a loss in efficiency, generally from pulses like the one shown in Fig. 7.16,

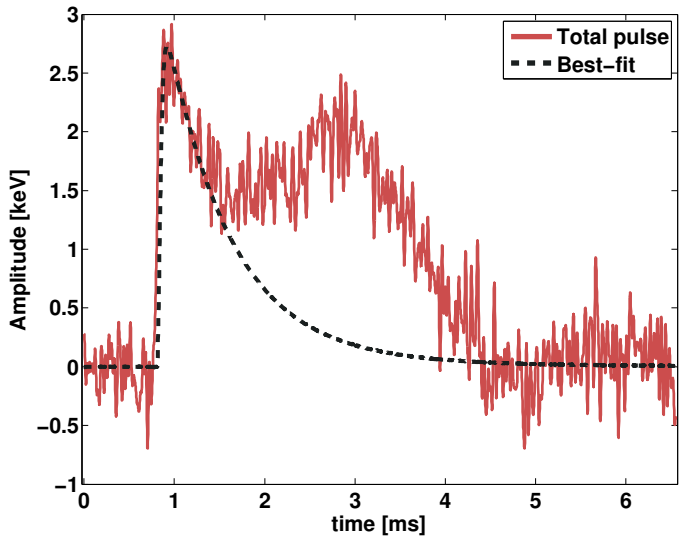

Figure 7.16: An example of a good event riding on low-frequency noise. The optimum filter routine finds the best-fit pulse with reasonable accuracy, however the low-frequency feature on the pulse's falling edge gives a spurious fall-time measure.

For the event shown in Fig. 7.16, there is low-frequency noise on the falling edge; however the optimum filter routine is able extract the essential energy or amplitude information rather well. Cases like this and pulse + noise MC studies discussed in Appendix D.1, showed that only a rise-time cut was required. Following the distribution shown in Fig. 7.17, the cut was defined as 4 ms $> \Delta_{\mathrm{rt,\ prim}} > 7\ \mu$s .

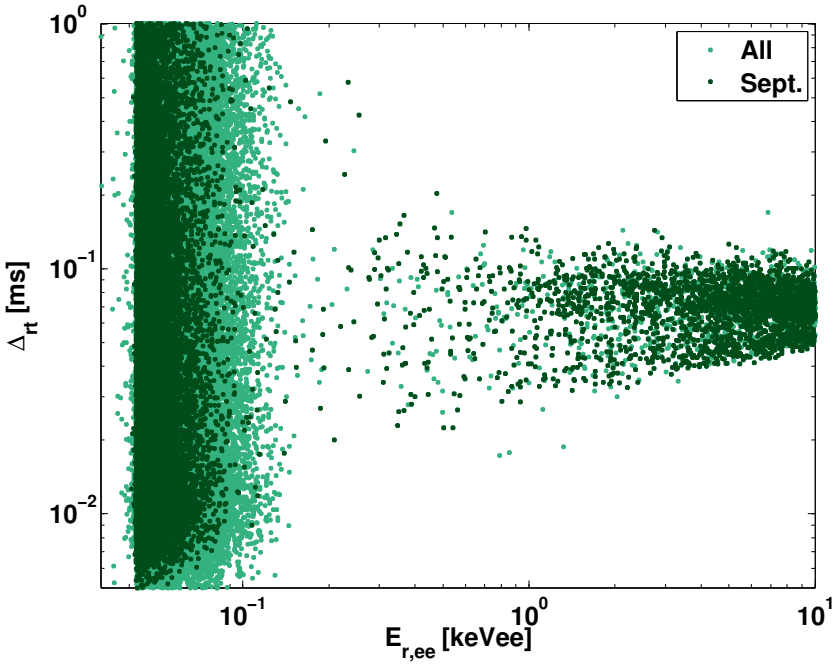

Figure 7.17: Log-log plot of $\Delta_{\mathrm{rt,\ prim}}$ versus ionization energy for Ba calibration data. Data from September (1/3rd of all data) is plotted separately as a cross-check, since the Luke gain was relatively constant during that period.

The passage fraction, proxy for efficiency, calculated on Ba data for this cut is shown in Fig. 7.18.

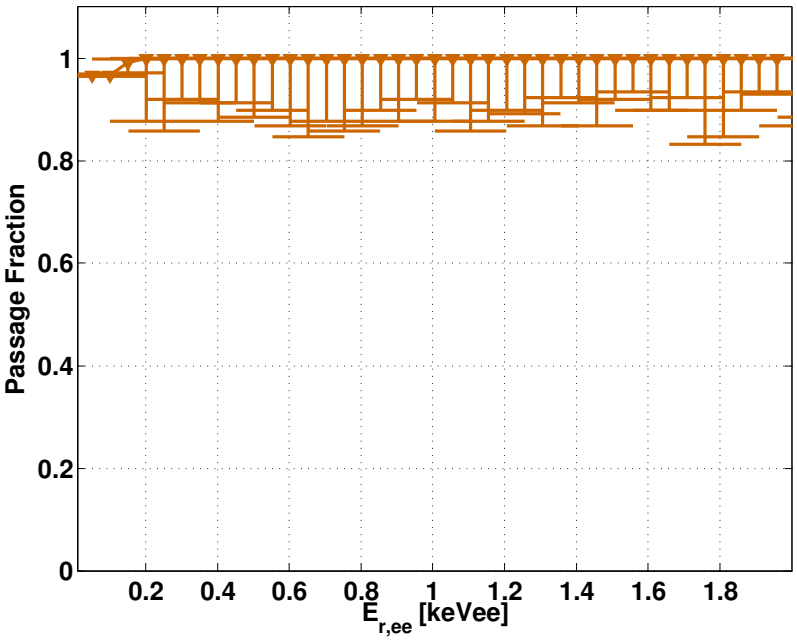

Figure 7.18: Efficiency of the $\Delta_{\mathrm{rt,\ prim}}$ cut evaluated on Ba calibration data.

This cut has $\sim$100% efficiency for energies $\gtrsim$150 $\mathrm{eV_{ee}}$.

7.3 Veto cut

The experiment is surrounded by 40 veto scintillator panels, as described in Sec. 3.2. Events occurring in the iZIPs coincident with any veto activity are rejected, particularly, if there is a veto trigger in the 50 μs history of a phonon trigger, or if any of the panel have signal pulses in (-185,20) μs around a phonon trigger, [134]. Redundancy exists in this definition to correct for possible inefficiency in the first level veto triggering mechanism. The efficiency of this cut, checked on randomly triggered events was 98.54%.

7.4 Singles cut

Multiple scattering events occur when photons or energetic ejectrons produce ionization and recoil in multiple iZIPs, and are clearly not caused by WIMPs. Three methods for rejecting multiple scatters were explored, [135]:

1. Restricting the total number of Tower 5 hits to one and requiring no hits in the other towers.
2. For an event in T5Z2, in a $\pm$50 μs window around its trigger time, require that no other iZIPs had a phonon trigger.
3. Select events where the summed energy in T5Z2 is above 99.87% ($\sim 3\ \sigma$ level) of its noise distribution and under this threshold for all other iZIPs.

All three cuts were checked on randomly triggered data and WIMP search data, and were seen to agree very closely, with <0.1% variations. Method 3 was the final implementation since this

method accounts for signal-to-noise limitation in a statistical sense.

Since the various selection cuts were designed to be nearly 100% efficient, the final data selection efficiency for Run 1 was essentially the product of the veto and the singles cut efficiencies,

$$\boxed{c_{\rm all}^{(T5Z2)} \approx c_{\rm sing}^{(T5Z2)} \times c_{\rm veto} \ : \quad \mathcal{E}\left(c_{\rm all}^{(T5Z2)}\right) = 98.50\%} \tag{7.3}$$

7.5 Trigger Efficiency

Having established cuts that select single-scatter physics events, we need to understand the triggering efficiency[6], especially for low-energy events.

7.5.1 Triggering: mechanism and expectations

Under $\mathcal{O}(1)$ keV$_{\rm t}$, trigger rates from noise events are very high, making the WIMP search inefficient. Thus, hardware trigger logic is employed in the warm electronics chain to prevent noise triggers from dominating data collection, Sec. 3.5.1. A global trigger is issued if the measured signal, after passing through a band-pass filter, exceeds a manually set voltage threshold (called P_{lo}, typically ∼10 mV). The filter bandwidth (0.9 - 18 kHz) is chosen where phonon pulses have more power over the noise, see Fig. 5.9. However, as the pulse amplitudes get smaller, the probability to trigger is dominated by noise, resulting in a reduction in trigger efficiency.

For every trigger event, the triggering amplitude is the result of a causal band-pass filter, whereas the event energy is obtained via an acausal optimal filter. Hence the strict hardware cut-off at P_{lo} does not correspond to a similar cut-off in energy scale. The presence of varying baseline noise during the time of triggering produces a smearing effect and so the trigger efficiency is modeled by a modified error-function. The general parametrization in terms of total energy measured, $E_{\rm t}$, is

$$\mathcal{E}_{\rm trig}(E_{\rm t}) = \frac{A_1}{2}\left(1 + {\rm Erf}\left[\frac{E_{\rm t} - A_2}{A_3}\right]\right). \tag{7.4}$$

The parameter A_1 is the asymptotic efficiency ≈ 1. The parameter A_2 corresponds to the energy where the triggering probability is 50% and is related to P_{lo}. The parameter A_3 is a measure of the dispersion in energy, and is related to the baseline resolution. If noise were Gaussian and white, then following Fig. 6.7, $A_3 = \sqrt{2}\sigma\,[E_{\rm t}] \approx \sqrt{2}{\times}14$ eV$_{\rm ee}$ × 12 [eV$_{\rm t}$/eV$_{\rm ee}$] = 238 eV$_{\rm t}$. From the non-gaussianity of measured noise, we expect this to be larger.

[6]This is the efficiency with which the DAQ triggers on pulses / events.

7.5.2 Calculation of trigger efficiency

Trigger efficiency was calculated using two methods, both relying on multiple triggers [136, 137]. At some energy, the trigger efficiency is the fraction of good events at that energy that caused T5Z2 to trigger. In this fraction, the methods vary in the definition of the denominator conditions, and are described in table 7.1.

Method I: Tower 5 detectors only	**Method II:** All detectors
Denominator Conditions (D_C) 1. Energy deposited in T5Z1 or T5Z3 is over 10 keV_t. 2. Trigger buffer, following the global trigger is longer than 50 μs. 3. Select events where $P_{lo} = 1$ for T5Z1 or T5Z3, and these triggers occur in (-3,77)μs of the global trigger. 4. Global trigger must not be issued by T5Z2. 5. Events pass general data quality selections.	**Denominator Conditions (D_C)** 1. Energy deposited any iZIP, with no constraints on T5Z2, is over 10 keV_t. 2. Trigger buffer, following the global trigger is longer than 50 μs. 3. Select events where $P_{lo} = 1$ for any non-T5Z2 detector, with no constraints on T5Z2, and these triggers must occur in (-3,77)μs of the global trigger. 4. Events pass general data quality selections.
Numerator Conditions (N_C) 1. T5Z2 had a trigger (not global) within 50 μs of the global trigger.	**Numerator Conditions (N_C)** 1. T5Z2 had a trigger within 50 μs of the global trigger.

Table 7.1: Table defining the numerator and denominator conditions for calculating the fraction of good events which triggered T5Z2.

The trigger efficiency at some energy E_t is the fraction whose numerator is the number of good events at that energy satisfying both numerator and denominator conditions (N_c & D_c), and whose denominator is the number of good events at that energy satisfying the denominator conditions (D_c).

Details regarding these methods

Both methods rely on samples with coincidence ($\sim$50 μs coincidence window) or multiple triggers [137]. Requiring the multiple trigger bits in the $\sim$50 μs history[7] ensures uncorrelated fluctuations do not affect the trigger measurements at low energies[8], thereby removing systematic bias driven by noise triggers. In Method I we deal with a subset of events, compared to Method II. This allows us to check if any tower related biases are present. The requirement that >10 keV_t energy was deposited in the coincidence detectors, is a parallel constraint on the requirement of proper multiple scattering. Sometimes electronic fluctuations can produce multiple triggers, but when their optimal filter reconstructed energies are compared, they are easily categorized as noise.

[7] Originally the trigger search window was (-1,50)μs; this was extended to (-3,77)μs to correct for loss of good triggers due to jitter in trigger time.

[8] Correlated noise can certainly pass such requirements, and thus the good events selection is necessarily imposed.

7.5.3 Trigger efficiency measurements

Measurements on Ba data

Trigger efficiency for Ba calibration data was measured as a function of energy collected on Side-1 of T5Z2. In order to profile the efficiency variation at low energies, bin sizes of $\mathcal{O}(100)$ $\mathrm{eV_t}$ were used. For such small bins the measurements become statistically limited, although the central points are all at 100% for measured energies $\gtrsim$1.8 $\mathrm{keV_t}$or 150 $\mathrm{eV_{ee}}$, see Fig. 7.19.

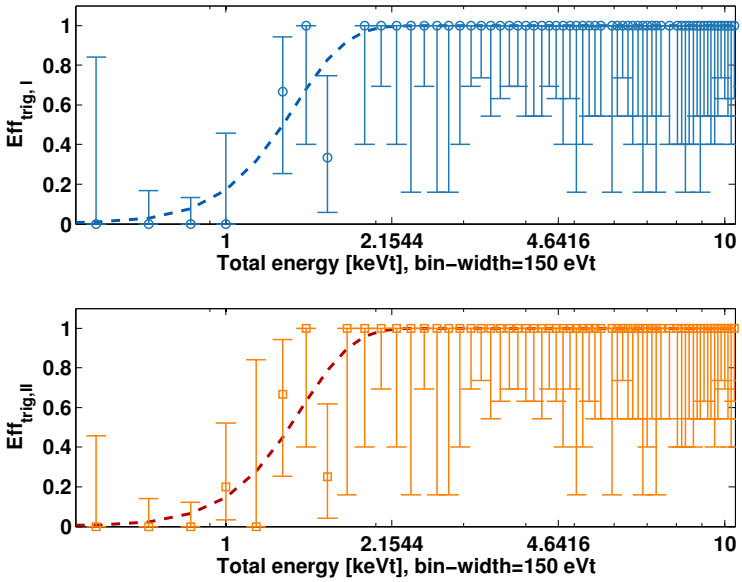

Figure 7.19: Trigger Efficiency calculated with Ba calibration data in CDMSlite Run 1. Methods I and II give practically identical results for measured energies over 1.5 $\mathrm{keV_t}$. Functional fits following Eq.(7.4), are shown with dashed lines. The fine bin-wdith of 150 $\mathrm{eV_t}$ results in large error bars, although the central points are all at 100% over ∼1.8 $\mathrm{keV_t}$ or 150 $\mathrm{eV_{ee}}$.

Fitting and error-estimation

The measurements are fit with the functional form from Eq. (7.4). The fit parameters are obtained via a nonlinear regression fitter, `nlnfit` routine in MATLAB. The parametric errors are obtained from $\sqrt{\mathrm{diag}\left[\mathrm{Cov}(A_k)\right]}$. The relevant numbers are listed in table 7.2 , rounded to four significant figures.

Method I: Tower 5 detectors only	**Method II:** All detectors
Best fit parameters and 1 σ error estimates:	**Best fit parameters and 1 σ error estimates:**
• $A_1 = 1.000,\ \delta A_1 = 0.001$	• $A_1 = 1.000,\ \delta A_1 = 0.001$
• $A_2 = 1.300,\ \delta A_2 = 0.012$	• $A_2 = 1.340,\ \delta A_2 = 0.012$
• $A_3 = 0.448,\ \delta A_3 = 0.025$	• $A_3 = 0.458,\ \delta A_3 = 0.025$

Table 7.2: Best-fit parameters and parametric errors (1 σ standard errors), from fitting Eq. (7.4) to the measurement trigger efficiency from Ba data.

Verification on background data and Trigger Threshold

The trigger efficiency calculations were verified on WIMP search data, Ref. [136]. Because of lower statistics, the error bars were larger and thus the Ba measurements were used for final estimations. As shown in Fig. 7.20, the efficiency for triggering is 100% over ∼1.8 $\mathrm{keV_t}$ (or 150 $\mathrm{eV_{ee}}$).

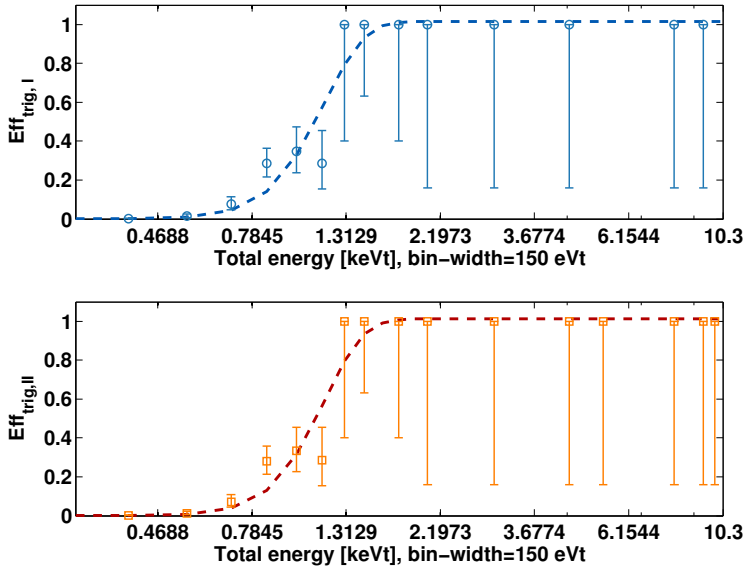

Figure 7.20: Trigger Efficiency calculated with WIMP search data in CDMSlite Run 1. Methods I and II give practically identical results over 1.3 $\mathrm{keV_t}$. Functional fits following Eq.(7.4), are shown with dashed lines.

Fitting and error-estimation for WIMP search data

The measurements are fit with the functional form from Eq.(7.4) and the results are presented in table 7.3.

Method I: Tower 5 detectors only	**Method II:** All detectors
Best fit parameters and 1 σ error estimates:	**Best fit parameters and 1 σ error estimates:**
• $A_1 = 1.016,\ \delta A_1 = 0.046$	• $A_1 = 1.012,\ \delta A_1 = 0.036$
• $A_2 = 1.112,\ \delta A_2 = 0.044$	• $A_2 = 1.116,\ \delta A_2 = 0.039$
• $A_3 = 0.342,\ \delta A_3 = 0.085$	• $A_3 = 0.331,\ \delta A_3 = 0.076$

Table 7.3: Best-fit parameters and parametric errors (1 σ standard errors), from fitting Eq.(7.4) to the measurement trigger efficiency from WIMP search data.

Setting a threshold

From the best-fit parameters and curve shown in Fig. 7.19, we calculated the loss in efficiency, and error in efficiency, as a function of energy. We chose an analysis threshold of 2.04 $\mathrm{keV_t}$, or 170 $\mathrm{eV_{ee}}$, since, for the best-fit function, the variation and loss[9] were both $< 1\%$ for $E_\mathrm{t} \geq 2.04$ $\mathrm{keV_t}$, see Fig 7.21. From the sparse measurements of the background data shown in Fig. 7.20, the loss and variation in trigger efficiency both $\lesssim 2\%$ for $E_\mathrm{t} \geq 2.04$ $\mathrm{keV_t}$.

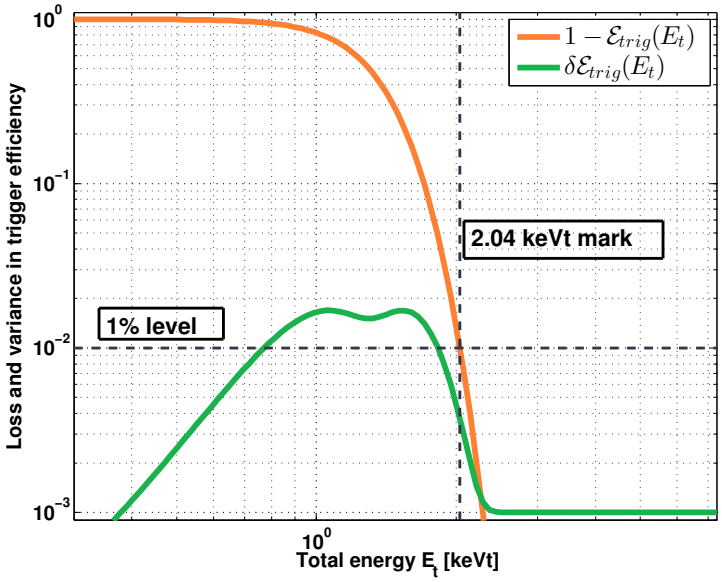

Figure 7.21: Loss in efficiency, $1 - \mathcal{E}_\mathrm{trig}$ and variation in efficiency $\delta\mathcal{E}_\mathrm{trig}$ as function of total energy for Ba data. The 1% level and the chosen threshold of 2.04 $\mathrm{keV_t}$ are marked with dashed lines. A threshold of 2.04 $\mathrm{keV_t}$or 170 $\mathrm{eV_{ee}}$ gives us trigger efficiencies that are robustly at 100% with less than 1% uncertainty.

Convoluting the net analysis efficiency from Eq.(7.3), the total efficiency of the CDMSlite experiment was 98.5% above 170 $\mathrm{eV_{ee}}$. This is the lowest threshold for any large (over few hundred grams) germanium dark-matter detector, and generally one of the lowest thresholds achieved to date in direct detection experiments.

[9]Variation and loss of efficiency are defined as $\delta\mathcal{E}_\mathrm{trig}(E_\mathrm{t}) = \sqrt{\sum_k \left(\partial_{A_k}\mathcal{E}_\mathrm{trig}(E_\mathrm{t})|_{A_k} \times \delta A_k\right)^2}$ and $1 - \mathcal{E}_\mathrm{trig}(E_\mathrm{t})$.

Chapter 8

WIMP search sensitivity for CDMSlite Run 1

The event selection process described in the previous chapter, when applied to CDMSlite Run 1 data, provides an ionization spectrum. This spectrum is converted from ionization energy to nuclear recoil energy scale. Then, accounting for efficiencies, comparisons with expected WIMP rates allow us to test for the presence of a WIMP signal in the data. This chapter will detail these steps, concluding with CDMSlite Run 1's sensitivity to light WIMPs.

8.1 Final ionization spectrum from CDMSlite Run 1

Fig. 8.1 shows the final ionization energy spectrum result from event selection described in Chapter 7, together with the selection efficiency.

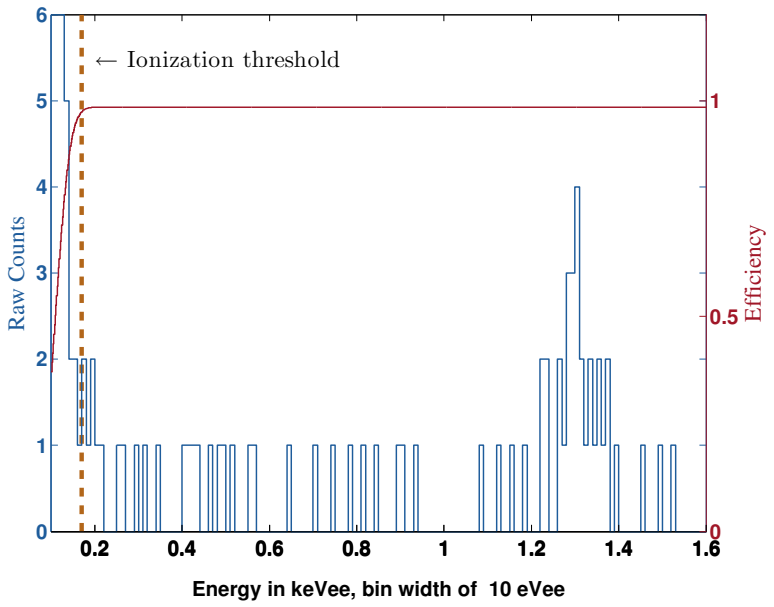

Figure 8.1: The final spectrum of events assuming 100% ionization production is shown in blue. Here we zoom-in on the low energy region which encompasses the 1.29 keV_{ee} activation line. The threshold is marked with a vertical dashed line. The net efficiency is shown in red.

Recall that CDMSlite measures the total phonon energy. Eq (4.2) is used to convert the measured total phonon energy to ionization energy, under the assumption that the events are electron recoils. This is a conservative assumption as we cannot discriminate between electron and nuclear recoils, thus considering electron recoil backgrounds a part of the nuclear recoil signal necessarily limits the WIMP search sensitivity.

8.1.1 Expected rates

The spectrum shown in Fig. 8.1 consists of activation lines discussed in Sec. **??**, and a background of gamma rays from Compton scattering. Previous CDMS analyses [138, 97] have derived a roughly flat Compton scattering rate of $\sim$ 1.5-2 Counts/ keV$_{ee}$/ kg / day . Table 8.1 shows the rates deduced from Fig 8.1 in three flat regions between activation peaks.

Energy range:(in keV$_{ee}$)	**Counts:**($\pm 1\sigma$ Poisson errors)	**Counts/ keV$_{ee}$/ kg / day**
0.17-1.07	31 $\pm$ 5.57	5.51$\pm$ 0.99
1.5-7.5	103$\pm$ 10.15	2.74 $\pm$ 0.27
12-22	94 $\pm$ 9.70	1.50 $\pm$ 0.15

Table 8.1: Rate of events measured in various regions between activation lines.

During the time this study was published, no clear measurements existed under $\sim$500 eV$_{ee}$. While the rates in the upper two ranges are in rough agreement with previous measurements, a relative excess is clearly noted in the lowest energy range. Since this is the energy range where we are most sensitive to light WIMP recoils, various studies were performed to understand this relative excess.

Excess correlated with neutron exposure

Exposure to ^{252}Cf (neutrons) can produce short lived activations, resulting in different background rates after the exposure than before. The data were split into "Pre-Cf" and "Post-Cf" periods surrounding the calibration performed on August 22, 2012, and the corresponding spectra are shown in Fig. 8.2. These periods had live-times of 38 and 77 hours, with 9 and 17 good events, without single scatter selection, in 0.17-1.07 keV$_{ee}$, respectively. Scaling with live-time, the Post-Cf to Pre-Cf ratio of counts in this energy range is $(38/77) \times (1.89 \pm 0.78) = 0.932 \pm 0.38$.

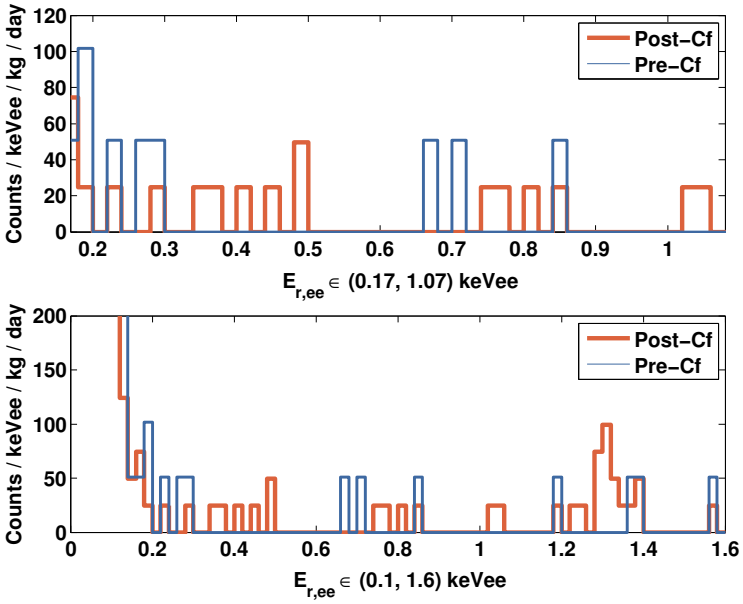

Figure 8.2: Exposure weighted spectrum of events pre and post-^{252}Cf (neutron) exposure. The top plot is zoomed in to the energy range of interest, and the bottom plot covers a larger range, just beyond the 1.29 keV$_{ee}$ activation line.

A Kolmogorov-Smirnov (KS) test was performed to estimate the level of statistical difference between the two spectra. This accepts the hypothesis that these two spectra are drawn from similar underlying distributions. In a standard KS test the acceptance threshold is a p-value of 5%. With a relative fraction of 0.932 and a KS test p-value of 16.43% $>$ 5%, neutron exposure thus cannot statistically account for the low-energy excess.

Multiples versus Singles check

WIMPs are expected to scatter extremely rarely. Thus, if the spectrum of singly-scatter events is statistically similar to that for multiply-scattered events, then any excess of single scatters is likely to be a background rather than a WIMP signal. This statistical statement is valid only when the WIMP spectrum is different than that expected from the background. At the very low energies of $\mathcal{O}(100)$ $\mathrm{eV_{ee}}$, not much is known about the spectral shape of Compton recoils, particularly after accounting for charge trapping near detector edges. Table 8.2 shows the comparison of single and multiple scattered events for CDMSlite Run 1 data, and Fig. 8.3 shows the energy spectra.

Energy range:(in $\mathrm{keV_{ee}}$)	**Multiple scatters:**	**Single scatters:**	**Singles / Multiples:**
0.17-1.07	12 $\pm$ 3.46	31 $\pm$ 5.57	2.58 $\pm$ 0.89
1.5-7.5	55 $\pm$ 7.42	103$\pm$10.15	1.87 $\pm$ 0.31
12-22	95 $\pm$ 9.75	94 $\pm$ 9.70	0.98 $\pm$ 0.14

Table 8.2: Multiples / single scatter counts (with $\pm 1\sigma$ Poisson errors) in regions between activation lines. The last column shows the singles-to-multiples ratio.

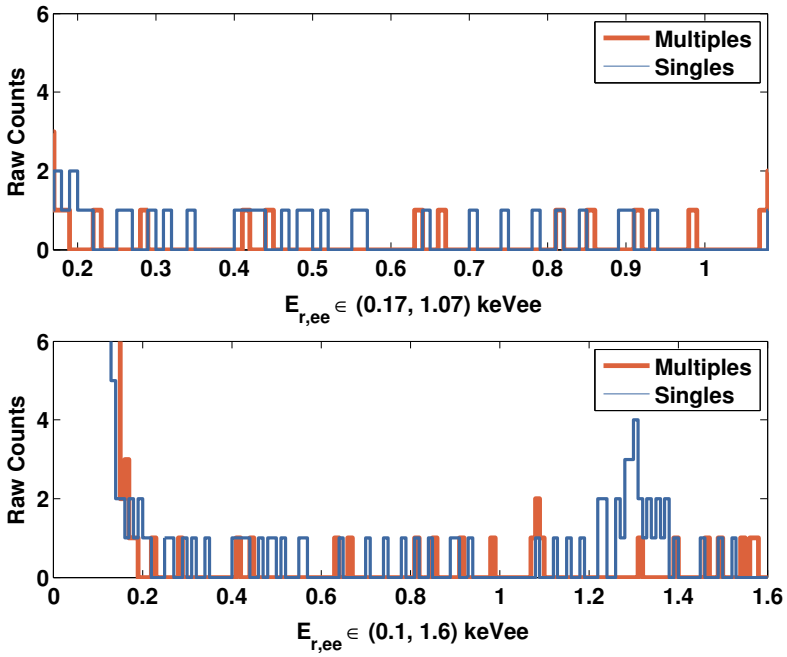

Figure 8.3: Spectra of single and multiple scatters events. The top plot is zoomed in to the energy range of interest, and the bottom plot covers a larger range, just beyond the 1.29 $\mathrm{keV_{ee}}$ activation line.

A KS test on the hypothesis that these two spectra are drawn from the same underlying distribution gives a p-value of 79.24%, well above the 5% hypothesis acceptance value, and statistically the singles distribution and multiple distributions are similar. Thus, the excess in the singles spectrum at low energy is likely due to backgrounds.

8.1.2 Conversion to nuclear recoil energy scale

In CDMSlite selection of nuclear recoils based on yield measurement is not possible, since standard ionization measurement threshold is $\gtrsim 1$ keV$_{\rm ee}$, see Sec 3.1.1. In order to derive conservative limits on WIMPS, we make the assumption that all of the events are due to nuclear recoils, although we have already noted that this is very unlikely. The ionization energies are converted to nuclear recoil energies as shown in Eq. (8.1).

$$E_{\rm r,nr} = E_{\rm r,ee} \times \frac{(1+g_L)}{(1+Y(E_{\rm r,nr})g_L)} \tag{8.1}$$

Here $g_L(V_b) \equiv eV_b/\varepsilon_\gamma$ is the Luke-gain and $Y(E_{\rm r,nr})$ is the ionization yield, discussed in Sec. 3.1.1.

Measurements of ionization yield of Ge at low energies ($\lesssim 1$ keV$_{\rm nr}$) are very difficult to make and the data is sparse. Furthermore, systematic effects of temperature and local electric fields on ionization yield are not fully understood[1]. We thus use the canonical Lindhard yield model to calculate our main nuclear recoil energy scale, and consider other models to study the effect of yield on WIMP sensitivity; details on these models may be found in Refs. [110, 139, 140].

The spectrum of events, interpreted as nuclear recoils with energy calculated using the Lindhard model, is shown in Fig 8.4. Also shown are expected rates from two different WIMP spectra corresponding to the signal excesses as inferred by CoGeNT and CDMS-Si, [94, 97].

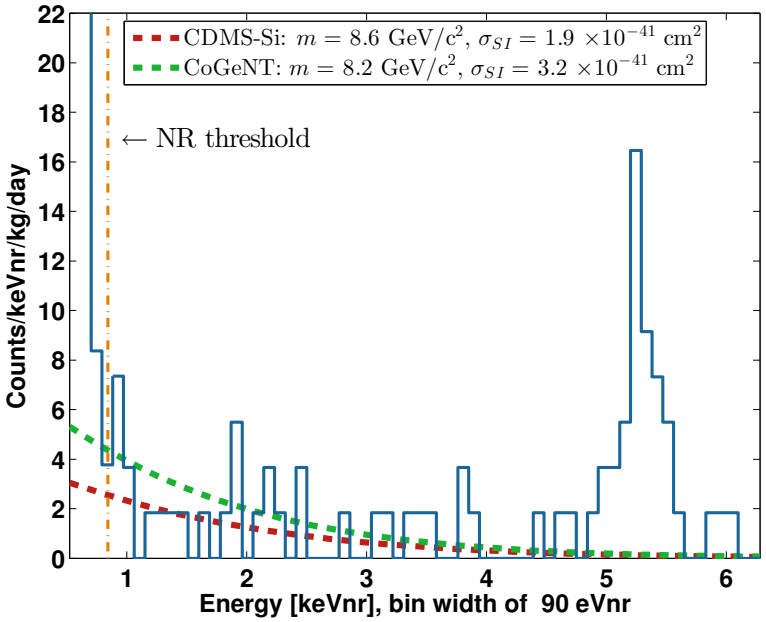

Figure 8.4: The final spectrum of event energies in keV$_{\rm nr}$ units, assuming Lindhard yield model. The low energy region encompassing the 1.29 keV$_{\rm ee}$ activation line, which appears at ∼5.3 keV$_{\rm nr}$, is shown here. The threshold at 840 eV$_{\rm nr}$ is marked with a vertical dashed line. In red and green dashed lines, WIMP spectra corresponding to the signal excesses as inferred by CoGeNT and CDMS-Si are shown, [94, 97].

[1]Electric fields determine the efficiency of charge extraction, and temperature affects the density of phonon states thereby controlling energy transport.

8.2 WIMP search limits from CDMSlite Run 1

We now compare the nuclear recoil spectrum derived from our measurements with various WIMP models to statistically comment on whether there is evidence for such WIMPs in CDMSlite Run 1 data. This section will discuss WIMP search limits for various WIMP-nuclear interactions, dark matter halo models and detector response models.

8.2.1 Spin Independent limits

Upper limits to various WIMPs can be computed by comparing the nuclear recoil spectrum with expected WIMP rates, as shown in Fig. 8.4. We use Steve Yellin's optimal interval method, [141, 142] to calculate sensitivity to light WIMPs with these data.

In this method, from all pairs of energies bounding an interval, we find the *optimal-interval* that rejects the possibility of a WIMP at 90% confidence level, given WIMP mass and cross-section. This is done by maximizing the difference between the measured distribution and the expected distribution in this interval, taking into account appropriate statistical penalties. This method is particularly powerful when unknown backgrounds with distributions dissimilar from WIMPs are present, as is the case for CDMSlite. In energy intervals where the measured distribution is different from the WIMP spectra, strong upper limits can be set.

The spin-independent limits are shown in Fig. 8.5, along with patches representing tentative signals reported by various experiments [143].

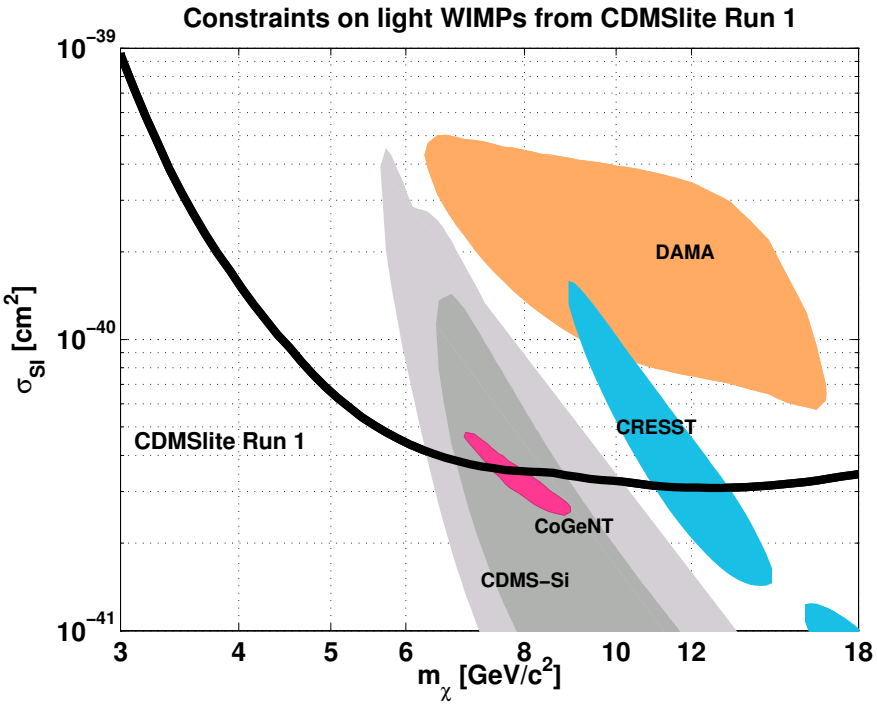

Figure 8.5: The black curve is the WIMP limit obtained via the optimum interval method from CDMSlite Run 1, under the canonical Lindhard yield assumption. The colored patches are interpretations of excess events as WIMP signals by, CDMS II Si (light and dark gray correspond to 68% and 90% CL regions respectively) [94], CRESST II (blue) [98], DAMA (orange) [99, 144], CoGeNT (pink) [97].

8.2.2 Comparison with other experiments

Fig. 8.5 showed the CDMSlite Run 1 90% upper limit compared with hints of signals reported by other experiments, but there are also upper limits from experiments in this region. It is worth pointing out some subtleties in computing such limits before we compare them.

Subtleties in comparing limits

Experiments such as CDMSlite, XENON10-S2-only, CoGeNT and CDEX effectively measure ionization and convert these to nuclear recoil energies using models of ionization production. Systematic uncertainties exist in this experimental conversion scheme in the sub-keV region, and are extremely difficult to verify with measurements. For CDMSlite Run 1 we tested various yield models to see the effect of yield on WIMP sensitivity, as discussed in Sec. 8.2.2.

Many of the other experiments attempt to subtract known backgrounds when computing limits. The systematic effects of background modeling, particularly at low energies where measurements are sparse, may not be accurately accounted for in some cases. In this CDMSlite Run 1 analysis, no background subtraction was performed and only an upper conservative limit was calculated.

Given a dark matter halo model and detector threshold, there is a lower limit to the WIMP masses that may be probed. For example, assuming the standard halo model with escape velocity of 544 km/s, the energy spectrum for a 2.5 GeV/c^2 WIMP terminates sharply at $\sim$1 keV$_{\rm nr}$. For CDMSlite Run 1's 840 eV$_{\rm nr}$ threshold this mass cut-off is $\sim$2.2 GeV/c^2. Energy smearing, from base-line resolution, can provide sensitivity to lighter WIMPs by exploiting statistical fluctuations. Some experiments smear the rate near threshold in this manner. This is allowable only if the noise distribution below threshold is well known, and this is typically a challenging characterization. Due to the excellent resolution of CDMSlite, such smearing makes little difference, and since the error on the velocity distribution and fundamental noise are not known to extreme precisions, we conservatively compute the sensitivity down to 3 GeV/c^2 only, without performing any smearing.

WIMP limits should actually be compared within their systematic error bands. Since these are not available in most cases, we compare the central limits and discuss possible systematic effects due to nuclear recoil yield, likely the dominant unknown.

Comparison with limits available at time of publication

The CDMSlite Run 1 spin-independent limit is shown in Fig 8.6, together with upper limits from other experiments available at the time of publication, September 2013 [143].

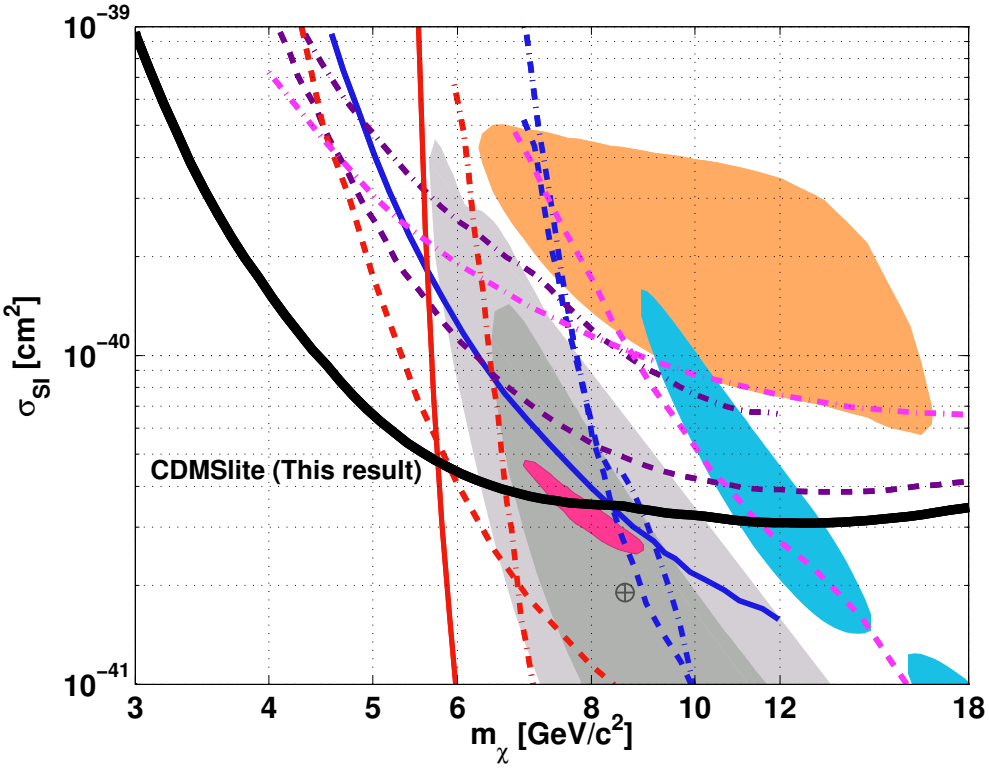

Figure 8.6: The 90% upper confidence limit from CDMSlite Run 1 is shown with exclusion limits from other experiments, as available at time of publication. These are grouped as Ge bolometers in blue: CDMS II Ge regular (dot-dash) [96], CDMS II Ge low threshold (solid) [102], EDELWEISS II low threshold (dash) [101]; point-contact Ge detectors in purple: TEXONO (dash) [145], CDEX (dot-dash) [146]; liquid Xenon in red: XENON100 (dot-dash) [104], XENON10 S2 only (dash) [147, 103]; and other technologies in magenta: Low threshold reanalysis of CRESST II data (dot-dash) [148], PICASSO (dash) [149]. The contours are from CDMS II Si (light and dark gray correspond to 68% and 90% CL regions respectively) [94], CRESST II (blue) [98], DAMA (orange) [99, 144], CoGeNT (pink) [97].

Comparison with other world leading limits

Since September of 2013, the SuperCDMS Low-Threshold (in red) and LUX (in blue) experiments have released world leading limits [113, 150]. The CDMSlite Run 1 spin-independent limits (in black) are compared with these results in Fig. 8.7.

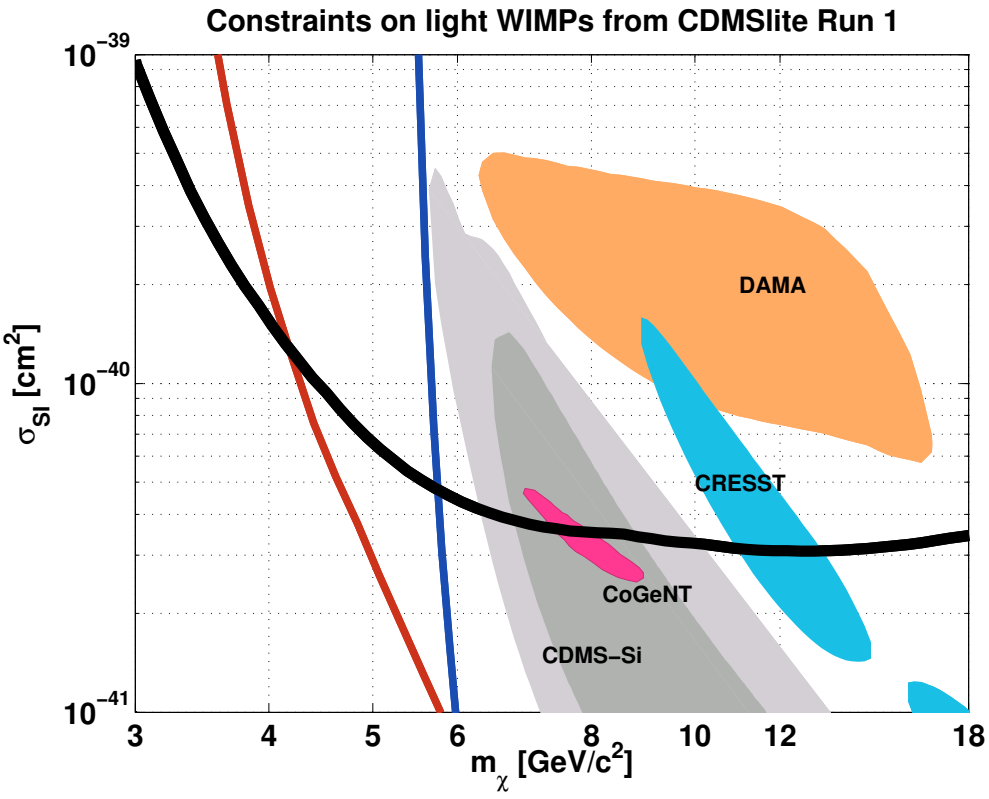

Figure 8.7: The 90% upper confidence limit from CDMSlite Run 1 (in black) is shown with exclusion limits from SuperCDMS Low Threshold (in red) and LUX (in blue), [143, 113, 150].

CDMSlite Run 1 had no in-situ background rejection. The experiment was background limited with an exposure of ∼6.3 kg-days and the limit was computed without subtracting any known backgrounds. In comparison, SuperCDMS Low Threshold and LUX had exposures of 577 kg-days and 10065 kg-days respectively, with electron recoil rejection of >99% in both cases. It is the extremely low threshold of CDMSlite that makes it a competitive experiment for very low mass WIMPs ($m_\chi < 4$ GeV/c^2).

Effect of varying ionization yield models

In CDMSlite, we used the Lindhard model [110] for conversion of ionization energies to nuclear recoil equivalent energies. The agreement between the Lindhard model and measurements is excellent at high energies, but begins to degrade at lower energies due to measurement difficulties, and systematic effects[2], and often an empirical models are used, Ref. [140, 139].

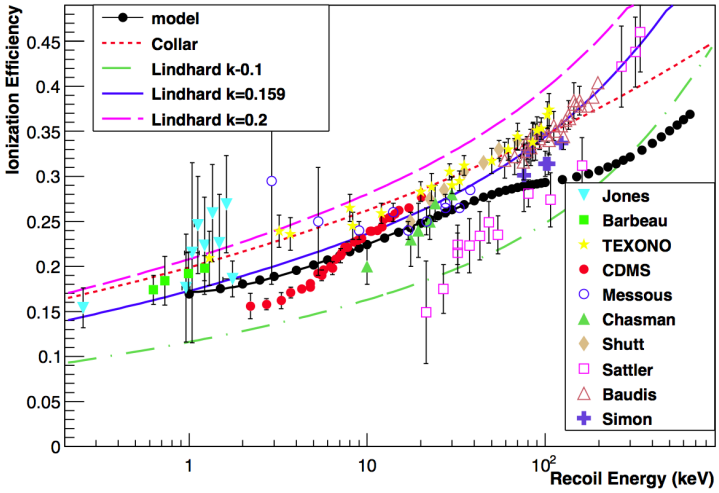

Figure 8.8: The landscape of ionization efficiency / yield measurements and various theoretical / empirical models, from Ref. [139]. Here, "Collar" refers to the yield model used by CoGeNT [97], "model" refers to a model developed by the authors [139], and the various Lindhard-k values refers to a parameter in the Lindhard model (canonically k=0.157).

The effect on upper limits from changing the yield model[3] is shown in Fig. 8.9.

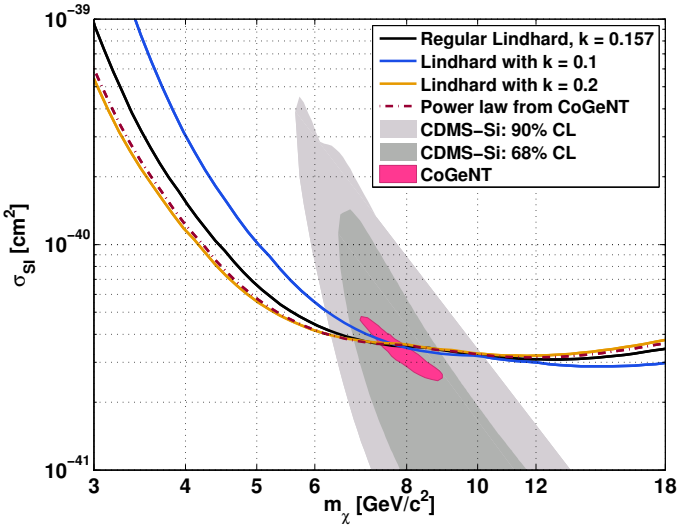

Figure 8.9: Effect on 90% upper limits obtained from CDMSlite Run 1 data by varying ionization yield models.

Apart from the very conservative yield model ($k = 0.1$), the others are in close agreement and make little difference to the sensitivity over 5 GeV/c^2. Under 5 GeV/c^2, the regular Lindhard yield gives a more conservative upper limit compared to CoGeNT's.

[2]There are challenges in measuring yield at low energies. Factors such as levels of impurities, distribution of charge traps, local variations in electric fields, thermodynamics of the experiment etc. can affect the number of charges produced and efficiently collected. The various atomic binding energies are in the eV range, and these issues are relevant primarily at very low energies.

[3]In Fig. 8.8 from Ref. [140, 139], the plot legend k=0.159 is a typographical error, k= 0.157 is the correct value.

Effect of Luke-gain variation

In the CDMSlite Run 1 data a $\lesssim$10% variation in the Luke-gain was observed in Run 1 data, and in Sec. 6.4 and Appendix C a scheme for correcting this time variation was discussed. In this subsection we discuss the effect of possible uncorrected $\sim$10% variations by quantifying the effects of gain variation on energy scale. For a given ionization energy we compute the nuclear recoil energy from having full gain and 10% reduced gain. In Fig. 8.10 the left-axis shows the expected nuclear recoil energy given some ionization. The right axis shows the fractional difference in the computed nuclear recoil energy from having a 10% lower gain.

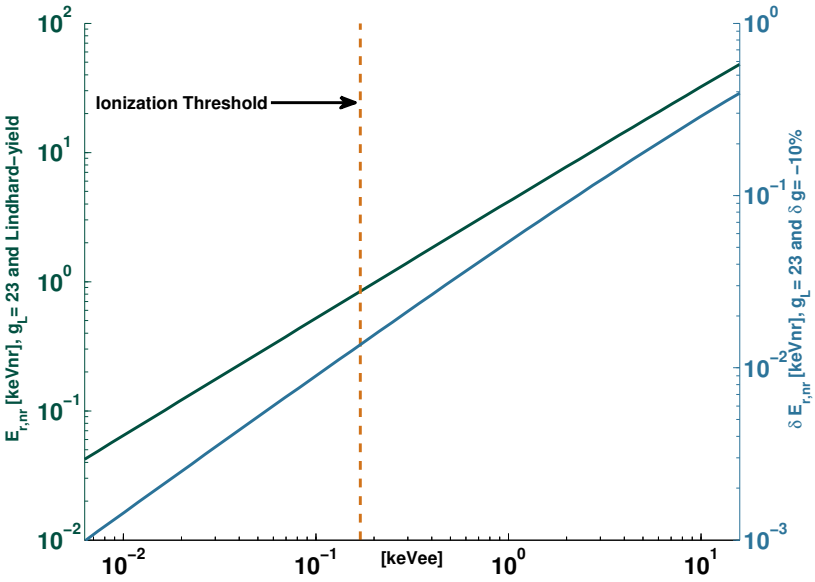

Figure 8.10: Effect of 10% drop in Luke-gain on nuclear recoil energy scale, as a function of ionization energy. The blue curve shows the level of correction required for a 10% drop in gain. The green curve shows the nuclear recoil energy assuming perfect gain, $g_L = e \times 69\text{V}/\varepsilon_\gamma = 23$. The orange-dashed line marks the 170 eV_{ee} threshold. The standard Lindhard yield was used for computing these variations.

If the gain were consistently lower by 10%, then Fig. 8.10 shows that the effective threshold would be lower by 1.3 eV_{nr} from the 840 eV_{nr}[4]. While this is the maximal change, the overall effect is minimal, $|\delta E_{\text{r,nr}}/E_{\text{r,nr}}| < 1.5 \times 10^{-3}$, and the conclusion remains unaffected by varying yield models. The difference in 90% cross-section upper limit is <1% for m_χ <5 GeV/c^2.

[4]This is the nuclear recoil threshold assuming Lindhard yield and no gain drop.

8.2.3 Limits from varying WIMP astrophysics

As discussed in Ch. 4 and shown in Fig. 4.1, the expected rate of WIMP interactions depends on the velocity distribution of galactic dark matter. Thus it is important to quantify the effect of varying dark matter velocities on the derived spin independent cross-section limit.

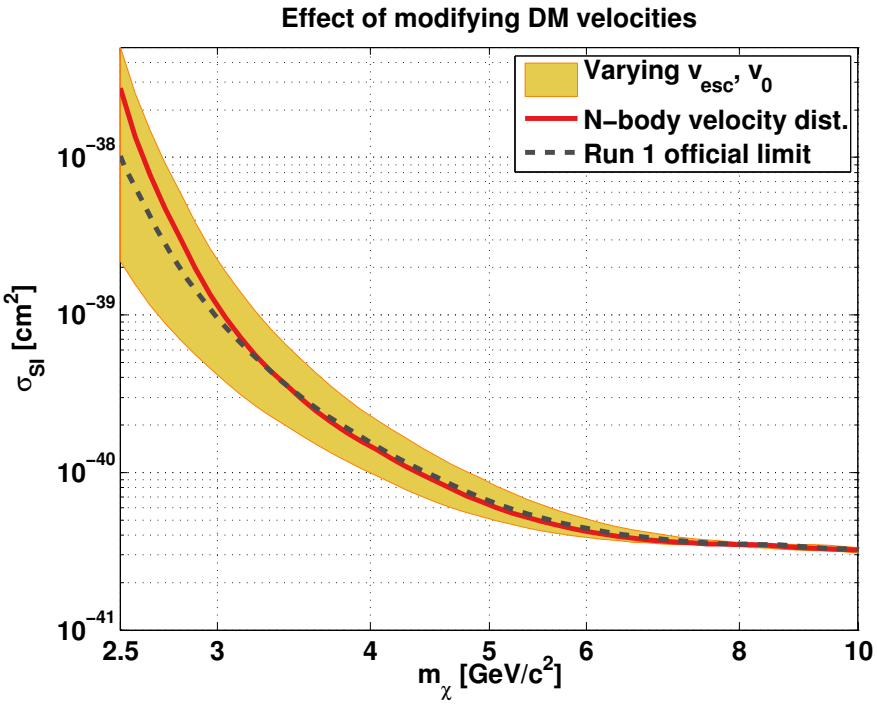

Figure 8.11: Effect on the 90% upper limit due to varying WIMP velocity distributions. The band is the span of limits from maximal and minimal central and escape velocities. The lower and upper bounds on each velocity are v_0 = 195, 255 km/s and v_{esc} = 498, 608 km/s respectively, Refs. [77, 78, 79, 80]. The red curve is the limit from N-body simulations' velocity distribution, and the dashed gray dashed line is the Run 1 limit [151, 152]

Fig. 8.11 compares the Run 1 limit to those obtained from variations of the Standard Halo Model (SHM) as outlined in Ch. 4. The yellow band is constructed from the SHM with a range of v_0 and v_{esc} velocities. Another velocity profile suggested by N-body structure formation simulations was also used to compute an alternative limit. In this particular model $f(v) \propto \exp\left(-v/v_0\right)\left(v_{esc}^2 - v^2\right)^p$, and a reasonable value of $p = 2.7$ has been used following Refs. [151, 152]. Since velocity dispersion primarily affects the signal strength for light WIMPs, the mass-range is limited to 10 GeV/c^2. We note that the effect of astrophysical uncertainties can produce an order of magnitude difference in the light WIMP interpretations from these data, particularly for WIMPs with mass of a few GeV/c^2. For $m_\chi > 6$ GeV/c^{2}the effects are not very large.

8.2.4 A Log-Likelihood scheme

While the power of CDMSlite lies in the low threshold, ultimately electron recoil backgrounds limit the scale of cross-sections that may be probed from the Run 1 data. If we properly model the known background contributions, then a log-likelihood analysis of signal+background can allow us to improve the experiment's sensitivity. While this work is beyond the scope of this thesis, a first attempt is discussed here outlining the framework that may be used.

Mathematical framework

The extended likelihood function for n observed events, ν expected events, given a generic probability density[5] f is obtained by multiplying all probabilities as,

$$\mathcal{L}(\theta) = \frac{e^{-\nu}\nu^n}{n!}\prod_{i=1}^{n} f(x_i;\theta)\delta x. \tag{8.2}$$

We take the log of Eq.(8.2) and drop all non-parametric constants to get the function, which when maximized, gives the best-fit parameters.

$$\ln \mathcal{L}(\theta) = -\nu(\theta) + \sum_{i=1}^{n} \ln\left(\nu(\theta) f(x_i;\theta)\right). \tag{8.3}$$

The exact distribution f is derived from measurements. For CDMSlite, we measure or estimate rates[6], dR/dE in units of Counts/ $\mathrm{keV_{nr}}$/ kg / day . For an exposure MT with energy-efficiency $\mathcal{E}(E)$, the expected number of counts in an energy range $E \pm \delta E/2$ is $\Gamma(E) = dR/dE(E)\delta E \times MT/\mathcal{E}(E)$. Over an energy range B, the probability of having an event with energy $E_i \in B$, for model parameters θ is given by Eq.(8.4).

$$f(E_i;\theta)\delta E = \frac{\Gamma(E_i;\theta)\delta E}{\int_{E\in B} dE\ \Gamma(E;\theta)} \tag{8.4}$$

Since we are probing light WIMPs, $B = (0.17, 3)$ $\mathrm{keV_{ee}}$ is a reasonable energy range. Here we have known backgrounds from Compton and L-shell photons, and possibly WIMP signals. The total distribution for CDMSlite is given by Eq.(8.5).

$$f(E;\theta)\delta E = \left(\Gamma_W(E;\theta) + \Gamma_C(E;\theta) + \Gamma_L(E;\theta)\right)\delta E/\nu(\theta) \tag{8.5}$$

In Eq.(8.5) parametric dependencies are: Compton and L-shell rates have scale parameters, and WIMP rates have two parameters associated with WIMP mass and WIMP nucleon cross-section. Note that our backgrounds are thus a flat Compton spectrum and a Gaussian for the L-shell activation with its mean and width set by the data.

[5]The parametric probability density is $f(x;\theta)$. Here the model parameters are θ and the probability of an observation $x \in x_k \pm \delta x/2$ is $f(x_k;\theta)\delta x$. Factoring in Poisson probabilities is important when low event rates make results susceptible to $\sim\sqrt{n}$ fluctuations.

[6]I use E for energy and whether it's $\mathrm{keV_{ee}}$ or $\mathrm{keV_{nr}}$, the mathematical framework is identical.

The H1 / H0 hypothesis

For the hypothesis that a signal is measured, maximizing Eq.(8.2) gives us the best fit parameters for the WIMP signal component; this is called the H1 hypothesis. The null or H0 hypothesis is necessary to test the significance of the H1 hypothesis, and is done by maximizing Eq.(8.2) assuming no signal component is present. If the maximum log-likelihoods for these hypotheses are designated $\mathcal{L}_{0/1}$, then the quantity $q_0 = -2\ln(\mathcal{L}_0 - \mathcal{L}_1)$ is roughly $\sim \chi^2$, and a high q_0 indicates the presence of signals with high significance.

For these data, the H1 hypothesis is best fit with a WIMP component along with the electron recoil backgrounds. The best fit WIMP has $m_\chi = 6.6$ GeV/c^2, and $\sigma_{\chi n} = 1.9\times10^{-41}$cm^2. The log-likelihood ratio test gives $q_0 \approx 18.5$ indicating a strong preference for a WIMP component. The best-fit WIMP component is very likely a background that has not been accounted for. Recall the discussion in Sec. 8.1.1, KS test with the multiple and single-scatter rates indicated this excess is likely some background; this is further instantiated since the SuperCDMS-LT results rule out such a WIMP model [113]. Further analysis explaining this as a non-WIMP component will be discussed in the concluding chapter.

90% Confidence Level contours

If one considers the H1 (WIMP) hypothesis to be correct at face-value, since the log-likelihood has a best fit WIMP model, one may look at contours of confidence to quantify the statistical dispersion in the best fit parameters. Those (m_χ , $\sigma_{\chi n}$) which fall in the 90% Confidence Level around the best fit $\hat{m}_\chi$, $\hat{\sigma}_{\chi n}$ satisfy the condition $\ln\mathcal{L}(m_\chi, \sigma_{\chi n}) = \ln\mathcal{L}(\hat{m}_\chi, \hat{\sigma}_{\chi n}) - 4.61/2$. Here 4.61 is the 90% (or 2σ) mark for a χ^2 distribution with 2 degrees of freedom. The final contour obtained from a m_χ , $\sigma_{\chi n}$ grid scan is shown in Fig. 8.12.

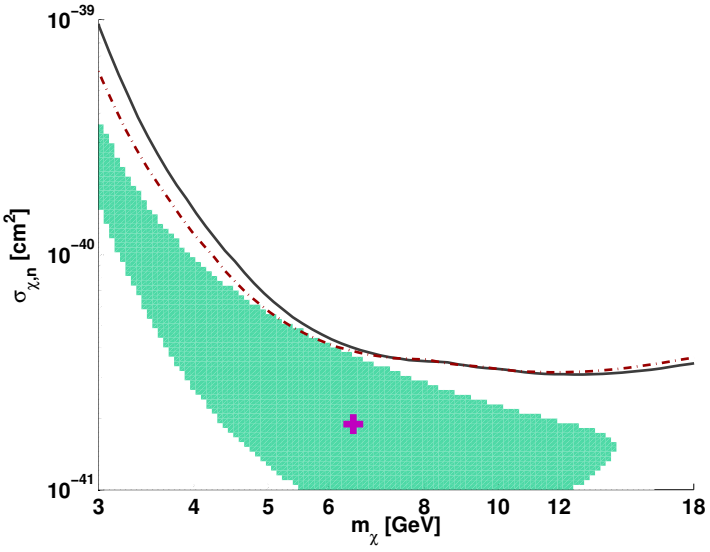

Figure 8.12: 90% CL log-likelihood contours for CDMSlite Run 1 data assuming a backgrounds are a flat Compton rate and 1.29 keV$_{ee}$ activation line. Also shown are the 90% CL limits derived with Lindhard (black curve) an CoGeNT yield (brown dash-dot curve). The best fit WIMP mass and cross-section are 6.6 GeV/c^2 and 1.9×10^{-41}cm^2.The contour was obtained from a mass cross-section grid search, hence the pixelation.

8.2.5 Spin Dependent limits

Most of the abundant Ge isotopes in the iZIPs have zero net spin. However ^{73}Ge (present at ∼7.73% level with 41 neutrons) can be used to set limits on spin dependent WIMP scattering. We compute the 90% CL sensitivity by assuming the interaction happens exclusively through coupling to either protons or neutrons.

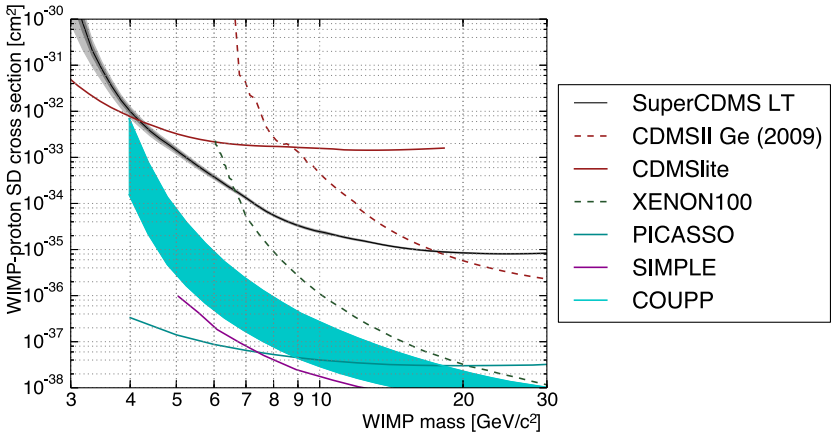

Figure 8.13: 90% spin dependent confidence limits, assuming 100% WIMP proton spin coupling.

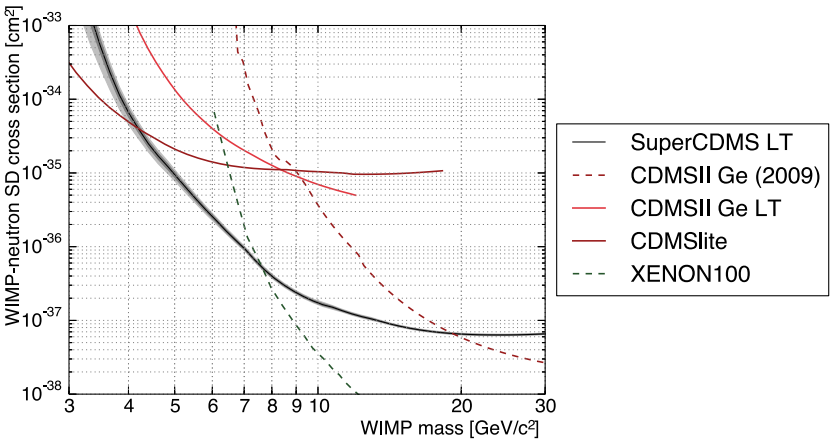

Figure 8.14: 90% spin dependent confidence limits, assuming 100% WIMP neutron spin coupling.

Chapter 9

Conclusions and Outlook

9.1 Conclusion

This thesis outlined the light dark matter problem and described CDMSlite as a novel experiment capable of very low detector thresholds. Utilizing the emission of Luke-Neganov phonons in drifting ionization, we were able to drastically amplify the strength of the ionization signals. Luke amplification of $\sim \times 24$, enabled us to operate a Ge iZIP detector with a threshold of 170 eV_{ee} (or 840 eV_{nr}) and baseline noise resolution of $\sim$14 eV_{ee}. With 6.25 kg-days of exposure, CDMSlite Run 1 was able to probe new light WIMP parameter space. While this first run demonstrated the power of CDMSlite, it also allowed us to identify key areas of improvement. I will conclude this thesis with discussions on these improvements, the prospects of CDMSlite Run 2 at Soudan, and finally the future of the CDMSlite within SuperCDMS SNOLAB.

9.2 Hardware improvements

9.2.1 Threshold reduction via noise monitoring

The WIMP energy spectrum is exponential and one benefits substantially from lower detector thresholds, see Fig. 2.8. In CDMSlite Run 1, the 170 eV_{ee} threshold was impressive, but the 14 eV_{ee} resolution indicates that further progress is possible. Low-frequency noise was the main problem, and reduction in this noise would allow for a significantly lower threshold. Low-frequency noise makes the noise distribution non-gaussian, Sec. 6.5.1, and resultantly causes a high rate of noise triggers ($\mathcal{O}(10)$ kHz compared to acceptable rates of $<\mathcal{O}(10)$ Hz). Thus for threshold reduction low-frequency noise must be identified and abated.

A primary source of microphonic noise was identified to be a cryo-cooler on the e-stem, used to reduce the heat from room temperature that would otherwise heat the detector electronics situated in the 4K and colder volumes. Two vibration sensors, a piezoelectric sensor and an accelerometer, were deployed to monitor cryo-cooler activity, see Fig. 9.1. In the inset of Fig. 9.1 the pumping system is shown. The motion of the pistons and valves in the cryo-cooler are the main source of low frequency noise. The noise monitors recorded periodic vibrations corresponding to the cryo-cooler period of 810 ms. To study correlation of iZIP phonon noise with this cycle, we designed electronics to amplify and trigger on the vibration sensor signals. Fig. 9.2 shows how noise monitor signals are electronically processed. This electronics chain digitizes the noise signals and stores noise trigger times in a history buffer. This allows for causal correlation analyses.

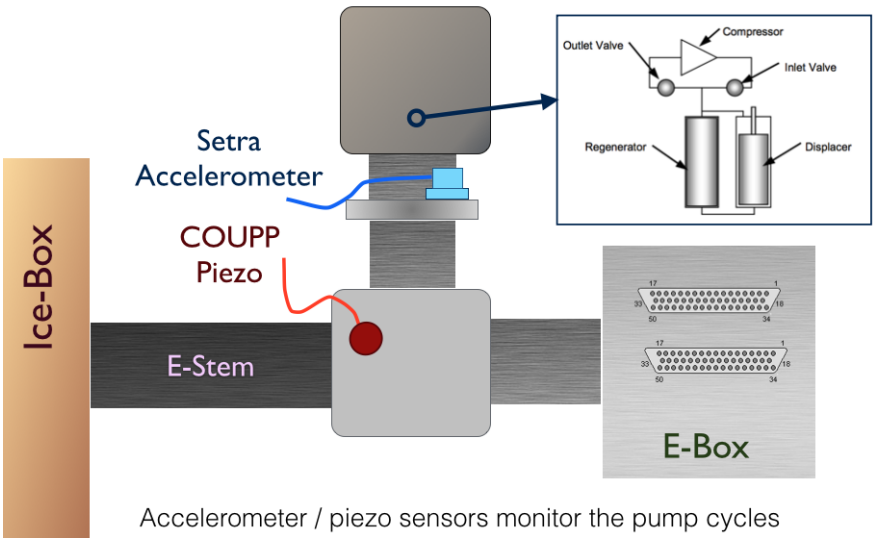

Figure 9.1: Gifford-McMahon cryo-cooler used to maintain electronics readout at low temperatures. The inset shows the internal pump mechanism. The noise monitor installation on the E stem is also shown.

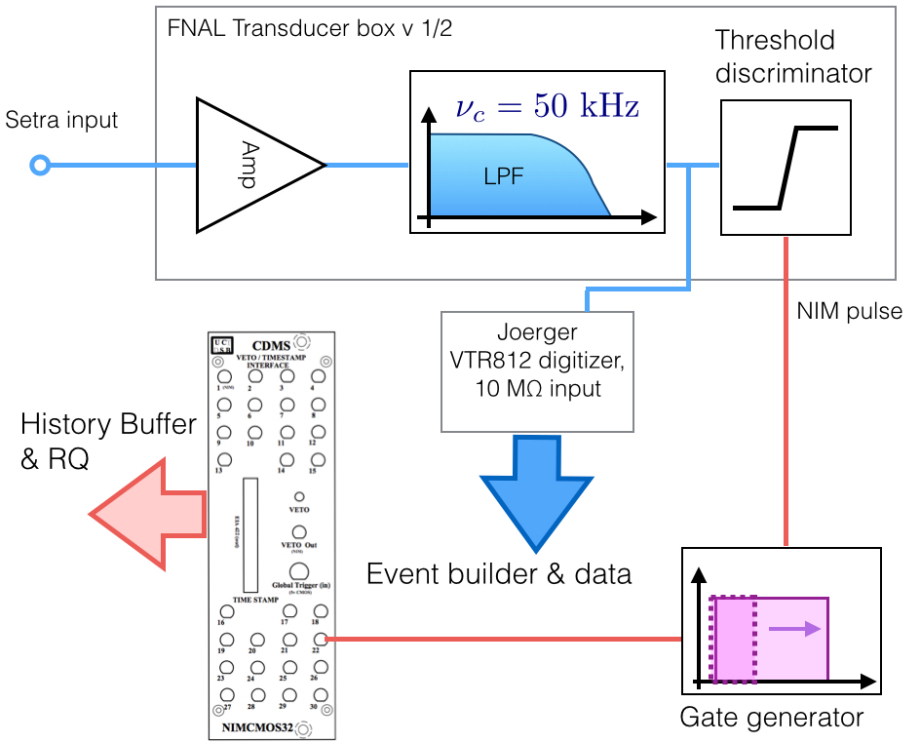

Figure 9.2: Schematic of electronics chain designed to read noise monitor signals, record time domain pulses and trigger time in history buffer. Sensor outputs are amplified and pass through a low pass filter. Following this, the signal is split with one output being digitized. The other output goes to a threshold discriminator which issues a NIM pulse when the signal is high. The NIM pulse is used to issue a time-stamp when the circuit triggers. This time stamp is accessible in the data stream as a reduced quantity (RQ) for further analysis.

From the cryo-cooler trigger time obtained via the electronics chain shown in Fig. 9.2, we construct a "time-since" variable (t_-). This variable is the time differential between a noise monitor trigger and a phonon trigger. It is the essential variable for studying noise correlations. Measured phonon energy as a function of time-since is shown in Fig. 9.3, and T5Z2 triggered events are highlighted. We note that the noise in T5Z2 has clear time correlated bursts.

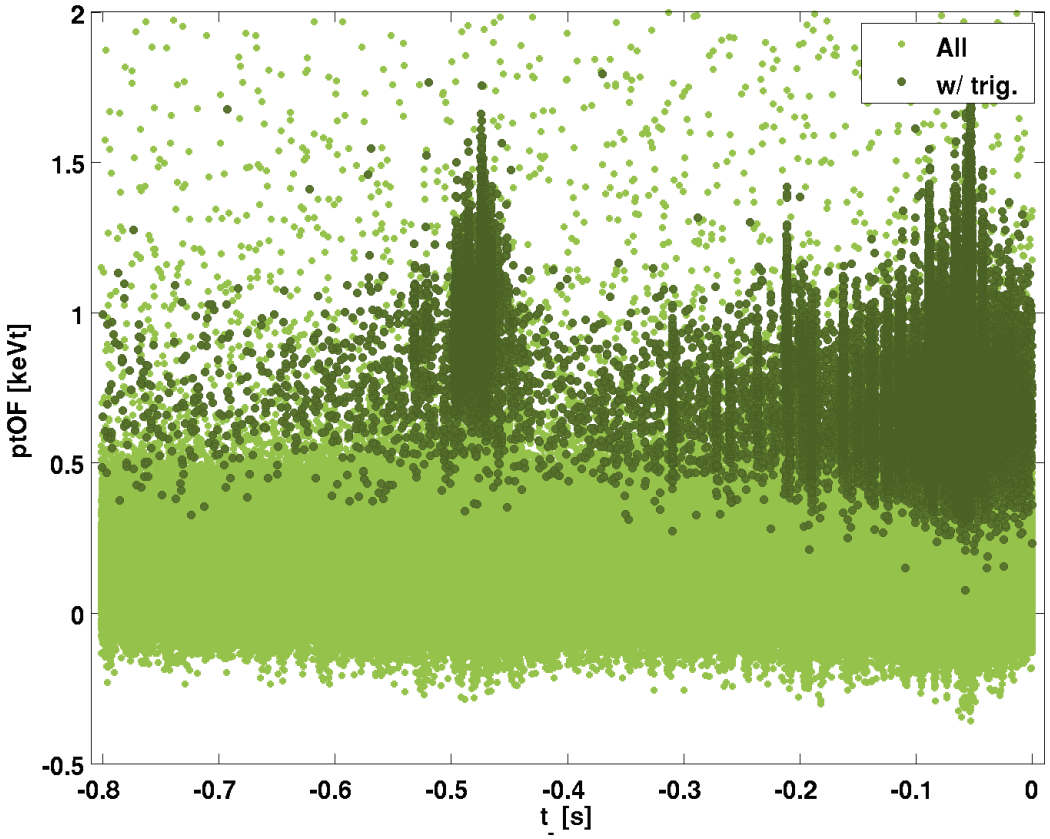

Figure 9.3: Total Phonon energy estimated via optimum filtering ("ptOF" in $\mathrm{keV_t}$ units) as a function of time-since (t_-) last cryo-cooler cycle. Since t_- is a look-back time it spans (-0.81,0) s. Instances where T5Z2 triggered are highlighted as dark green markers. Very clear correlation in periods of high noise are seen.

In Fig. 9.3 of phonon noise versus time-since, there are two marked periods of excess noise at $t_- \approx 0$ and -0.45 s, corresponding to the compression and rarefaction cycle of the cryo-cooler. From these data we compute the baseline resolution when the cryo-cooler is inactive ($t_- \ni ((-0.25, 0) \vee (-0.65, -0.45))$ s) which is[1] ≈ 0.11 $\mathrm{keV_t}$. For these runs T5Z2 had 70 V of bias, thus the base-line resolution expected after removing periods of high cryo-cooler activity is ≈ 9 $\mathrm{eV_{ee}}$. While official results will be presented in future publications, for Run 2 we have demonstrated another world leading low baseline resolution of $\lesssim 10$ $\mathrm{eV_{ee}}$ which implies a achievable trigger threshold of ~ 80 $\mathrm{eV_{ee}}$.

[1]The noise energy histograms are non-gaussian and these are approximate 1 σ estimates which have been rounded.

9.2.2 Current monitoring

The high voltage power supply used in biasing the CDMSlite detector has been improved, and it can now measure the current drawn. Thus for parasitic resistances which may cause time varying gains as discussed in Sec. 6.1.2, we will have a direct calibration handle. The corrections, instead of being empirical, can rather be *derived* from the measured bias current and voltage (I_b, V_b). If, following the bias resistor, some current leaks via time-varying parasitic resistances, then the effective detector bias may be modeled as $V_{\text{eff}}(t) = V_b - I_b(t)R_b$; and we can use this time dependent effective bias for the Luke gain.

9.3 Software improvements / background analysis

The Run 1 exclusion limits were computed in a conservative manner by assuming all events were nuclear recoils. In attempting to account for two known electron recoil backgrounds, the flat Compton rate and the 1.29 keV_{ee} activation line, in a log-likelihood approach, we saw that the low energy excess was picked up as a WIMP-like signal, Fig. 8.12. The KS-tests mentioned in Sec. 8.1.1 indicate that this excess is likely some background, especially since the SuperCDMS-LT results [113] rule out the best fit WIMP model. The source of this background must be understood before future improvements in low-mass WIMP sensitivity are possible.

9.3.1 Electric field anisotropy

In CDMSlite we measure the total phonon energy. To better understand the measured spectrum we need to factor in details of detector physics more accurately. Consider the electric field geometry for the one-sided basing scheme used in Run 1, as shown in Fig. 9.4.

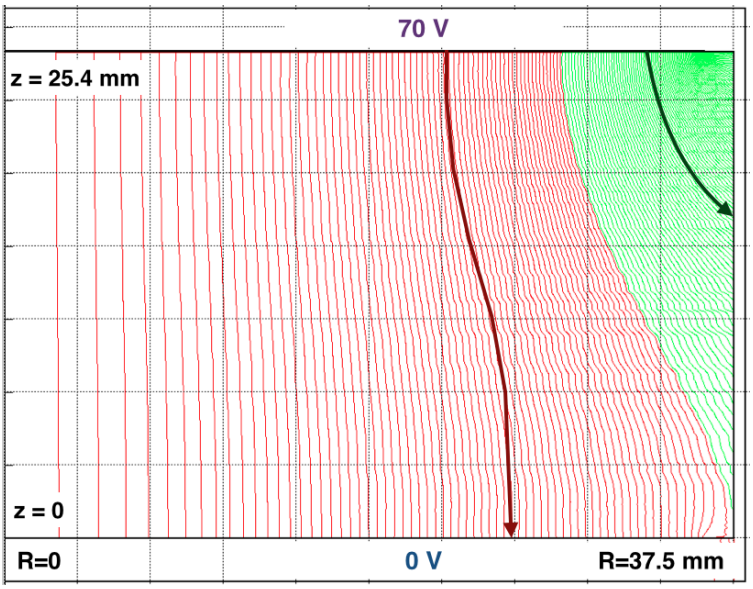

Figure 9.4: Electric field geometry for 1 sided CDMSlite operation with 70 V / 0 V on top / bottom. Field lines terminating on bare Ge wall are colored in green (25%), and field lines connecting both faces in drawn in red (75%). Thus an ionizing event happening in the green area will have <100% Luke gain.

From the field geometry it is clear that ionizing events at high radii near the biasing side will not experience 100% Luke gain. Hence if we uniformly illuminated the iZIP with 10.36 keV_{ee} photons, then after averaging over all photons, a peak at 10.36 keV_{ee} does not translate to a peak at $10.36 \times (1 + eVb/\varepsilon_\gamma)$. Instead there is a "bump" at $10.36 \times (1 + eVb/\varepsilon_\gamma)$ that ramps down continuously to lower energies, as some events traverse potential drops $< V_b$.

The electric field simulations can be used to generate position dependent gain maps, whose ultimate effects may be empirically modeled via energy smearing. The measured spectrum, after calibrating for absolute gain (i.e. dividing by the expected gain of $(1+eVb/\varepsilon_\gamma)$), will be a smeared form of the input spectrum. Fig. 9.5 shows the effect of such smearing on the Ge activation lines (K-shell line at 10.36 keV_{ee} and L-shell line at 1.29 keV_{ee}). In this figure two smearing functions are shown corresponding to two locations in the crystal, and they set the expectations of how much low energy excess may be produced from electric field anisotropies. We note that if the Compton spectrum is not identically flat, then such smearing will necessarily produce further skew of the measured spectrum at low energies.

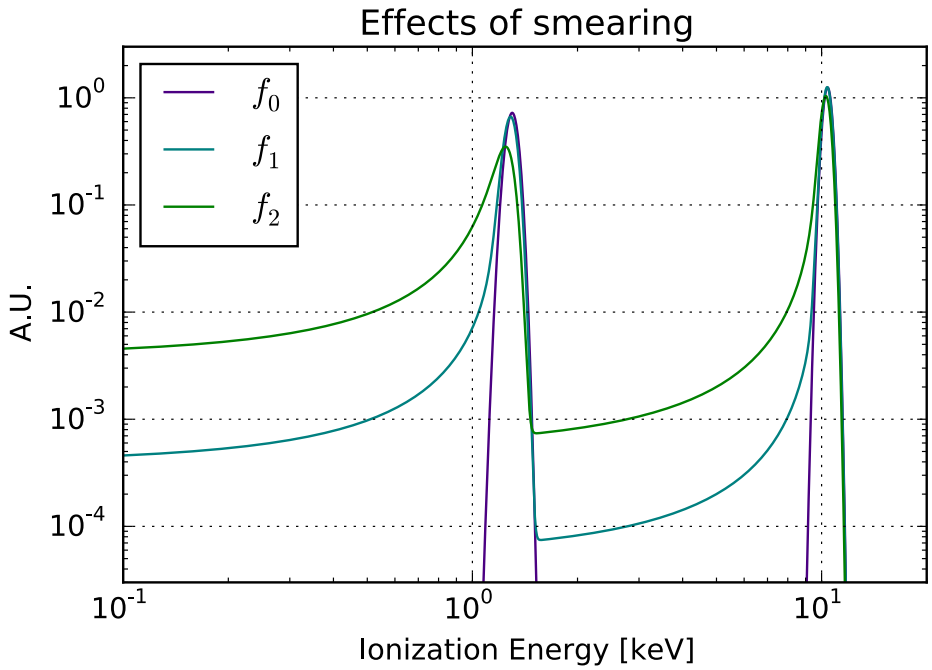

Figure 9.5: The smearing effect of position dependent Luke gain on measured spectra. The input spectrum has two Gaussians representing the known K and L-shell lines at 10.36 keV_{ee} and 1.29 keV_{ee} respectively; this is designated f_0. This is convoluted with two representative smearing functions derived from electric field simulations such as the one shown in Fig. 9.4, and the final smeared spectra are f_1, f_2. The two functions correspond to two locations in the crystal, f_2 showing maximal smearing and f_1 showing the expected average smearing.

With this understanding of detector physics it is likely that the excess rate at low energies in Run 1 data was due to detector effects. This study has to be formalized and these demonstrative models will be improved via proper detector Monte Carlo efforts, which are under development. This future project will be a part of the Run 2 analysis.

9.3.2 Fiducialization

Following the Run 1 analysis, we undertook analysis to to better define bulk recoil events, and distinguish them from the more problematic surface recoils. Events near the detector boundaries suffer from various systematics related to charge trapping and reduced Luke amplification. Recall that the iZIPs have an outer ring of phonon sensors and three inner phonon sensing channels. The energy measured from these can be used to create a phonon radial partition variable, prpart ≡(Phonon energy in outer channel)/(Total phonon energy). The radial energy distribution is shown in Fig. 9.6.

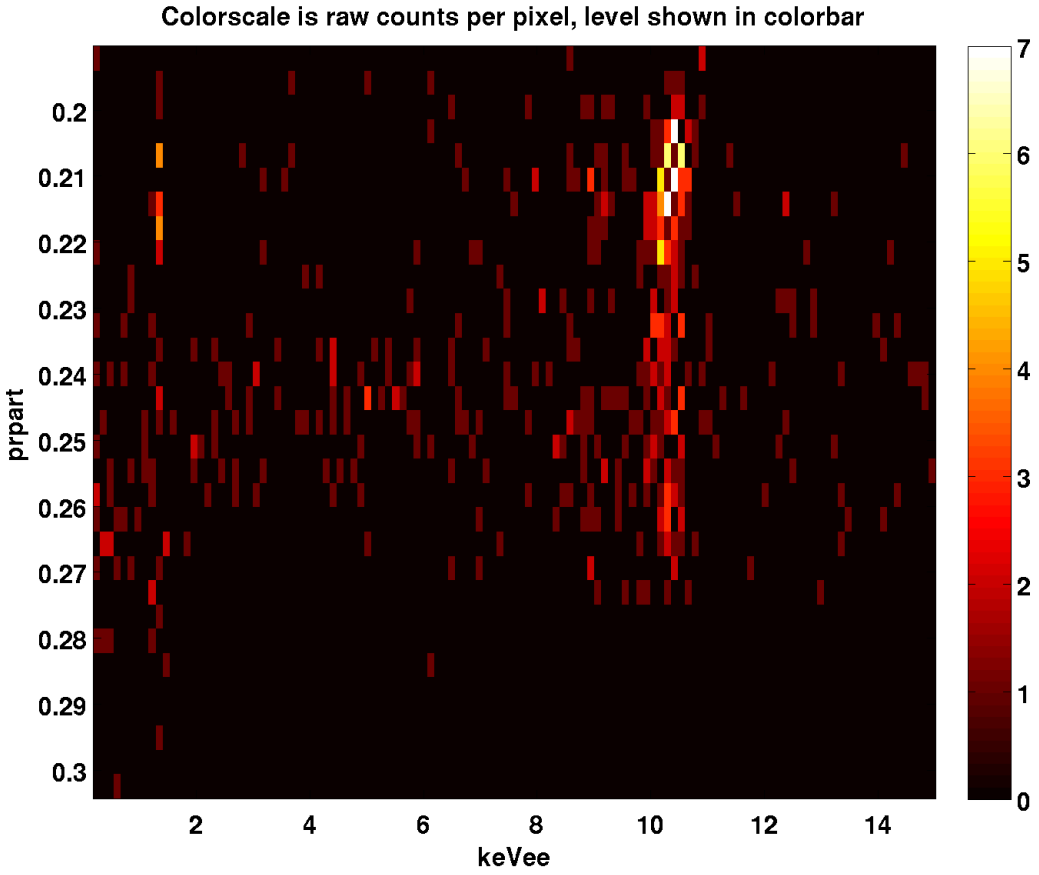

Figure 9.6: Radial partition of phonon energy as a function of total phonon energy. Radial partition or prpart is the ratio of the phonon energy collected in the outer ring sensor to the total energy deposited. Here we clearly see the activation lines indicating much of the electron recoil backgrounds are at high radii, i.e., prpart > 0.23

In Fig. 9.6, following the activation lines at 1.29 and 10.36 keV_{ee} it appears that most of the electron recoilbackgrounds are at high radii. Thus if we apply a crude fiducial volume cut of prpart > 0.23, we will be suppressing background contributions to the data. The challenge is in understanding the efficiency of such a fiducial cut at low energies. A further complication arises from position dependence of Luke gain described in the previous section. Dedicated detector Monte Carlo efforts will be pursed to understand and utilize fiducial selection cuts in the near future.

9.4 Run 2 benchmarks

9.4.1 Live-Time projections

A second CDMSlite Run was done with the hardware improvements mention earlier to not only collect data at lower energies, but also to obtain higher statistics so that rigorous low energy background modeling may be pursued. The running time for Run 2 has been over four months. The detectors were pre-biased and no more time is lost to initial leakage current. In this scheme before data taking the detector is maintained at an over-voltage (intended bias + 10 V) for 10 minutes for trapped charges to equilibrate. The primary loss in live-time will be from removing time periods of high cryo-cooler activity, estimated to be a ∼25-30% loss. For WIMP sensitivity, purely in signal strength, we gain exponentially in reducing thresholds and lose linearly from reducing live-time, thus ultimately Run 2 will be a big improvement of the science reach. Coupled with the 70% experiment live-time, CDMSlite Run 2 should yield about 60 live-days of data..

9.4.2 Efficiencies and Background rate projections

The analysis efficiency is expected to be dominated by the muon veto cut and multiple scattering cut, leading to a overall efficiency of ∼98%, much like Run 1.

It is difficult to estimate background rejection efficiency until the work is done to correctly model the position-dependent Luke gain. Nevertheless, I will provide some rough projections and leave the more accurate studies for future publications.

We measured a flat Compton rate of 1.5 Counts/ keV_{ee}/ kg / day in Run 1 at high energies. For 2 months of live-time and a 3 keV_{ee} energy range[2] we thus expect $\sim$ 162 Compton recoils. Let's assume that signal plus background modeling is able to suppress backgrounds up to Poisson fluctuations. We thus expect $\sqrt{162} \approx 13$ events uniformly distributed in the 3 keV_{ee} range. Along with the Compton recoils, the 1.29 keV_{ee} activation will also provide photons. Following Run 1 results presented here and other SuperCDMS studies, this line can be approximated via a Gaussian with amplitude, μ and σ of $\sim$ 6.1 Counts/ keV_{ee}/ kg / day , 1.29 keV_{ee} and 40 eV_{ee} respectively. From this simple model we can proceed to compute the expected science reach of Run 2 [3].

9.4.3 WIMP sensitivity projections

Fig. 9.7 shows optimal interval limits using mock spectra from the background model described in the previous section. If the background model is found to have larger systematics with energy than assumed, the limits will degrade. Thus Fig. 9.7 gives an indication of the best that we are likely to achieve with CDMSlite Run 2 at Soudan. We look forward to the analysis of the Run 2 data and hope to probe the light WIMP parameter space with greater sensitivity.

[2] We are interested in light WIMPs, hence energies over 3 keV_{ee} do not gain us much in terms of sensitivity.

[3] Corresponding to the K and L shell X-rays we also expect an M-shell line at 160 eVee. The amplitude is ∼10% of the L-shell line. Since this is a fairly small number and since we are unaware of the total activation of Run 2 yet, I disregard the M shell line here; although I look forward to our first measurements of this feature!

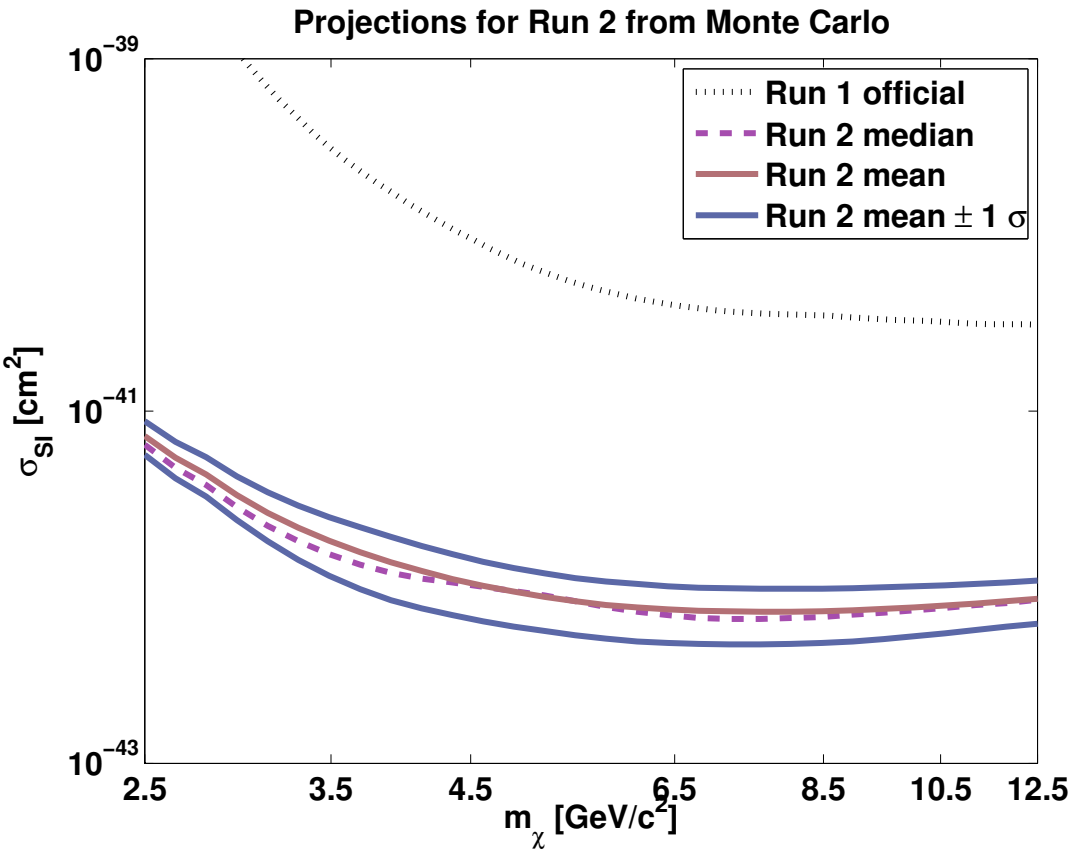

Figure 9.7: CDMSlite Run 2 projections as optimum interval limits computed from mock spectra with 80eV_{ee} detector thresholds and two months of live-time. The backgrounds are modeled as Poisson fluctuations of Compton recoils and the 1.29 keV_{ee} activation line, following tentative background subtraction.

9.5 CDMSlite with SuperCDMS SNOLAB

As a key next generation direct detection experiment, SuperCDMS will start operations at SNOLAB in the next few years. The main improvements at SNOLAB over Soudan will be drastic reduction of backgrounds from going deeper underground and from using construction material with much lower radioactivity. Furthermore, the net detector mass at SNOLAB will be larger than Soudan, currently estimated at ∼50 kg with both Ge and Si iZIPs and a whole tower dedicated to CDMSlite style high-voltage low-threshold operations.

We are optimistic that newer schemes of high voltage testing will drastically improve the low energy reach; particularly efforts where better integration of readout and biasing electronics allowing for CDMSlite modes where both sides of an iZIP are read out. This naturally leads to a $\sqrt{2}$ noise suppression. Further improvements in the biasing circuit and guard rings may also lead to better shaping of electric fields thus abating the issue of energy smearing, reducing the low energy background contamination discussed in Sec. 9.3.1. Finally fundamental advancement of the TESs sensors will lead to better overall energy resolutions.

The preliminary projections from SuperCDMS SNOLAB are shown in Fig. 9.8. Here for the CDMSlite / high-voltage (HV) limits, we expect to have lower intrinsic detector thresholds from optimized phonon sensors and higher gains from having larger detectors [90].

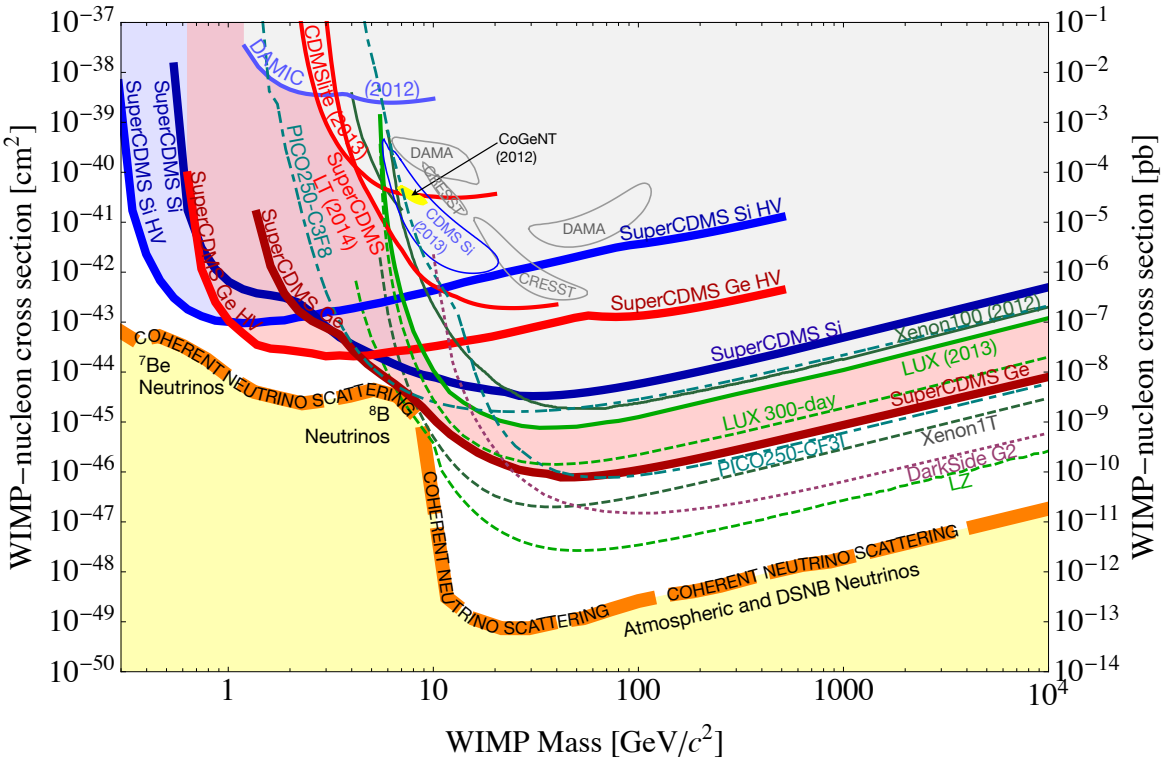

Figure 9.8: Expected WIMP sensitivity projections from SuperCDMS SNOLAB [90]. Newer iZIPs optimized for CDMSlite (HV) operations along with lower backgrounds and detector thresholds allow for orders of magnitude improvement in WIMP sensitivities.

Standard direct detection experiments (SuperCDMS, LZ, PICO etc.) will ultimately be limited by coherent scattering of solar, atmospheric and diffuse supernova neutrinos. Here the CDMSlite / SuperCDMS-HV experiments will have the extraordinary power of being sensitive to the coherent scattering of ^{8}B neutrinos, the measurement of which will in itself be a major scientific accomplishment. Our principal hope is directly detecting dark matter before we approach the neutrino floor. An exciting and revelatory future lies ahead !

Appendix A

The Biasing network for the CDMSlite adapter board

In the hardware section for CDMSlite I described a particular adapter board being used to properly float one side of an iZIP at the desired high bias while reading out phonon and charge signals from the other side. As mentioned there in Fig. 5.5, there is a biasing resistance network on every iZIP adapter board.

A.1 Design of High-Voltage Bias Network

To start, consider the ionization read out circuit shown in Fig A.1.

We see that the electrodes are capacitatively coupled to the amplifier. Furthermore the coupling capacitor has 40 MΩ resistors on the bias and feedback ends. Now this coupling capacitor cannot withstand more than ∼30 V across it. Thus while we attempt to put twice or thrice that voltage on one side of an iZIP, we should take care to not damage this capacitor. Primarily because it sits in the icebox and cannot be replaced without dismantling the tower.

This means that all connections that are not the charge bias or feedback lines, should have identical impedances. This is also to ensure uniform electric field across the biased side of the detector. Finally the FET (in the same circuitry) requires heaters, as at 4 K the charge carriers freeze-out. Since the heaters are not required here, we simply disconnect them. So all in all the biasing network has four types of resistors: 0 Ω for all charge bias and feedback, breaks for FET heater lines and 40 MΩ for all others.

Finally, barring these "local" protective measures, an important "global" protective measure is imposed: all the connected lines go through a large load or bias resistor to the power supply. The necessity for this is best seen in a simplified version of the main circuit by considering the possibility of an internal short to ground at some point following the coupling capacitor on the feedback line, see Fig. A.2. In the limit that the short is 0 Ω, the voltage drop across the capacitor is $V_{\text{bias}}\left(1 - R_{\text{load}}/\left(R_{\text{load}} + R_{\text{bias}}\right)\right)$. Conservatively limiting the drop to 10 V, necessitates $R_{\text{load}} \geq$ 360 MΩ. In practice the desired resistances were not available in stock with the correct footprint, and thus we approximated them. The following schematic summarizes the bias resistance network as used on the first generation of adapter boards.

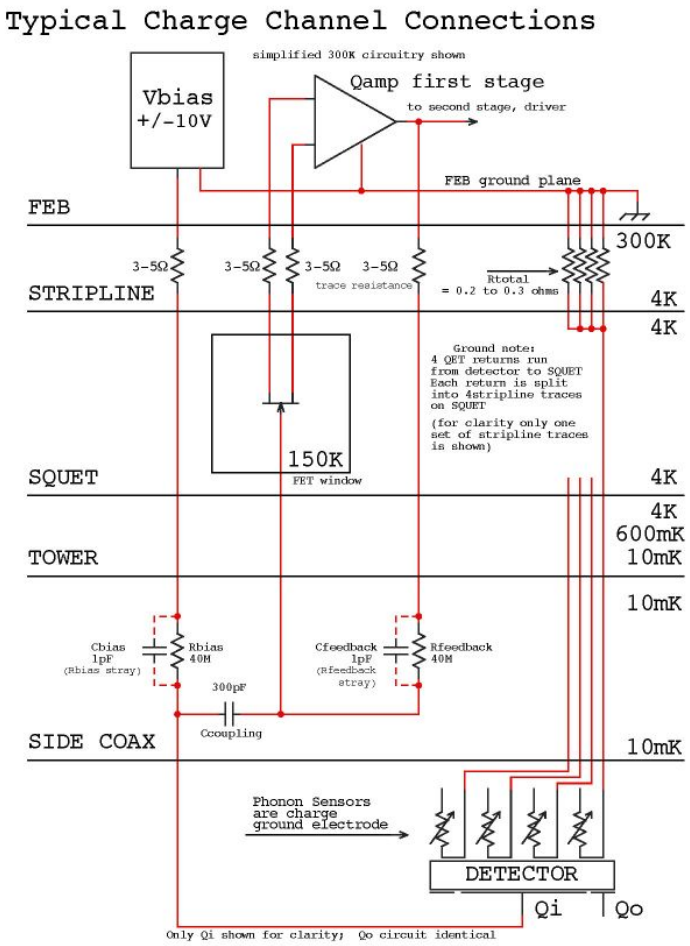

Figure A.1: Circuit for operating and reading charge electrodes

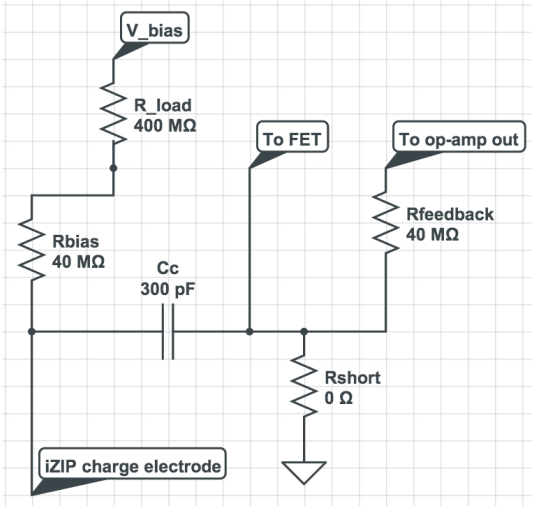

Figure A.2: Charge circuit with potential short on feedback end. Note we want to ensure that the potential across the coupling capacitor is under 30 volts at all times. Therefore a short like this necessitates a larger bias resistor (called **R-load** in this schematic)

Following all this, the last protection was to paint the adapter board with *humi-seal*, a highly resistive epoxy coating to prevent any accidental onboard shorts. With this adapter board ready

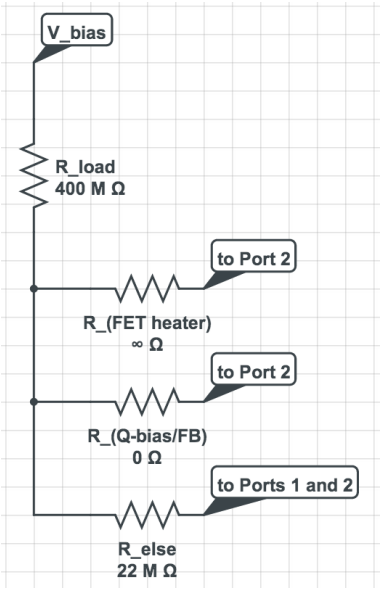

Figure A.3: Summary of all resistors used in biasing network for the first generation of iZIP adapter boards.

we proceeded to operate and iZIP in CDMSlite mode.

A.2 Humi-seal blues

During the first trials of the CDMSlite at Soudan, we saw that several lines that were supposed to be disconnected were not, and resistances of at the level of $\sim$5 M Ω/cm. This humi-seal epoxy had degraded with time, acquired a blue hue[1] and had become conductive. To understand why this resistance limits operation, note the resistances of the on-board biasing network described in the previous subsection. Thus the first step involved mechanically removing this coating.

The data from Run 1 showed that having no humi-seal exposed the board to humidity which lead to voltage drops (via parasitic resistances from moisture and dust), and an effective variation of $\lesssim$10% in energy scale 6.1.2. For Run 2, we cleaned these boards in an ultrasonic bath, baked them overnight and applied a better court of humi-seal, which shows $> \times 10$ increase in parasitic resistances. As tested with a Keithley source meter, currents of $\sim$20 pA were measured with 96 V of bias, implying parasitic resistances $> \mathcal{O}(100)$ GΩ; compare this to $\mathcal{O}(10)$ GΩ for the Run 1 setup.

[1] Pun-intended with the title !

Appendix B

Theory of initial leakage current

The physics of leakage current can be understood by considering how trapped charges can behave in applied electric fields, following Fig. B.1. The theory of charge trapping has been dealt with in depth by Sundqvist in chapter 5 of Ref. [107]. For the simplest case consider a positive trapping site for electrons (ex: Singly charged states may be formed from neutral capture and they remain in stable equilibrium at the low temperatures of ∼50 mK, see Sec. 5.2 of [107]). Electrons trapped here can be tunneled out by shifting the potential in the vicinity with an applied electric field.

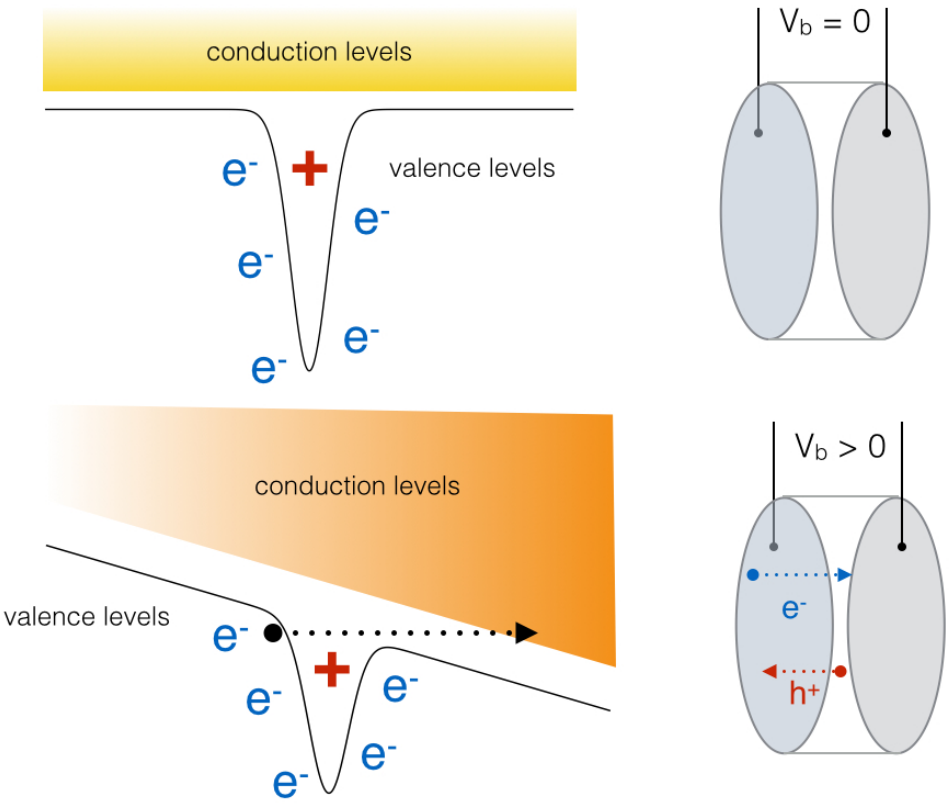

Figure B.1: A sketch demonstrating how electrons stuck on a positive charged trap can tunnel out on application of a constant electric field i.e. by applying non-zero bias voltages. This is merely a first order demonstration. Other complicated processes such as impact-ionization can further effect the nature of trap clearing in the presence of electric fields.

In principle we can find a time constant (τ_{TC}) and leakage-current(I_L) for such trap-clearing processes. Assuming a uniform electric field, the time constant can be found by calculating,

$$\tau_{TC}^{-1} \approx \left(U(\vec{r}) + e\vec{F} \cdot \vec{r} - e\vec{F} \cdot \{\vec{r} + \delta\vec{r}\} \right) / \hbar \tag{B.1}$$

Here $U(\vec{r})$ is the average energy per trap and $\vec{F}$ is the applied electric field and is proportional to bias voltage. The escape rate is thus dependent on the drop in potential across some small distance δr, in the direction of the potential floor. This is closely related to polarization / barrier radii which is described in equations 5.54 / 5.39 from Ref. [107]. Furthermore we can pursue simple WKB approximations to obtain the tunneling probability as,

$$\mathcal{T}(F) \approx \frac{e^{-2g(F)}}{\left(1 + 0.25 \times e^{-2g(F)}\right)^2} \tag{B.2}$$

Here $g(F) \propto \int dr \sqrt{U'(r,F) - E}$, where E is the energy of the charge particle that is tunneling out, and $U'(r,F)$ is the potential model shown in lower case in Fig. B.1. The key point is due to the applied field, this potential decreases with distance (parallel to electric field) and its gradient on average scales with field strength viz. $\langle \partial_r U'(r,F) \rangle \propto F$. It's worth pointing out that such effects are only expected for $F \gg 1$ V/cm. Recall that the average photon energy required to excite a charge pair (in equilibrium) is ε_γ =3 eV. Thus for a crystal that is 2.5 cm thick, we must have a gradient sufficiently larger than 3 V/2.5 cm or $F \gg 1$ V/cm, making this discussion pertinent to CDMSlite.

If one can calculate these quantities then the leakage current follows as, $I_L \approx \int d^3r \; e \; n_T \; \mathcal{T} \; \tau_{TC}^{-1}$, where n_T is the density of trapped charges. Now there is time dependence to this mechanism. In an adiabatic limit where the transmission coefficient and rate of trap clearing is constant, the current should exponentially decrease with time. This is easily seen if we express the above relations with volumetric current[1] ($j_L = -\partial_t \; e n_T$),

$$j_L = -\partial_t \; e n_T \approx e \; n_T \; \mathcal{T} \; \tau_{TC}^{-1} \tag{B.3}$$

The solution to $n_T(t)$ is therefore an exponential falling with time. The current is simply $I_L(t) = \int d^3r j_L(t, \vec{r})$ and thus it is also expected to decay exponentially with time.

While calculating this current, the spatial average is difficult to evaluate given the non-linearity of the potentials and the density of charge traps. This is only a first order estimate and can have non-trivial higher order corrections, particularly when we consider the probabilities of re-trapping and impact-ionization amongst other things. Re-trapping refers to the possibility that a charge that clears a shallow trap can get stuck in a deeper trap later on, resulting in a diminished current, see Fig.B.2. Impact ionization acts in opposite, where a charge that cleared a trap gathers enough kinetic energy to impact other trapped charges enhancing their tunneling probabilities, and increasing this current, see Fig.B.3.

[1] Since we are draining trapped charges, the time derivative carries an explicit negative sign.

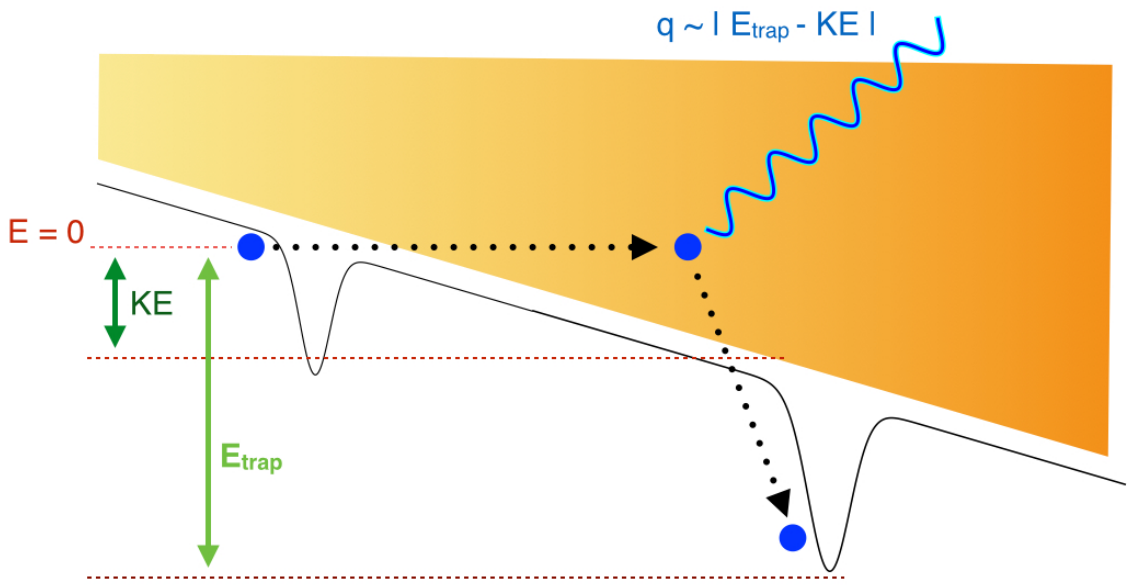

Figure B.2: A sketch demonstrating how an electron tunneled out by the applied field, can "fall" into a deeper trapping site via phonon emission (blue wavy line); such a process reduces the rate of leakage current.

Fig. B.3 shows a sketch of impact ionization. An electron (red) is tunneled out, gains sufficient kinetic energy to impact and knock out successive electrons in shallow traps (blue and purple).

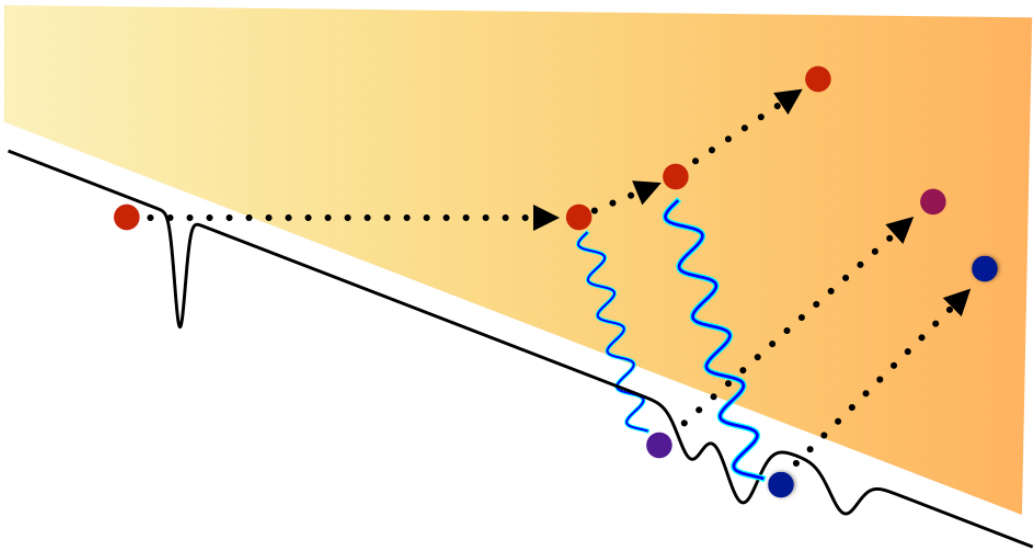

Figure B.3: A sketch demonstrating production of ionization via impacts (phonon exchanges shown by blue wavy lines) from electrons that tunnel out, drift and gain sufficient kinetic energy. Such cascade like processes can enhance the rate of leakage current.

The combination of these varied many-body phenomena forces such calculations to be out side the scope of this thesis. This section simply argues from basic physics, why CDMSlite detectors should have an initial leakage current that settles with time, and how the expectations are crudely matched by measurements.

Appendix C

Algorithm for calibrating total phonon energy to ionization energy

CDMSlite is an ionization only experiment and our main energy scale is ionization energy or keV_{ee}. To calibrate from keV_{t} to keV_{ee} units we need a map $\mathbf{f} : E_{\text{t}} \rightarrow E_{\text{r,ee}}$ following Eq. (4.3). Due to Luke-gain fluctuations, the time dependent map is, $\mathbf{f}(\text{time}) \equiv 10.36/E_{\text{t}}(\text{time})$. The intensity of 10.36 keV_{ee} photon emission is typically low ($\lesssim$ 10 counts/day/iZIP), thus time here has to be coarsely discretized. We implemented the following algorithm:

- Coarsely discretize time in sets of four consecutive non-overlapping series. There are 144 series leading to a set of time bins $\mathbb{T} = \{t_n \ : \ n = 1 \ldots 36\}$.
- For each $t_n \in \mathbb{T}$, consider events with total-energy $150 > E_{\text{t}}[\text{keV}_{\text{t}}] > 90$. This brackets the expected and observed region of interest for the K-shell γs. Histogram the event energies and find the mean ($\mu_K(t_n)$) and width ($\sigma_K(t_n)$).
- Fit low order polynomials (avoid overfitting) as a function of time t (time-stamp of event in seconds) to the data points within $\mu_K(t \in \mathbb{T}) \pm \sigma_K(t \in \mathbb{T})$; call this $\bar{E}(t)$. Note that $t \in \mathbb{T}$ is causally ordered.
- The map is then obtained via polynomial rescaling, $\mathbf{f} = 10.36 \times \bar{E}^{-1}(t)$. This map when applied to any event, say event # j, converts the measured total-energy $E_{\text{t}}\ [j]$, using the event's time-stamp $t\ [j]$, to a calibrated $E_{\text{r,ee}}\ [j]$ given by $E_{\text{r,ee}}\ [j] = \ \mathbf{f}\{E_{\text{t}}\ [j],\ t\ [j]\} = E_{\text{t}}\ [j] \times 10.36 \times \bar{E}^{-1}(t = \ t\ [j])$.

Instead of one continuous polynomial spanning the whole run, we split the entire period into 4 segments (black vertical lines in figure C.1). This was done since some periods (ex: green points in Fig. 6.3) clearly benefit from a quartic polynomial rescaling, while other periods could be calibrated with a simple constant (blue points in Fig. 6.3). This piecewise polynomial $\bar{E}(t)$, along with the $\mu_K \pm \sigma_K$ bands are shown in figure C.1.

Figure C.1: Fit to time variance of the K-shell photon energies. Gray markers show data following Fig. 6.3. Coarse discretization of time ($\mathbb{T}$) and the statistical bands $\mu_K(t \in \mathbb{T}) \pm \sigma_K(t \in \mathbb{T})$ are shown with magenta lines. The piecewise polynomial $\bar{E}(t)$ is shown with solid colored lines. Three colors (red, green, blue) correspond to three major run periods, each bounded by solid vertical black lines. The first run period is split due to different activation levels (hence K-shell γ intensities) following the first neutron calibration. The first part has a constant scaling and the second a quadratic. This splitting is represented by the dashed vertical black line. The following two periods (blue and green) receive quartic and constant scaling respectively.

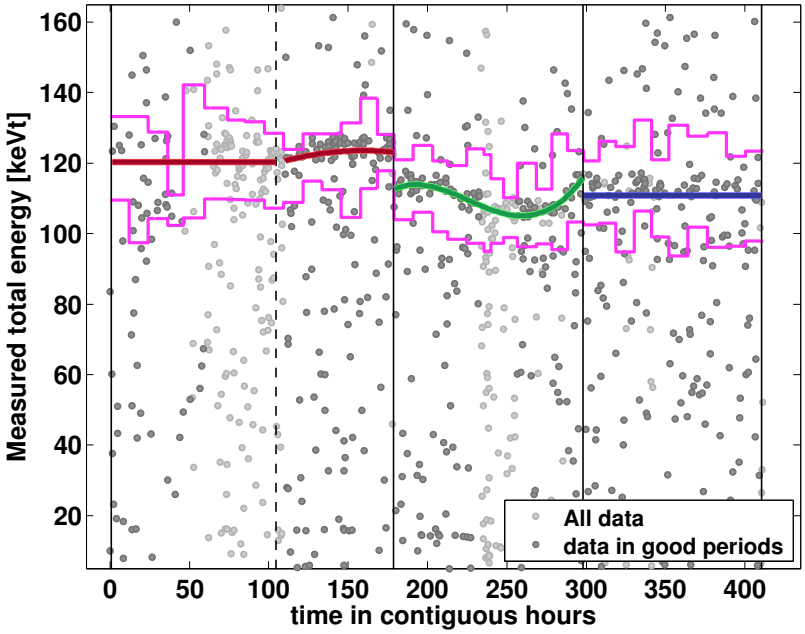

Appendix D

The Pulse + Noise Monte Carlo

This section describes a Monte Carlo simulation technique for adding pulses of varying amplitudes and shapes to a data-base of noise events, and testing how a cut performs on these simulated events. Several versions of this technique were developed over time. I will first outline the scheme in general and then comment on the details behind each version.

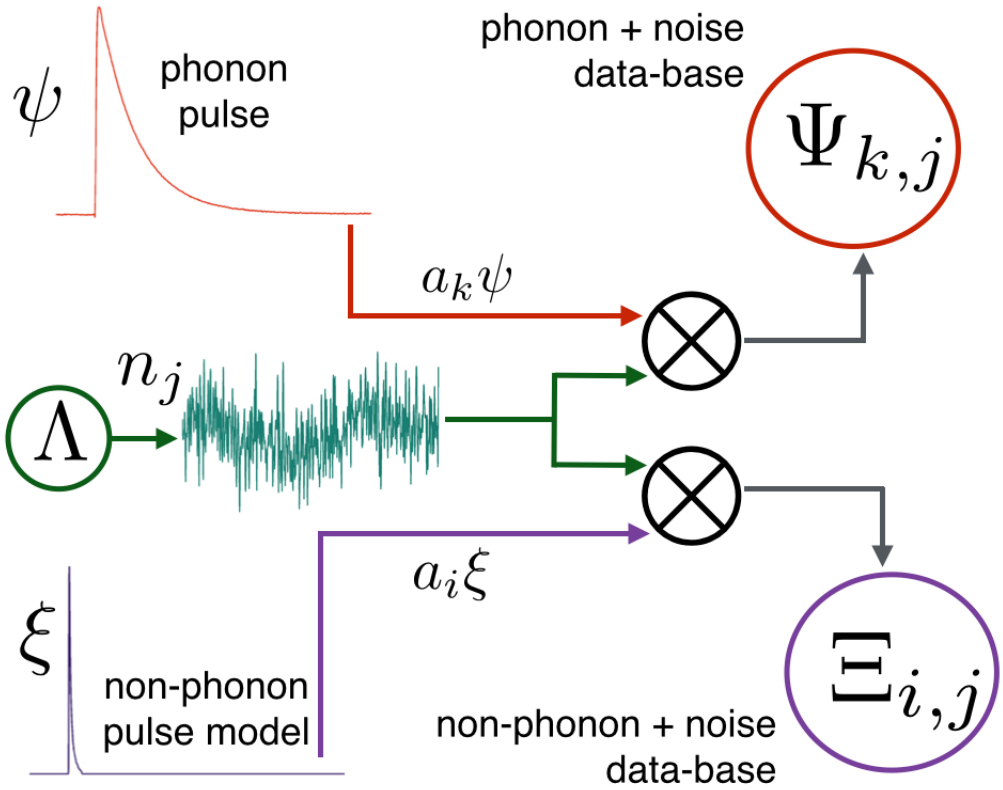

Figure D.1: Schematic for the generating pulse + noise data bases.

For the description in this section, I will use the following notations: ψ is a model for a phonon pulse (red pulse in Fig. D.1) , ξ is a model for a non-phonon pulse (such as glitches, purple pulse in Fig. D.1), and n represents noise events (green pulse in Fig. D.1) . In general noise events are directly selected from a data-base (Λ) of randomly triggered low-amplitude/ noise events[1]. Both ψ

[1]Since in WIMP-search mode physics events are rare, randomly triggering gives us good noise samples.

and ξ are of unit height and n's are as recorded. To test a selection or rejection cut we first choose an energy spectrum (probability distribution), $\mathcal{A}$, to study cut performance for a desired distribution of energies. In the simplest case this is a uniform distribution. Then for randomly drawn amplitudes $\{a_i \in \mathcal{A} \mid i = 1 \dots M\}$, and noise events $\{n_j \in \Lambda \mid j = 1 \dots N\}$ we make M × N, MC event sets: $\Psi = \{a_i\psi + n_j \mid i = 1 \dots M,\ j = 1 \dots N\}$ and $\Xi = \{a_i\xi + n_j \mid i = 1 \dots M,\ j = 1 \dots N\}$.

Suppose we want to test a cut $\hat{\mathcal{C}}$. If this is a good selection cut, then in principle $\hat{\mathcal{C}}[\Psi_{i,j}] = \mathbf{1}$ and $\hat{\mathcal{C}}[\Xi_{i,j}] = \mathbf{0}$ for all $\{i,\ j\}$ pairs. However in the low energy limit, $a_i \lesssim \sqrt{\langle n_j^2 \rangle}$, the classification power of this cut decreases[2]. For every unique amplitude a_i we find the power of good-event selection by computing $\mathcal{E}_{\hat{\mathcal{C}}}(a_i) = \sum_j \hat{\mathcal{C}}[\Psi_{i,j}]/M$. Assuming binomial trials, one can compute the error[3] on this efficiency estimate as $\pm(1-\alpha/2)\sqrt{\left(\mathcal{E}_{\hat{\mathcal{C}}}(a_i) - \mathcal{E}_{\hat{\mathcal{C}}}(a_i)^2\right)/M}$. Here α the error percentile is typically fixed at 5%, i.e., we compute results at 95% confidence level. This strategy can be applied identically to the set of non-phonon pulses, to find the efficiency of this cut in tagging such non-physics events. This scheme also allows for calculating passage fractions on mixed data, i.e., without discriminating between phonon, non-phonon and noise pulses, to mimic real data sets. In such cases the cut is evaluated on $\Psi \oplus \Xi \oplus \Lambda$, where relative event populations can be varied.

D.1 Version for low-frequency tests

This version was designed to study how good pulses can be separated from spurious triggering events, particularly low-frequency noise, [153]. For good events the relative location of a recoil to a phonon channel introduces systematic bias in the rising edge of the phonon pulse. If the event happens close to the surface, then the closest TESs absorb more power than the farthest ones, thereby making the pulse rise quicker and have a smaller rise-time, see D.2.

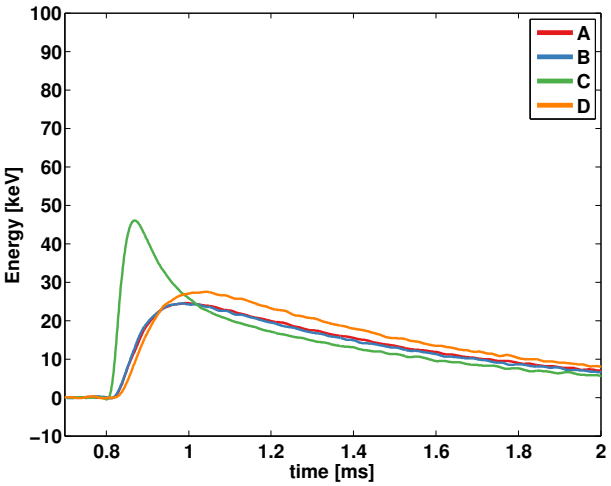

Figure D.2: A recoil primarily under channel D on Side 1 of T5Z2. Note the difference in pulse shapes between channels, particularly the steep rising edge of the primary phonon pulse (D).

[2]Here a_i is a number, but n_j, a noise-trace, is a time series.

[3]This is the normal approximation error, which works in the large sample approximation. In MATLAB Clopper-Pearson intervals are generally calculated with `binofit`, at 95% confidence level.

Constraining the 10-100% rise-time of the phonon pulse from a primary channel, allows us to differentiate good events from low-frequency noise, see the comparison presented in Fig. 7.11 and Fig. 7.12. To test this idea, a pulse+noise MC was performed. From the main text, Sec. 7.2.1, recall that we want to simulate primary phonon pulses for studying $\Delta_{\mathrm{rt,prim}}$ and the total phonon pulse for studying $\Delta_{\mathrm{ft,pt}}$. To simulate these we had to understand the manner in which the primary channel's pulse shape and energy varied with respect to the total phonon pulse and it's energy. To gauge energy variation, we first consider the fraction of total-phonon energy that the primary channel contains, defined as $f_{\mathrm{prim}}(E_t) = E_{\mathrm{prim}}/E_t$.

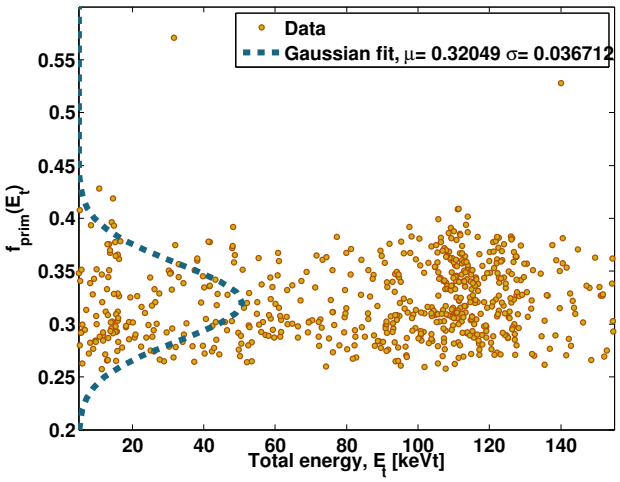

Figure D.3: Ratio of energy carried by primary channel to total energy deposited. The distribution is generally energy independent and can be approximated with a normal p.d.f.

The distribution of f_{prim} allows us to estimate, for a simulated event, how the primary pulse should be scaled compared to the total phonon pulse. The total phonon pulse, ψ_t, is essentially the regular phonon template. The peaky primary pulse is modeled as a double exponential, $\psi_{\mathrm{prim}}(t) = e^{-(t-t_0)/\tau_f} \times \left(1 - e^{-(t-t_0)/\tau_r}\right)$, where t_0, τ_r, and τ_f represent the delay, rise-time and fall-times. In the MC such a primary pulse is made by randomly drawing the three time measures from proper data driven distributions. The simulation now works as follows:

1. Consider noise traces from each phonon channel c for some event k, $n_k^c(t)\ \forall\ k \in \Lambda$.
2. Choose amplitude $a_j \in \mathcal{A}$ for the total phonon pulse, i.e., E_t from Fig. D.3. For the primary pulse we randomly pick $\rho_j \in \mathcal{N}(\mu, \sigma)$ which represents a realization of f_{prim}. The (μ, σ) come from the distribution shown in Fig. D.3.
3. For every such $\{k, j\}$ pair we construct two traces: (a) For fall-time calculations, $\sum_c n_k^c(t) + a_j \times \psi_t(t)$ and (b) for rise-time calculations $n_k^{c'}(t) + \rho_j a_j \times \psi_{\mathrm{prim}}(t)$, here c' is randomly chosen channel.
4. From these pulses we find the requisite fall and rise-times, $\Delta_{ft,pt}^{k,j}$ and $\Delta_{rt,prim}^{k,j}$.
5. Finally for (every energy value)j, we average over (noise realizations) k. This gives us mean and standard deviation of the fall and rise times as a function of energy, see Fig. D.4 and Fig. D.5.

From these distributions, we can calculate the performance of various cuts; these cuts are simple selection bounds on $\Delta_{\mathrm{rt,ft}}$. For each variation of the cut boundaries, a family of passage fractions / efficiencies were obtained.

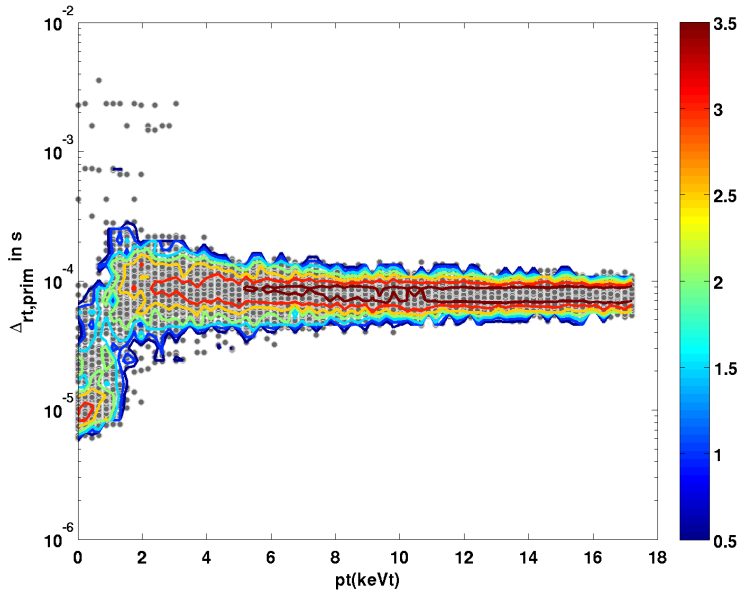

Figure D.4: $\Delta_{\mathrm{rt,prim}}$ as a function of energy from 100 noise sample MC. Each gray marker is on MC sample. Density contours are drawn with colored lines. The color-scale is the number of counts in log scale. The x-axis is in side 1 total energy, same as Fig. 6.1. Thus 200 $\mathrm{eV_{ee}} \mapsto$ 2.4 $\mathrm{keV_t}$here.

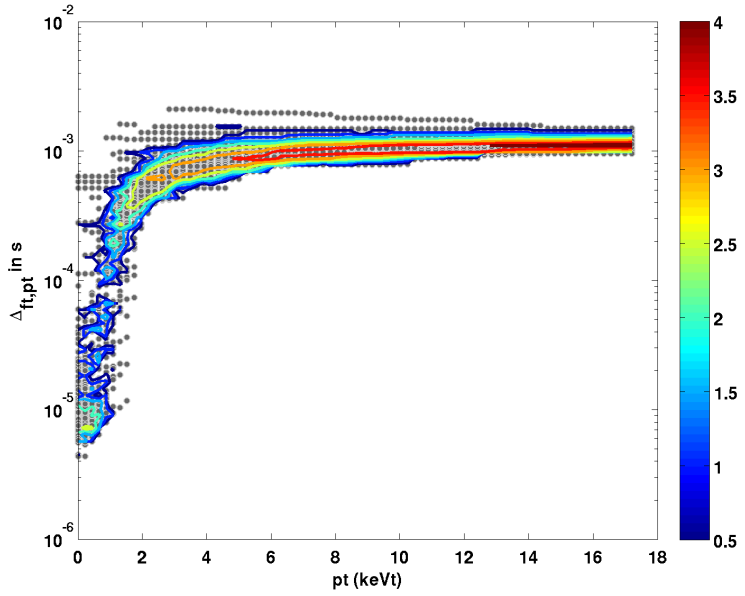

Figure D.5: $\Delta_{\mathrm{ft,pt}}$ as a function of energy from 100 noise sample MC. Each gray marker is on MC sample. Density contours are drawn with colored lines. The color-scale is the number of counts in log scale. The x-axis is in side 1 total energy, same as Fig. 6.1. Thus 200 $\mathrm{eV_{ee}} \mapsto$ 2.4 $\mathrm{keV_t}$here.

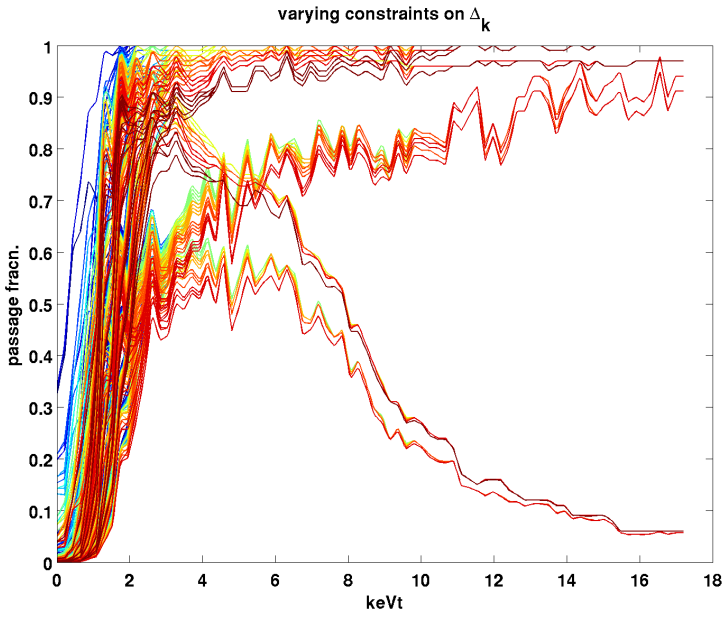

Figure D.6: Family of passage fraction (equivalent to efficiency here) curves for varying constraints on $\Delta_{\mathrm{ft,pt}}$ and $\Delta_{\mathrm{rt,prim}}$. The x-axis is in side 1 total energy, same as Fig. 6.1. Thus 200 $\mathrm{eV_{ee}} \mapsto$ 2.4 $\mathrm{keV_t}$here.

Much of the loss in efficiency was brought about by the fall time cut. An example of low-frequency noise affecting a good event was shown in Fig. 7.16. Another example found to affect the MC, was driven by noise with upward drifts, see Fig D.7.

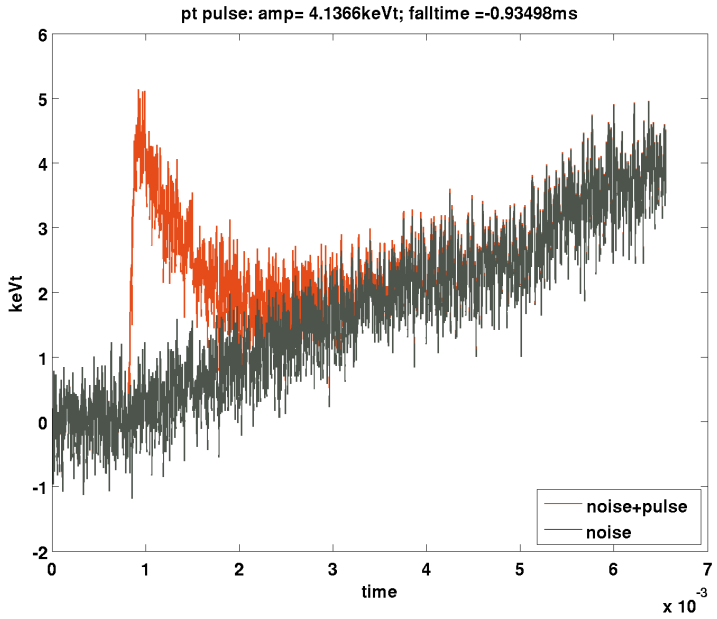

Figure D.7: An example of spurious noise that makes the fall-time cut inefficient.

The passage fractions from the simulation showed clearly that unexpected noise fluctuations could make the efficiency of this cut low at 200-500 eV_{ee} if fall-time constraints were imposed. The rise-time cut was however verified to be highly efficient; one can see this by noting that most MC points in Fig. D.6 are within the (7 μs, 4 ms) boundaries for energies > 2 keV_t (≈ 167 eV_{ee}). The final cut was driven by studies performed on Ba calibration data, see the main section for details, Sec. 7.2. This MC was used as a cross-check, and not as the final scheme to set cuts, since such simulation is computationally intensive if one has to sample noise from most periods of the 15 day run time.

D.2 Version for glitch tests

This version of the pulse + noise MC was used to study glitch-rejection, [133]. For discriminating glitches based on pulse shapes, we perform template fitting and compare goodness of fit measures, see section 7.1.2 for general description of the problem. Variance in the goodness of fit can be introduced from differences in phonon pulses. Depending on energy and position, phonon pulses can have different rising-edge profiles. We model the phonon pulse with a double exponential as: (1) $\psi(t) = e^{-(t-t_0)/\tau_f} \times \left(1 - e^{-(t-t_0)/\tau_r}\right)$, (2) $\psi(t) \mapsto \psi(t)/\max\{\psi\}$. For this phonon pulse of unit-height, t_0, τ_r, and τ_f represent the delay, rise-time and fall-times. In the MC such a pulse is made by randomly drawing the three time measures from proper data driven distributions. The phonon pulse is scaled with an "energy" (a_i) and then added to a noise event from the noise data-set to make a MC event of a known energy, see Fig. D.1. This process is repeated with a glitch template as well (here we don't alter rise/fall times). From this, following Fig. D.1, a data-base of events is generated constituting of 3 populations: just noise (Λ), phonon + noise (Ψ) and glitch + noise (Ξ). For every event in this population, goodness of fit is calculated with a phonon and glitch template, called χ^2_{ph} and χ^2_{gl} respectively. From these, $\Delta\chi^2 = \chi^2_{ph} - \chi^2_{gl}$ metrics are calculated, see Figs. D.8 and D.9 and the glitch rejection cut performance is studied. The general description of this is present in section 7.1.2.

Passage fractions calculated via this simulation for the glitch rejection cut cut $\Delta\chi^2 < 10$, are shown in the main text, see Figs. 7.9 and 7.10.

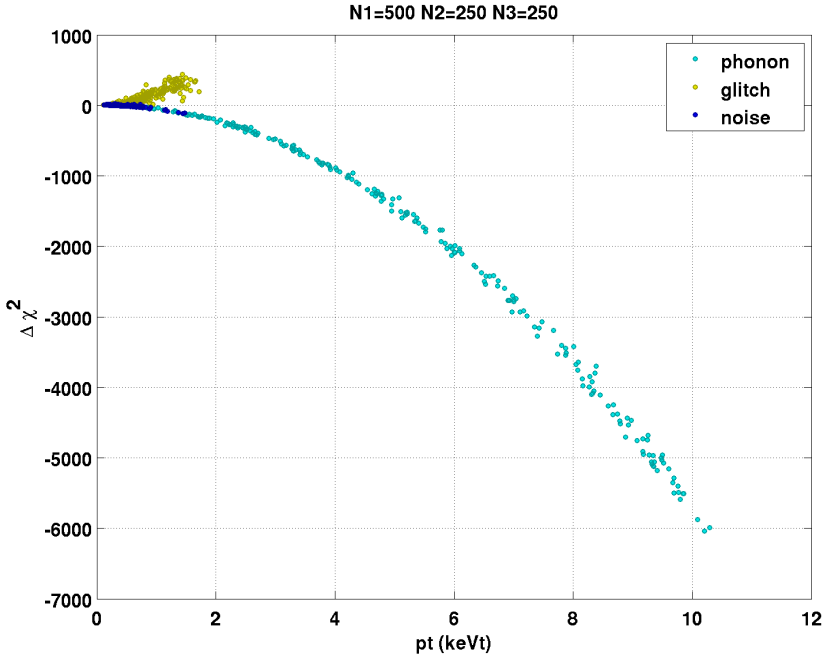

Figure D.8: $\Delta\chi^2-$Energy plane: The plot shows the distributions for MC events. In this plane, $\Delta\chi^2 > 0 \rightarrow$ glitches and $\Delta\chi^2 < 0 \rightarrow$ phonons. Here we have three populations (1) 500 noise events (2) 250 phonon+noise events (3) 250 glitch+noise events. The pulse height are varied from 0 to 10 keV_t. The zoomed plot is shown next.

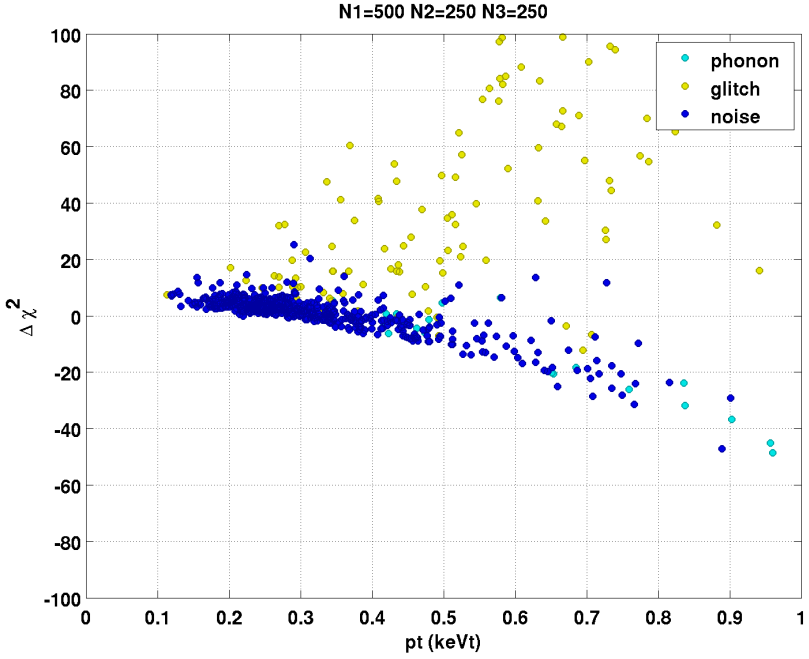

Figure D.9: $\Delta\chi^2-$Energy plane (zoomed low energy plot corresponding to D.8): The plot shows the distributions for MC events. In this plane, $\Delta\chi^2 > 0 \rightarrow$ glitches and $\Delta\chi^2 < 0 \rightarrow$ phonons. Here we have three populations (1) 500 noise events (2) 250 phonon+noise events (3) 250 glitch+noise events.

Appendix E

Optimum Filter Theory

Material based on theses of Sunil Golwala, Jeff Fillipini and personal notes from Matt Pyle.

E.1 Introduction

This section develops the general notion of a χ^2. I develop a mathematical formalism that is used to calculate the χ^2 for the various Optimal Filter algorithms described in section 2 and later. If the reader is comfortable with how χ^2 routines work, then this section should be casually skimmed.

E.1.1 Notations and basic definitions

Fourier Transforms

I will follow Jeff Fillipini's notation [82]:

$$\psi(t) = \int_{-\infty}^{+\infty} d\nu \quad \tilde{\psi}(\nu) e^{-i2\pi\nu t} \tag{E.1}$$

$$\tilde{\psi}(\nu) = \int_{-\infty}^{+\infty} dt \quad \psi(t) e^{i2\pi\nu t} \tag{E.2}$$

This renders the discretization procedure quite trivial i.e.
$\int dx \times f(x) \leftrightarrow \sum 1 \times f(x)$. See eqn A.5 in Jeff's thesis.

Correlations and Power Spectrum

We define a simple 1D autocorrelation function as $\xi(r) = \int dx f(x+r)^* f(x)$. As the name and definition suggests, it is a single valued measure of how a function correlates with itself when evaluated between two points of separation r.

The Fourier Transform of the autocorrelation function is known as the Power Spectral Density (PSD). This is defined as $J(\nu) = \int dr e^{i2\pi\nu r} \xi(r) = |\tilde{f}(\nu)|^2$. If the function is a random field then we take an ensemble average.

It is a quick and good exercise to see that for Gaussian noise (i.e. noise $n(t)$ is some number picked randomly from a Gaussian distribution $(2\pi\sigma)^{-\frac{1}{2}} e^{\left(\frac{x-\mu}{\sqrt{2}\sigma}\right)^2}$), the PSD is $J(\nu) = \langle |\tilde{n}(\nu)|^2 \rangle = \sigma^2$.

E.1.2 χ^2 Discriminant

The regular χ^2

This section discusses the definition of a standard scalar discriminant called χ^2. In the *Theory of Probability and Statistics*, this is a very well developed topic. In this section, I will present simple ideas which give the reader a good feeling for the mathematics and formalism, albeit not with perfect mathematical rigor. For a formal understanding see section B.2 of Jeff's thesis, or chapter 8.4 from F. James' textbook [1].

The main idea is to find a scalar called a discriminant, from some input consisting of an expectation (fit function, or some center measure) and raw data. Typically we have no handle over the data set, it is literally a set of numbers that come from some experiment. The expectation is generally a function we'd like to fit. It comes with some free parameters, say $\{a\}$. These are the knobs whose best setting we seek here. Optimizing the scalar χ^2 is presumably going to give us the best parameter values for the fit function.

Let's say we have a data set $Data(x)$ and a fit function $Fit(x, \{a\})$, where for all practical purposes x is a discrete index. Then,

$$\chi^2(\{a\}) \equiv \sum_x \frac{\|Data(x) - Fit(x, \{a\})\|}{N} \tag{E.3}$$

This is a sum of absolute measures of deviation, evaluated at every point x. N is some customary normalization factor, unimportant for now. Clearly the best parameters, called $\{\hat{a}\}$, will be the ones for which this sum is minimum i.e we solve for

$$\frac{\partial \chi^2}{\partial a_k} = 0 \quad and \quad \frac{\partial^2 \chi^2}{\partial a_k^2} > 0 \; \forall a_k \in \{a\} \tag{E.4}$$

From equation 4 we note that it's exactly solvable if every k^{th} equation is linear in the a's. Nonlinearities in parameter dependance will make this process harder. In this respect, the rather nonlinear $\| \cdot \|$ is a poor choice when we attempt to obtain a system of linear equations post differentiation. Thus we replace $\| \cdot \| \mapsto (\cdot)^2$ for convenience.

The correct way to design a χ^2 is to follow the notion of standardized variables. Suppose we have a random number X drawn from a distribution with mean μ and variance σ^2. It can be shown easily that $Y \equiv (X - \mu)/\sigma$ is a standardized version of X. This means its distribution has mean $= 0$ and variance $= 1$. One can conveniently put a set of random numbers X or $Data(x)$ in vector form $\vec{X}$. Similarly the set $Fit(x)$ is put into a "center" vector $\vec{C}$. Then the discriminant scalar is simply obtained from the standardized vectors as [2],

$$\chi^2(\{a\}) \equiv \vec{Y} \cdot \vec{Y} = \sum_{i,j} \frac{[X^i - C^i(\{a\})]\delta_{ij}[X^j - C^j(\{a\})]}{\sigma^2} \tag{E.5}$$

[1] Pg. 182, "Statistical Methods in Experimental Physics", Frederick James; 2^{nd} edition, 2008, World Scientific Publication

[2] The Kornecker delta may seem redundant. However when dealing with crosstalk, we will see the importance of explicitly writing it out. For compactness I will use Einstein notation later i.e $\sum_k a_k b_k \mapsto a_k b^k$

The $\vec{Y}$s can be thought of as an error vector or a vector that is a measure of the deviation of data variable X from some expectation μ, standardized in a nice way. If we have complex valued functions then, we must modify the above as,

$$\chi^2(\{a\}) \equiv \vec{Y^*} \cdot \vec{Y} \tag{E.6}$$

Generalizing the χ^2

The generalization comes in when we talk about multi-dimensional sets. This simply means, instead of one set $Data(x)$ and the associated $Fit(x)$, we have a collection i.e set of sets, $\{Data(x)\}$ and $\{Fit(x)\}$.

Let us consider the following thought experiment to develop the χ^2 routine. Suppose that we have *one* current carrying wire coming out of a detector. We wish to extract some signal via the current reading. Then the χ^2 technology from the previous section works well as we try to fit some pulse profile to the output signal. We might make the time of collection a discrete index Δt. Then at every $n\Delta t \ \ni n \in \mathbb{Z}$ we have some magnitude of the signal recorded.

In the case where we have a realistic experiment with many detectors, we have a set of signals. Naively, we can do a χ^2 calculation wire by wire. But in real life these wires are in some proximity and there will be crosstalk (via electromagnetic induction etc.). So we need to device a multidimensional method that will do the fitting while accounting for any such crosstalk or correlations between each wire i.e each data set or signal.

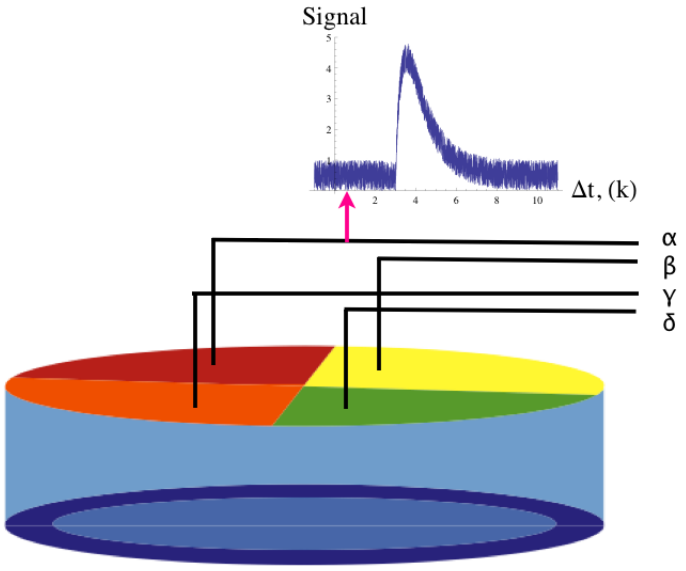

Figure E.1: CDMS II detectors. Each colored quadrant is a separate phonon channel. We label these channels with greek indices. Each channel carries a signal, whose ADC bins or time slices are labelled with latin indices.

This physical situation is succinctly addressed in a simple mathematical formalism. Recall the vector structure from equation 5. Now each effective signal i.e the standardized Y is a vector. But

we have a set of these signals. So we can elevate Y from a vector to a matrix, $Y^k \mapsto Y^{\alpha k}$. Think of α as the index for "which wire". Then given a wire number, k refers to a particular data point as before. Thus $Y^{3,19}$ stands for the current in the third wire collected at 19^{th} microsecond since initialization of the experiment, see Fig.1.

Since we seek a scalar discriminant a generic definition is [3],

$$\chi^2 \sim Y^{\alpha k}\, \mathbf{M}_{\alpha\beta}\, \mathbf{N}_{kj} Y^{\beta j} \tag{E.7}$$

I will now explain this postulate, part by part:

1) The latin indices $\{i, j, k \ldots\}$ represent the "coordinate" where a particular data point is present (ex: time of collection). Consider a single wire or data set i.e fix α. For a single wire [4] there's no crosstalk business, so $Y^{\alpha k}\ \mathbf{N}_{kj}\ Y^{\alpha j}\ \mathbf{M}_{\alpha\alpha}$ should reduce to equation 5. This can only happen if $\mathbf{N}_{kj} \equiv \delta_{kj}$.

What does this mean? Well, in constructing equation 5 we assumed that data collected at one instance will not be influenced by data collected at another time.[5]. So in practical situations we don't bother to make the χ^2 accountable for such weird behavior. The definition in eqn 7 was done keeping in mind these two modes of convolution i.e. time-time ($\mathbf{N}$) and separately wire-wire ($\mathbf{M}$). We now have,

$$\chi^2 \sim Y^{\alpha k}\, \mathbf{M}_{\alpha\beta}\, \delta_{kj}\, Y^{\beta j} \tag{E.8}$$

Based on the arguments above, we see that the sum on k can be made implicit without any issues. Thus, $Y^{\alpha k}\delta_{kj}Y^{\beta j} \mapsto Y^{\alpha}Y^{\beta}$. We can now work in a conveniently reduced space of "wire" indices only. This leaves us with,

$$\chi^2 \equiv Y^{\alpha}\, \mathbf{M}_{\alpha\beta}\, Y^{\beta} \tag{E.9}$$

2) We now focus on the *mixing matrix*: The matrix $\mathbf{M}$ is summed on the greek indices. Clearly any non-diagonal entries must be relatable to the correlation or crosstalk between two wires. Now let's consider a simple situation: the wires are far apart and hence no crosstalk. So $\mathbf{M}$ is diagonal; and for a particular wire we necessarily have $\mathbf{M}_{\beta\beta} = 1$. This will exactly reproduce the $\chi^2(\{a\}) \equiv \vec{Y} \cdot \vec{Y}$ from equation 5. Thus to $\mathcal{O}(0)$, $\mathbf{M}_{\alpha\beta} = \delta_{\alpha\beta}$ and to $\mathcal{O}(\epsilon)$, $\mathbf{M}_{\alpha\beta} = \delta_{\alpha\beta} + \epsilon \mathbf{J}_{\alpha\beta}$. Here ϵ represents the "smallness" of the correlations beyond 0. Now let us bring the wires a little closer, that is consider a small correlation to understand this first order nontrivial $\mathbf{J}$.

[3] If complex quantities are involved $\chi^2 \equiv Y^{*\alpha k}\, \mathbf{M}_{\alpha\beta}\, \mathbf{N}_{kj} Y^{\beta j}$.

[4] No sum on α here, as we look at only the α^{th} wire. This also means we treat $M_{\alpha\alpha}$ as number or a simple $\propto$-ity factor.

[5] For cases where noise is time dependent, we will deal with some nontrivial $\mathbf{N}$. It's obvious that $\mathbf{N}$ is related to the discretized autocorrelation function. This will show up later in the optimal filter developed for non-stationary noise.

To some $\mathcal{O}(\epsilon)$, we may write the correlation, $\rho_{\alpha\beta}$, between wire α and wire β as $\rho_{\alpha\beta} = \delta_{\alpha\beta} + \epsilon\zeta_{\alpha\beta}$. In the previous paragraph we concluded that in the small correlations scenario, $\mathbf{M}_{\alpha\beta} = \delta_{\alpha\beta} + \epsilon\mathbf{J}_{\alpha\beta}$. Each element of this crosstalk matrix $\mathbf{J}$ now has an obvious characterization: $\mathbf{J}_{\alpha\beta} \sim \zeta_{\alpha\beta}$. Which means, if the signals in the two wires have nontrivial correlations, then their mixing in the χ^2 discriminant should depend on their correlation strength.

To understand how $\mathbf{J}$ and ζ are related, we need to look at the correlation matrix.

$$\rho^{\alpha\beta} \equiv \frac{E[(X^\alpha - \mu_X^\alpha)(X^\beta - \mu_X^\beta)]}{\sigma_X^\alpha \sigma_X^\beta} \tag{E.10}$$

Since $\vec{Y}$ contains standardized variables only, we get the simple relation, $\rho^{\alpha\beta} = E[Y^\alpha Y^\beta]$. Let us pursue a rough calculation by finding the expectation value of our χ^2:

$$E[\chi^2] = M_{\alpha\beta} E[Y^\beta Y^\alpha] \ = p \quad p \in \mathbf{R}^+ \tag{E.11}$$

In writing the above we assume that $\mathbf{M}$ does not contain any statistical variable i.e. no X or Y dependence, and that $E[\chi^2]$ is constant, p. This leads us to[6],

$$\mathbf{M}_{\alpha\beta}\rho^{\beta\alpha} = p \ \Rightarrow \ Tr[\mathbf{M} \cdot \rho] = \frac{p}{N} Tr[\mathbf{I}] \tag{E.12}$$

The transition from a trace equation to a complete matrix equation (compare eqns. 12 and 13), is true only if the matrices are heavily diagonal. This works here since we are dealing with small perturbations; we finally get:

$$\mathbf{M} = \frac{p}{N}\rho^{-1} \tag{E.13}$$

If our estimates are good then typically, χ^2 per degree of freedom is 1 i.e. $p \approx N$ or $M \approx \rho^{-1}$.

Now that we have a handle on M, we can explicitly write down the full discriminant,

$$\chi^2 = \left(\frac{X - C}{\sigma}\right)^{\alpha k} \left(\rho^{-1}\right)_{\alpha\beta} \left(\frac{X - C}{\sigma}\right)_k^\beta \tag{E.14}$$

Identifying the covariance matrix[7] as $V_{\mu\nu} = \sigma_\mu \rho_{\mu\nu} \sigma_\nu$, we have a complete expression for the generalized χ^2 :

$$\chi^2 = (X - C)^{\alpha k} V_{\alpha\beta}^{-1} (X - C)_k^\beta \tag{E.15}$$

[6] Note $Tr[\mathbf{I}] = N$ in $N \times N$ space

[7] See for example Pg. 68, "Statistical Methods in Experimental Physics", Frederick James; 2^{nd} edition, 2008, World Scientific Publication. **Note** here the μ, νs are not summed over.

E.2 One Trace, One Template Optimal Filtering

Suppose we have some signal or trace $S(t)$ with noise $n(t)$. We want to fit a particular profile or template to this. Given our knowledge of the PSD function of the noise, Optimal Filtering tries to find the "strength" or correct "amplitude" such that the template best fits the signal.

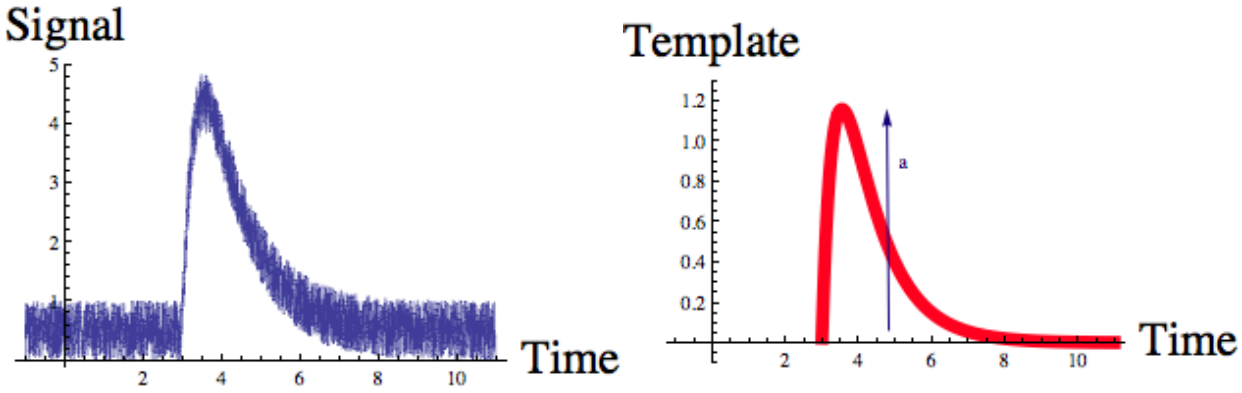

Figure E.2: *Left plot:* Data= $S(t) + n(t)$
Right plot: Fit= a$\times A(t)$

For an example see figures 2 and 3. They show some sample data and some sample fit. For example, the data signal is a pulse of known time constants, but we need to extract the amplitude, "a".

As per Jeff's notation we will write the problem as $S(t) = aA(t) + n(t)$. Here $A(t)$ is the fixed template we want to fit by tuning the amplitude a. The spectral noise density is known i.e $\tilde{J}(\nu) = \langle \tilde{n}^2(\nu) \rangle$ assuming Gaussian stationary noise. The problem is approached in frequency domain via discrete Fourier Transforms. This leads us to the estimator,

$$\chi^2(a) \equiv \sum_{\nu} \frac{|\tilde{S}(\nu) - a\tilde{A}(\nu)|^2}{\tilde{J}(\nu)} \tag{E.16}$$

We can show by solving $\frac{\partial \chi^2}{\partial a} = 0$ that $\hat{a} = \frac{\sum_\nu Re[\tilde{S}(\nu)\tilde{A}^*(\nu)]/\tilde{J}(\nu)}{\sum_\nu \tilde{A}(\nu)\tilde{A}^*(\nu)/\tilde{J}(\nu)}$ is the amplitude that fits best.

A customary simplification on the numerator of $\hat{a}$ is done as follows. First note $Re[z] = \frac{z+z^*}{2}$ implies,

$$\sum_{\nu} Re[\tilde{S}(\nu)\tilde{A}^*(\nu)]/\tilde{J}(\nu) = \frac{1}{2}\{\int d\nu \frac{\tilde{S}(\nu)\tilde{A}^*(\nu)}{\tilde{J}(\nu)} + \int d\nu \frac{\tilde{S}^*(\nu)\tilde{A}(\nu)}{\tilde{J}(\nu)}\} \tag{E.17}$$

Now for a real function $f(x)$ defined on $(-\infty, +\infty)$, its Fourier Transform follows the identity $\tilde{f}(\nu)^* = \tilde{f}(-\nu)$. Since by definition $\tilde{J}(\nu) = \tilde{J}(-\nu)$, the two integrals are equal. This gives the standard result of $\hat{a} = \frac{\sum_\nu \tilde{S}(\nu)\tilde{A}^*(\nu)/\tilde{J}(\nu)}{\sum_\nu \tilde{A}(\nu)\tilde{A}^*(\nu)/\tilde{J}(\nu)}$

Next we attempt at using this technology to find the optimal offset time along with the amplitude. If the signal is offset by some time t_0 then, we have,

$$\psi(t) = \int_{-\infty}^{+\infty} d\nu\ \tilde{\psi}(\nu) e^{-i2\pi\nu(t-t_0)} \ \Rightarrow\ \chi^2(a, t_0) = \sum_{\nu} \frac{|\tilde{S}(\nu) - ae^{-i2\pi\nu t_0}\tilde{A}(\nu)|^2}{\tilde{J}(\nu)} \tag{E.18}$$

We first solve for $\hat{a}(t_0)$ via $\frac{\partial\chi^2}{\partial a} = 0$. Due to exponential non-linearities, solving $\partial_{t_0}\chi^2 = 0$ proves hard. However we see that $\partial_{t_0}\chi^2 \propto \partial_{t_0}\hat{a}$. So it turns out that, in this case, from $max\{\hat{a}(t_0)\}$ we get the $\hat{t}_0$ which minimizes the χ^2. This is a good coincidence.

Resolution

Here we attempt to answer what is the resolution of the best amplitude. The resolution is given as $\sigma^2_{\hat{a}} = \left(\sum_\nu |\tilde{A}|^2/\tilde{J}\right)^{-1}$. In practice, note that $\tilde{J}$ has units of ADC^2/Hz. And our amplitude estimator must have units of ADC, since A is a template (generally normalized to unit height).

The follow up to this is Two Traces, Four Templates Optimal Filter used for the charge channels. Jeff has an excellent section on this, see section A.3. I will briefly outline the idea here.

Suppose we have two channels and hence two signals $S_1(t)$ and $S_2(t)$. The optimal filtering problem is now to find the corresponding amplitudes, $a_1(t)$ and $a_2(t)$. However the two channels may have cross talk and thus in generality we must consider four templates. This reduces to:

$$\chi^2_{tot}(a_1, a_2) \approx \chi^2_1 + \chi^2_2 \quad \ni \quad \chi^2_i \equiv \sum_{\nu} \frac{|\tilde{S}_i(\nu) - \tilde{A}_{ij}(\nu)a^j|^2}{\tilde{J}_i(\nu)} \tag{E.19}$$

For compactness, the sum on j is in Einstein notation. It represents the cross talk behavior including both amplitudes per channel. If there was no cross talk, A_{ij} would be diagonal. Another key thing to note is that the decomposition of the χ^2 rests on the assumption that $\langle\tilde{J}(\nu), \tilde{J}(\nu + \nu')\rangle = \delta(\nu')$.

E.3 One Trace, N-templates Optimal Filtering

The problem in this case is formulated as $S(t) = a^j A_j(t - t_0) + n(t)$. The idea is that we want to fit more than one template, each with the same time offset t_0. The sum over templates is on $j = 1, 2...N$. I use Einstein convention.
This gives us,

$$\chi^2(\vec{a}, t_0) = \sum_{\nu} \frac{|\tilde{S}(\nu) - e^{-i2\pi\nu t_0}a^j\tilde{A}_j(\nu)|^2}{\tilde{J}(\nu)} \tag{E.20}$$

The strategy is just an extension of the one from the previous section. We first aim at finding $\hat{\vec{a}}(t_0)$. Once we have this, we will have to find the $\hat{t}_0$. This is the only parameter for the best fit amplitude vector, and "should" solve our problem.

First I will tackle the simpler version with $t_0 = 0$. We look for the best $\vec{a}$ by looking at $\frac{\partial\chi^2}{\partial a^k} = 0$. This gives us ,

$$\sum_{\nu} \frac{\tilde{A}_k^*(\nu)\{\tilde{S}(\nu) - a^j \tilde{A}_j(\nu)\}}{\tilde{J}(\nu)} = 0 \quad \forall\, k = 1, 2 \ldots N \tag{E.21}$$

This is a simple problem of N-equations with N-unknowns. The easiest way to solve this is to write the equation in matrix vector for as $\mathbf{P} \cdot \vec{a} = \vec{q}$. We define the respective quantities as,

$$\mathbf{P}_{kj} \equiv \sum_{\nu} \frac{\tilde{A}_k^*(\nu)\tilde{A}_j(\nu)}{\tilde{J}(\nu)} \quad and \quad q_k \equiv \sum_{\nu} \frac{\tilde{A}_k^*(\nu)\tilde{S}(\nu)}{\tilde{J}(\nu)} \tag{E.22}$$

Thus assuming measures of inversibility, $\hat{\vec{a}} = \mathbf{P^{-1}} \cdot \vec{q}$.

It will be easy now to solve the full problem for $S(t) = a^j A_j(t - t_0) + n(t)$. We are dealing with the estimator from eqn 6. The phase is simply carried over. So $\frac{\partial \chi^2}{\partial a^k} = 0$ gives us ,

$$\sum_{\nu} \frac{\tilde{A}_k^*(\nu)\{e^{i2\pi\nu t_0}\tilde{S}(\nu) - a^j \tilde{A}_j(\nu)\}}{\tilde{J}(\nu)} = 0 \quad \forall\, k = 1, 2 \ldots N \tag{E.23}$$

This is again reduced to $\mathbf{P} \cdot \vec{a} = \vec{q}(t_0)$. The new quantities are:

$$\mathbf{P}_{kj} \equiv \sum_{\nu} \frac{\tilde{A}_k^*(\nu)\tilde{A}_j(\nu)}{\tilde{J}(\nu)} \quad and \quad q_k(t_0) \equiv \sum_{\nu} \frac{\tilde{A}_k^*(\nu)\tilde{S}(\nu)e^{i2\pi\nu t_0}}{\tilde{J}(\nu)} \tag{E.24}$$

The equation above is a slightly more general version to A.12 from Jeff's thesis, i.e. multiple templates. Thus we now have $\hat{\vec{a}}(t_0) = \mathbf{P^{-1}} \cdot \vec{q}(t_0)$.

The simplest way[8] to solve the problem is to rewrite χ^2 explicitly as a function of t_0 only. We can then minimize $\chi^2(t_0)$ w. r. t t_0. Analytically finding the minima of the nonlinear $\chi^2(t_0)$ can be very hard. But computationally we solve the problem via $min\{\chi^2(t_0)\}$, where the domain for t_0 is expected, bound and tractable, such as a trigger window setting.

However we may actually simplify the full χ^2 expression such that the computation time may be reduced. To do this we will start by expanding the original χ^2 from eqn 23 keeping in mind that we have calculated $\hat{\vec{a}}$ as a function of t_0.

$$\chi^2(t_0) = \sum_{\nu} \frac{1}{\tilde{J}(\nu)} \left(\tilde{S}^*(\nu)\tilde{S}(\nu) + \hat{a}^j \tilde{A}_j^*(\nu)\tilde{A}_k(\nu)\hat{a}^k - 2e^{+i2\pi\nu t_0}\hat{a}^l \tilde{A}_l^*(\nu)\tilde{S}(\nu) \right) \tag{E.25}$$

In the above we used the property that $\tilde{X}(\nu) = \tilde{X}^*(-\nu) \quad \forall\, X \in \mathbf{R}$. The last term above is the same as the second, with the factor of -2. This is comes from eqn 23, viz. $\sum_\nu e^{+i2\pi\nu t_0}\tilde{A}_l^*(\nu)\tilde{S}(\nu)/\tilde{J}(\nu) = \sum_\nu \tilde{A}_l^*(\nu)\tilde{A}_m(\nu)\hat{a}^m/\tilde{J}(\nu)$. Making this simplification and plugging in in $\hat{\vec{a}}(t_0) = \mathbf{P^{-1}} \cdot \vec{q}(t_0)$ our working discriminant is:

$$\chi^2(t_0) = \sum_{\nu} \frac{1}{\tilde{J}(\nu)} \left(\tilde{S}^*(\nu)\tilde{S}(\nu) - \left[\mathbf{P^{-1}} \cdot \vec{q}(t_0)\right]^j \tilde{A}_j^*(\nu)\tilde{A}_k(\nu) \left[\mathbf{P^{-1}} \cdot \vec{q}(t_0)\right]^k \right) \tag{E.26}$$

[8] Previously we performed $max\{\hat{a}(t_0)\}$ to pick the best offset $\hat{t}_0$ to get the best "scalar" $\hat{a}(\hat{t}_0)$. Now the amplitude is a vector, so the sorting mechanism must work by components. To this effect the solution is not guaranteed, as the $\hat{t}_0$ extracted from $max\{\hat{a}_2(t_0)\}$ may be different from the one we get via $max\{\hat{a}_5(t_0)\}$.

E.4 N Traces, M templates Optimal Filtering

Before we embark on solving the final problem, I would like to refer the reader to section 1.2.2. We will be using the same practical construct of many wires with signal crosstalk.

Consider N wires hence N traces for an experiment. Per wire (represented by greek indices like $\alpha,\ \beta, \ldots$) we have a set of M templates (represented by latin indices $i,\ j, \ldots$). We seek the best amplitudes for every template.

So in frequency domain, we attempt to fit the signal $\tilde{S}_\alpha(\nu)$ with $a^j \tilde{A}_{j\alpha}(\nu)$. To compactify our notation, we recognize that quantities capped with "tilde" are in Fourier space hence they are functions of ν and so we make the ν parameter and the overall sum on ν implicit. Invoking the generalized χ^2 , we thus get the discriminant to be:

$$\chi^2 = [\tilde{S}^{*\alpha} - e^{+i2\pi\nu t_0} a^j \tilde{A}_j^{*\alpha}]\{\tilde{\mathbf{V}}^{-1}_{\alpha\beta}\}[\tilde{S}^\beta - e^{-i2\pi\nu t_0} a^k \tilde{A}_k^\beta] \tag{E.27}$$

Let us start the minimization routine by calculating, $\frac{\partial \chi^2}{\partial a^l} = 0$.

$$[e^{+i2\pi\nu t_0} \tilde{A}_l^{*\alpha}]\{\tilde{\mathbf{V}}^{-1}_{\alpha\beta}\}[\tilde{S}^\beta - e^{-i2\pi\nu t_0} a^k \tilde{A}_k^\beta] + [\tilde{S}^{*\alpha} - e^{+i2\pi\nu t_0} a^j \tilde{A}_j^{*\alpha}]\{\tilde{\mathbf{V}}^{-1}_{\alpha\beta}\}[e^{-i2\pi\nu t_0} \tilde{A}_l^\beta] = 0 \tag{E.28}$$

This equation is in the form of $z + z^* = 0$. We may simplify this to give $z = 0$ following the same scheme from eqns. 19-20. The key ingredients for the simplification are $\tilde{X}(\nu) = \tilde{X}^*(-\nu) \quad \forall\ X \in \mathbb{R}$ and $\tilde{\mathbf{V}}^{-1}_{\alpha\beta}(\nu) = \tilde{\mathbf{V}}^{-1}_{\beta\alpha}(-\nu)$. The later follows from the definition of the covariance matrix particularly it's Hermicity. Thus in the second term in the sum above becomes identical to the first when $\nu \mapsto -\nu$.

Thus the set of best parameters, $\hat{\vec{a}}$ satisfy the following[9]:

$$[\tilde{A}_l^{*\alpha}]\{\tilde{\mathbf{V}}^{-1}_{\alpha\beta}\}[\tilde{S}^\beta e^{+i2\pi\nu t_0} - \hat{a}^k \tilde{A}_k^\beta] = 0 \tag{E.29}$$

We can solve the above as a vector matrix system of equations $\mathbf{P} \cdot \vec{a} = \vec{q}(t_0)$. Thus assuming measures of inversibility, $\hat{\vec{a}} = \mathbf{P^{-1}} \cdot \vec{q}(t_0)$. The quantities are[10] :

[9] Keep in mind that the LHS is summed over ν

[10] keep in mind that while we sum over ν explicitly, all contracted indices are summed over implicitly. This is for brevity.

$$\begin{aligned}\mathbf{P}_{lk} &= \sum_{\nu} \tilde{A}_l^{*\alpha}(\nu)\{\tilde{\mathbf{V}}^{-\mathbf{1}}_{\alpha\beta}(\nu)\}\tilde{A}_k^{\beta}(\nu) \\ q_l(t_0) &= \sum_{\nu} \tilde{A}_l^{*\alpha}(\nu)\{\tilde{\mathbf{V}}^{-\mathbf{1}}_{\alpha\beta}(\nu)\}\tilde{S}^{\beta}(\nu)e^{+i2\pi\nu t_0}\end{aligned}$$

With the best amplitudes parametrized by t_0, we can write the χ^2 from eqn 31 entirely in terms of t_0. Then we simply perform $min\{\chi^2(t_0)\}$ computationally. However as we saw in the previous section, we can simply the expression for $\chi^2(t_0)$ to make computation faster. This is done by expanding the entire $\chi^2(t_0)$ expression and using eqn 33. With the simplification scheme, we get our new working discriminant to be,

$$\chi^2(t_0) = \tilde{S}^{*\alpha}\{V^{-1}_{\alpha\beta}\}\tilde{S}^{\beta} - [\mathbf{P^{-1}}\cdot\vec{q}(t_0)]^j\tilde{A}^{*\alpha}_j\{V^{-1}_{\alpha\beta}\}\tilde{A}^{\beta}_k[\mathbf{P^{-1}}\cdot\vec{q}(t_0)]^k \tag{E.30}$$

E.5 Non-Stationary Optimal Filter (NSOF)

This is a further generalization of the Optimal Filter methods described above. In all the cases discussed so far, a subtle simplification existed: Since we assumed stationary noise (i.e no time correlations), the Fourier modes were independent. Real life is not always so nice. We can often have time dependent noise. An archetypical example is the jump in r.m.s fluctuation around the sudden onset of a signal pulse. However the CDMS implementation is a little different.

The iZIP phonon pulses are very uniform. However position dependence gives rise to fluctuations in the first 100 μs. The goal of NSOF here is to de-weight this portion in the χ^2. The way we do it is the following: (1) Take a bunch of pulses/traces with the same start time and create an average fitting template from this. Fig.4.a (2) Subtract this template from all the pulses and obtain the residuals . Fig.4.b

We treat this residual as time dependent noise in our NSOF algorithm which I will discuss in the next section. Keep in mind that this is not real noise, since if you knew how a pulse shape varies with position, we can make "perfect" templates and the residual would be stationary noise. We are just encoding our ignorance in this fancy noise idea.

E.5.1 One Trace One Template NSOF

We will start of with the simplest case. Recall the general formulation from eqn 7. Since we have just one trace $\mathbf{M}_{\mu\nu} = \delta_{\mu\nu}$. Because of time correlations, we need to figure out $\mathbf{N}$, and we will do this in frequency space. So the discriminant now is $\chi^2 = Y^{\alpha k}\delta_{\alpha\beta}\mathbf{N}_{kj}Y^{\beta j}$. Since the greek indices here have no importance, let's ignore them, and so we have,

$$\chi^2 \equiv Y^k\ \mathbf{N}_{kj}\ Y^j \tag{E.31}$$

Mathematically, there's no difference between this equation and eqn.9. The physical interpretation is of course different. In eqn 9, we have no time/frequency correlation, but mixing between the

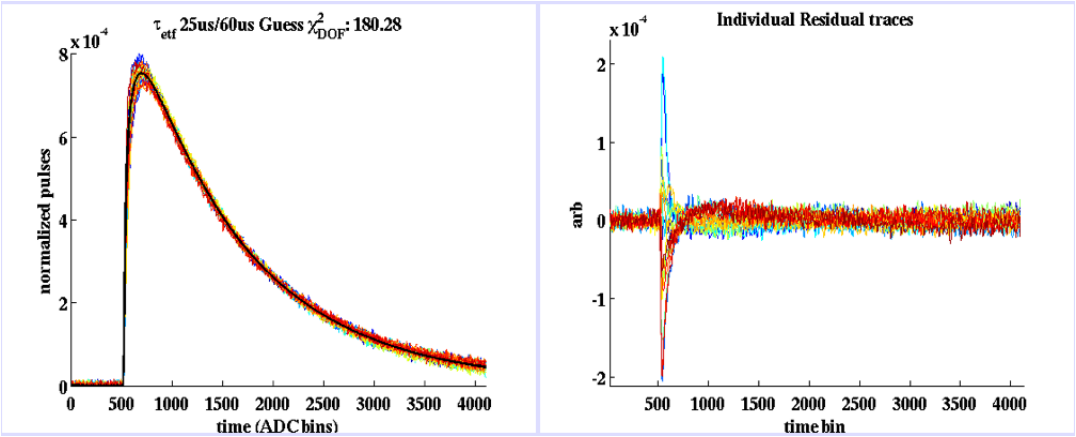

Figure E.3: a) A bunch of sample pulses with the template in balck. b) pulses with template subtracted: note the noise spike around onset of pulse.

wires/traces. Here it's the complement. Since there's no mathematical difference we can explicitly follow the general calculation developed in eqns 9-15. Now what we need is the covariance matrix in frequency space to calculate,

$$\chi^2 = (X - C)^k V^{-1}_{kj} (X - C)^j \tag{E.32}$$

The general definition of covariance matrix is

$$V^{ij} \equiv E[(X^i - \mu^i_X)(X^j - \mu^j_X)] \tag{E.33}$$

We have a special case: Since in the above i, j correspond to particular times/frequencies of the *same* trace we need to consider the auto-covariance matrix instead. And to be very clear I will use explicit time coordinates,

$$V(t,t') = E[(X(t) - \mu(t))(X(t') - \mu_X(t'))] = E[X(t)X(t')] - \mu(t)\mu(t') \;\equiv\; V_1(t,t') + V_2(t,t') \tag{E.34}$$

Looking at V_1

The first term is the autocorrelation function. Let's evaluate $V_1(t, t+\tau)$:

$$V_1(t, t+\tau) = E\left[\int\int d\nu_1 d\nu_2 \tilde{X}^*(\nu_1) e^{i2\pi\nu_1 t} \tilde{X}(\nu_2) e^{-i2\pi\nu_2 t} e^{-i2\pi\nu_2 \tau}\right] \tag{E.35}$$

$$= \int\int d\nu_1 d\nu_2 E\left[\tilde{X}^*(\nu_1)\tilde{X}(\nu_2)\right] e^{-i2\pi(\nu_2-\nu_1)t} e^{-i2\pi\nu_2\tau} \tag{E.36}$$

Now let's do a Fourier Transform of eqn 37 w.r.t the variable t i.e we evaluate $\int dt V_1(t, t+\tau) e^{i2\pi\nu_3 t}$.

The exponentials with t can be combined and we get an integral $\sim \int dt e^{-i2\pi(\nu_2-\nu_1-\nu_3)t}$. This is

just a dirac-delta $\delta(\nu_2 - \nu_1 - \nu_3)$, and then integrating over ν_1 gives us

$$\int dt V_1(t, t+\tau) e^{i2\pi\nu_3 t} = \int\int d\nu_1 d\nu_2 E\left[\tilde{X}^*(\nu_2 - \nu_3)\tilde{X}(\nu_2)\right] e^{-i2\pi\nu_2\tau} \tag{E.37}$$

And finally we do another Fourier Transform on eqn 38, w.r.t. τ to obtain the covariance matrix in frequency space,

$$\int d\tau \left(\int dt V_1(t, t+\tau) e^{i2\pi\nu_3 t}\right) e^{i2\pi\nu_4\tau} = E\left[\tilde{X}^*(\nu_4 - \nu_3)\tilde{X}(\nu_4)\right] \tag{E.38}$$

Thus we obtain,

$$\tilde{V}_1(\nu, \nu') = E\left[\tilde{X}^*(\nu' - \nu)\tilde{X}(\nu)\right] \tag{E.39}$$

In effect, we just calculated the Fourier transform of the two point auto correlation function, and hence eqn 40 is our PSD. It is very important to note that V_1 hence V is not diagonal and therefore is non-commutative in frequency space. Simply put $\vec{f}(\nu)^T\tilde{V}(\nu, \nu') \neq \tilde{V}(\nu, \nu')\vec{f}(\nu)$ and similarly with $\vec{f}$ replaced by a matrix.

Looking at V_2

Just like the above, we will first represent V_2 in Fourier space and then invert it.

$$V_2(t, t+\tau) = \int\int d\nu_1 d\nu_2 \tilde{\mu}^*(\nu_1) e^{i2\pi\nu_1 t}\tilde{\mu}(\nu_2) e^{-i2\pi\nu_2 t} e^{-i2\pi\nu_2\tau} \tag{E.40}$$

$$= \int\int d\nu_1 d\nu_2 \tilde{\mu}^*(\nu_1)\tilde{\mu}(\nu_2)\ e^{-i2\pi(\nu_2 - \nu_1)t} e^{-i2\pi\nu_2\tau} \tag{E.41}$$

I will invert on t and τ right away,

$$\int dt \int d\tau\ V_2(t, t+\tau) e^{i2\pi\nu_3 t} e^{i2\pi\nu_4\tau} = \int\int dt d\tau \int\int d\nu_1 d\nu_2 \tilde{\mu}^*(\nu_1)\tilde{\mu}(\nu_2)\ e^{-i2\pi(\nu_2 - \nu_1 - \nu_3)t} e^{-i2\pi(\nu_2 - \nu_4)\tau} \tag{E.42}$$

From this it is clear that

$$\tilde{V}_2(\nu, \nu') = \tilde{\mu}^*(\nu' - \nu)\tilde{\mu}(\nu) \tag{E.43}$$

Now that we have a covariance matrix ($\tilde{V} = \tilde{V}_1 + \tilde{V}_2$), we can calculate the χ^2 in frequency space. But there's one more subtle issue we need to address quickly. Because we are addressing the situation where the change in noise is associated with the arrival of the pulse, the noise should be phase-locked to the template. As a result the data signal must be time shifted to match the template+noise (recall we are modeling the signal as $S(t) = aA(t) + n(t)$). With all this in mind we have,

$$\chi^2 \equiv \sum_{\nu\nu'} \left[\tilde{S}^*(\nu) e^{i2\pi\nu t_0} - a\tilde{A}^*(\nu)\right] \{\tilde{V}(\nu, \nu')^{-1}\} \left[\tilde{S}(\nu') e^{-i2\pi\nu' t_0} - a\tilde{A}(\nu')\right] \tag{E.44}$$

We know $S(t) \in \mathbb{R} \rightarrow \tilde{S}^*(\nu) = \tilde{S}(-\nu)$ and that $\tilde{V}$ is Hermitian. This allows us to simplify the expansion of the above as:

$$\begin{aligned}\chi^2 = &\sum_{\nu\nu'} \left[\tilde{S}^*(\nu)e^{i2\pi\nu t_0}\right] \{\tilde{V}(\nu,\nu')^{-1}\} \left[\tilde{S}(\nu')e^{-i2\pi\nu' t_0}\right] \\ &- 2a \left[\tilde{S}^*(\nu)e^{i2\pi\nu t_0}\right] \{\tilde{V}(\nu,\nu')^{-1}\} \left[\tilde{A}(\nu')\right] \\ &+ a^2 \left[\tilde{A}^*(\nu)\{\tilde{V}(\nu,\nu')^{-1}\}\tilde{A}(\nu')\right]\end{aligned} \tag{E.45}$$

Performing $\partial\chi^2/\partial a = 0$ thus gives us the best amplitude in terms of the offset time,

$$\hat{a}(t_0) = \frac{\sum_{\nu\nu'} \tilde{S}^*(\nu)e^{i2\pi\nu t_0}\{\tilde{V}(\nu,\nu')^{-1}\}\tilde{A}(\nu')}{\sum_{\nu\nu'} \tilde{A}^*(\nu)\{\tilde{V}(\nu,\nu')^{-1}\}\tilde{A}(\nu')} \tag{E.46}$$

We went from two unknowns a and t_0 to one, and hence we can write down the final irreducible χ^2 in terms of t_0. Notice that with our $\hat{a}(t_0)$, the second term of eqn 42 is the same as the third, upto a factor of -2. With this small simplification we get,

$$\chi^2(t_0) = \sum_{\nu\nu'} \tilde{S}^*(\nu)e^{i2\pi\nu t_0}\{\tilde{V}(\nu,\nu')^{-1}\}\tilde{S}(\nu')e^{-i2\pi\nu' t_0} - \hat{a}^2(t_0)\tilde{A}^*(\nu)\{\tilde{V}(\nu,\nu')^{-1}\}\tilde{A}(\nu') \tag{E.47}$$

This χ^2 is very nonlinear and we will need to numerically find the minima. A simple way to minimize computation time is to start around an expected value for t_0 and scan over a reasonable neighborhood around this number.

E.5.2 Comparison of OF and NSOF

The final power of NSOF over the OF algorithm is seen when we compare the L-shell and K-shell γ peaks. Since the K-shell peak has better statistics, an all iZIP survey was done with that. Apart from T5Z3 which suffers from bad noise pick-up, all detectors show better resolution for the NSOF energies. This is generally true for the L-shell peak as well, as shown with CDMSlite data.

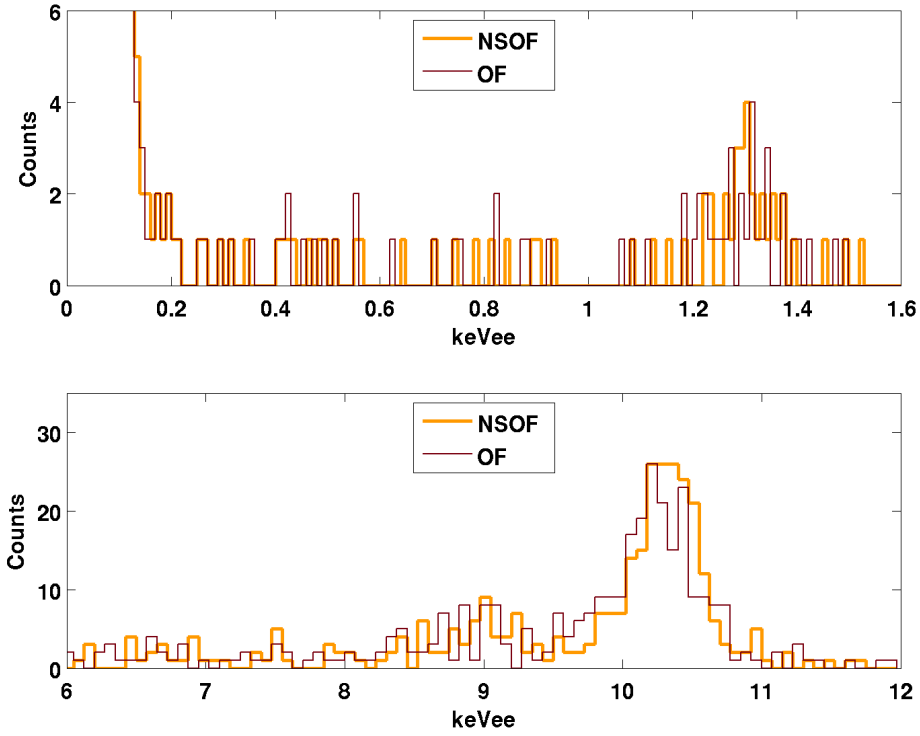

Figure E.4: The .129 keV L-shell peak and the 10.36 keV K-shell peak are compared with with NSOF and OF energy estimation. It is clear the NSOF does a better job, and the peaks are narrower.

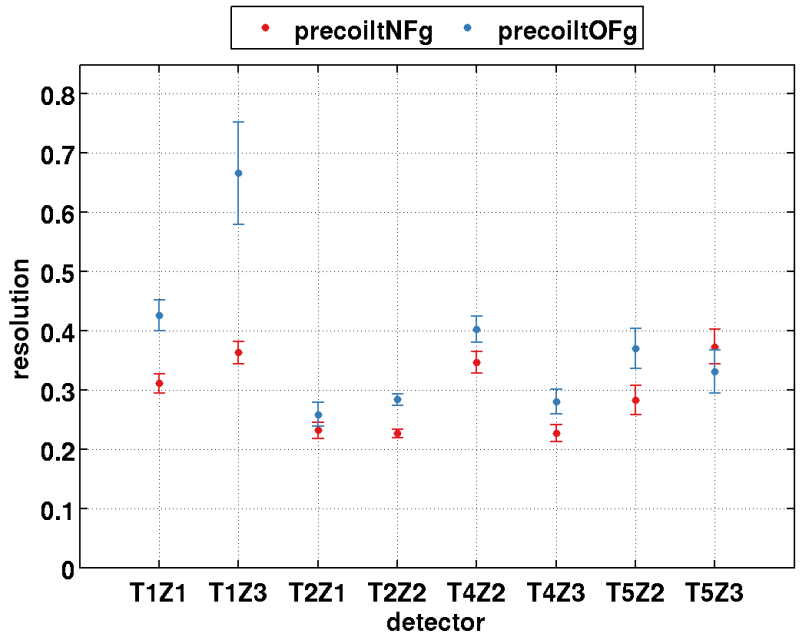

Figure E.5: The 10.36 keV K-shell peak's resolution is compared with with NSOF and OF energy estimation across all iZIPs and NSOF gives better resolution.

References

[1] S. van den Bergh, "The early history of dark matter," *Publications of the Astronomical Society of the Pacific*, vol. 111, no. 760, pp. pp. 657–660, 1999.

[2] K. Freeman and G. McNamara, *In Search of Dark Matter*. Springer Praxis Books, 2006.

[3] M. J. Rees, "Dark matter: Introduction," *Phil.Trans.Roy.Soc.Lond.*, vol. 361, pp. 2427–2434, 2003.

[4] R. Caldwell and M. Kamionkowski, "Dark matter and dark energy," *Nature*, vol. 458, pp. 587–589, 2009.

[5] "Planck's new cosmic recipe." `http://sci.esa.int/planck/51557-planck-new-cosmic-recipe/`.

[6] P. Ade *et al.*, "Planck 2013 results. XVI. Cosmological parameters," 2013.

[7] P. Ade *et al.*, "Planck 2013 results. I. Overview of products and scientific results," 2013.

[8] S. Dodelson, *Modern Cosmology*. Academic Press, 2003.

[9] S. Weinberg, *Cosmology*. Oxford University Press, 2008.

[10] E. Kolb and M. Turner, *The Early Universe*. Westview Press, 1994.

[11] S. Weinberg, *The First Three Minutes: A Modern View Of The Origin Of The Universe*. Basic Books, 1993.

[12] "The history of structure formation in the universe." `http://sci.esa.int/planck/51560-the-history-of-structure-formation-in-the-universe/`.

[13] K. Nakamura *et al.*, "Review of particle physics," *J.Phys.*, vol. G37, p. 075021, 2010.

[14] B. Fields and S. Sarkar, "Big-Bang nucleosynthesis (2006 Particle Data Group mini-review)," 2006.

[15] D. G. York *et al.*, "The Sloan Digital Sky Survey: Technical Summary," *Astron.J.*, vol. 120, pp. 1579–1587, 2000.

[16] L. E. Strigari, J. S. Bullock, M. Kaplinghat, J. D. Simon, M. Geha, *et al.*, "A common mass scale for satellite galaxies of the Milky Way," *Nature*, vol. 454, pp. 1096–1097, 2008.

[17] J. D. Simon and M. Geha, "The Kinematics of the Ultra-Faint Milky Way Satellites: Solving the Missing Satellite Problem," *Astrophys.J.*, vol. 670, pp. 313–331, 2007.

[18] M. Walker, "Dark matter in the galactic dwarf spheroidal satellites," in *Planets, Stars and Stellar Systems* (T. Oswalt and G. Gilmore, eds.), pp. 1039–1089, Springer Netherlands, 2013.

[19] A. W. McConnachie, "THE OBSERVED PROPERTIES OF DWARF GALAXIES IN AND AROUND THE LOCAL GROUP," 2012.

[20] M. G. Walker, M. Mateo, E. W. Olszewski, O. Y. Gnedin, X. Wang, *et al.*, "Velocity Dispersion Profiles of Seven Dwarf Spheroidal Galaxies," 2007.

[21] V. C. Rubin and W. K. Ford, Jr., "Rotation of the Andromeda Nebula from a Spectroscopic Survey of Emission Regions," *ApJ*, vol. 159, p. 379, Feb. 1970.

[22] Y. Sofue and V. Rubin, "Rotation curves of spiral galaxies," *Ann.Rev.Astron.Astrophys.*, vol. 39, pp. 137–174, 2001.

[23] Y. Sofue, "Rotation Curve and Mass Distribution in the Galactic Center — From Black Hole to Entire Galaxy —," 2013.

[24] G. Squires, N. Kaiser, A. Babul, G. Fahlman, D. Woods, D. M. Neumann, and H. Boehringer, "The Dark Matter, Gas, and Galaxy Distributions in Abell 2218: A Weak Gravitational Lensing and X-Ray Analysis," *ApJ*, vol. 461, p. 572, Apr. 1996.

[25] D. C. Moore, "A search for low-mass dark matter with the cryogenic dark matter search and the development of highly multiplexed phonon-mediated particle detectors,"

[26] V. Springel, C. S. Frenk, and S. D. White, "The large-scale structure of the Universe," *Nature*, vol. 440, p. 1137, 2006.

[27] V. Springel, S. D. White, A. Jenkins, C. S. Frenk, N. Yoshida, *et al.*, "Simulating the joint evolution of quasars, galaxies and their large-scale distribution," *Nature*, vol. 435, pp. 629–636, 2005.

[28] L. Anderson *et al.*, "The clustering of galaxies in the SDSS-III Baryon Oscillation Spectroscopic Survey: Baryon Acoustic Oscillations in the Data Release 10 and 11 galaxy samples," 2013.

[29] W. Hu and S. Dodelson, "Cosmic microwave background anisotropies," *Ann.Rev.Astron.Astrophys.*, vol. 40, pp. 171–216, 2002.

[30] J. Beringer *et al.*, "Review of Particle Physics (RPP)," *Phys.Rev.*, vol. D86, p. 010001, 2012.

[31] E. Pointecouteau and J. Silk, "New Constraints on MOND from galaxy clusters," *Mon.Not.Roy.Astron.Soc.*, vol. 364, pp. 654–658, 2005.

[32] G. Jungman, M. Kamionkowski, and K. Griest, "Supersymmetric dark matter," *Phys. Rep.*, vol. 267, no. 5Äì6, pp. 195 – 373, 1996.

[33] J. Formaggio and G. Zeller, "From eV to EeV: Neutrino Cross Sections Across Energy Scales," *Rev.Mod.Phys.*, vol. 84, p. 1307, 2012.

[34] K. Jedamzik and M. Pospelov, "Big Bang Nucleosynthesis and Particle Dark Matter," *New J.Phys.*, vol. 11, p. 105028, 2009.

[35] G. Bertone, D. Hooper, and J. Silk, "Particle dark matter: Evidence, candidates and constraints," *Phys.Rept.*, vol. 405, pp. 279–390, 2005.

[36] S. P. Martin, "A Supersymmetry primer," *Adv.Ser.Direct.High Energy Phys.*, vol. 21, pp. 1–153, 2010.

[37] G. Bertone, J. Silk, B. Moore, J. Diemand, J. Bullock, *et al.*, "Particle Dark Matter: Observations, Models and Searches," 2010.

[38] M. Maniatis, "The Next-to-Minimal Supersymmetric extension of the Standard Model reviewed," *Int.J.Mod.Phys.*, vol. A25, pp. 3505–3602, 2010.

[39] C. F. Berger, J. S. Gainer, J. L. Hewett, and T. G. Rizzo, "Supersymmetry Without Prejudice," *JHEP*, vol. 0902, p. 023, 2009.

[40] A. Arbey, M. Battaglia, and F. Mahmoudi, "Supersymmetry with Light Dark Matter confronting the recent CDMS and LHC Results," *Phys.Rev.*, vol. D88, p. 095001, 2013.

[41] K. Hagiwara, S. Mukhopadhyay, and J. Nakamura, "10 GeV neutralino dark matter and light stau in the MSSM," *Phys.Rev.*, vol. D89, p. 015023, 2014.

[42] T. Han, Z. Liu, and S. Su, "Light Neutralino Dark Matter: Direct/Indirect Detection and Collider Searches," 2014.

[43] P. Mitropoulos, "Dark matter in the Next-to-Minimal Supersymmetric Standard Model,"

[44] J. Cao, C. Han, L. Wu, P. Wu, and J. M. Yang, "A light SUSY dark matter after CDMS-II, LUX and LHC Higgs data," *JHEP*, vol. 1405, p. 056, 2014.

[45] M. Cahill-Rowley, R. Cotta, A. Drlica-Wagner, S. Funk, J. Hewett, *et al.*, "Complementarity of Dark Matter Searches in the pMSSM," 2014.

[46] A. Arbey, M. Battaglia, and F. Mahmoudi, "Light Neutralino Dark Matter in the pMSSM: Implications of LEP, LHC and Dark Matter Searches on SUSY Particle Spectra," *Eur.Phys.J.*, vol. C72, p. 2169, 2012.

[47] K. Petraki and R. R. Volkas, "Review of asymmetric dark matter," *Int.J.Mod.Phys.*, vol. A28, p. 1330028, 2013.

[48] D. E. Kaplan, M. A. Luty, and K. M. Zurek, "Asymmetric Dark Matter," *Phys.Rev.*, vol. D79, p. 115016, 2009.

[49] K. M. Zurek, "Asymmetric Dark Matter: Theories, Signatures, and Constraints," *Phys.Rept.*, vol. 537, pp. 91–121, 2014.

[50] E. Hardy, R. Lasenby, and J. Unwin, "Annihilation Signals from Asymmetric Dark Matter," 2014.

[51] I. Lopes and J. Silk, "Solar constraints on asymmetric dark matter," *Astrophys.J.*, vol. 757, p. 130, 2012.

[52] J. Kumar, "WIMPless Dark Matter: Models and Signatures," *PoS*, vol. ICHEP2010, p. 438, 2010.

[53] J. Kumar, "New Signatures of WIMPless Dark Matter," *PoS*, vol. IDM2010, p. 091, 2011.

[54] J. Kumar and J. L. Feng, "WIMPless Dark Matter," *AIP Conf.Proc.*, vol. 1200, pp. 1059–1062, 2010.

[55] R. Essig, J. A. Jaros, W. Wester, P. H. Adrian, S. Andreas, *et al.*, "Working Group Report: New Light Weakly Coupled Particles," 2013.

[56] S. Andreas, "Dark Forces and Dark Matter in a Hidden Sector," pp. 60–63, 2011.

[57] D. Hooper, N. Weiner, and W. Xue, "Dark Forces and Light Dark Matter," *Phys.Rev.*, vol. D86, p. 056009, 2012.

[58] P. W. Graham, D. E. Kaplan, S. Rajendran, and M. T. Walters, "Semiconductor Probes of Light Dark Matter," *Phys.Dark Univ.*, vol. 1, pp. 32–49, 2012.

[59] M. I. Gresham and K. M. Zurek, "Light Dark Matter Anomalies After LUX," *Phys.Rev.*, vol. D89, p. 016017, 2014.

[60] J. E. Kim, "A Review on axions and the strong CP problem," *AIP Conf.Proc.*, vol. 1200, pp. 83–92, 2010.

[61] I. P. Stern, "Axion Dark Matter Searches," *AIP Conf.Proc.*, vol. 1604, pp. 456–461, 2014.

[62] L. D. Duffy and K. van Bibber, "Axions as Dark Matter Particles," *New J.Phys.*, vol. 11, p. 105008, 2009.

[63] S. Asztalos *et al.*, "A SQUID-based microwave cavity search for dark-matter axions," *Phys.Rev.Lett.*, vol. 104, p. 041301, 2010.

[64] R. Essig, J. A. Jaros, W. Wester, P. H. Adrian, S. Andreas, *et al.*, "Working Group Report: New Light Weakly Coupled Particles," 2013.

[65] D. Akerib *et al.*, "Exclusion limits on the WIMP-nucleon cross section from the first run of the Cryogenic Dark Matter Search in the Soudan Underground Laboratory," *Phys.Rev.*, vol. D72, p. 052009, 2005.

[66] M. Ackermann *et al.*, "Dark Matter Constraints from Observations of 25 Milky Way Satellite Galaxies with the Fermi Large Area Telescope," *Phys.Rev.*, vol. D89, p. 042001, 2014.

[67] M. Aartsen *et al.*, "IceCube Search for Dark Matter Annihilation in nearby Galaxies and Galaxy Clusters," *Phys.Rev.*, vol. D88, no. 12, p. 122001, 2013.

[68] M. Aguilar *et al.*, "First Result from the Alpha Magnetic Spectrometer on the International Space Station: Precision Measurement of the Positron Fraction in Primary Cosmic Rays of 0.5350 GeV," *Phys.Rev.Lett.*, vol. 110, p. 141102, 2013.

[69] H.-B. Jin, Y.-L. Wu, and Y.-F. Zhou, "Implications of the first AMS-02 measurement for dark matter annihilation and decay," *JCAP*, vol. 1311, p. 026, 2013.

[70] T. Daylan, D. P. Finkbeiner, D. Hooper, T. Linden, S. K. N. Portillo, *et al.*, "The Characterization of the Gamma-Ray Signal from the Central Milky Way: A Compelling Case for Annihilating Dark Matter," 2014.

[71] M. Ackermann *et al.*, "Search for Gamma-ray Spectral Lines with the Fermi Large Area Telescope and Dark Matter Implications," *Phys.Rev.*, vol. D88, p. 082002, 2013.

[72] P. J. Fox, R. Harnik, J. Kopp, and Y. Tsai, "Missing Energy Signatures of Dark Matter at the LHC," *Phys.Rev.*, vol. D85, p. 056011, 2012.

[73] V. A. Mitsou, "Shedding Light on Dark Matter at Colliders," *Int.J.Mod.Phys.*, vol. A28, p. 1330052, 2013.

[74] S. Bhattacharya, S. S. Chauhan, B. C. Choudhary, and D. Choudhury, "Quark Excitations Through the Prism of Direct Photon Plus Jet at the LHC," *Phys.Rev.*, vol. D80, p. 015014, 2009.

[75] J. Read, "The Local Dark Matter Density," *J.Phys.*, vol. G41, p. 063101, 2014.

[76] M. Kuhlen, N. Weiner, J. Diemand, P. Madau, B. Moore, *et al.*, "Dark Matter Direct Detection with Non-Maxwellian Velocity Structure," *JCAP*, vol. 1002, p. 030, 2010.

[77] C. McCabe, "The Astrophysical Uncertainties Of Dark Matter Direct Detection Experiments," *Phys.Rev.*, vol. D82, p. 023530, 2010.

[78] M. C. Smith, G. R. Ruchti, A. Helmi, R. F. G. Wyse, J. P. Fulbright, K. C. Freeman, J. F. Navarro, G. M. Seabroke, M. Steinmetz, M. Williams, O. Bienaym, J. Binney, J. Bland-Hawthorn, W. Dehnen, B. K. Gibson, G. Gilmore, E. K. Grebel, U. Munari, Q. A. Parker, R.-D. Scholz, A. Siebert, F. G. Watson, and T. Zwitter, "The rave survey: constraining the local galactic escape speed," *Monthly Notices of the Royal Astronomical Society*, vol. 379, no. 2, pp. 755–772, 2007.

[79] P. J. McMillan and J. J. Binney, "The uncertainty in Galactic parameters," 2009.

[80] S. E. Koposov, H.-W. Rix, and D. W. Hogg, "Constraining the Milky Way potential with a 6-D phase-space map of the GD-1 stellar stream," *Astrophys.J.*, vol. 712, pp. 260–273, 2010.

[81] A. Kurylov and M. Kamionkowski, "Generalized analysis of weakly interacting massive particle searches," *Phys.Rev.*, vol. D69, p. 063503, 2004.

[82] J. Filippini, "A Search for WIMP Dark Matter Using the First Five-Tower Run of the Cryogenic Dark Matter Search," 2008.

[83] J. Lewin and P. Smith, "Review of mathematics, numerical factors, and corrections for dark matter experiments based on elastic nuclear recoil," *Astropart. Phys.*, vol. 6, no. 1, pp. 87 – 112, 1996.

[84] J. Engel, "Nuclear form-factors for the scattering of weakly interacting massive particles," *Phys.Lett.*, vol. B264, pp. 114–119, 1991.

[85] J. Engel, S. Pittel, and P. Vogel, "Nuclear physics of dark matter detection," *Int.J.Mod.Phys.*, vol. E1, pp. 1–37, 1992.

[86] V. Dimitrov, J. Engel, and S. Pittel, "Scattering of weakly interacting massive particles from Ge-73," *Phys.Rev.*, vol. D51, pp. 291–295, 1995.

[87] S. A. Hertel, "Advancing the Search for Dark Matter: from CDMS II to SuperCDMS," 2012.

[88] Z. Ahmed *et al.*, "Search for annual modulation in low-energy CDMS-II data," 2012.

[89] E. Armengaud *et al.*, "Background studies for the EDELWEISS dark matter experiment," *Astropart.Phys.*, vol. 47, pp. 1–9, 2013.

[90] P. Cushman, C. Galbiati, D. McKinsey, H. Robertson, T. Tait, *et al.*, "Working Group Report: WIMP Dark Matter Direct Detection," 2013.

[91] R. Agnese *et al.*, "Demonstration of Surface Electron Rejection with Interleaved Germanium Detectors for Dark Matter Search," *ArXiv e-prints*, May 2013.

[92] N. Gehrels, "Confidence limits for small numbers of events in astrophysical data," *Astrophys.J.*, vol. 303, pp. 336–346, 1986.

[93] T. Saab, "An Introduction to Dark Matter Direct Detection Searches and Techniques," 2012.

[94] R. Agnese *et al.*, "Silicon Detector Dark Matter Results from the Final Exposure of CDMS II," *Phys.Rev.Lett.*, vol. 111, p. 251301, 2013.

[95] D. Akerib *et al.*, "Exclusion limits on the WIMP-nucleon cross section from the first run of the Cryogenic Dark Matter Search in the Soudan Underground Laboratory," *Phys.Rev.*, vol. D72, p. 052009, 2005.

[96] Z. Ahmed *et al.*, "Dark matter search results from the cdms ii experiment," *Science*, vol. 327, no. 5973, pp. 1619–1621, 2010.

[97] C. E. Aalseth, P. S. Barbeau, J. Colaresi, J. I. Collar, J. Diaz Leon, J. E. Fast, N. E. Fields, T. W. Hossbach, A. Knecht, M. S. Kos, M. G. Marino, H. S. Miley, M. L. Miller, J. L. Orrell, and K. M. Yocum, "Cogent: A search for low-mass dark matter using p-type point contact germanium detectors," *Phys. Rev. D*, vol. 88, p. 012002, Jul 2013.

[98] G. Angloher *et al.*, "Results from 730 kgäâdays of the cresst-ii dark matter search," *Eur. Phys. J. C*, vol. 72, no. 4, pp. 1–22, 2012.

[99] R. Bernabei *et al.*, "New results from dama/libra," *Eur. Phys. J. C*, vol. 67, no. 1-2, pp. 39–49, 2010.

[100] D. Hooper, J. I. Collar, J. Hall, D. McKinsey, and C. M. Kelso, "Consistent dark matter interpretation for cogent and dama/libra," *Phys. Rev. D*, vol. 82, p. 123509, Dec 2010.

[101] E. Armengaud *et al.*, "Search for low-mass wimps with edelweiss-ii heat-and-ionization detectors," *Phys. Rev. D*, vol. 86, p. 051701, Sep 2012.

[102] Z. Ahmed *et al.*, "Results from a Low-Energy Analysis of the CDMS II Germanium Data," *Phys.Rev.Lett.*, vol. 106, p. 131302, 2011.

[103] J. Angle, "Erratum: Search for light dark matter in xenon10 data [phys. rev. lett. 107, 051301 (2011)]," *Phys. Rev. Lett.*, vol. 110, p. 249901, Jun 2013.

[104] E. Aprile *et al.*, "Dark matter results from 225 live days of xenon100 data," *Phys. Rev. Lett.*, vol. 109, p. 181301, Nov 2012.

[105] J. L. Feng, J. Kumar, D. Marfatia, and D. Sanford, "Isospin-Violating Dark Matter," *Phys.Lett.*, vol. B703, pp. 124–127, 2011.

[106] M. C. Pyle, "Optimizing the design and analysis of cryogenic semiconductor dark matter detectors for maximum sensitivity,"

[107] K. M. Sundqvist, "Carrier Transport and Related Effects in Detectors of the Cryogenic Dark Matter Search,"

[108] S. Leman, "Review Article: Physics and Monte Carlo Techniques as Relevant to Cryogenic, Phonon and Ionization Readout of CDMS Radiation-Detectors," *Rev.Sci.Instrum.*, vol. 83, p. 091101, 2012.

[109] J. Dubeau, L. Hamel, and T. Pochet, "Radiation ionization energy in a-Si:H.," *Physical review. B, Condensed matter*, vol. 53, pp. 10740–10750, Apr. 1996.

[110] J. Lindhard, V. Nielsen, M. Scharff, and P. Thomsen, *Integral equations governing radiation effects*. Munksgaard i komm., 1963.

[111] P. Luke, J. Beeman, F. Goulding, S. Labov, and E. Silver, "Calorimetric ionization detector," *Nucl. Instrum. Meth. A*, vol. 289, no. 3, pp. 406 – 409, 1990.

[112] B. Neganov and V. Trofimov *Otkrytiya, Izobret*, vol. 146, p. 215, 1985.

[113] R. Agnese *et al.*, "Search for Low-Mass WIMPs with SuperCDMS," 2014.

[114] D. Mei and A. Hime, "Muon-induced background study for underground laboratories," *Phys.Rev.*, vol. D73, p. 053004, 2006.

[115] G. Wang, "Phonon emission in germanium and silicon by electrons and holes in applied electric field at low temperature," *J. Appl. Phys.*, vol. 107, no. 9, p. 094504, 2010.

[116] K. M. Sundqvist and B. Sadoulet, "Carrier transport and phonon emission in germanium detectors of the cryogenic dark matter search," *Journal of Physics: Conference Series*, vol. 92, no. 1, p. 012182, 2007.

[117] D. Akerib, M. Dragowsky, D. Driscoll, S. Kamat, T. Perera, *et al.*, "Demonstration of feasibility of operating a silicon ZIP detector with 20-eV threshold," *Nucl.Instrum.Meth.*, vol. A520, pp. 163–166, 2004.

[118] J. Hall, "**CDMSlite**: First results with **T2Z1**." `http://titus.stanford.edu/cdms_restricted/Soudan/R125-128/ebook/080924/CDMSlite_FirstResults.html`, 2008.

[119] R. Basu Thakur, "**CDMSlite** study: **T3Z2 (G25)** detector with 40 volts bias.." `http://titus.stanford.edu/cdms_restricted/Soudan/R130/ebook/040111/litenote1.html`, 2011.

[120] R. Basu Thakur, "**CDMSlite** noise study: **T3Z2 (G25)** detector with 40 volts bias.." `http://titus.stanford.edu/cdms_restricted/Soudan/R130/ebook/061511/`, 2011.

[121] M. Pyle *et al.*, "Surface electron rejection from ge detector with interleaved charge and phonon channels," *AIP Conf. Proc.*, vol. 1185, no. 1, pp. 223–226, 2009.

[122] J. Sander, Z. Ahmed, A. Anderson, S. Arrenberg, D. Balakishiyeva, *et al.*, "SuperCDMS status from Soudan and plans for SNOLab," *AIP Conf. Proc.*, vol. 1534, pp. 129–135, 2012.

[123] R. Basu Thakur and M. Pyle, "First note on feasibility of cdmslite with **iZIPs**: Runs from **UCB TF**." http://titus.stanford.edu/cdms_restricted/Soudan/R130/ebook/082411/.

[124] R. Basu Thakur and A. Anderson, "**R133**: Phonon **OF** resolution." http://titus.stanford.edu/cdms_restricted/Soudan/R133/ebook/120710_2/index.html.

[125] P. Redl, "**R133** - gamma rate and leakage estimations." http://titus.stanford.edu/cdms_restricted/Soudan/R133/ebook/130718/GammaRateNote/index.html, 2013.

[126] R. Basu Thakur, "**CDMSlite**:**T5Z2** with 80 volts bias and barium source.." http://titus.stanford.edu/cdms_restricted/Soudan/R133/ebook/120612/, 2012.

[127] R. Basu Thakur, "**CDMSlite Run 2** - main voltage scan reports." http://titus.stanford.edu/cdms_restricted/Soudan/R133/ebook/140110/note1.html, 2014.

[128] L. Baudis and T. Saab, "Measuring the abundance and decay rate of the 10 kev triplet." http://titus.stanford.edu/cdms_restricted/R21/ebook/020507_6/10keV_triplet.html.

[129] D. Hooper and C. Kelso, "Implications of cogent's new results for dark matter," 2011.

[130] R. Bunker, "Initial study of r133 glitch events." http://titus.stanford.edu/cdms_restricted/Soudan/R133/ebook/120530/, 2012.

[131] R. Basu Thakur, "**CDMSlite** - summary of all cuts, efficiencies and live times." http://titus.stanford.edu/cdms_restricted/Soudan/R133/ebook/130628/Cut_alleff_summary.html, 2013.

[132] R. Basu Thakur, "**CDMSlite** - glitch cut(s) efficiencies on large ba set." http://titus.stanford.edu/cdms_restricted/Soudan/R133/ebook/130417/note2.html, 2013.

[133] R. Basu Thakur, "**CDMSlite** - glitch monte carlo." http://titus.stanford.edu/cdms_restricted/Soudan/R133/ebook/130429/note1.html, 2013.

[134] R. Basu Thakur, "**CDMSlite** - application of the r133 veto cut." http://titus.stanford.edu/cdms_restricted/Soudan/R133/ebook/130824/note1.html, 2013.

[135] R. Basu Thakur, K. Schneck, and J. Hall, "**CDMSlite** - singles efficiency." http://titus.stanford.edu/cdms_restricted/Soudan/R133/ebook/130226/note2.html.

[136] R. Basu Thakur, "**CDMSlite** - trigger efficiency calculations." http://titus.stanford.edu/cdms_restricted/Soudan/R133/ebook/130806/note_Ba_heat_lite.html, 2013.

[137] J. Sander, "Results from the cryogenic dark matter search using a chi squared analysis," 2007.

[138] Z. Ahmed *et al.*, "Search for Axions with the CDMS Experiment," *Phys.Rev.Lett.*, vol. 103, p. 141802, 2009.

[139] D. Barker and D.-M. Mei, "Germanium detector response to nuclear recoils in searching for dark matter," *Astropart. Phys.*, vol. 38, no. 0, pp. 1 – 6, 2012.

[140] D. Barker, W.-Z. Wei, D.-M. Mei, and C. Zhang, "Ionization efficiency study for low energy nuclear recoils in germanium," *Astroparticle Physics*, vol. 48, no. 0, pp. 8 – 15, 2013.

[141] S. Yellin, "Extending the optimum interval method," *ArXiv e-prints*, Sept. 2007.

[142] S. Yellin, "Finding an upper limit in the presence of an unknown background," *Phys. Rev. D*, vol. 66, p. 032005, Aug 2002.

[143] R. Agnese *et al.*, "CDMSlite: A Search for Low-Mass WIMPs using Voltage-Assisted Calorimetric Ionization Detection in the SuperCDMS Experiment," *Phys.Rev.Lett.*, vol. 112, p. 041302, 2014.

[144] C. Savage, G. Gelmini, P. Gondolo, and K. Freese, "Compatibility of DAMA/LIBRA dark matter detection with other searches," *J. Cosmol. Astropart. P.*, vol. 0904, p. 010, 2009.

[145] H. B. Li, Liao, *et al.*, "Limits on spin-independent couplings of wimp dark matter with a p-type point-contact germanium detector," *Phys. Rev. Lett.*, vol. 110, p. 261301, Jun 2013.

[146] W. Zhao *et al.*, "First results on low-mass WIMP from the CDEX-1 experiment at the China Jinping underground Laboratory," 2013.

[147] J. Angle *et al.*, "Search for light dark matter in xenon10 data," *Phys. Rev. Lett.*, vol. 107, p. 051301, Jul 2011.

[148] A. Brown, S. Henry, H. Kraus, and C. McCabe, "Extending the cresst-ii commissioning run limits to lower masses," *Phys. Rev. D*, vol. 85, p. 021301, Jan 2012.

[149] S. Archambault *et al.*, "Constraints on low-mass {WIMP} interactions on 19f from {PICASSO}," *Phys. Lett. B*, vol. 711, no. 2, pp. 153 – 161, 2012.

[150] D. Akerib *et al.*, "First results from the LUX dark matter experiment at the Sanford Underground Research Facility," *Phys.Rev.Lett.*, vol. 112, p. 091303, 2014.

[151] Y.-Y. Mao, L. E. Strigari, R. H. Wechsler, H.-Y. Wu, and O. Hahn, "Halo-to-Halo Similarity and Scatter in the Velocity Distribution of Dark Matter," *Astrophys.J.*, vol. 764, p. 35, 2013.

[152] Y.-Y. Mao, L. E. Strigari, and R. H. Wechsler, "Connecting Direct Dark Matter Detection Experiments to Cosmologically Motivated Halo Models," *Phys.Rev.*, vol. D89, p. 063513, 2014.

[153] R. Basu Thakur, "**CDMSlite** - pulse + noise simulations to study timing cuts." `http://titus.stanford.edu/cdms_restricted/Soudan/R133/ebook/130125/note2.html`, 2013.